

**UNIVERSIDADE DE SÃO PAULO**

*Formas de Utilização dos Raios-X na Investigação das Propriedades  
Estruturais de Novos Materiais*

*Tese apresentada para o concurso de  
Professor Livre-Docente, junto ao  
Departamento de Física Aplicada do  
Instituto de Física da Universidade de  
São Paulo.*



***Profa. Dra. Márcia Carvalho de Abreu Fantini***

São Paulo

1995

SBI-IFUSP



305M810T2304

*Dedico esta Tese aos Abreu-Fantini.*

## Agradecimentos

*Este trabalho foi realizado nos últimos cinco anos, e contou com a colaboração de vários pesquisadores e estudantes. Meus sinceros agradecimentos a todos.*

*À Profa. Inês Pereyra e à Profa. Annette Gorenstein, que não mediram esforços na produção de amostras, sempre mostrando entusiasmo, interesse e competência durante os experimentos, análise de resultados, apresentação e publicação dos mesmos.*

*Aos colaboradores mais distantes, Prof. Micha Tomkiewicz, Dr. Wu-Mian Shen, Prof. Richard L. Kurtz, Prof. Richard L. Stockbauer, Dra. Anne-Marie Flank e Prof. Walter Estrada, pelas oportunidades oferecidas.*

*Aos colaboradores mais próximos, Prof. Renato F. Jardim, Dr. Valmor Mastelaro, Prof. Roberto M. Torresi, Prof. Richard Landers, Profa. Sandra C. Castro, Prof. Franco Decker, Prof. Paulo V. dos Santos, Dr. George H. Bezerra, Prof. Adnei M. Andrade e Prof. Diomar R. S. Bittencourt, pelo trabalho empreendido e incentivo constante.*

*Aos estudantes do IF-USP, POLI-USP, IFGW-UNICAMP e CAMD-Louisiana-USA, Ms. Paulo A. Suzuki, Ms. Elvira L. Z. Velasquez, Srta. Patrícia S. P. Cardona, Dr. Marcelo N. P. Carreño, Srta. Heloísa Takahashi, Ms. Carla M. P. Fonseca, Ms. Irval C. Faria, Ms. Airton Lourenço, Srta. Cláudia R. C. Carvalho, Mr. K. Subramanian e Mr. N. Mainkar, que tanto colaboraram no decorrer das pesquisas.*

*Aos professores do Laboratório de Cristalografia (LCr), Prof. Aldo F. Craievich, Profa. Vivian Stojanoff, Profa. Rosângela Itri e Dr. Carlos A. M. Carvalho, pelo indispensável espírito de equipe, incentivo ao trabalho e discussões científicas. Em especial, à Profa. Lia Queiroz do Amaral.*

*Ao suporte técnico sempre presente do Ms. Douglas A. Bulla e Sr. Sérgio A. Silva do LCr, e aos funcionários técnico-administrativos do IF-USP.*

*Às agências de fomento, FINEP, CNPq e FAPESP pelo apoio financeiro.*

## ÍNDICE

Introdução	(1)
Capítulo I - Filmes Amorfos e Multicamadas a Base de Si e suas Ligas	(3)
I.1. - Estado da Arte	(3)
I.2. - Filmes de Carbetto de Silício Amorfo Hidrogenado	(3)
I.2.1. - Obtenção dos Filmes de $a\text{-Si}_{1-x}\text{C}_x\text{:H}$	(4)
I.2.2. - Caracterização dos Filmes de $a\text{-Si}_{1-x}\text{C}_x\text{:H}$	(5)
I.2.3. - Resultados e Discussão	(6)
I.2.4. - Conclusões	(15)
I.3. - Multicamadas de $a\text{:Si-H}/a\text{-Si}_{1-x}\text{C}_x\text{:H}$	(15)
I.3.1. - Obtenção das Multicamadas	(16)
I.3.2. - Caracterização das Super-redes	(17)
I.3.3. - Resultados e Discussão	(17)
I.3.4. - Conclusões	(20)
Capítulo II - Filmes Finos Eletrocromicos de Metais de Transição	(21)
II.1. - Estado da Arte	(21)
II.2. - Filmes de Óxido de Cobalto	(22)
II.2.1. - Preparação dos Filmes de $\text{Co}_x\text{O}_y$	(23)
II.2.2. - Caracterização dos Filmes de $\text{Co}_x\text{O}_y$	(24)
II.2.3. - Resultados e Discussão	(24)
II.2.4. - Conclusões	(25)
II.3. - Filmes de Óxido de Níquel	(25)

II.3.1. -Preparação dos Filmes de $\text{NiO}_x$	(28)
II.3.2. -Caracterização dos Filmes de $\text{NiO}_x$	(28)
II.3.3. -Resultados e Discussão	(29)
II.3.4. -Conclusões	(44)
 Capítulo III - Materiais Supercondutores e Precursores	 (45)
III.1. - Estado da Arte	(45)
III.2. - Fases do Bi-Sr-Co-O	(45)
III.2.1. -Preparação das Fases do Bi-Sr-Co-O	(46)
III.2.2. -Caracterização das Fases do Bi-Sr-Co-O	(46)
III.2.3. -Resultados e Discussão	(47)
III.2.4. -Conclusões	(49)
III.3. - Fitas Supercondutoras a Base de Bismuto	(49)
III.3.1. -Preparação das Fitas de Bi(Pb)-Sr-Ca-Cu-O	(50)
III.3.2. -Caracterização das Fitas	(50)
III.3.3. -Resultados e Discussão	(50)
III.3.4. -Conclusões	(52)
 Referências	 (53)
 Anexo A	 (60)
A1. - Trabalhos sobre Silício e suas Ligas Amorfas	(61)
A2. - Trabalhos sobre Materiais Eletrocromicos	(62)
A3. - Trabalhos sobre Supercondutores e Precursores	(63)

## RESUMO

Neste trabalho, foram investigados três tópicos relacionados ao estudo das propriedades estruturais de novos materiais, utilizando técnicas de difração (XRD) e espalhamento (SAXS) de raios-X: (a) filmes e heteroestruturas, amorfos, a base de a-Si:H e a-Si<sub>1-x</sub>C<sub>x</sub>:H, crescidos por descarga luminescente (PECVD), (b) filmes finos eletrocromicos policristalinos de Co<sub>x</sub>O<sub>y</sub> e NiO<sub>x</sub>, crescidos por *rf-sputtering* reativo e (c) compostos de Bi-Sr-Co-O, isotípicos aos supercondutores Bi-Sr-Ca-Cu-O, e fitas supercondutoras a base de Bi.

Os filmes de a-Si<sub>1-x</sub>C<sub>x</sub>:H, crescidos por PECVD em condições de *starving* plasma, apresentam *gap* óptico crescente com a incorporação de carbono, são isolantes elétricos e resistentes à corrosão química. As medidas de caracterização química, morfológica e estrutural mostraram que as condições de deposição de *starving* plasma promovem o crescimento de um material mais homogêneo e com tendência à ordem química do carbeto de silício cristalino. Multicamadas formadas por a-Si:H/ a-Si<sub>1-x</sub>C<sub>x</sub>:H com interfaces mais abruptas foram obtidas com crescimento sobre uma camada *buffer*, tempos de plasma *etching* de hidrogênio de, pelo menos, 2 min., e camadas de a-Si<sub>1-x</sub>C<sub>x</sub>:H crescidas com mais alta concentração de CH<sub>4</sub> na mistura gasosa e em condições de baixa potência e baixo fluxo de silano (*starving plasma*).

Filmes finos de óxido de cobalto com diferentes composições, determinadas por XRD e espectroscopia de fotoelétrons (XPS), foram investigados quanto às suas propriedades eletrocromicas. Estas dependem das condições de deposição, mas após ciclos de intercalação/de-intercalação, filmes, inicialmente com estequiometrias diferentes, apresentam propriedades muito similares, com eficiência comparável à de outros materiais eletrocromicos. As propriedades estruturais de filmes eletrocromicos de NiO<sub>x</sub> foram investigadas por XRD, em processos eletroquímicos na presença de diferentes eletrólitos aquosos. Parâmetros estruturais foram analisados para amostras crescidas em

diferentes condições, e correlacionados com medidas de variações de tensão mecânica e massa dos filmes, mostrando que o processo de intercalação ocorre no *bulk* dos cristalitos, e depende dos componentes do eletrólito. A tensão mecânica depende do grau de cristalinidade dos filmes. Espectroscopias de modulação óptica e de banda de valência foram empregadas no estudo das propriedades eletrônicas do  $\text{NiO}_x$ , indicando a presença de níveis associados ao material não-estequiométrico, e a formação de estados acima do nível de Fermi no material em estado escuro.

A substituição catiônica de Cu por Co em supercondutores a base de Bi foi estudada para se determinar as condições de sinterização ideais na formação de materiais com fase única. As técnicas de XRD, análise térmica diferencial (DTA) e medidas de resistividade elétrica foram empregadas na caracterização dos compostos. A dependência da formação das fases com a estequiometria inicial, a atmosfera e temperatura de sinterização foi estabelecida. Em fitas supercondutoras a base de Bi foi estudado o efeito de sucessivos tratamentos termo-mecânicos sobre a textura e morfologia das fitas, através das técnicas de XRD e microscopia eletrônica de varredura (SEM), acompanhando o desempenho da densidade de corrente após cada processo. Os resultados mostraram uma saturação na densidade de material cristalino e na orientação preferencial após o terceiro ciclo de esforço mecânico-aquecimento. Fitas prensadas apresentam melhores resultados de densidade de corrente crítica.

## Introdução

Desde a descoberta dos raios-X como ferramenta versátil e não-destrutiva de determinação da estrutura da Matéria Condensada, métodos experimentais cada vez sofisticadas vêm sendo desenvolvidas no sentido de poder, não só, melhorar a qualidade dos dados obtidos, como também ampliar o espectro de problemas a serem solucionados. Este é o caso dos sistemas amorfos, nos quais a inexistência de ordem estrutural de médio ou longo alcance, impedem a investigação destes sistemas pelas técnicas convencionais de difração de raios-X (XRD).

Sistemas mais ordenados, como é o caso dos materiais mono e poli cristalinos, são comumente estudados por difração de raios-X, na geometria convencional de varredura  $\theta$ - $2\theta$  [1], muito útil no estudo de amostras espessas e de filmes finos, permitindo análises de caráter composicional e estrutural. Nos casos de sistemas com baixa correlação estrutural, mas que possuem variações de densidade eletrônica da ordem de dezenas a centenas de Angstrons, o espalhamento de raios-X a baixo ângulo (SAXS) tem se mostrado uma ferramenta adequada na obtenção de informação de caráter morfológico, ou mesmo estrutural [2].

Com o advento e difusão das fontes de radiação síncrotron, em que feixes de raios-X intensos, das mais variadas energias, podem ser obtidos com alta colimação e com polarização, foram abertas novas perspectivas no estudo da estrutura da matéria.

Neste trabalho iremos focalizar aspectos estruturais de três tipos de materiais, largamente estudados por técnicas associadas aos raios-X : sistemas a base de silício amorfo hidrogenado; óxidos de metais de transição eletrocromicos, policristalinos; e, os novos supercondutores de alta temperatura crítica ( $T_c$ ), particularmente, os sistemas a base de Bi.



A apresentação do trabalho estará assim distribuída:

No Capítulo I são descritos nossos resultados recentes obtidos na investigação das propriedades químicas, morfológicas, ópticas e estruturais de filmes finos amorfos de  $a\text{-Si}_{1-x}\text{C}_x\text{:H}$  e multicamadas de  $a\text{-Si}/a\text{-Si}_{1-x}\text{C}_x\text{:H}$ , crescidos pela técnica de *Plasma Enhanced Chemical Vapor Deposition* (PECVD).

No Capítulo II descreveremos nossos resultados sobre o estudo das propriedades eletrocromicas de filmes de óxidos de metais de transição, particularmente,  $\text{Co}_x\text{O}_y$  e  $\text{NiO}_x$ , crescidos por *rf-sputtering* reativo, focalizando a relação do desempenho eletrocromico com a estequiometria e a estrutura dos compostos estudados.

No Capítulo III mostraremos resultados acerca da utilização da difração de raios-X, como técnica fundamental na investigação da cinética de formação de fases supercondutoras ou precursores, bem como efeitos de textura cristalina, através do estudo de materiais como o  $\text{Bi-Sr-Co-O}$ , e de fitas supercondutoras de  $\text{Bi(Pb)-Sr-Ca-Cu-O}$ .

As referências vêm numeradas por capítulo ao fim do texto.

No Anexo A, cópia dos principais trabalhos descritos nesta tese estão anexados.

## Capítulo I

### Filmes Amorfos e Multicamadas a Base de Si e suas Ligas

#### I.1. - Estado da Arte

Nos últimos vinte anos, a obtenção e o estudo de materiais semicondutores amorfos e suas ligas, têm merecido atenção por parte dos pesquisadores na área de Ciência dos Materiais. Em particular, o crescimento de ligas de silício amorfo hidrogenado,  $a\text{-Si}_{1-x}\text{A}_x\text{H}$  ( $A = \text{Ge}, \text{N}, \text{C}, \text{O}, \text{etc.}$ ) [1,2] tem se destacado, pela possibilidade de controlar o *gap* óptico do material, variando apenas a concentração do elemento da liga. Muito embora as propriedades elétricas do material piorem com adições pequenas do elemento da liga, inúmeras aplicações tecnológicas têm sido encontradas para estes compostos [2-5]. Multicamadas amorfas, além das aplicações em dispositivos, são sistemas muito atrativos, pois combinam a homogeneidade na direção paralela ao crescimento, com propriedades estruturais anisotrópicas na direção perpendicular ao substrato, sem as restrições impostas pelo casamento de parâmetros de rede, freqüentemente necessárias ao crescimento de heteroestruturas cristalinas [6-8]. Encontram-se no Anexo A1 os trabalhos que serão descritos neste Capítulo I.

#### I.2. - Filmes de Carbeto de Silício Amorfo Hidrogenado

Trabalhos anteriores sobre carbeto de silício amorfo hidrogenado,  $a\text{-Si}_{1-x}\text{C}_x\text{H}$ , mencionam a obtenção deste material com alto *gap* para utilização em janelas de células solares [9,10]. Outra aplicação para estes carbetos é como camada isolante em transistores de filmes finos (TFT), onde ao alto *gap*,

deve associar-se também uma alta resistividade elétrica [2,3]. A necessidade de adaptar as propriedades deste material às aplicações específicas, conduziram a uma série de estudos fundamentais sobre suas propriedades físicas [11,12]. Estes estudos mostravam a dificuldade em aumentar o *gap* acima de 3 eV, o que correspondia a concentrações de carbono em torno de apenas 50% na fase sólida. Para concentrações maiores, aglomerados de carbono na forma grafítica eram formados, com uma conseqüente redução no *gap* óptico.

Em trabalhos recentes [13] foi mostrada a possibilidade de produzir filmes de  $a\text{-Si}_{1-x}\text{C}_x\text{:H}$  com valores de *gap* óptico em torno de 4 eV, resistividade maior que  $10^{15} \Omega \text{ cm}$ , com concentrações de carbono de até 70 at.%, devido a condições especiais de deposição, conhecidas como “starving” plasma [14], as quais promoviam, aparentemente, a formação de ligações C-C do tipo diamante. As condições que determinam a situação de “starving” plasma, são um baixo fluxo de silano, combinado a uma também baixa densidade de potência rf, e altas concentrações de metano na câmara de deposição. Devido à baixa densidade de potência rf, não há energia suficiente para quebrar as moléculas de metano, de forma que todas as reações químicas que ocorrem na deposição, são conduzidas pelos radicais de silano, estes sim, formados pela decomposição por plasma, mas em baixa concentração, donde o nome “starving”, ou faminto. Neste caso, a taxa de deposição é controlada pelo fluxo de silano, cujas moléculas são rapidamente consumidas pelo plasma de rf.

A utilização destes filmes em dispositivos do tipo TFT mostrou a existência de correntes de fuga, possivelmente causadas por microporos. Desta forma, decidimos por utilizar a técnica de SAXS para caracterizar o material.

### 1.2.1. - Obtenção dos Filmes de $a\text{-Si}_{1-x}\text{C}_x\text{:H}$

Os filmes de carbeto de silício amorfo hidrogenado foram depositados pelo método PECVD, a partir de misturas gasosas de silano e

metano, num reator de acoplamento capacitivo. A temperatura de substrato foi fixada em 250 °C, a pressão de deposição foi mantida a 1 Torr e a densidade de potência foi de 150 mW.cm<sup>-2</sup>. De forma a analisar separadamente a influência do fluxo de silano e da concentração da mistura gasosa nas propriedades do material, dois conjuntos de amostras foram produzidos: o primeiro, mantendo-se o fluxo de silano constante, e o segundo, variando-se a concentração de metano na mistura, para um fluxo fixo de silano. Na Tabela I-A apresentamos as amostras produzidas e algumas de suas propriedades.

TABELA I-A  
Filmes de a-Si<sub>1-x</sub>C<sub>x</sub>:H produzidos com concentração de carbono (x), fluxo de SiH<sub>4</sub> (F), pressão parcial de CH<sub>4</sub> (P) e energia de gap (E<sub>0</sub>).

Amostra	x	F(SiH <sub>4</sub> ) sccm	P(CH <sub>4</sub> ) %	E <sub>0</sub> (eV)
MVC2	0.66	10	98	3.7
MVC1	0.70	10	92	3.4
MVC3	0.56	10	72	3.0
MVC4	0.55	10	75	3.0
MVC5	0.46	10	50	2.0
MVC6	0.54	50	72	2.8 <sup>a</sup>
MVC7	0.51	100	72	2.6 <sup>a</sup>
MVC8	0.50	150	72	2.5 <sup>a</sup>

<sup>a</sup> Estimado dos valores de E<sub>0</sub>

### I.2.2. - Caracterização dos Filmes de a-Si<sub>1-x</sub>C<sub>x</sub>:H

Neste trabalho, investigamos um conjunto de filmes de a-Si<sub>1-x</sub>C<sub>x</sub>:H. Utilizamos SAXS, para detetar a formação de microporos; Espectroscopia de

Elétrons Auger (AES), para determinar a estequiometria ( $x$ ) da liga; espectrofotometria na região do visível e infravermelho (FTIR) para encontrar o valor do *gap* óptico e os tipos de ligações químicas dentro do material; Extended X-ray Absorption Fine Structure (EXAFS) e X-Ray Absorption Near Edge Spectroscopy (XANES), para explorar as características estruturais dos filmes. Detalhes experimentais se encontram nos artigos do Anexo A1.

### I.2.3. - Resultados e Discussão

Os resultados de medidas ópticas mostraram valores de *gap* crescentes para concentrações crescentes de metano na mistura gasosa, e que filmes obtidos fora da região de “starving” plasma possuem *gap* óptico menor.

Os resultados de SAXS são mostrados nas Figuras I-1(a) e (b), I-2 (a) e (b), I-3 e I-4.

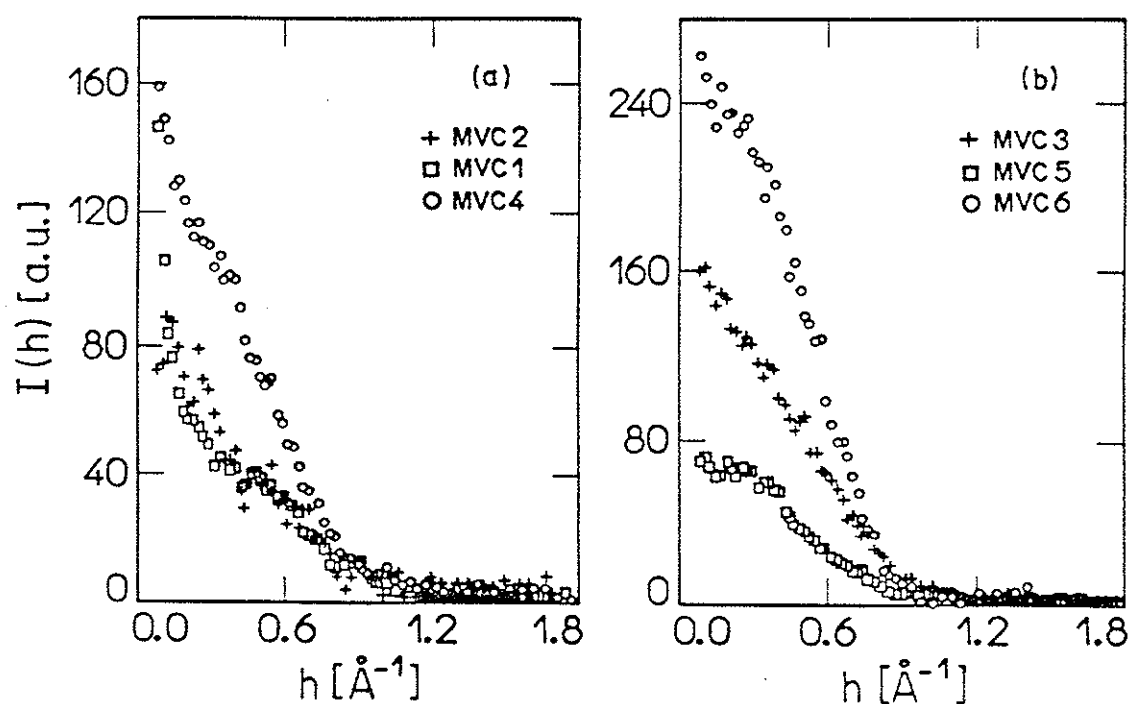


Fig. I-1. (a) e (b) - Intensidade SAXS [ $I(h)$ ] vs.  $h=4\pi\sin\theta/\lambda$  dos filmes (Tabela I-A)

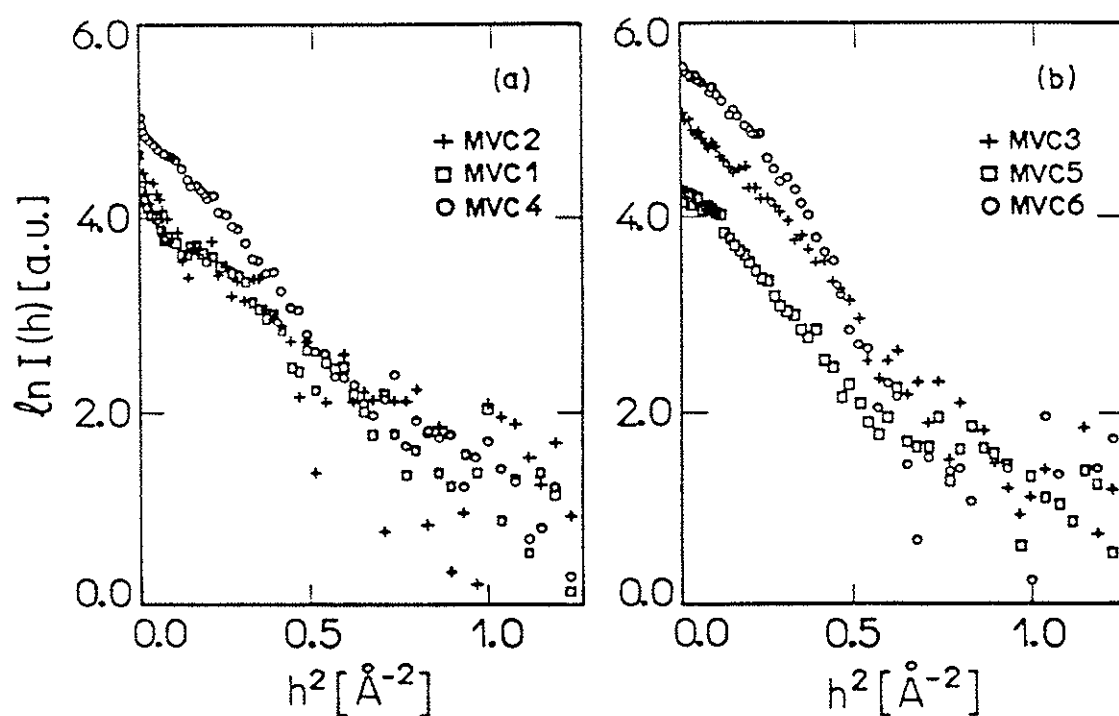


Fig. I-2. (a) e (b) - Curvas de Guinier dos filmes da Tabela I-A.

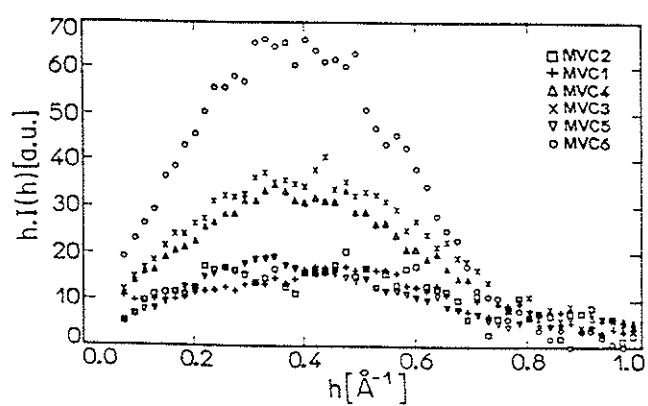


Fig. I-3. - A área sob a curva  $h[I(h)]$  vs.  $h$  é proporcional a  $\eta$ .

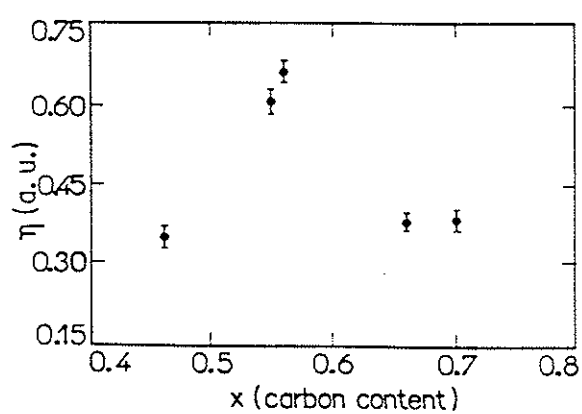


Fig. I-4. - Concentração relativa de microporos ( $\eta$ ) vs.  $[x]$ .

Na Tabela I-B mostramos os valores obtidos para o raio de giro e a concentração relativa de microporos presentes nas diferentes amostras.

TABELA I-B

Amostras de  $a\text{-Si}_{1-x}\text{C}_x\text{H}$  com raio de giro ( $R_1$  and  $R_2$ ) e concentração relativa de microporos ( $\eta$ ).

Amostra	$R_1$ (Å)	$R_2$ (Å)	$\eta \pm 0.02$ (a.u.)
MVC1	8.4	2.8	0.40
MVC3	—	3.2	0.68
MVC4	5.2	3.0	0.62
MVC5	—	3.2	0.36
MVC6	—	3.4	1.00
MVC7	—	2.6	0.99

Os resultados experimentais mostram que a concentração relativa de microporos é maior para filmes crescidos fora das condições de “starving” plasma. Os valores de raio de giro ( $R_1$ ) se mantêm praticamente inalterados com as mudanças das condições de crescimento, mas o aparecimento de raios de giro maiores ( $R_2$ ) em filmes com altas concentrações de carbono, indicam a formação de microporos maiores, ou mesmo de aglomerados de densidade eletrônica diferente da matriz de carbeto. Um resultado importante diz respeito ao fato de que a concentração de microporos não cresce em filmes com alto conteúdo de carbono ( $x$  ao redor de 0.7).

As Figuras I-5 e I-6 apresentam os resultados obtidos das medidas de FTIR para os dois conjuntos de amostras produzidas.

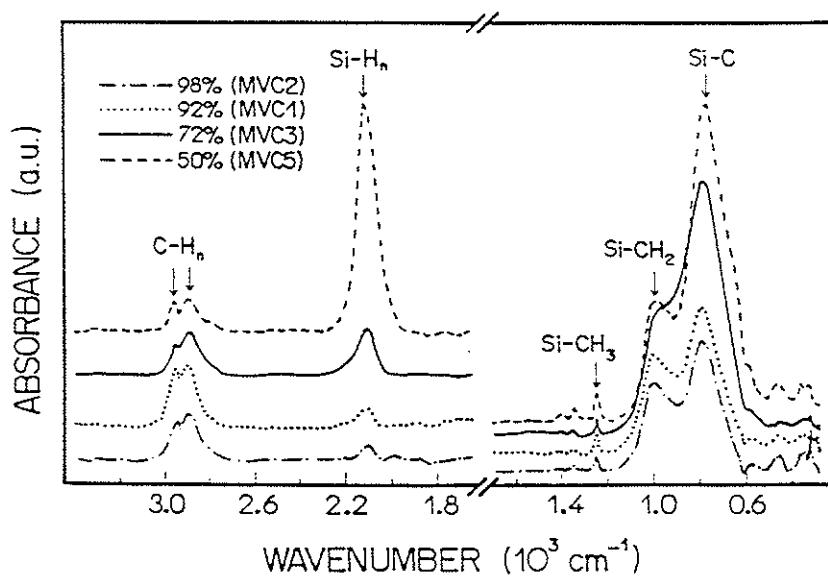


Fig. I-5. - Absorção em função do número de onda de filmes crescidos em condição de "starving", com diferentes pressões de  $\text{CH}_4$ .

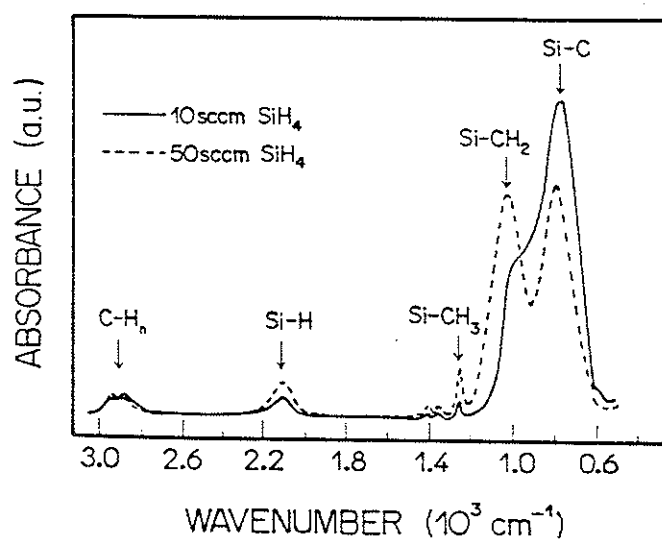


Fig. I-6. - Absorção em função do número de onda de filmes depositados com pressão parcial de metano de 72% e diferentes fluxos de silano.

Para o primeiro conjunto de amostras observa-se um decréscimo na banda correspondente ao Si-C à medida que a concentração de metano



aumenta, devido à menor disponibilidade de moléculas de silana na mistura gasosa. Entretanto, como as demais formas de incorporação de carbono permanecem praticamente inalteradas, os átomos excedentes de carbono devem estar incorporados na forma de ligações C-C, não detetáveis por FTIR. A formação de cadeias poliméricas é descartada, devido ao fato de que filmes com alto conteúdo de carbono não têm a concentração de ligações do tipo  $\text{CH}_n$  aumentada. Em contrapartida, filmes depositados com fluxo crescente de silano e pressão parcial de metano constante, correspondentes ao segundo conjunto de amostras, mostram uma incorporação maior de carbono na forma de ligações Si-C e uma diminuição de ligações do tipo Si-H<sub>n</sub> em filmes crescidos no regime de “starving” plasma.

As Figuras I-7 e I-8 mostram a transformada de Fourier dos dados de EXAFS. Uma interpretação qualitativa dos resultados das deposições em regime de “starving” (Fig. I-7) mostram que em filmes praticamente estequiométricos, a distância de primeiros vizinhos é muito similar à distância média Si-Si no a-Si:H. Por outro lado, à medida que a concentração de carbono na liga cresce, os resultados mostram claramente que a distância de primeiros vizinhos é similar à distância média Si-C, encontrada no carbeto de silício cristalino (c-SiC). Para o segundo conjunto de amostras (Fig. I-8) os resultados mostram que o número de ligações Si-C e Si-Si, associadas ao c-SiC, é menor em filmes crescidos fora do regime de “starving”. Além disso, um primeiro pico situado a aproximadamente 1.2 Å é observado e atribuído à presença de ligações Si-O.

O “fitting” dos resultados experimentais (Tabela I-C) para os casos extremos (amostras MVC1,  $x=0.70$  e MVC5,  $x=0.46$ ), mostram uma boa concordância entre o modelo de uma estrutura similar ao c-SiC em filmes com alto conteúdo de carbono (Fig. I-9), enquanto que o “fitting”, supondo o modelo de a-Si:H para a amostra com menor conteúdo de carbono (Fig. I-10), não fornece bons resultados. Na verdade, este último resultado era esperado, uma vez que a amostra MVC5 contém 46% de átomos de C, e sua estrutura não deveria ser descrita com base apenas em ligações Si-Si, similares ao a-Si:H.

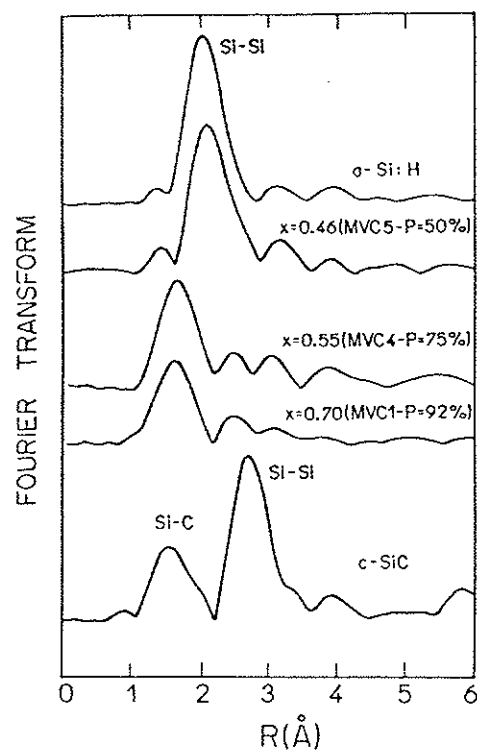


Fig. I-7. - Transformada de Fourier dos dados de EXAFS, para filmes depositados no regime de "starving" plasma e diferente pressão parcial de  $\text{CH}_4$ .

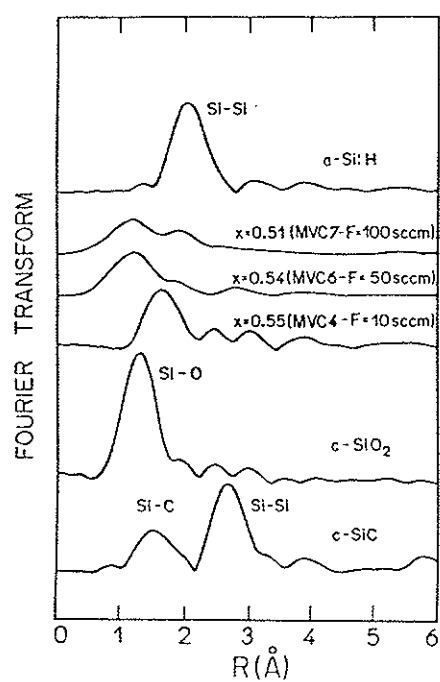


Fig. I-8. - Transformada de Fourier dos dados de EXAFS, para filmes depositados com pressão parcial de  $\text{CH}_4$  de 72% e diferente fluxo de  $\text{SiH}_4$ .

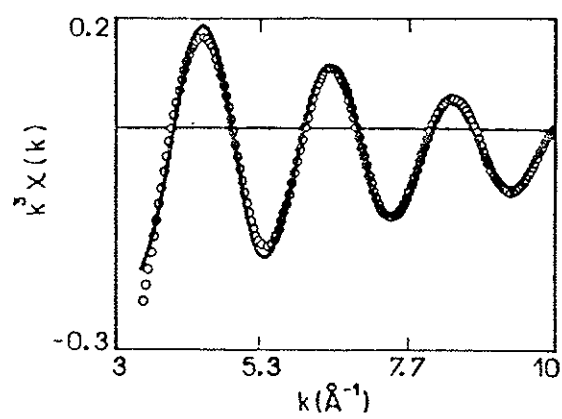


Fig. I-9. - Espectro de EXAFS da primeira camada (—) e curva calculada (°°°) com os parâmetros da Tabela I-C da amostra MVC1.

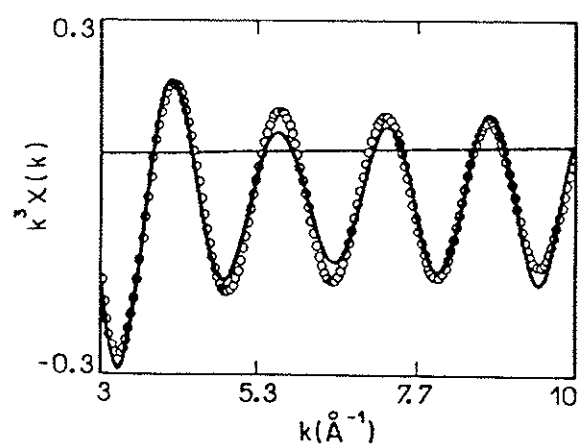


Fig. I-10. - Espectro de EXAFS da primeira camada (—) e curva calculada (°°°) com os parâmetros da Tabela I-C da amostra MVC5.

TABELA I-C

Resultados de "fitting" da primeira camada para as amostras MVC1 e MVC5

Amostra	$N_{Si-C}$	$R_{Si-C}$	$\Delta\sigma_{Si-C}$	$N_{Si-Si}$	$R_{Si-Si}$	$\Delta\sigma_{Si-Si}$
	( $\pm 0.5$ )	( $\pm 0.02$ )	( $\pm 0.02$ )	( $\pm 0.02$ )	( $\pm 0.02$ )	( $\pm 0.002$ )
MCV1	4.4	1.91	0.04	---	---	---
MVC5	---	---	---	3.7	2.36	0.0002

N e R são, respectivamente, o número e distância de primeiros vizinhos.

$\sigma$  é o fator de Debye-Waller.

As Figuras I-11 e I-12 mostram os espectros XANES dos dois conjuntos de amostras. Neste caso, observa-se novamente a similaridade entre os valores da borda de absorção e os espectros de amostras crescidas em regime de "starving" com mais alta concentração de carbono.

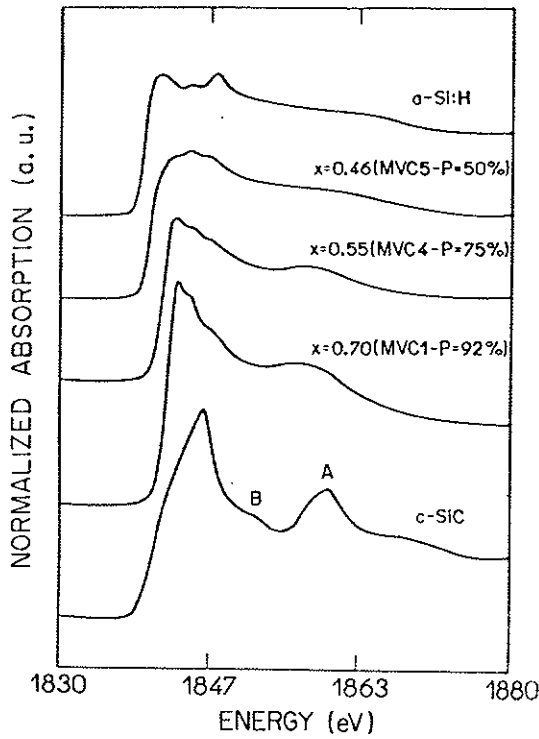


Fig. I-11. - Espectro XANES para filmes depositados no regime de "starving" plasma e diferente pressão parcial de CH<sub>4</sub>.

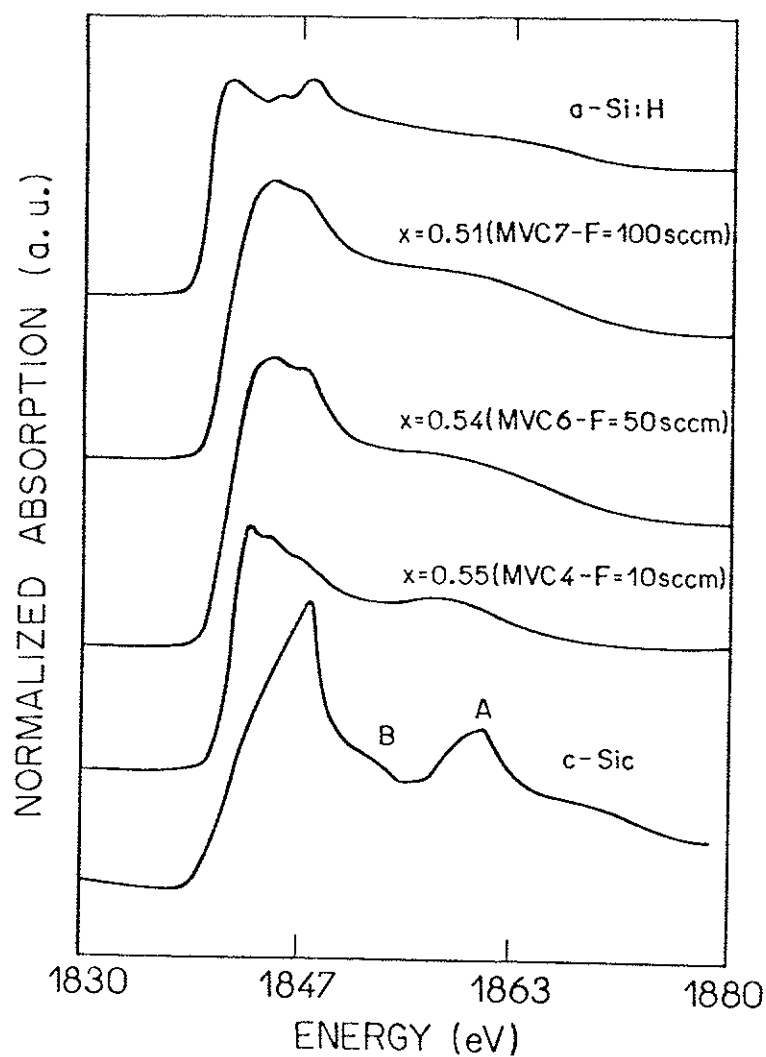


Fig. I-12. - Espectro XANES para filmes depositados com pressão parcial de  $\text{CH}_4$  de 72% e diferente fluxo de  $\text{SiH}_4$ .

Os resultados mostram que as características estruturais, morfológicas e as ligações químicas dos filmes estudados neste trabalho, depositados com diferente concentração de metano ou fluxo de silano, são muito distintas e não dependem apenas do nível de incorporação de carbono no material.

#### 1.2.4. - Conclusões

A deposição de filmes de  $a\text{-Si}_{1-x}\text{C}_x\text{:H}$  por PECVD em condições de “starving” plasma promove a formação de um material com alto conteúdo de carbono, química e estruturalmente similar ao  $c\text{-SiC}$ , tendo o silício preferencialmente coordenado ao carbono. Filmes crescidos com baixo conteúdo de carbono, ou depositados fora do regime de “starving”, possuem uma estrutura similar ao  $a\text{-Si:H}$ . A mudança de regime de baixo para alto fluxo de silano é prejudicial, uma vez que os materiais obtidos fora do regime de “starving” apresentam uma maior concentração de microporos, mais ligações do tipo  $\text{Si-CH}_n$  e uma estrutura menos similar ao  $c\text{-SiC}$ . Ligações C-C do tipo diamante podem explicar os valores de alto *gap* óptico obtidos.

#### 1.3. - Multicamadas de $a\text{:Si-H/a-Si}_{1-x}\text{C}_x\text{:H}$

Multicamadas de semicondutores amorfos, como  $a\text{-Si:H/a-Si}_{1-x}\text{C}_x\text{:H}$  e  $a\text{-Si:H/a-Ge:H}$  têm sido pesquisadas na última década [8, 5-19]. Estes sistemas, como muitos outros, são crescidos por técnicas como PECVD e “sputtering”, sendo usados na fabricação de dispositivos eletrônicos, sistemas ópticos e células solares, dentre outras aplicações [20,21]. As propriedades destes materiais são fortemente dependentes da condição de deposição e da presença ou não de hidrogênio ou outros elementos, durante o processo de crescimento.

Dentre as técnicas de análise utilizadas no estudo deste tipo de estruturas estão: difração de raios-X a baixo ângulo (SAXRD), espalhamento Raman, AES, microscopia eletrônica de transmissão (TEM), espectroscopia no infra-vermelho, difração de elétrons e nêutrons.

Neste trabalho, analisamos as propriedades das interfaces silício amorfo hidrogenado/carbeto de silício amorfo hidrogenado, através do estudo

por SAXRD, de super-redes destes materiais, variando-se a concentração de carbono na camada de carbeto. Em particular, a motivação deste estudo se deve à utilização destes dois compostos amorfos em dispositivos do tipo TFT, onde a qualidade das interfaces influenciam o desempenho dos mesmos.

I.3.1. - Obtenção das Multicamadas

Multicamadas de  $a\text{-Si:H}/a\text{-Si}_{1-x}\text{C}_x\text{:H}$ , com diferentes períodos, foram depositadas pela técnica de PECVD sobre vidro Corning 7059 e  $\text{Si-}n^+$  à temperatura de 250 °C, à potência rf de 25 mW/cm<sup>2</sup>, a partir de misturas apropriadas de  $\text{SiH}_4$  e  $\text{CH}_4$ . Ao todo dez períodos foram crescidos, alternado-se as deposições das camadas individuais sem interrupção do plasma. Variou-se: (i) a concentração de metano na camada de carbeto (pressões parciais de metano de 70%, 80% e 90%), (ii) o tempo de “etching” por plasma entre as deposições consecutivas e (iii) o tipo de substrato, com ou sem camadas de um “buffer” carbeto de silício amorfo hidrogenado, com diferente conteúdo de carbono. As diferentes amostras produzidas vêm apresentadas na Tabela I-D.

TABELA I-D  
Série de multicamadas e respectivas condições de deposição

Amostra	fluxo de <sup>a</sup> silano(sccm)	pressão de metano(%)	tempo de etching(min)	Buffer <sup>b</sup>
M80	50	80	1	---
M70-a	50	70	2.5	tipo 1
M90-a	10 <sup>c</sup>	90	2.5	tipo 1
M70-b	50	70	2.5	tipos 1-2
M90-b	10 <sup>c</sup>	90	2.5	tipos 1-2

<sup>a</sup> fluxo de silano para a deposição do carbeto. Para a deposição do silício f=50 sccm.

<sup>b</sup> tipo 1: buffer com 90% de  $\text{CH}_4$ ; tipo 2: buffer com 70% de  $\text{CH}_4$ .  $P_{rf}$  = 150 mW.cm<sup>-2</sup>.

<sup>c</sup> Regime de “starving” plasma.

### I.3.2. - Caracterização das Super-redes

As multicamadas foram caracterizadas por SAXRD e AES. Os resultados combinados permitiram estimar a espessura das interfaces. Os detalhes experimentais encontram-se em artigo do Anexo A1.

### I.3.3. - Resultados e Discussão

Os resultados experimentais permitiram determinar o período médio das multicamadas, a espessura das camadas individuais e as taxas de deposição, comparando-os com os valores nominais obtidos das taxas de deposição de filmes espessos. As constantes ópticas para os raios-X também foram avaliadas e comparadas com os valores calculados a partir de dados tabelados dos materiais cristalinos. As Figuras I-13, I-14 e I-15, mostram as curvas de difração para as séries crescidas com pressões parciais de metano de 70%, 80% e 90%.

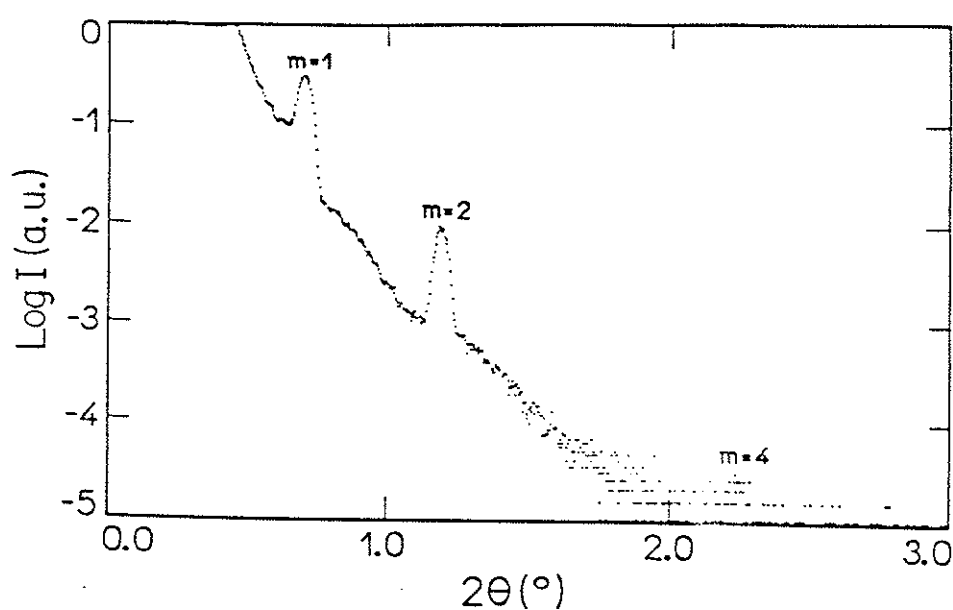


Fig. I-13. - Resultados de SAXRD para a amostra M70/4-a (Anexo A1).



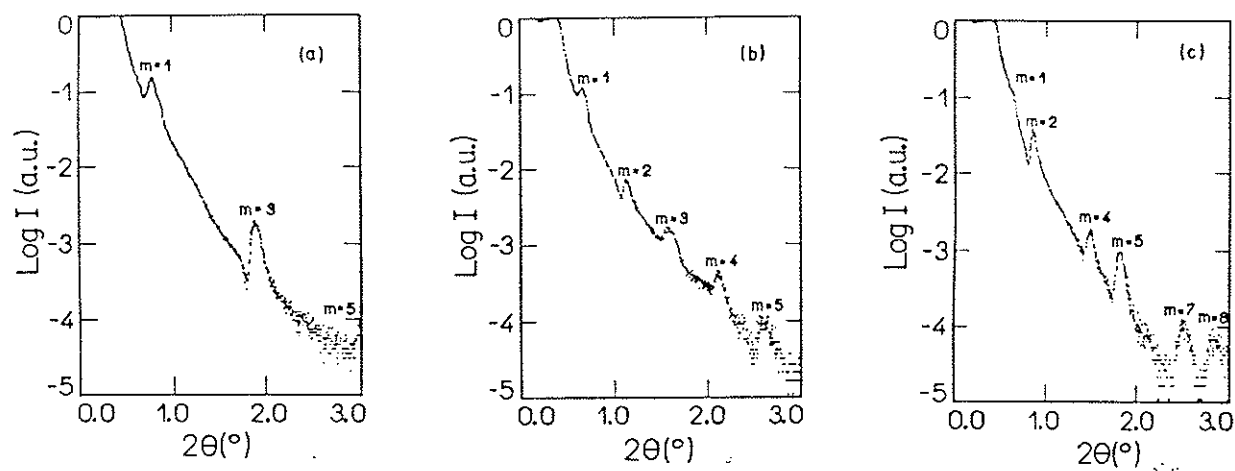


Fig. I-14. - Resultados de SAXRD para as amostras da série M80: (a) M80/2, (b) M80/3 e (c) M80/4 (Anexo A1).

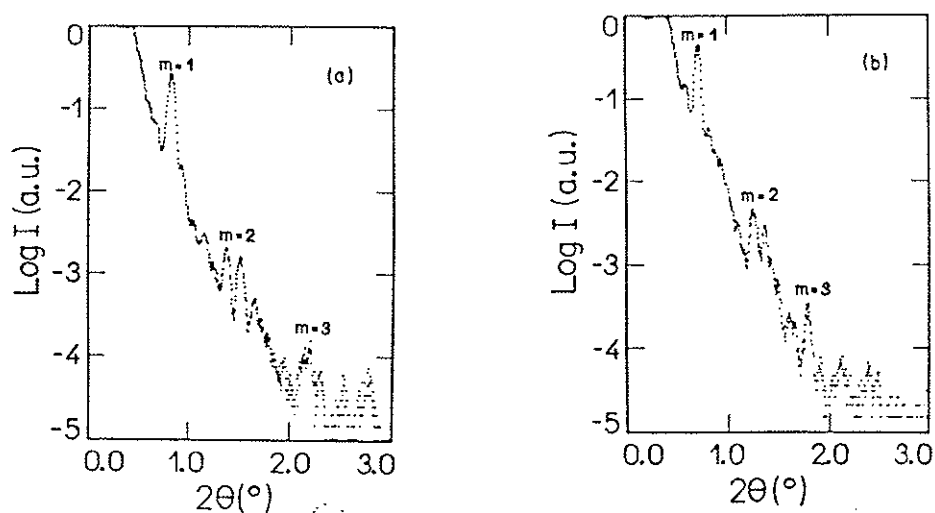


Fig. I-15. - Resultados de SAXRD para as amostras da série M90-a: (a) M90/3-a e (b) M90/4-a (Anexo A1).

Em cada série variou-se a espessura das camadas individuais, como mostram os resultados de SAXRD na Tabela I-E.

TABELA I-E

Espessura das camadas individuais  $d_{Si}$  e  $d_{SiC}$  e período ( $d \pm 3$ ) Å.

Amostra	$d_{Si}$ (Å)	$d_{SiC}$ (Å)	$d$ (Å)
M80/2	74	74	148
M80/3	96	78	174
M80/4	169	84	253
M70/4	107	53	160
M90/3	81	45	126
M90/4	108	45	153

Os valores obtidos por SAXRD e mostrados na Tabela I-E diferem dos valores esperados das taxas de deposição de filmes grossos, sendo maiores que os valores esperados. A diferença é maior para tempos de deposição curtos, e depende das características do reator, mais particularmente, da velocidade e do tempo de residência dos gases na câmara. Estes resultados demonstram a utilidade da técnica de SAXRD para caracterização das super-redes crescidas.

Com respeito às intensidades difratadas, os melhores resultados foram obtidos com filmes crescidos com tempos maiores de “etching” de plasma de hidrogênio, mostrando a eficiência deste processo na homogeneização das interfaces. Além disso, multicamadas crescidas nas mesmas condições, mas sobre substrato com camada “buffer”, apresentam melhores características de super-estruturas, o que comprova a importância do substrato no crescimento de multicamadas com periodicidade controlada e interfaces abruptas.

Os resultados de difração de raios-X, combinados com o perfil em profundidade, obtido por AES (Fig. I-16), possibilitou estimar a espessuras das interfaces, sendo estas menores (em torno de 10 Å) em multicamadas crescidas com mais alta porcentagem de carbono na camada de carvão e em regime de “starving” plasma. Este resultado concorda com dados anteriores (seção I.2), os quais mostram que de filmes de carvão de silício estruturalmente mais

ordenados e morfologicamente mais homogêneos são produzidos, quando a incorporação de carbono ocorre sob um regime de deposição de baixo fluxo de silano e baixa densidade de potência rf, *i.e.*, as condições de plasma “faminto”.

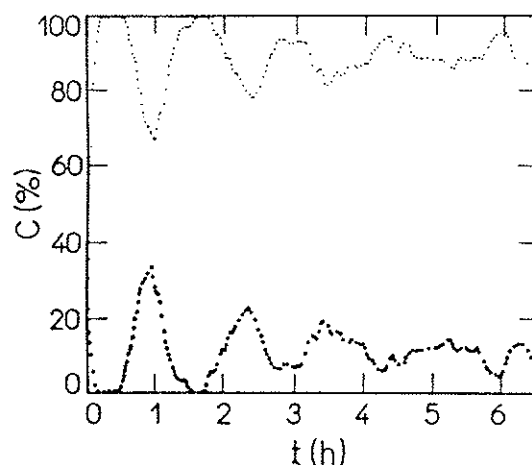


Fig. I-16. - Perfil AES da amostra M90/4-a: (•) Si e (o) C.

#### I.3.4. -Conclusões

Este trabalho mostrou que medidas de SAXRD contêm mais informação útil à caracterização de multicamadas amorfas, que a determinação usual do período. Pode-se, por exemplo, estimar espessuras individuais, determinar as constantes ópticas para os raios-X, necessárias em simulações da refletividade teórica, determinar em conjunto com a técnica de AES, a espessura aproximada das interfaces, bem como, obviamente, obter os períodos e taxas de deposição, independentemente dos valores nominais, muitas vezes imprecisos. O uso de um plasma-“etching” de  $H_2$  intermediário entre deposições consecutivas e também a presença da camada “buffer”, mostraram ser estratégias adequadas para o crescimento de super-redes estruturalmente mais ordenadas. A utilização de carbetto de silício amorfo hidrogenado, crescido em condições de “starving” plasma, com alto conteúdo de carbono, é promissora, devido às suas características morfológicas e estruturais mais homogêneas.

## Capítulo II

### Filmes Finos Eletrocrômicos de Metais de Transição

#### II.1. - Estado da Arte

“Materiais cromogênicos” [1-4] é o nome comum que se dá a uma classe de materiais que é capaz de alterar suas propriedades ópticas em resposta a mudanças nas condições que o circundam, tais como intensidade de iluminação (fotocrômicos), temperatura (termocrômicos), campo elétrico aplicado (eletrocrômicos), etc. As propriedades ópticas intercambiáveis incluem refletância, transmitância, absorvância e emitância.

Em particular, os materiais eletrocrômicos mudam suas propriedades ópticas devido à ação de um campo elétrico e podem retornar ao seu estado inicial pela simples reversão deste campo. O mecanismo por detrás destas mudanças é a inserção de pequenos íons dentro do material e a subsequente extração dos mesmos íons. Estes apresentam memória em circuito aberto, o que significa que só é necessário a aplicação de potencial, em torno de 1 V, quando se deseja alterar suas propriedades ópticas. Dispositivos usados como janelas, conhecidos como “smart windows”, ou em “display”, se constituem basicamente de: (a) uma fonte de íons (por exemplo, eletrólitos sólidos ou líquidos); (b) materiais eletrocrômicos de características reversas (coloração anódica ou catódica), um tipo de cada lado da fonte; e (c) vidros condutores transparentes (por exemplo,  $\text{SnO}_2$ ) nas extremidades, responsáveis pela distribuição do campo elétrico, e sobre os quais se depositam os filmes eletrocrômicos.

Vários tipos de compostos, orgânicos e inorgânicos apresentam propriedades ópticas dinâmicas [1-4]. Em particular, dentre os compostos inorgânicos, óxidos não estequiométricos de metais de transição, obtidos das mais diferentes formas, são conhecidos como materiais eletrocrômicos. Os

chamados bronzes metálicos de óxido de tungstênio, por exemplo,  $\text{Li}_x\text{W}_{1-x}\text{O}_y$ , são compostos largamente pesquisados, em virtude de suas propriedades ópticas variáveis. Os óxidos de níquel e de cobalto se constituem também em candidatos nessa tecnologia, sendo ambos materiais de coloração anódica.

Além das aplicações já mencionadas, materiais eletrocromicos são também utilizados em espelhos retrovisores de automóveis, experimentando um grande desenvolvimento tecnológico nos últimos anos. Normalmente os dispositivos a base de eletrocromicos possuem um filme fino de  $\text{WO}_3$  como elemento óptico ativo, mas como este material é de coloração catódica, duas diferentes estratégias podem ser seguidas para o desenvolvimento de contra eletrodos adequados. Uma alternativa é a utilização de contra eletrodos eletroquimicamente compatíveis e opticamente passivos. A outra estratégia envolve a utilização de eletrodos ativos, mas de coloração reversa : coloração anódica, como é o caso dos óxidos de cobalto e níquel. A grande maioria de dispositivos do tipo "rocking chair" fazem uso do óxido de níquel. Os óxidos de manganês e titânio também são uma possibilidade, embora tenham sido menos estudados.

## II.2. - Filmes de Óxido de Cobalto

O efeito eletrocromico em filmes finos de óxido de cobalto tem sido pouco explorado [5,6]. Recentemente, mostrou-se a existência de eletrocromismo em filmes de  $\text{CoO}_x$  hidratados, obtidos por via eletroquímica [7], com comportamento eletrocromico adequado e coloração anódica. Neste trabalho, foram depositados pela técnica de "rf-sputtering" reativo, filmes de  $\text{Co}_x\text{O}_y$ , com diferentes composições e avaliado seu desempenho eletroquímico/eletrocromico em eletrólito aquoso.

### II.2.1. - Preparação dos Filmes de $\text{Co}_x\text{O}_y$

Os filmes de óxido de cobalto foram preparados sobre substrato de vidro Corning 7059 (com ou sem  $\text{SnO}_2$ ), a partir de um alvo de cobalto, em atmosfera de oxigênio e argônio, pela técnica de "rf-sputtering"; com pressão total constante e potência rf de 100 W e 150 W. A pressão parcial de oxigênio foi variada a fim de se analisar a influência do fluxo de oxigênio e da taxa de deposição sobre a composição, estrutura e desempenho eletrocromico dos diferentes filmes. A Figura II-1 mostra as taxas de deposição em função da fração molar de oxigênio na mistura gasosa.

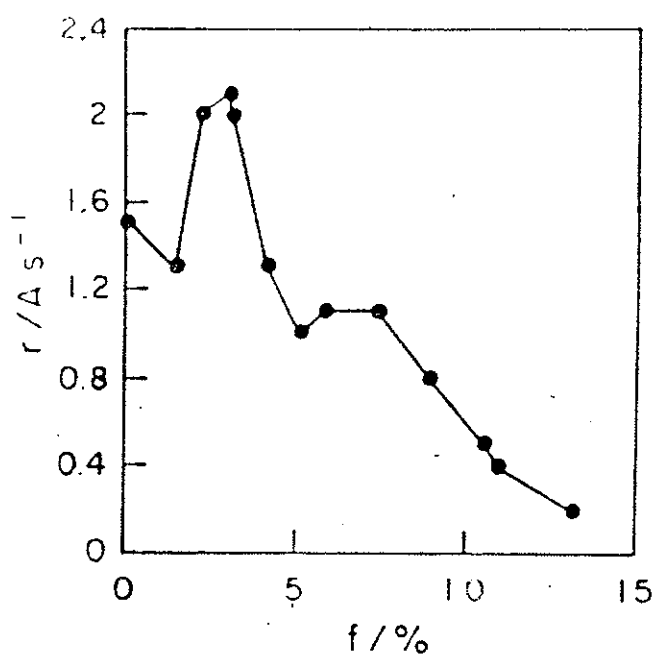


Fig. II-1. - Taxa de deposição ( $r$ ) em função da fração molar ( $f$ ) de  $\text{O}_2$ .

## II.2.2. - Caracterização dos Filmes de $\text{Co}_x\text{O}_y$

Além da voltametria cíclica, acompanhada de medidas *in-situ* da transmitância dos filmes, a estrutura e composição dos filmes no estado “as-grown” e depois de vários ciclos de clareamento/escurecimento, foram determinadas por XRD e espectroscopia de fotoelétrons (XPS). Detalhes experimentais são fornecidos no Anexo A2.

## II.2.3. - Resultados e Discussão

As Figuras II-2 (a)-(c) mostram os difratogramas das amostras no estado “as-grown”.

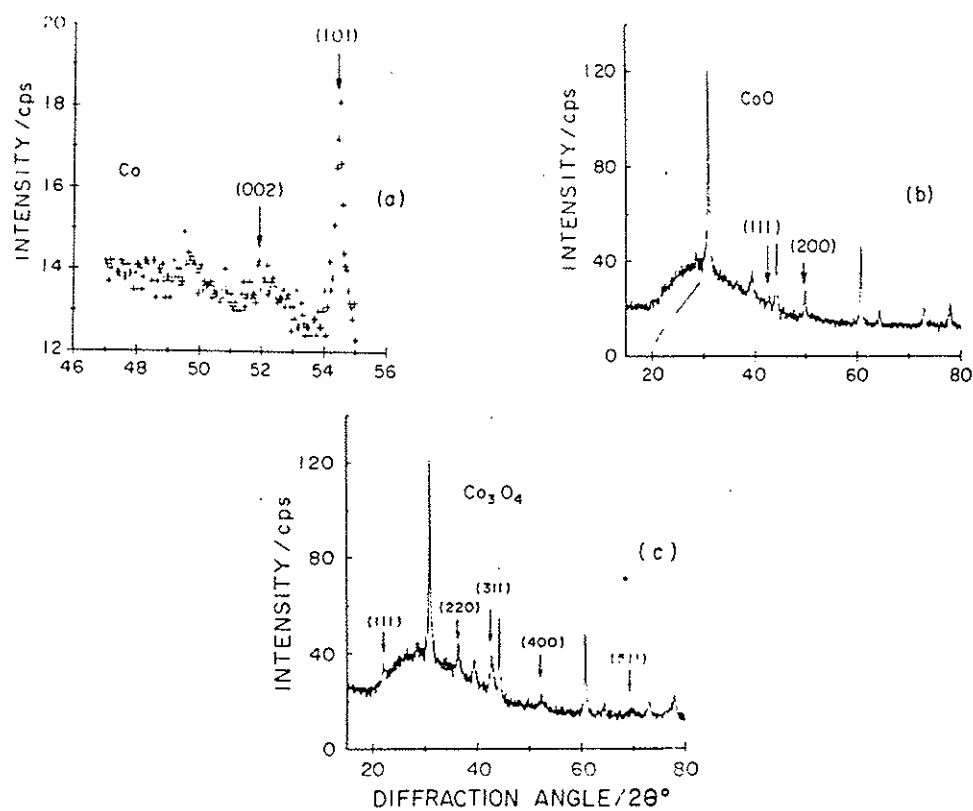


Fig. II-2 - XRD de  $\text{Co}_x\text{O}_y$  (as-grown): (a)  $f=0\%$ , (b)  $f=2.8\%$  e (c)  $f=10.5\%$ .

O material crescido sem oxigênio é o Co metálico, com estrutura hexagonal. A Fig. II-2(b) corresponde a um filme de CoO cúbico. A Fig. II-2(c) mostra a formação do  $\text{Co}_3\text{O}_4$  cúbico. Estes resultados demonstram claramente que a estequiometria dos filmes varia com o fluxo de oxigênio, sendo portanto possível pensar na obtenção, pela técnica de “rf-sputtering” reativo, de materiais com composição apropriada a uma melhor eficiência eletrocromica. Ou seja, maior variação de transmitância por unidade de carga injetada no dispositivo. Os dados obtidos por XPS concordam com os resultados obtidos por XRD, bem como a transmitância e refletância espectrais dos compostos.

Após um processo de estabilização dos filmes, mediante ciclos de clareamento e escurecimento, os resultados de XRD e XPS mostraram uma transição de fase, correspondente à formação do composto  $\text{CoOOH}$ , detetado por XRD. Os resultados obtidos permitiram inferir acerca das reações eletroquímicas que ocorrem no eletrodo.

#### II.2.4. - Conclusões

Mostramos neste trabalho a influência do fluxo de oxigênio na composição de filmes finos eletrocromicos de  $\text{Co}_x\text{O}_y$ , obtidos pelo método de “rf-sputtering” reativo. Ciclos eletroquímicos de clareamento/escurecimento transformam os filmes, originalmente diferentes, em um composto hidratado a base de Co (III). Após cerca de quarenta ciclos os filmes são estáveis e apresentam eficiência eletrocromica comparável à de outros materiais.

#### II.3. - Filmes de Óxido de Níquel

Filmes finos de óxido de níquel hidratados ou anidros, depositados por diferentes técnicas, são materiais eletrocromicos bem conhecidos [1-4].



O óxido de níquel não estequiométrico ( $\text{NiO}_x$ ) é considerado um bom candidato nas tecnologias que empregam eletrocromicos, devido ao fato ser um material de coloração anódica, óptica e eletroquimicamente compatível com o bem explorado óxido de tungstênio. As características desejáveis para aplicações nos mais variados dispositivos, incluem um tempo de resposta curto ( $< 100$  ms), uma grande variação de densidade óptica ( $> 50\%$ ), efeito de memória e longa durabilidade ( $10^5 - 10^7$  cycles) [3]. O funcionamento dos dispositivos baseados nas propriedades ópticas intercambiáveis dos eletrocromicos depende do transporte de íons, o que limita os tempos de resposta à faixa de milissegundos. Entretanto, para muitas aplicações práticas, como as chamadas “janelas-inteligentes”, tempos de resposta muito curtos não são necessários. Eficiências eletrocromicas entre  $20$  e  $30 \text{ cm}^2\text{C}^{-1}$  são facilmente obtidas para o  $\text{NiO}_x$ , independentemente da técnica utilizada para produzir o filme. Por outro lado, a obtenção de filmes uniformes e estáveis em grandes áreas, com longa durabilidade, não é uma tarefa fácil de ser cumprida, tornando-se, atualmente, o desafio tecnológico a ser enfrentado. Dentre os diferentes métodos de deposição, aqueles que se utilizam de técnicas químicas [8-10] e eletroquímicas [10-20] dão origem a filmes hidratados e porosos com tempos de resposta rápidos ( $20$  ms [1]) e com eficiências eletrocromicas notáveis ( $50 \text{ cm}^2\text{C}^{-1}$  [13]). Entretanto, filmes crescidos por esses métodos não são uniformes nem estáveis [8,11,12], apresentando efeitos de degradação, nos melhores casos, em torno de  $10^3$  ciclos de clareamento/escurecimento [17,18]. Diversos procedimentos experimentais têm sido propostos, no sentido de melhorar a durabilidade destes filmes mais baratos e de fácil deposição, incluindo tratamentos térmicos [15], ligas com outros elementos [16], eletrólitos não-aquosos [18] e outras estratégias de deposição [10,17,19,20]; entretanto, parece ser senso comum entre os especialistas, que tais filmes não são adequados às aplicações práticas, sendo necessário o desenvolvimento de outras técnicas de deposição, comercialmente compatíveis, para produzir filmes eletrocromicos de óxido de níquel mais duráveis. Dentre estes métodos, aqueles que empregam tecnologia de vácuo, como evaporação por feixe de elétrons [21-27] e dc ou rf “sputtering”

[28-39], dão origem a filmes com alta estabilidade (  $\sim 10^5$  ciclos), boa eficiência eletrocromica (  $\sim 35 \text{ cm}^2\text{C}^{-1}$  ) e tempos de resposta tão rápidos quanto 500 ms. Protótipos de dispositivos, usando óxido de níquel como material opticamente ativo, são descritos na literatura [ 40-43].

Durante os últimos dez anos, a pesquisa em  $\text{NiO}_x$  eletrocromico acumulou uma grande quantidade de conhecimento, mas ainda restam questões de caráter científico e tecnológico a serem resolvidas, ou que são pouco compreendidas. Por exemplo, o entendimento dos mecanismos responsáveis pelo comportamento eletrocromico neste material depende de informação acerca da reação de intercalação e da natureza dos íons intercalantes, bem como da dependência da eficiência eletrocromica com a morfologia, estrutura e estequiometria dos filmes estudados.

Nos últimos anos, temos nos dedicado ao estudo das características fundamentais de filmes finos eletrocromicos de  $\text{NiO}_x$ , depositados por "rf-sputtering" reativo, com o objetivo de entender e otimizar suas propriedades relevantes ao efeito eletrocromico. O objetivo de nosso trabalho tem sido o de caracterizar, da melhor forma possível e pelas mais diferentes técnicas, as propriedades: (i) estruturais, através da difração de raios-X, (ii) ópticas, por meio de medidas espectrofotométricas (iii) eletroquímicas (voltametria cíclica, variações de massa), (iv) físicas (tensão mecânica, microscopia) e (v) eletrônicas (resposta espectral, modulação óptica e elétrica, espectroscopia de elétrons). Neste trabalho, iremos apresentar resultados referentes a filmes crescidos em condições diferentes, com o intuito de correlacionar as diferentes propriedades dos mesmos com o efeito eletrocromico. A apresentação será separada em três trabalhos. No primeiro iniciamos a investigação estrutural dos filmes e apresentamos os resultados de medidas de modulação óptica; no segundo, estudamos o efeito do fluxo de  $\text{O}_2$  nas propriedades do material depositado e apresentamos resultados referentes a medidas de espectroscopia da banda de valência e, no terceiro, mostramos um estudo do processo de intercalação em diferentes eletrólitos. Estes trabalhos estão contidos no Anexo A2.

### II.3.1. - Preparação dos Filmes de NiO<sub>x</sub>

Todos os filmes estudados nestes trabalhos foram depositados a partir de um alvo de Ni em atmosfera de oxigênio e argônio, mantida à pressão total de  $7 \times 10^{-3}$  mbar, à temperatura ambiente (quando não especificada), com uma potência de rf igual a 100 W, e distância alvo-substrato em torno de 15 cm. O fluxo de O<sub>2</sub> (f) foi mantido constante em 2 sccm, exceto para as amostras, em que o estudo envolvia a variação de f. Os filmes foram sempre depositados sobre substrato de vidro recoberto com um filme semicondutor transparente, In<sub>2</sub>O<sub>3</sub>:Sn (ITO) ou SnO<sub>2</sub>, e também sobre outros substratos necessários às diferentes caracterizações efetuadas.

### II.3.2. - Caracterização dos Filmes de NiO<sub>x</sub>

Em todos os trabalhos, a voltametria cíclica, acompanhada de medidas *in-situ* da transmitância, foi a técnica empregada para uma primeira caracterização eletroquímica e óptica do material. Em seguida, a difração de raios-X foi utilizada para detectar a formação do óxido, analisar variações do parâmetro de rede em função do processo de intercalação, grau de cristalinidade, orientação preferencial e tamanho de grão cristalino. Nos primeiros trabalhos havíamos assumido a estrutura hexagonal do NiO como referência, uma vez que esta é a estrutura do material estequiométrico cristalino, à temperatura ambiente. Mais recentemente, considerando que o tamanho de grão de nossos filmes é pequeno (de 200 Å a 300 Å), optamos por adotar como referência a estrutura cúbica mais simples do NiO; e também, em razão da a distorção hexagonal ser pequena. Uma discussão completa sobre a estrutura do NiO se encontra em artigo do Anexo A2 ("*On the structural properties of electrochromic NiO<sub>x</sub> sputtered thin films*"). Medidas de fotocorrente e eletrorefletância foram efetuadas, bem como, espectroscopia de banda de

valência (UPS), com o objetivo de analisar mudanças nos estados eletrônicos em função do estado óptico. Medidas de tensão mecânica e de variação de massa durante o processo de intercalação/de-intercalação foram também efetuadas com o objetivo de analisar a reação eletroquímica de intercalação. Detalhes experimentais são descritos nos artigos contidos no Anexo A2.

### II.3.3. - Resultados e Discussão

#### Eletrorefletância e Fotorresposta de Filmes Finos de $\text{NiO}_x$

Na Fig. II-3 apresentamos uma curva típica de voltametria cíclica e variação de transmitância dos filmes crescidos em condições padrões ( $f=2$  sccm,  $P=100$  W e temperatura ambiente). Variações de cerca de 60% a 80% entre o estado claro e escuro do material são comumente obtidas.

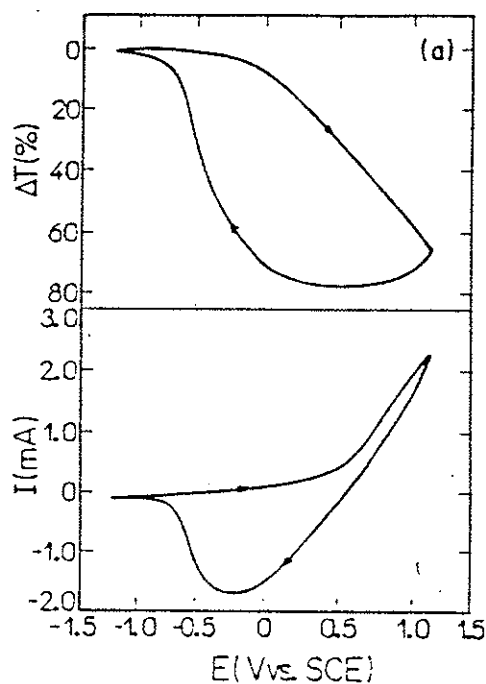


Fig. II-3. - Curva corrente-tensão e variação de transmitância do  $\text{NiO}_x$ .

Na Fig. II-4 as curvas de fotoresposta de um filme típico, em diferentes estados ópticos, mostram que o material no estado escuro possui uma taxa maior de recombinação de portadores, compatível com o modelo de defeitos na estrutura NiO deficiente em Ni ( $\text{NiO}_x$ ,  $x > 1$ , semiconductor do tipo p). Os resultados da fotoresposta permitiram avaliar a existência de duas energias de *gap*, uma direta em torno de 3 eV, praticamente invariante mediante as modificações na transmitância, e outra menor, indireta em torno de 2.5 eV, que se modifica ao longo do processo de intercalação.

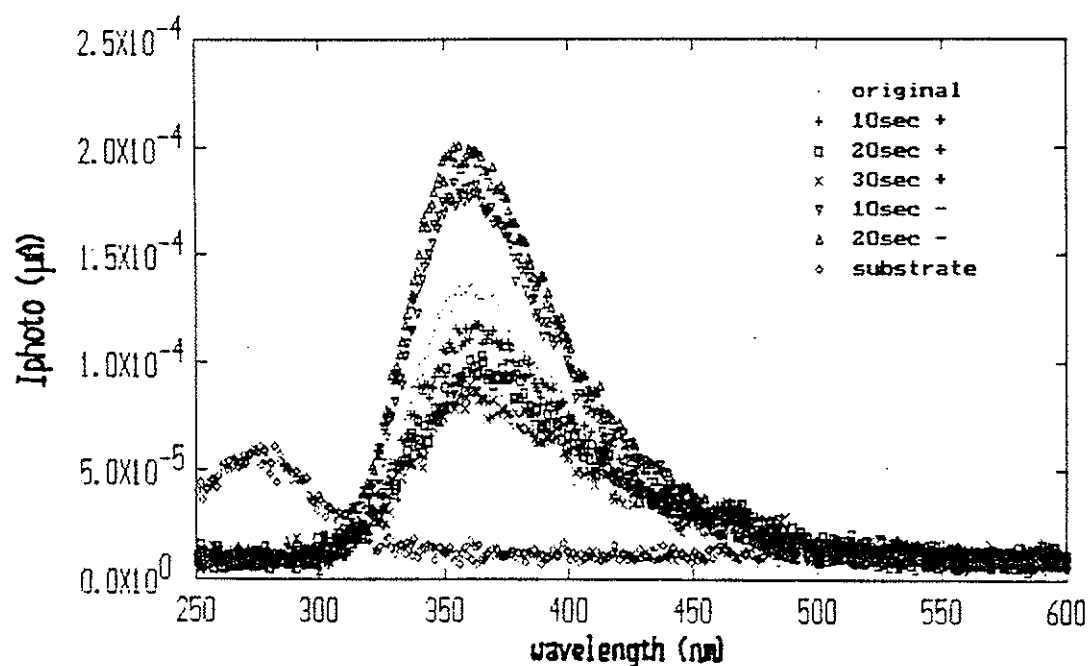


Fig. II-4. - Fotocorrente do  $\text{NiO}_x$  para vários potenciais.

Os resultados de eletrorefletância mostram, pela primeira vez, a existência de um nível eletrônico ( $E=2.15$  eV) atribuído à presença de vacâncias de Ni na estrutura. Na Fig. II-5 (a) e (b), estas medidas são apresentadas, onde se destaca o efeito de tratamento térmico sobre este nível eletrônico (Fig. II-5b). Após o processo de aquecimento a  $300^{\circ}\text{C}$ , por 24 hs em ar, o material perde suas propriedades eletrocromicas, possivelmente em decorrência de mudanças em sua estequiometria. O "fitting" dos perfis de linha do sinal de eletrorefletância permitiu avaliar a variação de quatro níveis eletrônicos com o potencial aplicado ao material, durante o processo de intercalação/de-intercalação. Na Fig. II-6 são apresentadas duas curvas, uma experimental e outra calculada, exemplificando os resultados obtidos para o potencial de 0 V vs. SCE, aplicado à cela eletroquímica.

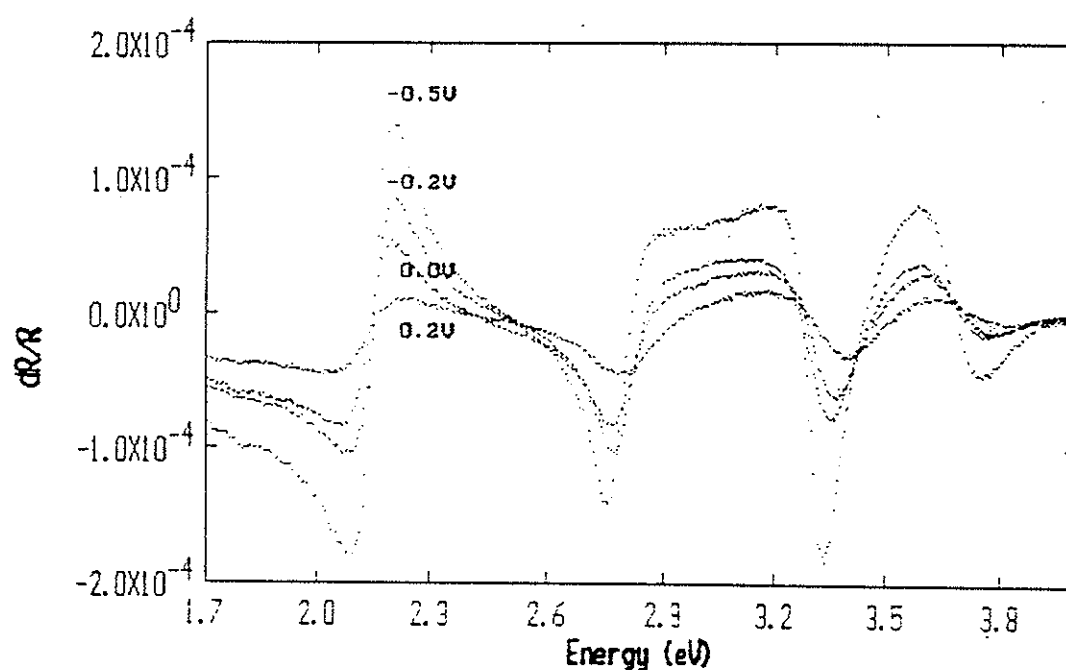


Fig. II-5(a) - Sinal de eletrorefletância em função do estado de coloração.

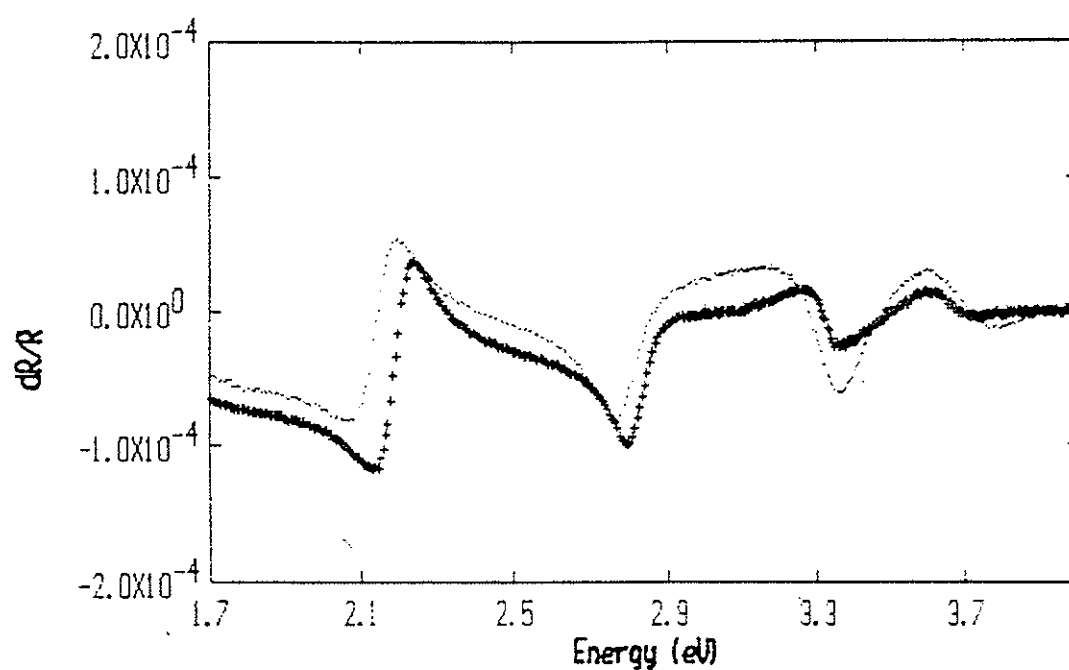


Fig. II-5(b) - Comparação entre amostra as-grown e aquecida : Eletrorefletância

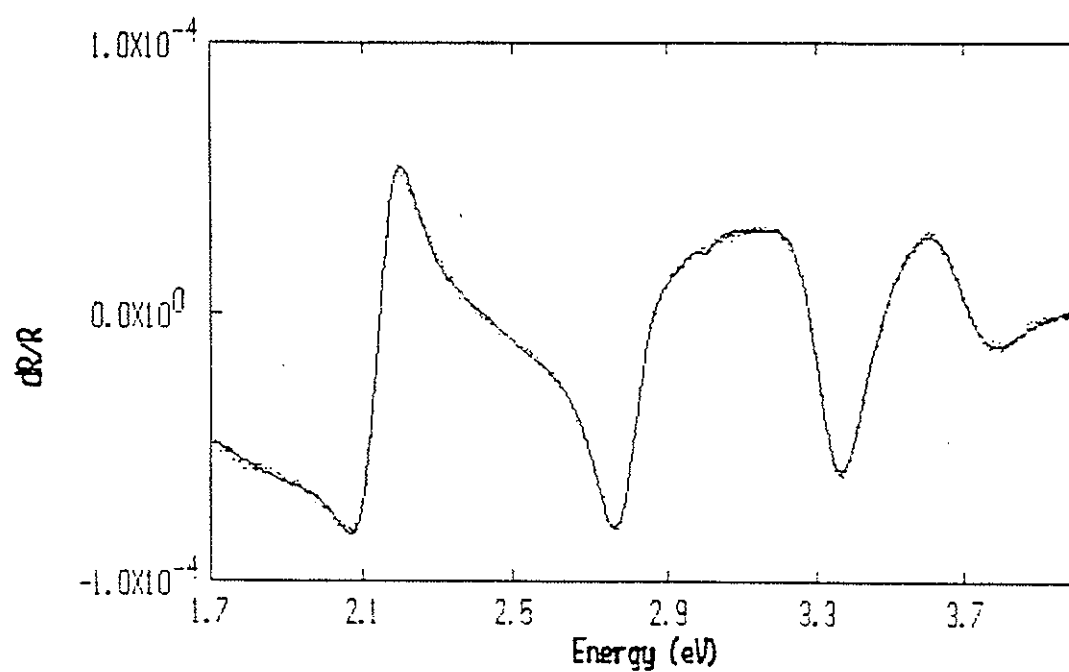


Fig. II-6. - Eletrorefletância de amostra "as-grown" ao potencial de 0 V vs. SCE:  
(•) experimental e (—) teórico

Os primeiros resultados de difração de raios-X nos filmes finos de  $\text{NiO}_x$  que temos estudado mostraram a formação de um material policristalino, com parâmetro de rede maior que o valor do  $\text{NiO}$  estequiométrico. Estes resultados preliminares indicam, após a análise de filmes crescidos a temperatura de substrato diferente, que maiores valores de parâmetro de rede não implicam em melhor eficiência eletrocromica. Neste caso, a estequiometria do composto, ou valor de  $x$ , é o parâmetro relevante na análise do comportamento do material. Após tratamentos térmicos, os filmes não apresentam efeito de eletrocromismo, o que novamente indica mudanças na estequiometria, com uma conseqüente diminuição do parâmetro de rede. A temperatura de substrato afeta não somente a composição do material, mas também a orientação preferencial de crescimento de cristalitos. A orientação preferencial de grãos paralelos à superfície do filme fino pode influenciar o desempenho eletrocromico uma vez que este processo envolve a entrada e saída de íons no material, modificando seu parâmetro de rede.

#### Estudos da Banda de Valência de Filmes Finos Eletrocromicos de $\text{NiO}_x$

Neste trabalho investigamos sistematicamente as variações que ocorrem nos filmes finos de  $\text{NiO}_x$ , crescidos com fluxo de  $\text{O}_2$  ( $f$ ) diferente. Pudemos observar que o processo de intercalação (estado claro) resulta num aumento do volume da cela unitária, enquanto que a de-intercalação (estado escuro) promove uma diminuição neste mesmo volume. A modificação do fluxo de oxigênio acarreta modificações na estrutura do material (parâmetro de rede, orientação preferencial, tamanho de grão e grau de cristalinidade), na transmitância, na cinética de intercalação e possivelmente em sua composição. Resultados de Rutherford Back Scattering (RBS) apontam  $x=1.07\pm0.02$ , em filmes típicos, crescidos com  $P=100$  W,  $f=2$  sccm e temperatura ambiente.

Os resultados de medidas de espectroscopia de elétrons na região do ultravioleta (UPS), realizadas com uma fonte de radiação síncrotron (CAMD,



Baton Rouge, LA, USA) permitem analisar modificações que ocorrem na banda de valência do material, em decorrência do processo eletrocromico. A importância destas medidas reside no fato de que as ligações químicas são feitas com elétrons da banda de valência e modificações nestas ligações devem existir para filmes em diferentes estados de coloração. Nas Figuras II-7 a II-10 mostram os resultados obtidos destas medidas. O resultado mais importante diz respeito ao aumento de estados que cruzam o nível de Fermi (Fig. II-10), formando um tipo de banda de condução no filme colorido. Neste caso a formação de estados dentro do *gap* podem explicar as modificações nas propriedades ópticas e eletrônicas do  $\text{NiO}_x$  eletrocromico nos estados claro e escuro. Este modelo de bandas é consistente com um mecanismo de transferência de cargas entre estados separados por pequenas bandas de energia e é compatível com os resultados de fotocorrente e eletrorefletância, por nós obtidos anteriormente.

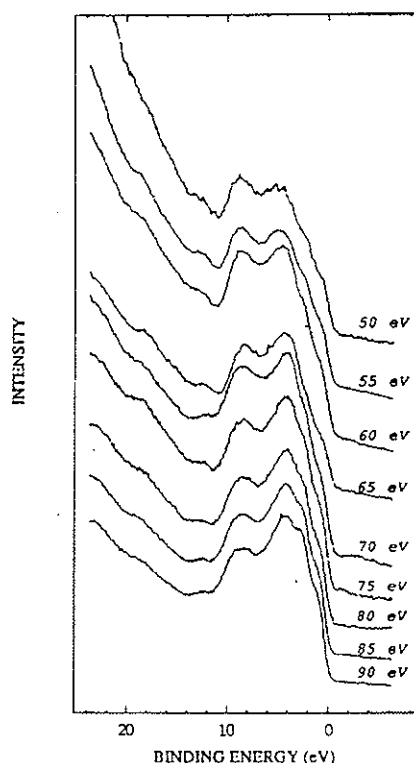


Fig. II-7. - Espectros da banda de valência para diferentes energias de fótons incidentes ( $h\nu$  em eV).

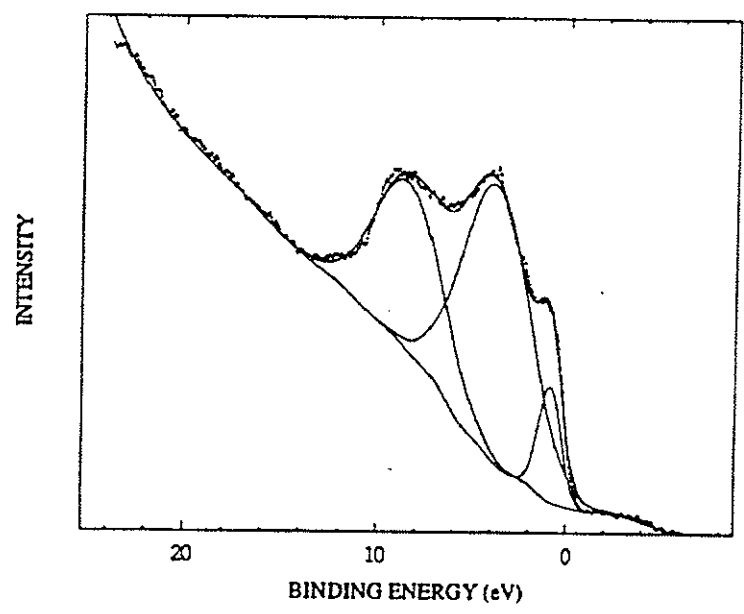


Fig. II-8. - "Fitting" da banda de valência por três funções Gaussianas

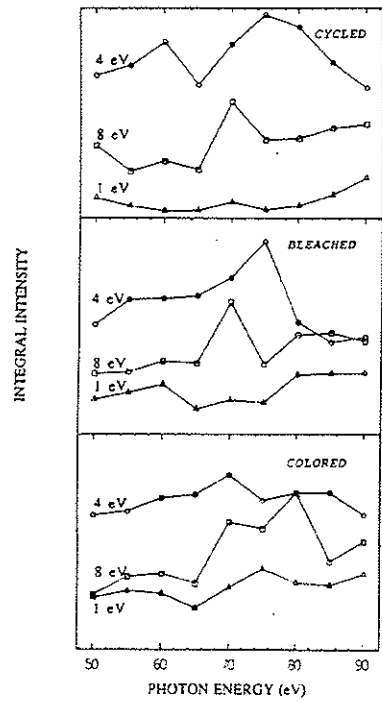


Fig. II-9. - Intensidade integrada dos três picos da banda de valência em função da energia do fóton incidente.

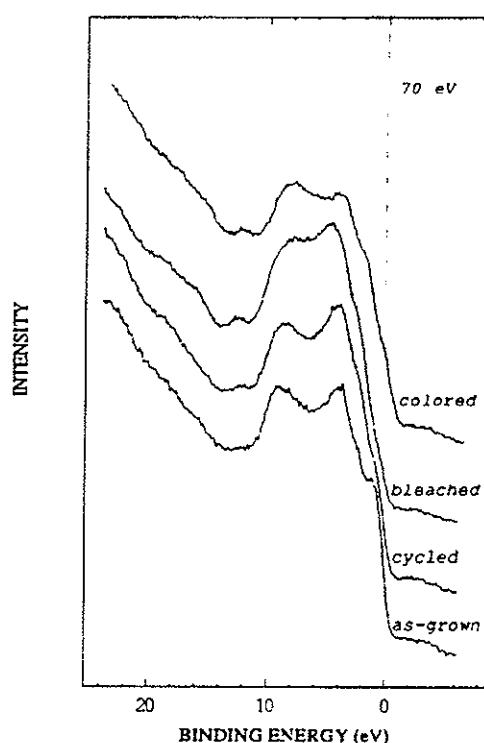


Fig. II-10. - Dados de UPS de uma amostra de  $\text{NiO}_x$ , crescida com  $f = 6$  sccm, em diferentes estados de coloração, medidas com  $h\nu = 70$  eV.

#### Sobre as Propriedades Estruturais de Filmes Finos de $\text{NiO}_x$

A Fig. II-11 mostra os resultados de XRD para duas amostras (M e N) de  $\text{NiO}_x$ , com diferentes graus de cristalinidade. Estas amostras foram cicladas em eletrólitos a base de  $\text{LiOH}$ ,  $\text{NaOH}$ ,  $\text{KOH}$ ,  $\text{RbOH}$  e  $\text{CsOH}$ , a fim de se avaliar a dependência do processo de intercalação com a composição do eletrólito. Medidas de variação na tensão mecânica ( $\Delta\sigma$ ) e variação de massa ( $\Delta M$ ) em função da carga ( $\Delta Q$ ) [41-43], mostradas nas Figs. II-12(a) e (b) e Fig. II-13, apresentam mudanças que dependem da composição do eletrólito. Os resultados de XRD, apresentados na Fig. II-14 para filmes nos estados claro e escuro, mostram também que ocorrem variações no volume da cela unitária,

que dependem da composição do eletrólito. Nas Tabelas II-A e II-B apresentamos os valores obtidos para os parâmetros de rede ( $a$ ) e volumes ( $V$ ) da cela unitária para os filmes da série M e N, respectivamente, em diferentes estados de coloração e nos vários eletrólitos investigados.

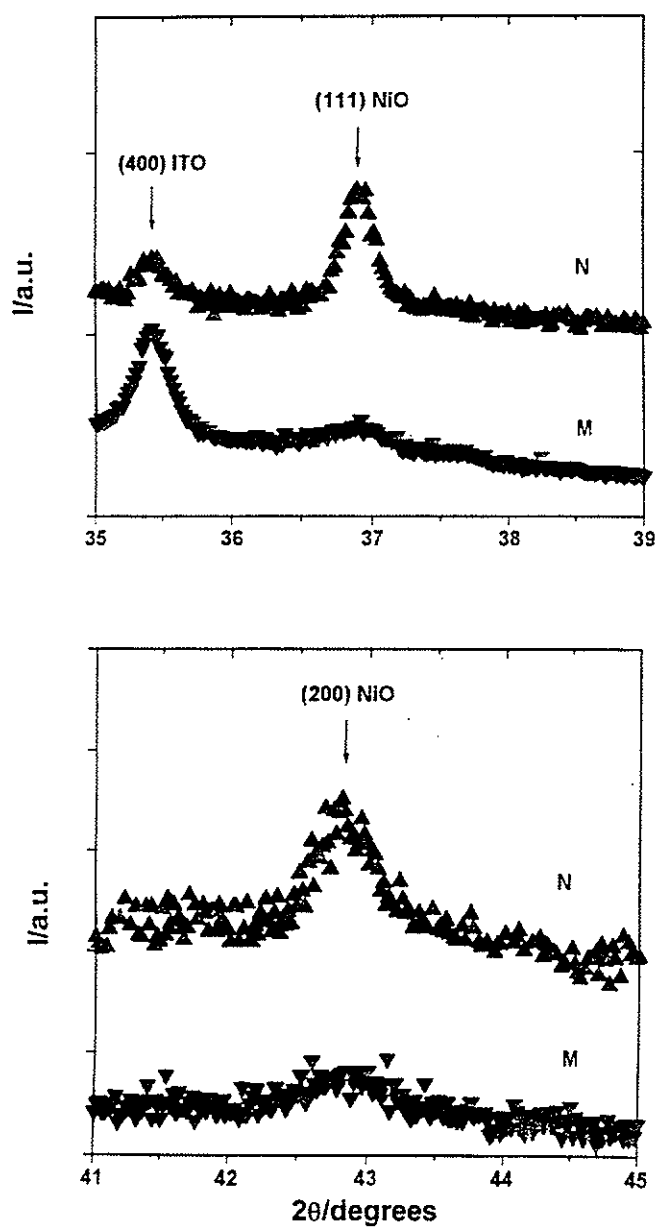


Fig. II-11. - Difratogramas de duas amostras (M e N), depositadas sobre ITO/vidro ( $\lambda=1.5418 \text{ \AA}$ )

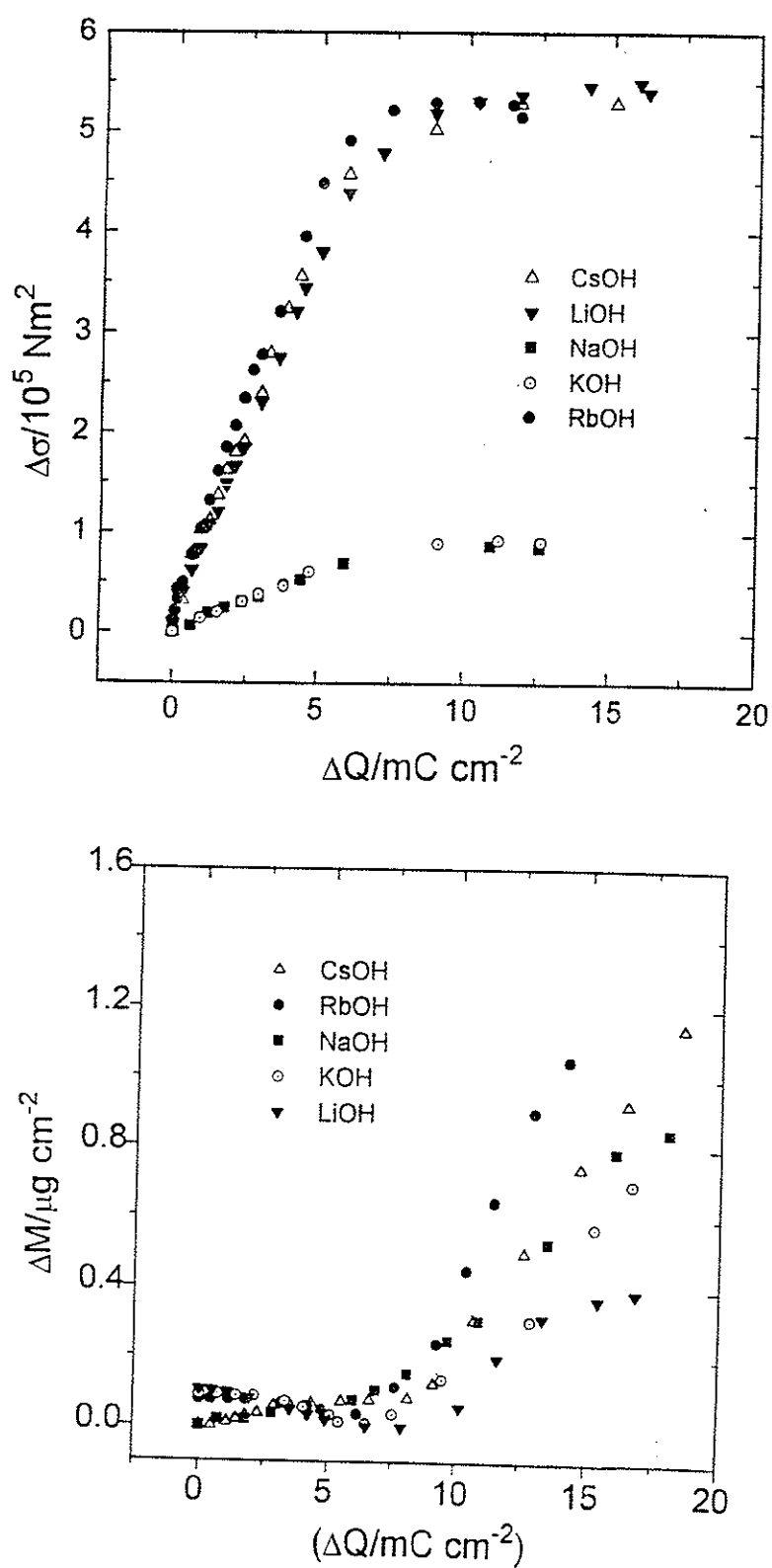


Fig. II-12. - (a) Variação de tensão, (b) Variação de massa.  
Amostra M, ciclo anódico

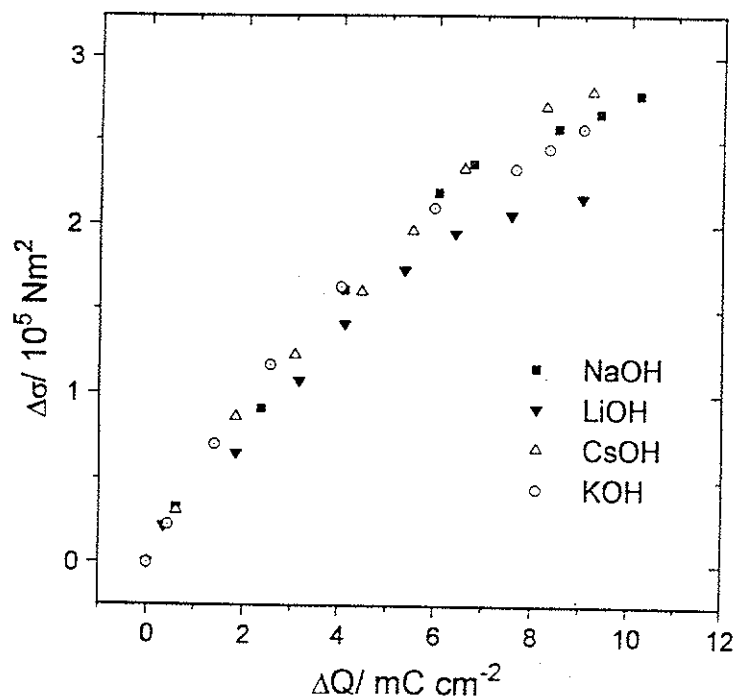


Fig. II-13. - Variação de tensão. Amostra N, ciclo anódico.

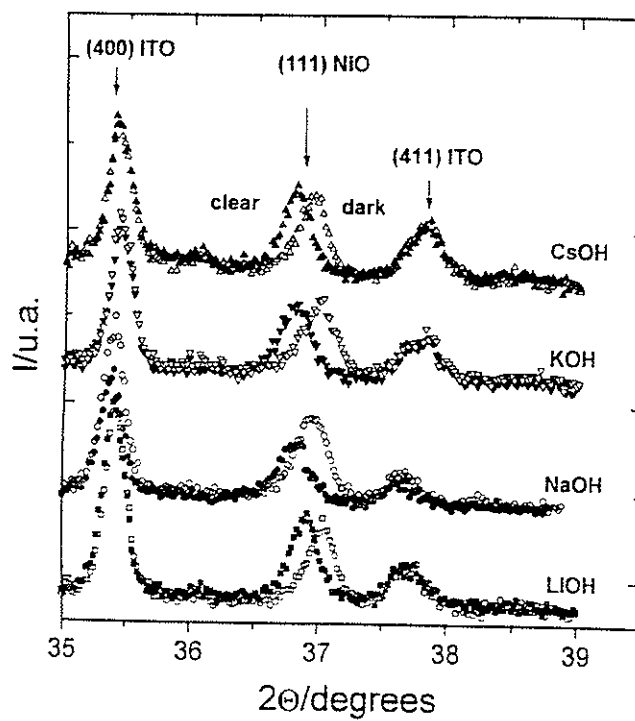


Fig. II-14. - Difratomogramas da amostra N no estados claro e escuro ( $\lambda=1.5418 \text{ \AA}$ ).

TABELA II-A

Parâmetro de rede (a), Volume da cela unitária (V) das amostras da série M

Amostra	a (Å)	V (Å <sup>3</sup> )
M-a	4.2181±0.0034	75.05±0.18
M-c (KOH)	4.2235±0.0010	75.34±0.005
M-e (KOH)	4.2037±0.0028	74.28±0.15 (1.06)
M-c (LiOH)	4.2194±0.0036	75.12±0.19
M-e (LiOH)	4.2031±0.0073	74.25±0.39 (0.87)

Números entre parênteses são a diferença de volume entre os estados claro e escuro.  
a: as-grown/ c: claro/ e: escuro

TABLE II-B

Parâmetro de rede (a), Volume da cela unitária (V) das amostras da série N

Amostra	a (Å)	V (Å <sup>3</sup> )
N-a	4.2223±0.0037	75.27±0.20
N-c (LiOH)	4.2221±0.0028	75.26±0.15
N-e (LiOH)	4.2133±0.0076	74.79±0.40 (0.47)
N-c (NaOH)	4.2331±0.0049	75.85±0.26
N-e (NaOH)	4.2177±0.0050	75.03±0.27 (0.82)
N-c (KOH)	4.2353±0.0057	75.97±0.31
N-e (KOH)	4.2208±0.0065	75.19±0.35 (0.79)
N-c (CsOH)	4.2316±0.0053	75.77±0.29
N-e (CsOH)	4.2174±0.0099	75.01±0.53 (0.76)

Números entre parênteses são a diferença de volume entre os estados claro e escuro.  
a: as-grown/ c: claro/ e: escuro

Os resultados difração de raios-X apontam uma diminuição no volume da cela unitária no ciclo de escurecimento para ambas as séries de amostras (M e N), como era se esperar se a reação de oxidação é um processo

de de-intercalação. Além disso os valores da série N mostram claramente uma diferença menor para o filme intercalado em LiOH, o que concorda com o resultado de tensão mecânica. Os resultados da série M são de difícil interpretação, dado o baixo grau de cristalinidade destas amostras; entretanto, como a tensão mecânica é maior, provavelmente o grau de cristalinidade influencia a tensão nos filmes. A variação da transmitância óptica é igual para as duas séries de amostras, em todos os eletrólitos. Os resultados de tensão mecânica apontam uma diminuição de volume no ciclo anódico, mas que varia com a composição do eletrólito. O comportamento inverso é detectado no ciclo catódico. Há um aumento de massa no ciclo anódico, na região de potencial dos principais processos eletroquímicos. Novamente as variações de massa dependem do eletrólito.

Vários estudos exploraram as propriedades morfológicas e estruturais de filmes finos eletrocromicos a base de níquel [13,20,32,37,39,47,52]. Nesses trabalhos observamos que as características destes filmes dependem não apenas do método de deposição mas também das condições de crescimento para cada técnica particular. Independentemente do método de preparação a morfologia e estrutura do filme influenciam o processo eletrocromico, sendo necessário controlar estas propriedades a fim de se atingir um bom desempenho do material [32,51-53]. Entretanto não há uma conclusão clara acerca da influência dos contornos de grão no processo de (de)intercalação, ou mesmo acerca da influência do grau de cristalinidade e orientação cristalina preferencial. Alguns autores concluem que filmes mais porosos e heterogêneos apresentam menor eficiência e durabilidade [13,32,34,51,52]. Por outro lado, outros pesquisadores mencionam que o processo de (de)intercalação ocorre nos contornos de grão e portanto, espera-se um aumento na eficiência eletrocromica de filmes mais porosos. Há claras evidências que a reação de eletrocromismo ocorre no interior dos cristalitos, pois são observadas variações nos parâmetros de rede de amostras em diferentes estados de coloração [47,53]. É razoável supor que a porosidade afeta o transporte do eletrólito através do filme, mas a reação de troca dos íons



se passa do contorno para o volume interno dos cristalitos, sendo governada pela disponibilidade de defeitos, ou estequiometria, como também, pela orientação cristalográfica dos cristalitos, ou o melhor caminho na rede para o transporte de íons. Resultados anteriores de XRD claramente demonstram variações nos parâmetros de rede [47,53] e mudanças de fase [54], decorrentes do processo eletroquímico/eletrocromico. A idéia de usar a difração de raios-X para investigar modificações nos parâmetros de rede, causadas pela (de)intercalação de amostras idênticas em eletrólitos diferentes, foi baseada na hipótese de que os cátions alcalinos, além do  $H^+$ , podem entrar e sair reversivelmente da rede cristalina. Esta hipótese se baseava também em resultados anteriores, que indicavam a participação de outros íons, como os alcalinos e  $OH^-$ , na reação eletroquímica [10, 25,27,55-60].

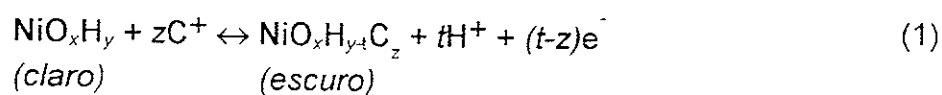
Neste trabalho, assumimos a estrutura cúbica do  $NiO$ , mais simples, desprezando a distorção hexagonal do composto à temperatura ambiente ou mesmo falhas de estequiometria [61-66]. Em cálculos de estrutura de bandas do material estequiométrico a distorção da rede também é desprezada [ 67,68].

Nossos resultados mostram claramente que o processo de eletrocromismo acontece devido a uma reação de intercalação pois volume (tensão mecânica e XRD) e massa (EQCM) variam. Em particular os resultados de XRD demonstram que a intercalação dos íons no filme eletrocromico é um fenômeno de volume. As mudanças de tensão mecânica e massa descartam a incorporação de íons  $OH^-$  como explicação para as diferenças observadas nos vários eletrólitos [60]. Os resultados indicam que a deintercalação dos prótons ocorre simultaneamente à intercalação de cátions no ciclo anódico e que o processo de deintercalação dos cátions ocorre em potenciais catódicos menores. Verifica-se também que a intercalação de prótons é mais favorável em potenciais catódicos maiores. Considerando os raios iônicos dos diferentes cátions e a possibilidade de hidratação, os dados de tensão mecânica e massa são concordantes. As mudanças em volume são consequência das variações

dos parâmetros de rede e podem ser diferentes nos vários eletrólitos, dependendo do grau de cristalinidade e orientação dos cristalitos.

Os resultados de tensão mecânica são diferentes nas duas séries de amostras, sendo menor no filme mais cristalino. Este resultado pode indicar que filmes mais cristalinos possuem durabilidade maior uma vez que grandes mudanças em tensão mecânica podem acarretar desgastes em dispositivos. Os resultados de variação de massa da série M mostram uma quantidade maior de íons de  $\text{Li}^+$  trocados, em comparação com íons  $\text{K}^+$ , mas como lítio é mais leve que potássio, variações menores de massa são obtidas em eletrólito contendo lítio. Em princípio o processo de intercalação pode ocorrer em posições atômicas substitucionais ou intersticiais. O tamanho do íon  $\text{Li}^+$ , 0.68 Å, é da ordem do raio iônico do  $\text{Ni}^{2+}$ , 0.70 Å. Conseqüentemente o lítio pode se inserir nas vacâncias de níquel, com pequenas modificações na rede. Esta pode ser a explicação pela qual se observa menor variação na tensão mecânica da amostra M ciclada em LiOH. Por outro lado espera-se grandes modificações nos parâmetros de rede para os íons maiores e mais pesados, quer seja em posições intersticiais ou substitucionais. Como neste caso menos íons são trocados [60], a tensão mecânica não aumenta proporcionalmente com o número atômico do íon alcalino. Os dados de XRD não permitem distinguir entre as duas possibilidades de sítios de intercalação dentro dos cristalitos ou mesmo descartar a presença de íons nos contornos de grão.

Em resumo, os resultados experimentais de difração de raios-X, indicam, junto com as medidas de variação de tensão mecânica e massa, que o íon alcalino participa na reação eletrocromica. Devido ao acréscimo de massa no ciclo anódico, o íon alcalino (C) entra na rede, enquanto o hidrogênio sai, de acordo com o seguinte processo de troca proposto:



### II.3.4. - Conclusões

Os nossos resultados de investigação da estrutura eletrônica de filmes finos eletrocromicos de  $\text{NiO}_x$ , crescidos por "rf-sputtering" reativo mostraram a existências de níveis associados a vacâncias de Ni e transições óticas de *gap* indireto na região do espectro visível. A formação de uma banda de condução em material no estado escuro pode explicar as mudanças de condutividade elétrica e óticas observadas no processo eletrocromico e apontam para um modelo de mecanismo de transferência de cargas através de níveis de impurezas que são destruídos e criados no processo de intercalação/deintercalação.

As condições de deposição dos filmes interferem em suas propriedades óticas e estruturais, sendo necessário estipular métodos bem controlados de crescimento a fim de se otimizar a eficiência do material. Os resultados de XRD mostraram que não apenas o volume da cela unitária deve ser considerado para os propósitos de intercalação. Provavelmente o grau de cristalinidade e a orientação preferencial de crescimento de grãos são parâmetros a serem otimizados. O processo de intercalação ocorre no volume interno dos cristalitos e é responsável pelas variações observadas nos parâmetros de rede entre os estados claro e escuro do material. O grau de cristalinidade não determina a variação de densidade ótica mas pode afetar a tensão mecânica no filme. Todos os resultados de XRD, tensão mecânica e variação de massa, indicam a participação do íon alcalino no processo de coloração.

## Capítulo III

### Materiais Supercondutores e Precursores

#### III.1. -Estado da Arte

Desde a descoberta dos supercondutores de alta temperatura crítica ( $T_c$ ) em 1986 [1], muitos trabalhos científicos e de aplicações tecnológicas vêm sendo produzidos. A descoberta de uma fase supercondutora com  $T_c = 30$  K no sistema Ba-La-Cu-O abriu novas frentes de pesquisa sobre supercondutividade. Os limites do fenômeno são testados, dentre outras formas, pela substituição de elementos constituintes dos materiais, pelo conhecimento de diagramas de fase e por alterações estruturais. Sob estes aspectos a difração de raios-X tem sido empregada como técnica fundamental na elucidação do fenômeno. Neste trabalho apresentamos, resumidamente, duas aplicações da difração de raios-X no estudo destes novos compostos supercondutores. A primeira envolve o estudo da cinética de formação da fase Bi-Sr-Co-O, isotípica à fase supercondutora contendo Cu em lugar de Co e a segunda trata da investigação da textura cristalina de fitas supercondutoras a base de Bi, produzidas mediante tratamentos termo-mecânicos. No Anexo A3, encontram-se os artigos decorrentes desta pesquisa.

#### III.2. -Fases do Bi-Sr-Co-O

A dependência da temperatura crítica com o número de camadas  $n$  de Cu-O nos supercondutores a base de bismuto foi extensivamente estudada, mostrando que  $T_c$  cresce com  $n$  [2,3]. Os compostos  $\text{Bi}_2\text{Sr}_2\text{Ca}_{n-1}\text{Cu}_n\text{O}_y$ , com  $n=1$ , 2 e 3, apresentam modulações incomensuráveis em sua estrutura [4,5].

Investigou-se então a relação desta modulação com o fenômeno de supercondutividade, através da substituição de Cu por Fe, Co e Mn [6]. O fato destes materiais serem isotípicos aos compostos de interesse a base de Bi, que contêm Cu, mas apresentarem modulações comensuráveis, permitiu a completa determinação de suas estruturas. Essas estruturas se transformaram numa fonte de referência para aquelas de modulação incomensurável. Entretanto observou-se que a obtenção das fases com substituição catiônica depende do processo de sinterização e que informações a respeito da cinética de formação destes compostos era incompleta. O nosso trabalho se concentrou nas fases a base de Co, pela facilidade em crescer fase única e monocristais.

### III.2.1. - Preparação das Fases do Bi-Sr-Co-O

As amostras foram preparadas pelo método de reação de estado sólido com uso de material em pó. Os tratamentos térmicos envolveram o processo de calcinação (780 °C por 50 hs) e posterior sinterização em diferentes temperaturas e atmosferas por 24 hs. Detalhes experimentais estão no Anexo A3. Amostras com 2-2-0-1 (fase n=1) e 2-3-0-2 (fase n=2) de estequiometria correspondem à notação de proporção molar Bi:Sr:Ca:Co.

### III.2.2. - Caracterização das Fases do Bi-Sr-Co-O

A análise dos compostos obtidos foram feitas por XRD (radiação Cu K $\alpha$ ) e DTA. Detalhes se encontram no Anexo A3.

### III.2.3. - Resultados e Discussão

As Figuras III-1, III-2 e III-3 mostram os difratogramas obtidos após os processos de tratamento térmico em diferentes atmosferas, partindo de estequiometrias diferentes.

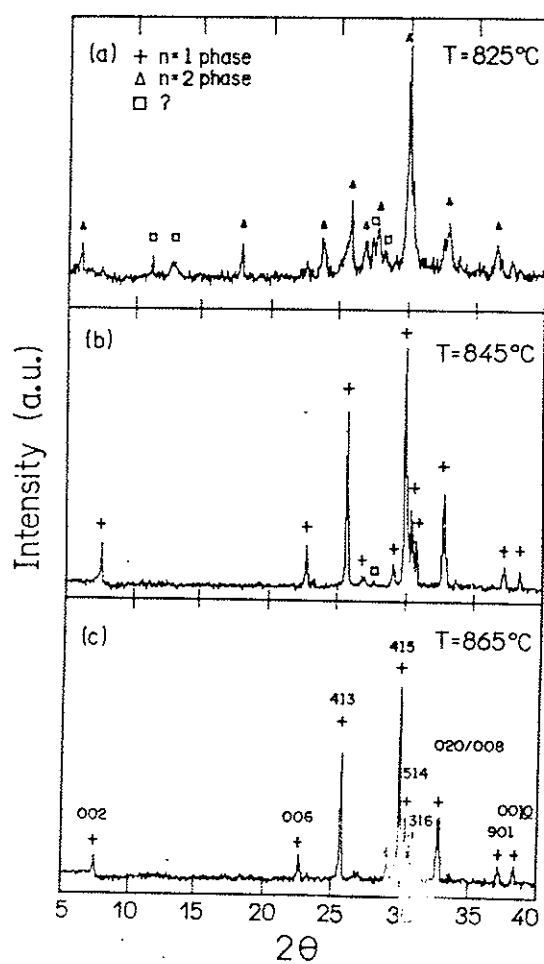


Fig. III-1. - XRD para a estequiometria 2-2-0-1, amostras tratadas em  $N_2$ .

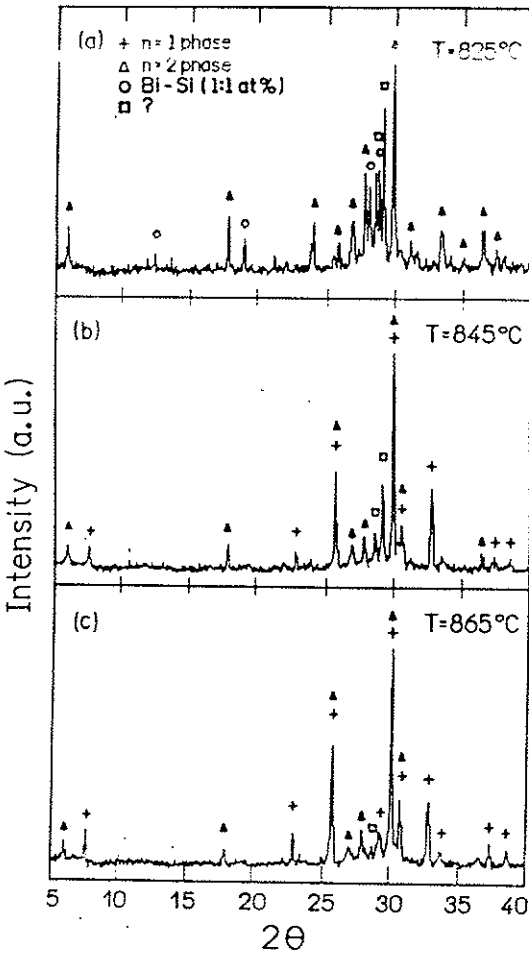


Fig. III-2. - XRD para a estequiometria 2-2-0-1, amostras tratadas em ar.

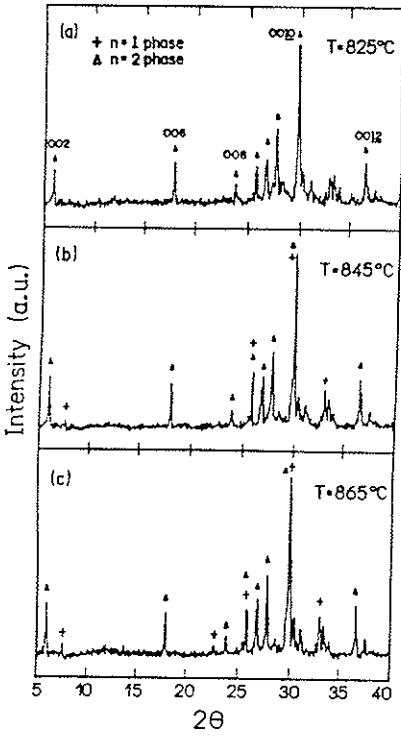


Fig. III-3. - XRD para a estequiometria 2-3-0-2, amostras tratadas em ar.

A fase  $n=1$  foi obtida em tratamentos térmicos em nitrogênio, mas não em ar. Por outro lado a fase  $n=2$  é formada em atmosfera parcialmente oxidante, indicando que esta fase é instável em ambiente redutor. Os resultados indicam que a valência do Co na fase  $n=1$  é menor que na fase  $n=2$ , pois a fase  $n=1$  é obtida apenas em atmosfera redutora. Foi verificada a facilidade de crescer monocristais da fase  $n=1$ .

#### III.2.4. - Conclusões

Este trabalho possibilitou um estudo sistemático da cinética de formação das fases  $\text{Bi}_2\text{Sr}_2\text{CoO}_x$  e  $\text{Bi}_2\text{Sr}_3\text{Co}_2\text{O}_x$ , bem como mostrou a facilidade de crescer monocristais destas fases sem a necessidade de fluxo e com altas taxas de resfriamento.

#### III.3. - Fitas Supercondutoras a Base de Bismuto

Com a descoberta dos novos materiais supercondutores esforços têm sido feitos no sentido de desenvolver fitas flexíveis destes materiais, encapsulados em prata. Muitos estudos têm sido conduzidos para determinar as condições de sinterização que levem a altos valores de corrente crítica ( $J_c$ ). Valores de densidade de corrente crítica em torno de  $10^4$  e  $10^5 \text{ A.cm}^{-2}$  foram obtidos em fitas de  $((\text{Bi,Pb})_2\text{Sr}_2\text{Ca}_{n-1}\text{Cu}_n\text{O}_x)$ , com  $n=2$  e  $n=3$  [7,8] em  $B=0$  e à temperatura de 77 K. Valores desta ordem de grandeza também podem ser obtidos em fitas de  $\text{YBa}_2\text{Cu}_3\text{O}_x$ . Neste trabalho investigamos a textura de fitas de  $(\text{Bi,Pb})_{2.2}\text{Sr}_2\text{Ca}_2\text{Cu}_3\text{O}_x$ , obtidas pelo método conhecido como *pó dentro do tubo*. Realizamos um estudo comparativo entre fitas prensadas e laminadas.



### III.3.1. - Preparação das Fitas de Bi(Pb)-Sr-Ca-Cu-O

A partir de óxidos de Bi, Pb, Sr, Ca e Cu os pós foram preparados na estequiometria 2223. As amostras foram calcinadas em ar a 840 °C por 24 hs, moídas e calcinadas novamente por 100 hs. Após o processo de calcinação a fase obtida é a 2212. Os pós são então inseridos em tubos de Ag, para posterior tratamento termo-mecânico. Os tratamentos térmicos foram efetuados a 850 °C por 110 hs. Os tratamentos mecânicos envolveram prensagem (P) e laminação (R). Detalhes experimentais encontram-se no Anexo A3.

### III.3.2. - Caracterização das Fitas

As fitas obtidas foram analisadas por difração de raios-X (XRD), microscopia eletrônica de varredura (SEM) e foi medida a densidade de corrente crítica após cada processo. Aspectos experimentais mais detalhados podem ser encontrados no Anexo A3.

### III.3.3. - Resultados e Discussão

Os difratogramas obtidos antes do processamento das fitas (primeiro resultado) e após os tratamentos termo-mecânicos são mostrados na Fig. III-4, onde L representa a fase 2212, H é a fase 2223 e o símbolo \* está relacionado a fases não identificadas. Os resultados de XRD mostraram variações de densidade, tamanho de grão e orientação preferencial até o terceiro ciclo de esforço mecânico e aquecimento, responsáveis pelo aumento de  $J_c$ . O valor de  $J_c$  também depende da interconexão entre os grãos orientados, que é obtida com a transformação da fase 2212 na fase 2223, através de uma reação líquida. Os baixos valores de  $J_c$  apresentados por





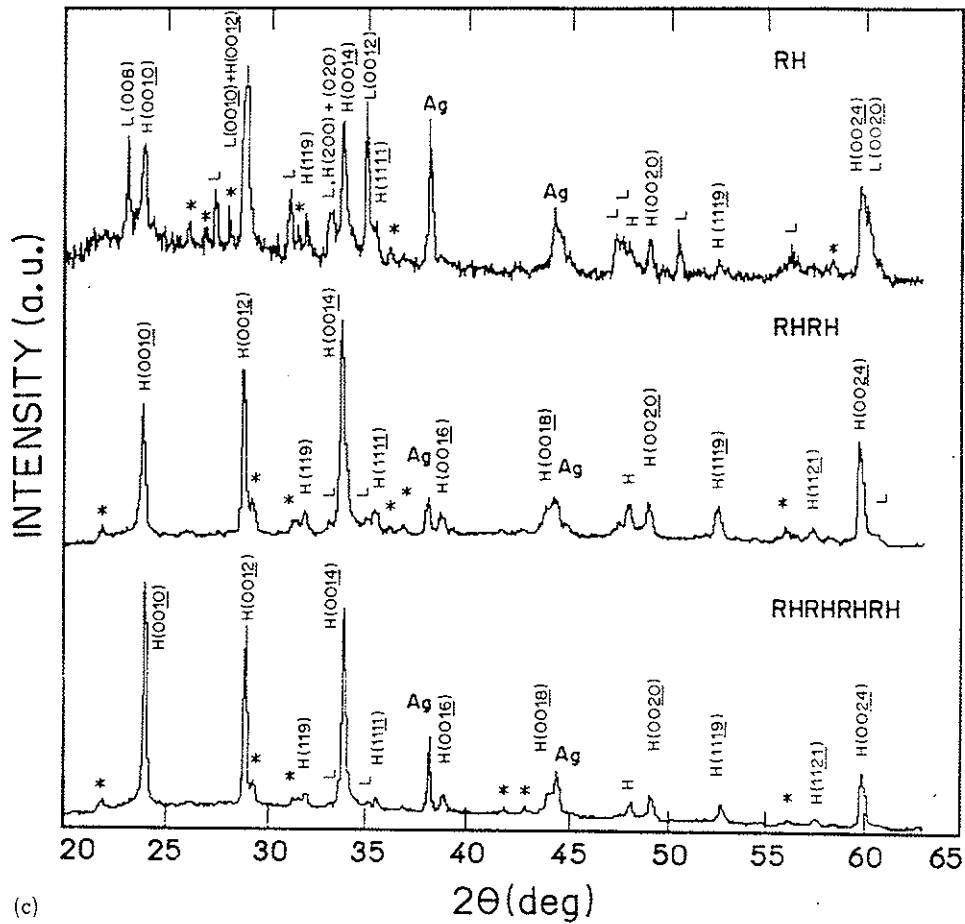


Fig. III-4.- XRD das fitas supercondutoras a base de Bi (*cont.*)

### III.3.4. - Conclusões

Este trabalho mostrou que a técnica de difração de raios-X, associada à microscopia eletrônica de varredura, permite avaliar a textura de fitas supercondutoras, uma vez que este fator é determinante para o incremento da densidade de corrente crítica. Fitas prensadas apresentam melhores valores de  $J_c$ , devido a existência apenas de forças perpendiculares à superfície das fitas. Na laminação forças paralelas a esta mesma superfície, fazem com que a incidência de placas isoladas seja maior. A diminuição da espessura e empacotamento inicial maior do pó são recomendados.

## Referências

### Introdução

- [1] H.P. Klug and L.E. Alexander, "X-Ray Diffraction Procedures for Polycrystalline and Amorphous Materials", Ed. John Wiley & Sons, NY (1974).
- [2] A. Guinier and S.G. Fournet, "Small Scattering of X-Rays", Ed. John Wiley & Sons, NY (1955).

### Capítulo I - Filmes Amorfos e Multicamadas a Base de Si e suas Ligas

- [1] D.A. Anderson and W.E. Spear, Phil. Mag. 35, 1 (1977).
- [2] A. Madan and M.P. Shaw, "Physics and Applications of Amorphous Semiconductors", Academic Press, NY, p.149 (1988).
- [3] IEEE Trans. Electron Dev. 36, 2753, 2839 (1989).
- [4] Phys. Mag B 60, 3, 11,23, 35 (1989).
- [5] P.G. LeComber, J. Non-Cryst. Solids 115, 1 (1989).
- [6] B. Abeles and T. Tiedje, Phys. Rev. Lett. 51, 2003 (1983).
- [7] P.V. Santos and L. Ley, Phys. Rev. B 36, 3325 (1987).
- [8] P.V. Santos, M. Hundhausen, L. Ley and C. Viczian, J. Appl. Phys. 69, 778 (1991).
- [9] Y. Tawada, M. Kondo, H. Okamoto and Y. Hamakawa, "XV IEEE Photovoltaics Specialist Conference", Orlando, FL, May 1981, p. 245, IEEE, NY (1981).
- [10] D.E. Carlson, IEEE Trans. Electron Dev. 36, 2775 (1989).
- [11] J. Bulloot and M.P. Schmidt, Phys. Status Solidi B 143, 345 (1987).
- [12] K. Mui, D.K. Basa and F.W. Smith, Phys. Rev B 35, 8089 (1987).
- [13] R.K. Onmori, I. Pereyra, C. Sasaki and M.N.P. Carreño, Proc. 9<sup>th</sup> European

- Photovoltaic Solar Energy Conference, ed. W. Palz, G.T. Wrixon, and P. Helm, Kluwer Academic, p.33, Dordrecht, (1989).
- [14] I. Solomon, M.P. Schmidt and H. Tran-Quoc, Phys. Rev. B 38, 9895 (1988).
  - [15] H. Munekata and H. Kukimoto, Jpn. J. Appl. Phys. 22, L544 (1983).
  - [16] S. Nishikawa, H. Kakinuma, H. Fukuda, T. Watanabe and K. Nihei, J. Non-Cryst. Solids 77&78, 1077 (1985).
  - [17] S. Nishikawa, H. Kakinuma, T. Watanabe and K. Nihei, Jpn. J. Appl. Phys. 25, 1141 (1986).
  - [18] M. Yoshimoto, T. Fuyuki and H. Matsunami, Jpn. Appl. Phys. 25, L922 (1986).
  - [19] S. Tsuda, H. Tarui, T. Matsuyama, T. Takahama, S. Nakayama, Y. Hishikawa, N. Nakamura, T. Fukatsu, M. Ohnishi, S. Nakana and Y. Kawano, Jpn. J. Appl. Phys. 26, 28 (1987).
  - [20] Y. Hamakawa, Proc. Intersol'85, Montreal, Canadá (1985).
  - [21] Y. Nakayama, S. Akita, H. Takamura, K. Wakita and T. Kawamura, MRS Symposium Proc. Vol. 118, "Amorphous Silicon Technology", 423 (1988).

## Capítulo II - Filmes Finos Eletrocromicos de Metais de Transição

### Aspectos gerais

- [1] C.M. Lampert, Solar Energy Mater., 11,1 (1984).
- [2] A. Donnadieu, Mater. Sci. Eng., B, 185 (1989).
- [3] S.K. Deb, Solar Energy Mater. and Solar Cells, 25, 327 (1992).
- [4] Large Area Chromogenics: Materials and Devices for Transmittance Control, C.M. Lampert and C.G. Granqvist, Editors, SPIE Publ., Bellingham, WA, U.S.A. (1991).

### Óxido de Cobalto

- [5] T. Seike and J. Nagai, *Solar Energy Mater.* 22, 107 (1991).
- [6] L.D. Burke and O.J. Murphy, *J. Electroanal. Chem.* 109, 373 (1980).
- [7] C.M.P. Fonseca, Marco-A. De Paoli and A. Gorenstein, *Adv. Mater.* 3, 553 (1991).

### Óxido de Níquel

- [8] M.C.A. Fantini, G.H. Bezerra, C.R.C. Carvalho and A. Gorenstein, *SPIE Proc. Series*, 1536, 81 (1991).
- [9] A. Gorenstein, F. Decker, M. Fantini and W. Estrada in *Large Area Chromogenics: Materials and Devices for Transmittance Control*, C.M. Lampert and C.G. Granqvist, Editors, SPIE Publ., Bellingham, WA, U.S.A., pp. 71, (1991).
- [10] Z.C. Orel, M.G. Hutchins and G. Mc Meeking, *Solar Energy Mater. and Solar Cells*, 30, 327 (1993).
- [11] C.M. Lampert, T.R. Omstead and P.C. Yu, *Solar Energy Mater.*, 14, 161 (1986).
- [12] P.C. Yu, G. Nazri and C.M. Lampert, *Solar Energy Mater.*, 16, 1 (1987).
- [13] M.K. Carpenter, R.S. Connell and D.A. Corrigan, *Solar Energy Mater.*, 16, 333 (1987).
- [14] M. Fantini and A. Gorenstein, *Solar Energy Mater.*, 16, 487 (1987).
- [15] S. Morisaki, K. Kawakami and N. Baba, *Jpn. J. Appl. Phys.*, 27, 314 (1988).
- [16] D.A. Corrigan and M. K. Carpenter in "Large Area Chromogenics: Materials and Devices for Transmittance Control", C.M. Lampert and C.G. Granqvist, Editors, SPIE Publ., Bellingham, WA, U.S.A., pp. 299, (1991).
- [17] J. Joseph, H. Gomathi and G.P. Rao, *Solar Energy Mater.*, 23, 1 (1991).
- [18] D.A. Corrigan, *Solar Energy Mater. and Solar Cells*, 25, 293 (1992).
- [19] M.G. Hutchins and G. Mc Meeking, *SPIE Proc. Series*, 1728, 66 (1992).

- [20] M. Chigane and M. Ishikawa, *J. Chem. Soc. Faraday Trans.*, 88, 2203 (1992).
- [21] P. Delichère, S. Joiret, A. Hugot-Le-Goff, K. Bange and B. Hetz, *J. Electrochem. Soc.*, 135, 1856 (1988).
- [22] N.R. Lynam and H. R. Habib, *SPIE Proc. Series*, 1016, 63 (1988).
- [23] C.R. Otterman, A. Temmink and K. Bange, *Thin Solid Films*, 193/194, 409 (1990).
- [24] T. Seike and J. Nagai, *Solar Energy Mater.*, 22, 107 (1991).
- [25] S.I. Cordoba -Torresi, C. Gabrielli, A. Hugot-Le Goff and R. Torresi, *J. Electrochem. Soc.*, 138, 1548 (1991).
- [26] S.I. Cordoba -Torresi, A. Hugot-Le-Goff and S. Joiret, *J. Electrochem. Soc.*, 138, 1554 (1991).
- [27] A. Nemetz, A. Temmink, K. Bange, S.I. Cordoba -Torresi, C. Gabrielli, R. Torresi and A. Hugot-Le-Goff, *Solar Energy Mater.*, 25, 93 (1992).
- [28] J. S. E. M. Svensson and C.G. Granqvist, *Appl. Phys. Lett.*, 49, 1566 (1986).
- [29] J.S.E.M. Svensson and C.G. Granqvist, *Appl. Opt.*, 26, 1554 (1987).
- [30] J.S.E.M. Svensson and C.G. Granqvist, *Solar Energy Mater.*, 16, 19 (1987).
- [31] S. Yamada, T. Yoshioka, M. Miyashita, K. Urabe and M. Kitao, *J. Appl. Phys.*, 63, 2116 (1988).
- [32] W. Estrada, A.M. Andersson and C.G. Granqvist, *J. Appl. Phys.*, 64, 3678 (1988).
- [33] A. Gorenstein, F. Decker, W. Estrada, C. Esteves, A. Andersson, S. Passerini, S. Pantaloni and B. Scrosati, *J. Electroanal. Chem.*, 277, 277 (1990).
- [34] D.A. Wruck, A.M. Dixon, M. Rubin and S.N. Bogoy, *J. Vac. Sci. Technol.*, 19, 2170 (1991).
- [35] G. Campet, B. Morel, M. Bourrel, J.M. Chabagno, D. Ferry, R. Garie, C. Quest, C. Geoffroy, J.J. Videau, J. Portier, C. Delmas and J. Salardenne, *Mater. Sci. Eng.*, B, 303 (1991).
- [36] F. Decker, R. Pileggi, S. Passerini and B. Scrosati, *J. Electrochem. Soc.*, 138, 3182 (1991).

- [37] R.S. Conell, D.A. Corrigan and B.R. Powell, *Solar Energy Mater. and Solar Cells*, 25, 301 (1992).
- [38] J. Scarminio, W. Estrada, A.Andersson, A. Gorenstein and F. Decker, J. *Electrochem. Soc.*, 139, 1236 (1992).
- [39] D.A. Wruck and M. Rubin, J. *Electrochem. Soc.*, 140, 1097 (1993).
- [40] S. Passerini, B. Scrosati, A. Gorenstein, A. M. Andersson and C.G. Granqvist, J. *Electrochem. Soc.*, 136, 3394 (1989).
- [41] C.G. Granqvist, *Thin Solid Films*, 193/194, 730 (1990).
- [42] C.G. Granqvist, *Solid State Ionics*, 53-56, 479 (1992).
- [43] M.P. Cantão, A. Lourenço, A. Gorenstein, S.I. Cordoba -Torresi, R.M. Torresi, *Mater. Sci. Eng.*, B, 157 (1994).
- [44] J. Scarmínio, A. Gorenstein, F. Decker, S. Passerini, R. Pillegi and B. Scrosati, *SPIE Proc. Series*, 1536, 70 (1991).
- [45] C.Gabrielli, M. Keddam and R.M. Torresi, J. *Electrochem. Soc.*, 138, 2657 (1991).
- [46] G. Sauerbrey, *Z. Phys.*, 144, 206 (1955).
- [47] A.M. Andersson, W. Estrada, C.G. Granqvist, A. Gorenstein and F. Decker, *SPIE Proc. Series*, 1272, 96 (1990).
- [48] C.A. Melendres, W. Paden, B. Tani and W. Walczak, J. *Electrochem. Soc.*, 134, 762 (1986).
- [49] D.A. Corrigan and S.L. Knight, J. *Electrochem. Soc.*, 136, 613 (1989).
- [50] J.S.E.M. Svensson and C.G. Granqvist in "Large Area Chromogenics: Materials and Devices for Transmittance Control", C.M. Lampert and C.G. Granqvist, Editors, SPIE Publ., Bellingham, WA, U.S.A., pp. 285, (1991).
- [51] A. Agrawal, H.R. Habibi, R.K. Agrawal, J.P. Cronin, D.M. Roberts, R.S. Caron-Popowich and C.M. Lampert, *Thin Solid Films*, 221, 239 (1992).
- [52] X. Hu, X. Chen and V. Song, *SPIE Proc. Series*, 2017, 172 (1993).
- [53] M.C.A. Fantini, A. Gorenstein, W.M. Shen and M. Tomkiewicz, *SPIE Proc. Series*, 1728, 41 (1992).
- [54] W. Estrada, M.C.A. Fantini, S.C. Castro, C.M.P. Fonseca and A. Gorenstein, *J. Appl. Phys.*, 74, 5835 (1993).



- [55] J. Desilvestro, D.A. Corrigan and M.J. Weaver, *J. Electrochem. Soc.*, 135, 885 (1988).
- [56] R. Barnard, C.F. Randell and F.L. Tye, *J. Appl. Electrochem.*, 11, 517 (1991).
- [57] H. Xingfang, C. Xiaofeng and M.G. Hutchins, *SPIE Proc. Series*, 1728, 73 (1992).
- [58] I.C. Faria, R.M. Torresi and A. Gorenstein, *SPIE Proc. Series*, 1728, 54 (1992).
- [59] J.M. Rosolen, F. Decker, M. Fracastoro-Decker, A. Gorenstein, R.M. Torresi and S.I. Cordoba -Torresi, *J. Electroanal. Chem.* 354, 273 (1993).
- [60] I.C. Faria, R.M. Torresi and A. Gorenstein, *Electrochimica Acta*, 38, 2765 (1993).
- [61] H.P. Rooksby, *Nature*, 152, 304 (1943).
- [62] H.P. Rooksby, *Acta Cryst.*, 1, 226 (1948).
- [63] N.C. Tombs and H.P. Rooksby, *Nature*, 165, 442 (1950).
- [64] Powder Diffraction Files, Joint Committee of Powder Diffraction Standards (J.C.P.D.S.) of the International Center for Diffraction Data, Swarthmore, PA, U.S.A. (1992).
- [65] International Tables for X-Ray Crystallography, Vol. I., N.F. Henry and K. Lonsdale, Editors, Kynoch Press, Birmingham, U.K. (1969).
- [66] J.V. Martins, M.H. Tabacniks, M.C.A. Fantini and A. Gorenstein, *Proc. Intern. Workshop Surf. Eng.*, Rio de Janeiro, Brazil, pp. 42, (1993).
- [67] D. Adler and J. Feinleib, *Phys. Rev. B*(2), 3112 (1970).
- [68] J.B. Goodenough, *Prog. Sol. St. Chem*, 5, 145 (1971).
- [69] K. Katada, K. Nakahigashi and Y. Shimomura, *Japan. J. Appl. Phys.*, 9, 1019 (1970).

### Capítulo III - Materiais Supercondutores e Precursores

#### Aspectos Gerais

- [1] T.G. Bednorz and K.A. Muller, Z. Phys. B 64, 189 (1986).

#### Fases do Bi-Sr-Co-O

- [2] J.M. Tarascon, W.R. McKinnon, P. Barboux, D.M. Hwang, B.G. Bagley, L.H. Greene, G.W. Hull, Y. le Page, N. Stoffel and M. Giroud, Phys Rev. B 38, 8885 (1988).
- [3] A. Maeda, M. Hase, I. Tsukada, K. Noda, S. Takebayashi and K. Uchinokura, Phys. Rev. B 41, 6418 (1990).
- [4] M.A. Subramanian, C.C. Torardi, J.C. Calabrese, J. Gopalakrishnan, K.J. Morrissey, T.R. Askew, R.B. Flippen, U. Chowdhry and A. W. Sleight, Science 239, 1015 (1988).
- [5] Y. Gao, P. Lee, P. Cooper, M.A. Subramanian and A.W. Sleight, Science 241, 954 (1988).
- [6] W.R. McKinnon, E. Tselepis, Y. le Page, S.P. McAlister, G. Pleizier, J. M. Tarascon, P.F. Micelli, R. Ramesh, G.W. Hull, J.V. Waszczak, J.J. Rhyne and D.A. Newmann, Phys Rev. B 41, 4489 (1990).

#### Fitas Supercondutoras a Base de Bi

- [7] N. Enomoto, H. Kikuchi, N. Uno, H. Kumakura, K. Togano and K. Watanabe, Jpn. J. Appl. Phys. 29L447 (1990).
- [8] Y. Yamada, B. Obst and R. Flükiger, Supercond. Sci. Technol. 4, 165 (1991).

---

Anexo A

---

## A1. - Trabalhos sobre Silício e suas Ligas Amorphas

---

# Microvoids in diamond-like amorphous silicon carbide

M. N. P. Carreno and I. Pereyra

*LME, Departamento de Engenharia Electronica, USP, CP 8174 05508-970 São Paulo (SP), Brazil*

M. C. A. Fantini

*Instituto de Física, FEP, USP, CP 20516, 01498-970 São Paulo (SP), Brazil*

H. Takahashi and R. Landers

*Instituto de Física, DFA, UNICAMP, CP 6165, 13081-970 Campinas (SP), Brazil*

(Received 27 May 1992; accepted for publication 28 July 1993)

The correlation between composition, microstructure, and optical properties of  $a\text{-Si}_{1-x}\text{C}_x\text{:H}$  thin films with different stoichiometries was established. The alloys were deposited by radio frequency glow discharge under "starving" plasma conditions from mixtures of  $\text{SiH}_4$  and  $\text{CH}_4$ . The samples were characterized by small angle x-ray scattering, ultraviolet-visible and infrared spectrometry, and Auger electron spectroscopy. The results showed the presence of microvoids with sizes between  $\approx 3 \text{ \AA}$  and  $\approx 8 \text{ \AA}$ . The relative microvoid volume fraction displayed a maximum for  $x$  around 55 at. % and decreased for higher values of  $x$ . High carbon content alloys ( $x \approx 70$  at. %) not only have a lower relative microvoid volume fraction, but show optical gaps as high as 3.7 eV, high resistivity, and very low refractive index, indicating the presence of a diamond-like C-C structure. These remarkable results are attributed to the deposition under "starving" plasma conditions.

## I. INTRODUCTION

Over the last years, much attention has been dedicated to the fabrication of hydrogenated amorphous silicon alloys,  $a\text{-Si}_{1-x}\text{A}_x\text{:H}$  ( $\text{A} = \text{Ge}, \text{N}, \text{C}, \text{O}, \text{etc.}$ ), due to the possibility of tailoring the optical gap when  $x$  varies.<sup>1,2</sup> On the other hand, all these studies have shown that the electrical properties of the semiconductor materials worsen with the addition of even small amounts of A. Nevertheless, such alloys have an extensive range of applications.<sup>2-5</sup> In particular, earlier work on amorphous silicon carbide,  $a\text{-Si}_{1-x}\text{C}_x\text{:H}$ , dealt with the production of wide gap compounds for utilization as window layers in amorphous silicon solar cells.<sup>6,7</sup> Another application is in insulating layers on  $a\text{-Si:H}$  based thin film transistors (TFTs), where the main required properties are a very low conductivity and a high optical gap.<sup>2,3</sup> The need for improving the material for specific applications has induced fundamental studies on the physical properties of these tetrahedrally bonded amorphous semiconductors.<sup>8-10</sup> These studies have shown that it is very difficult to increase the gap beyond  $\approx 3 \text{ eV}$ , which corresponds to a carbon concentration of about 50 at. % in the solid phase. For higher concentrations, graphite-like carbon clusters are formed, with the consequent reduction in the optical gap.

In earlier work,<sup>11</sup> we showed that it is possible to produce  $a\text{-Si}_{1-x}\text{C}_x\text{:H}$  films with the optical gap as high as  $\approx 4.0 \text{ eV}$  and resistivity higher than  $10^{15} \Omega \text{ cm}$ . The carbon concentration in the material can attain values up to 70 at. %, due to the use of deposition conditions, known as "starving" plasma<sup>12</sup> that, apparently, promotes C-C diamond-like bonds. The starving plasma deposition conditions are a combination of a low power regime with a very low  $\text{SiH}_4$  flow. Due to the low radio frequency (rf) power, the methane molecules are not broken, so the silane radicals are responsible for all the chemical reactions.

When there are very few  $\text{SiH}_4$  molecules, they are readily consumed by the deposition process and the deposition rate is controlled by the silane flow.<sup>12</sup> We believe that this starving situation is responsible for the notable properties of the  $a\text{-Si}_{1-x}\text{C}_x\text{:H}$  films. This material was used as an insulating layer in amorphous silicon TFTs, and performed well.<sup>13,14</sup> In some cases, small leakage currents were observed across the gate. This was attributed to the porosity of the films, as already reported in the literature.<sup>15-17</sup> In this work we analyze the correlation between porosity and carbon concentration in the solid phase, for samples deposited under starving plasma conditions. A combination of techniques was used to characterize the different silicon carbides and to correlate their properties: auger electron spectroscopy (AES) to determine the alloy chemical composition, small angle x-ray scattering (SAXS) to detect the microvoid formation, and ultraviolet-visible and infrared spectrometry to find the optical gap and the atomic bonds inside the material.

## II. EXPERIMENT

The  $a\text{-Si}_{1-x}\text{C}_x\text{:H}$  films were deposited by the conventional rf glow discharge technique from appropriate mixtures of  $\text{SiH}_4$  and  $\text{CH}_4$  in a capacitively coupled reactor. The substrate temperature was  $250^\circ \text{C}$  and the power density was  $150 \text{ mW cm}^{-2}$ . The silane flow was kept as low as possible ( $\approx 10 \text{ sccm}$ ) to provide the starving plasma condition.<sup>12</sup> The carbon content in the samples was varied by changing the  $\text{CH}_4$  partial pressure (see Table I), while maintaining the silane flow fixed for all the samples ( $10 \text{ sccm}$ ). For the sake of comparison, a sample which was deposited with a  $\text{CH}_4$  partial pressure equal to 72% (similar to MVC3-Table I), but in the nonstarving plasma condition, was also analyzed. When the silane flow is high, the deposition rate is not flow dependent, thus characterizing a

TABLE I.  $a\text{-Si}_{1-x}\text{C}_x\text{:H}$  samples produced with a deposition rate ( $g$ ), with thickness ( $t$ ), and optical gap ( $E_0$ ), having different relative amount of Si-C bonds. NSP: nonstarving plasma.

Sample	Partial pressure of $\text{CH}_4$ (%)	$g$ ( $\text{\AA}/\text{min}$ )	$t$ ( $\text{\AA}$ )	$E_0$ (eV)	Si-C $(\text{Si-C})_{\text{SiC}}$
MVC2	98	11.1	2500	3.7	0.4
MVC1	92	24.5	5880	3.4	0.4
MVC4	75	36.6	5500	3.0	0.9
MVC3	72	33.8	7020	3.0	0.8
MVC5	50	20.0	3000	2.2	1.0
MVC6	72 (NSP)	105.5	9500	2.8	0.6
MVS1	0 ( $a\text{-Si:H}$ )	...	6000	1.7	...

nonstarving regime. The thicknesses of the samples were controlled by the deposition rates and were measured by an Alpha-Step profile meter.

The carbon content in the solid phase was obtained from the AES measurements, using a varian cylindrical mirror analyzer with a coaxial electron gun operated in the differential mode. The surface contamination was removed by ion bombardment. The composition was calculated from the Si LMM and C KLL transitions, with statistical fluctuations of the order of 5%, using tabulated sensitivity factors.<sup>18</sup> It should be pointed out that the use of tabulated sensitivity factors may introduce an undetermined systematic error in the absolute concentration of the atomic species. We did not use a SiC standard because of charging and material dependent backscattering factor problems.

The microstructure of the samples was analyzed by SAXS in transmission geometry, using a small angle camera with automatic angle variation and acquisition control. The measurements were conducted in a step scanning mode ( $0.05^\circ$  in  $2\theta$ ), from  $2\theta$  between  $0.2^\circ$  and  $5^\circ$  and a counting time of 1000 s. For the SAXS experiments, the  $a\text{-Si}_{1-x}\text{C}_x\text{:H}$  films (see Table I) were deposited on 20- $\mu\text{m}$ -thick aluminum substrates. Stacks of 40 foils were measured to enhance the total thickness of the  $a\text{-Si}_{1-x}\text{C}_x\text{:H}$  films. We did not choose to analyze thicker films because they usually present mechanical deformations. The direct beam, the background, the bare substrate, and the film plus substrate SAXS intensities were recorded. The experimental setup was aligned for a line-collimated x-ray beam, using a high resolution slit setting (divergence slit of 0.2 mm, receiving slit of 0.1 mm, and two scattering slits of 0.05 and 0.1 mm). There were no Soller slits in the beam path, and data corrections due to the beam finite height are disregarded, because of the large moduli of the scattering vector  $h$ .<sup>19</sup> The SAXS measurements were performed with part of the white x-ray spectrum emitted by a conventional copper tube, operating at 40 kV and 30 mA. The scintillation detector electronics were adjusted to take only the more energetic radiation above the  $\text{CuK}\alpha$  characteristic radiation. The total spectrum was filtered by nickel to avoid part of the low energy radiation. By means of a standard, we determined the available x-ray mean wavelength,  $\lambda \pm \Delta\lambda = (0.31 \pm 0.08) \text{ \AA}$ , corresponding to the escape peak region (energy  $\approx 40 \text{ keV}$ ). At this wavelength the x-ray ab-

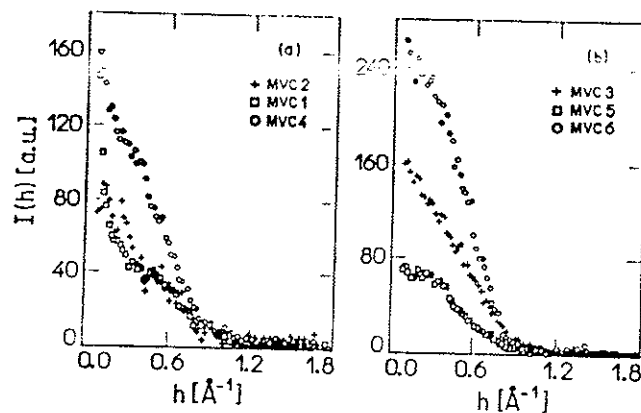


FIG. 1. (a) and (b) SAXS intensity [ $I(h)$ ] of the  $a\text{-Si}_{1-x}\text{C}_x\text{:H}$  films as a function of the scattering vector ( $h=4\pi \sin \theta/\lambda$ ).

sorption coefficient of the aluminum substrate is very small, and therefore, an extra filtering of the low energy radiation occurs. The SAXS data were always recorded with the same direct beam intensity and were not normalized to electronic units. We found no detectable scattering from the thin films when the SAXS measurements were performed with monochromatic x-ray radiation from a conventional source ( $\lambda=1.5418 \text{ \AA}$  for  $\text{CuK}\alpha$ ) and also from a synchrotron radiation source ( $\lambda=1.35 \text{ \AA}$ ), due to the high absorption of the substrate at these wavelengths.

The carbon, silicon, and hydrogen incorporation in the different films was studied by infrared spectral analysis in a FTS-40 BioRad Fourier transform infrared (FTIR) spectrometer. The samples used in these measurements were deposited on high resistivity crystalline silicon substrates, polished on both sides. An identical silicon wafer was used as a reference. The optical gaps were obtained from an ultraviolet-visible-infrared spectrometer (Varian Cary-2300 model).

### III. RESULTS

Table I presents the methane partial pressure during the film growth, the thickness ( $t$ ) of the samples, their corresponding deposition rate ( $g$ ), the Tauc optical gap ( $E_0$ ),<sup>20</sup> and the relative amount of Si-C bonds in the films, obtained from the infrared experiments.

Figure 1 depicts the SAXS intensity of the  $a\text{-Si}_{1-x}\text{C}_x\text{:H}$  films,  $I(h)$ , as a function of the scattering vector  $h=4\pi \sin \theta/\lambda$ . The raw data, measured for the film plus substrate, is given by  $I_m(h)$ , the dark count rate is  $I_d$ , and the substrate intensity is  $I_s(h)$ . Thickness normalization and absorption corrections were calculated from the same quantities using low intensity direct beam measurements. The  $I(h)$  values are given by:<sup>16</sup>

$$I(h) = \frac{[I_m(h) - I_d] - [I_s(h) - I_d] \exp(-\mu_f t_f)}{I_0 \mu_f t_f \exp(-\mu_f t_f - \mu_s t_s)}, \quad (1)$$

where  $\mu$  and  $t$ , with subscripts  $f$  and  $s$ , stand, respectively, for film and substrate absorption coefficient and thickness. The incident intensity  $I_0$  was kept constant for all the measurements. The intensities were not normalized to elec-

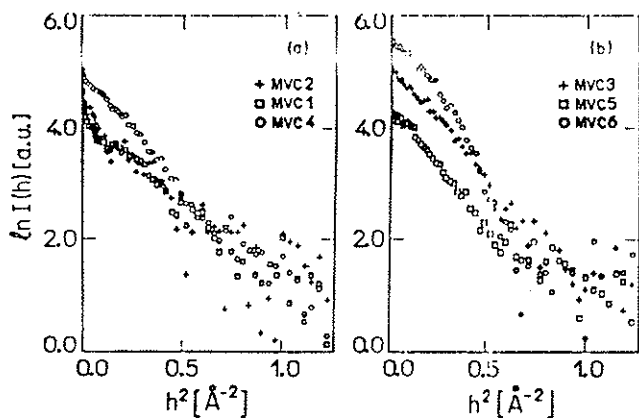


FIG. 2. (a) and (b) Guinier plots of the  $a\text{-Si}_{1-x}\text{C}_x\text{:H}$  films.

tronic units; therefore, our results consist of a comparative analysis of the small angle x-ray scattering of the studied films. The SAXS measurements conducted on our  $a\text{-Si:H}$  sample did not show any scattering, being an indication that the existence of microvoids in the film is below our detection limit of around 3% volume fraction.

Figure 2 shows the Guinier plots,<sup>19</sup> from which the gyration radius ( $R_g$ ) can be calculated. For the samples deposited from 75% and 92% methane partial pressure, two straight lines fitted the Guinier equation, indicating two sizes of microvoids ( $R_1$  and  $R_2$ ). Experiments performed with tilted samples gave identical  $R_g$  values, indicating either the presence of voids with spherical shape ( $R_{\text{sph}}=1.29R_g$ ) or a random orientation of nonspherical voids.

Figure 3 shows the  $hI(h)$  vs  $h$  plots. The area under these curves is proportional to the relative microvoid volume fraction ( $\eta$ ), which is given by<sup>19</sup>:

$$\eta(1-\eta) = k \frac{\int_0^\infty hI(h)dh}{\Delta\rho^2}, \quad (2)$$

where  $k$  is a constant and  $\Delta\rho = [(1-x)n_{\text{Si}} + xn_{\text{C}}] - \rho_0$ . In this equation,  $\rho_0$  is the empty void electron density ( $\rho_0=0$ ). The electron density of silicon ( $n_{\text{Si}}$ ) and carbon ( $n_{\text{C}}$ ) were determined using the silicon atomic volume of

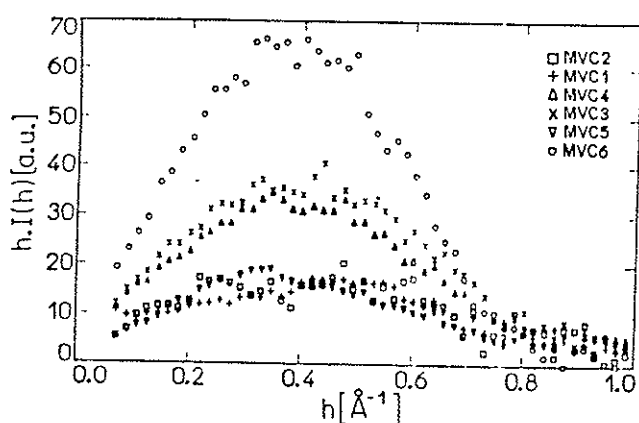


FIG. 3.  $hI(h)$  vs  $h$  curves of the  $a\text{-Si}_{1-x}\text{C}_x\text{:H}$  films. The area under the plots is proportional to the microvoid relative volume fraction ( $\eta$ ).

TABLE II. Carbon concentration ( $x$ ), gyration radius ( $R_1$  and  $R_2$ ) and microvoid relative volume fraction ( $\eta$ ) of the  $a\text{-Si}_{1-x}\text{C}_x\text{:H}$  films. NSP: nonstarving plasma.

Sample	$x$	$R_1$ (Å)	$R_2$ (Å)	$\eta \pm 0.02$ (a.u.)
MVC2	0.66	...	3.7	0.39
MVC1	0.70	8.4	2.8	0.40
MVC4	0.55	5.2	3.0	0.62
MVC3	0.56	...	3.2	0.68
MVC5	0.46	...	3.2	0.36
MVC6 (NSP)	0.54*	...	3.4	1.00

\*Estimated from  $E_g$  values.

$20 \text{ Å}^3$  for both types of atoms, supposing a random distribution of Si and C inside the films.<sup>16</sup> The silicon ( $1-x$ ) and carbon ( $x$ ) concentrations in the films were taken from the AES results. For the relative microvoid volume fraction calculation, we assume  $\eta(1-\eta) \sim \eta$ , since our preliminary transmission electron microscopy results indicate that  $\eta < 1$ .<sup>21</sup>

Table II presents the gyration radius ( $R_1$  and  $R_2$ ) that are connected to different microvoid sizes, together with the carbon content ( $x$ ) in the solid phase and the microvoid relative volume fraction ( $\eta$ ). The value of  $x$ , given for the sample MVC6, was estimated from the optical gap, due to charging during the AES experiments, which prevented the determination of  $x$  by this technique. Figure 4 shows the  $\eta$  vs  $x$  values.

The infrared spectra were obtained in the range of 400 up to  $4000 \text{ cm}^{-1}$ , where the typical vibration bands of the silicon-carbon-hydrogen groups appear, as shown in Table III.<sup>15</sup> The spectra obtained for the samples with different carbon content are shown in Fig. 5. The results obtained for the samples deposited at a  $\text{CH}_4$  partial pressure of 72% in starving and nonstarving plasma conditions are presented in Fig. 6. The integrated absorption was calculated for the fundamental absorption bands of amorphous silicon carbide, displayed in Table III. Since the bands in the  $600\text{--}1200 \text{ cm}^{-1}$  range overlap, a deconvolution procedure was performed in order to obtain the contribution of each individual peak. The results are shown in Table IV. As expected, the Si-C and the Si-H<sub>n</sub> bands increase when the SiH<sub>4</sub> concentration increases, but the C-H<sub>n</sub>, Si-CH<sub>2</sub>, and

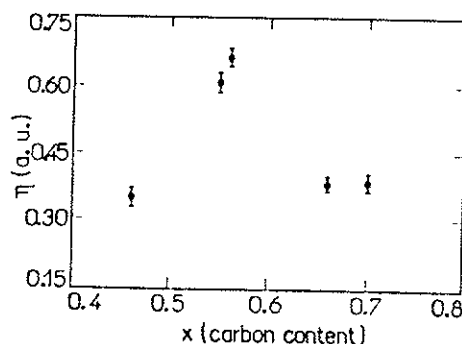


FIG. 4. Microvoid relative volume fraction ( $\eta$ ) vs carbon content ( $x$ ) of the  $a\text{-Si}_{1-x}\text{C}_x\text{:H}$  films.

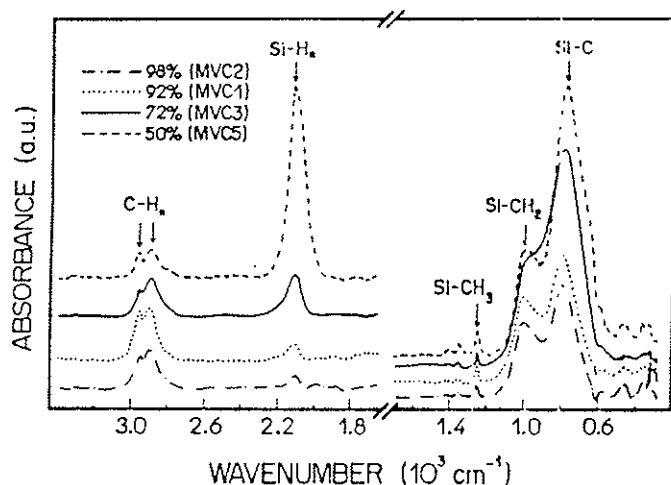
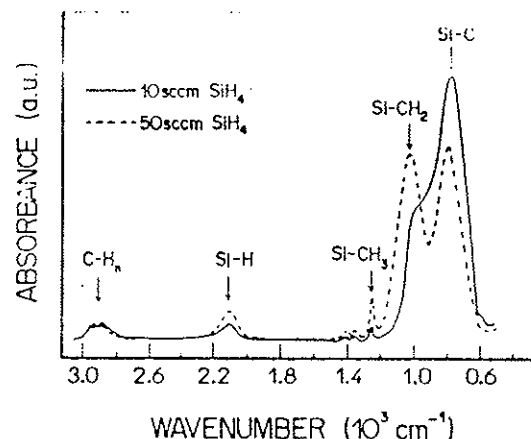
TABLE III. Silicon-carbon-hydrogen vibrational bands.

Group	wave number $k$ ( $10^3 \text{ cm}^{-1}$ )
Si-H <sub>2</sub>	2.09(stretching)
C-H <sub>n</sub>	2.80-3.00
Si-C	0.70-0.80
Si-CH <sub>n</sub>	0.90-1.10
Si-CH <sub>3</sub>	1.25

\*See Ref. 15.

Si-CH<sub>3</sub> bands, generally related to disorder and microvoids,<sup>16,17</sup> do not vary in any systematic way. The more remarkable results were observed for the samples deposited at a CH<sub>4</sub> partial pressure of 72% under starving and nonstarving plasma conditions (see Fig. 6). These two different deposition regimes lead to very different carbon incorporation inside the films. The sample deposited in starving plasma condition has more Si-C bonds, but less Si-H<sub>n</sub>, Si-CH<sub>2</sub>, and Si-CH<sub>3</sub> bonds. These results indicate that the starving regime favors the silicon-carbon bonding, as well as a more ordered material with less hydrogen incorporation.

Even though we had calculated the integrated absorption intensity for all the observed peaks with good precision, we could not provide the absolute hydrogen and carbon content inside our films, because the absorption strength and frequency depend on the atomic environment, i.e., the material matrix. For instance, the band at 2090  $\text{cm}^{-1}$  definitely corresponds to Si-H<sub>2</sub> bonding in a pure void free  $\alpha$ -Si:H matrix, but it can also correspond to Si-H bonding in porous  $\alpha$ -Si:H as well as in  $\alpha$ -Si<sub>1-x</sub>C<sub>x</sub>:H.<sup>22</sup> Also, the oscillator strength increases with carbon incorporation,<sup>23</sup> making a quantitative analysis very difficult to be accomplished.

FIG. 5. IR spectra normalized by the sample thickness of the  $\alpha$ -Si<sub>1-x</sub>C<sub>x</sub>:H films (absorbance/thickness vs wave number).FIG. 6. IR spectra normalized by the sample thickness of  $\alpha$ -Si<sub>1-x</sub>C<sub>x</sub>:H samples deposited at starving (—) and nonstarving (---) plasma conditions.

#### IV. DISCUSSION

The results show a very efficient incorporation of carbon, with  $x$  as high as 70 at. %, considering that the films were deposited with low rf power. The striking fact here is that this carbon incorporation is followed by increasing optical gaps. The optical gap of our samples increases beyond the carbon content for which the maximum Si-C peak occurs (see Table I). For carbon concentrations higher than 50%, monomolecular C-C bonds are expected to appear, generally in a graphite-like form, with a consequent reduction in the optical gap, as reported by other authors.<sup>8</sup> The fact that  $E_0$  increases continuously with  $x$ , indicates the presence of C-C diamond like bonds. This hypothesis is supported by an enormous electrical resistivity ( $> 10^{15} \Omega \text{ cm}$ ) and by an insensitivity to chemical etching showed by our  $\alpha$ -Si<sub>1-x</sub>C<sub>x</sub>:H films. An attempt to analyze the AES lineshape of the C KLL peak did not provide any conclusive answer about the carbon bonds in our films, due to the influence of the Ar<sup>+</sup> ion bombardment, which changes the surface bonding features.

The dependence of the microvoid size on the carbon content ( $x$ ) in the films showed that the gyration radius  $R_2$  did not change with respect to  $x$ . On the other hand, the gyration radius  $R_1$  was detected only for samples having higher  $x$  values, except for the thinnest MVC2 sample,

TABLE IV. Infrared integrated absorption of the fundamental bands.

Sample	Partial pressure of CH <sub>4</sub> (%)	$\eta$ (a.u.) Si-C	Integrated absorption (a.u.)			
			C-H <sub>n</sub>	Si-H <sub>n</sub>	Si-CH <sub>2</sub>	Si-CH <sub>3</sub>
MVC2	98	0.39	3.68	0.22	0.32	1.53
MVC1	92	0.40	4.04	0.34	0.59	1.88
MVC3	72	0.68	7.94	0.29	2.44	1.73
MVC5	50	0.36	9.43	0.23	12.8	1.60
MVC6*	72	1.00	5.63	0.21	3.90	5.93

\*Sample deposited under nonstarving regime, with a silane flow of 50 sccm.



whose signal to noise ratio of the scattered x-ray intensity presented large fluctuations that could mask the Guinier slope at very small angles (see Fig. 2).

The results show that higher carbon concentration and the presence of larger microvoids do not imply higher relative microvoid volume fraction. The highest  $\eta$  value was obtained for a carbon content of 56 at. %. When the carbon content increases up to around 70 at. %, the  $\eta$  value decreases to 40%. The decrease of the structural defects per unit area can be attributed to the formation of larger microvoids.

The infrared measurements are expected to elucidate which species were connected to the presence of microvoids. All the samples deposited in the starving regime showed absorption bands corresponding to Si-H<sub>2</sub>, C-H<sub>n</sub>, Si-C, Si-CH<sub>2</sub>, and Si-CH<sub>3</sub> groups, but the infrared results could not provide a straightforward relationship between the integrated intensity of the absorption bands and the relative microvoid volume fraction.

The deposition rate and the microvoid relative volume fraction obtained for the samples deposited at the same methane partial pressure of 72%, but under starving and nonstarving plasma conditions, are very different. However, the microvoid size does not depend on the deposition process. The 32% larger microvoid relative volume fraction, observed for the film deposited under nonstarving plasma conditions, can be attributed to the existence of different carbon bonds in the films, which promote discontinuities. In fact, the absorption band at 1250 cm<sup>-1</sup>, due to Si-CH<sub>3</sub> bonds, is more pronounced for the sample deposited under nonstarving plasma conditions (see Fig. 6). The larger integrated absorption intensities, related to the Si-CH<sub>2</sub> and Si-CH<sub>3</sub> bonds obtained for the MVC6 sample, when compared to its companion MVC3 sample (see Table IV), demonstrate that the CH<sub>n</sub> radicals connected to the Si atoms are responsible for the formation of microvoids: a result which agrees with previous reported data.<sup>16</sup> In other work,<sup>24</sup> we report that the starving regime leads to better films in relation to the topological microstructure and smoothness. The morphological and bonding features of those two films are determined by the growth kinetics, being very different under starving and nonstarving plasma deposition conditions.

## V. CONCLUSIONS

In this work we show that using glow discharge deposition, even in the low power regime it is possible to achieve high carbon incorporation in  $\alpha$ -Si<sub>1-x</sub>C<sub>x</sub>:H thin

films. The results indicate that the deposition under starving plasma conditions promotes diamond-like C-C bonds, leading to a material with a very high optical gap and smaller relative microvoid volume fraction. The formation of microvoids depends not only on the carbon content in the films, but critically on the deposition conditions.

## ACKNOWLEDGMENTS

We would like to thank J. Moraes and T. A. Fazan for help with the AES measurements. We wish to thank Professor G. G. Kleiman for the reading of the manuscript. This work was supported by FAPESP, CNPq, and FINEP, Brazil.

- <sup>1</sup>D. A. Anderson and W. E. Spear, *Philos. Mag.* **35**, 1 (1977).
- <sup>2</sup>A. Madan and M. P. Shaw, *Physics and Applications of Amorphous Semiconductors* (Academic, New York, 1988), p. 149.
- <sup>3</sup>IEEE Trans. Electron Dev. **36**, 2753, 2839 (1989).
- <sup>4</sup>*Philos. Mag. B* **60**, 3, 11, 23, 35 (1989).
- <sup>5</sup>P. G. LeComber, *J. Non-Cryst. Solids* **115**, 1 (1989).
- <sup>6</sup>Y. Tawada, M. Kondo, H. Okamoto, and Y. Hamakawa, *XV IEEE Photovoltaics Specialist Conference*, Orlando, FL, May 1981 (IEEE, New York, 1981), p. 245.
- <sup>7</sup>D. E. Carlson, *IEEE Trans. Electron Dev.* **36**, 2775 (1989).
- <sup>8</sup>R. S. Sussmann and R. Ogden, *Philos. Mag. B* **44**, 137 (1981).
- <sup>9</sup>J. Bullot and M. P. Schmidt, *Phys. Status Solidi B* **143**, 345 (1987).
- <sup>10</sup>K. Mui, D. K. Basa, and F. W. Smith, *Phys. Rev. B* **35**, 8089 (1987).
- <sup>11</sup>R. K. Onmori, I. Pereyra, C. Sasaki, and M. P. Carreño, *Proceedings of the 9th European Photovoltaic Solar Energy Conference*, edited by W. Palz, G. T. Wrixon, and P. Helm (Kluwer Academic, Dordrecht, 1989), p. 33.
- <sup>12</sup>I. Solomon, M. P. Schmidt, and H. Tran-Quoc, *Phys. Rev. B* **38**, 9895 (1988).
- <sup>13</sup>C. A. Sasaki, A. T. Arasaki, M. P. Carreño, A. Komazawa, and I. Pereyra, *J. Non-Cryst. Solids* **115**, 90 (1989).
- <sup>14</sup>M. P. Carreño, I. Pereyra, and A. M. Andrade, *Surface Science—Lectures on Basic Concepts and Applications*, edited by F. A. Ponce and M. Cardona (Springer, Berlin, 1992), p. 387.
- <sup>15</sup>J. Bullot and M. P. Schmidt, *Phys. Status Solidi B* **143**, 345 (1987).
- <sup>16</sup>D. L. Williamson, A. H. Mahan, B. P. Nelson, and R. S. Crandall, *Appl. Phys. Lett.* **55**, 783 (1989).
- <sup>17</sup>A. H. Mahan, D. L. Williamson, B. P. Nelson, and R. S. Crandall, *Solar Cells* **27**, 465 (1989).
- <sup>18</sup>L. E. Davis, N. C. McDonald, P. W. Palmberg, G. E. Riach, and R. E. Weber, *Handbook of Auger Electron Spectroscopy*, 2nd ed. (Perkin-Elmer, Physical Electronics Division, MN, 1976).
- <sup>19</sup>A. Guinier and S. G. Fournet, *Small Angle Scattering of X-Rays* (Wiley, New York, 1955).
- <sup>20</sup>*Amorphous and Liquid Semiconductors*, edited by J. Tauc (Plenum, New York, 1974), p. 173.
- <sup>21</sup>M. N. P. Carreño and I. Pereyra, TEM (unpublished results).
- <sup>22</sup>H. Wagner and W. Beyer, *Solid State Commun.* **48**, 585 (1983).
- <sup>23</sup>H. Wieder, M. Cardona, and C. R. Guarnieri, *Phys. Status Solidi B* **92**, 99 (1979).
- <sup>24</sup>E. L. Z. Velasquez, M. C. A. Fantini, M. P. Carreño, I. Pereyra, H. Takahashi, and R. Landers, *J. Appl. Phys.* **74**, 543 (1993).

# Effect of plasma etching, carbon concentration, and buffer layer on the properties of $a\text{-Si:H}/a\text{-Si}_{1-x}\text{C}_x\text{:H}$ multilayers

E. L. Z. Velasquez and M. C. A. Fantini

*Instituto de Física, DFE, USP, CP 20516, 01498-970 São Paulo (SP), Brazil*

M. N. P. Carreño and I. Pereyra

*LME, Departamento Engenharia Eletrônica, USP, CP 8174, 05508-970 São Paulo (SP), Brazil*

H. Takahashi and R. Landers

*Instituto de Física, DFA, CP 6165, 13081-970 Campinas (SP), Brazil*

(Received 27 May 1993; accepted for publication 28 August 1993)

Small angle x-ray diffraction was used to diagnose the structural properties of  $a\text{-Si:H}/a\text{-Si}_{1-x}\text{C}_x\text{:H}$  multilayers deposited by rf glow discharge. Precise deposition rates were obtained from the experimental data. Two growth parameters were varied: the methane concentration in the gaseous mixture and the intermediary plasma etching time between consecutive depositions. Some samples had an additional buffer layer between the substrate and the heterostructure. The sharpest interfaces were obtained on samples with the intermediate buffer layer, plasma etching times of at least 2 min, and diamond-like  $a\text{-Si}_{1-x}\text{C}_x\text{:H}$  layers. Profiling by Auger electron spectroscopy and small angle x-ray diffraction results were used to estimate the interface thickness.

## INTRODUCTION

Amorphous multilayers, besides their device applications, are very attractive systems. Many combinations of different materials can be obtained without the need for matching of lattice parameters. Amorphous superlattices present homogeneity in the horizontal plane and anisotropic structural properties perpendicular to the substrate.<sup>1-7</sup> In particular,  $a\text{-Si:H}/a\text{-Si}_{1-x}\text{C}_x\text{:H}$  systems have received a lot of attention in the pertinent literature.<sup>8-12</sup>

In previous work we reported rf glow discharge production of  $a\text{-Si:H}$  based thin film transistors (TFT), having diamond-like  $a\text{-Si}_{1-x}\text{C}_x\text{:H}$  as the insulating layer.<sup>13,14</sup> It is well known that the performance of these transistors is strongly dependent on the interface between the insulating and active layers. Therefore, we performed a series of small angle x-ray diffraction (SAXRD) experiments to analyze the properties of amorphous silicon/silicon carbide interfaces, for different carbon concentrations, through the study of multilayers composed by these materials. A study of  $a\text{-Si}_{1-x}\text{C}_x\text{:H}$  thin films was carried out by small angle x-ray scattering (SAXS) and the results are presented elsewhere.<sup>15</sup> As an attempt to improve the sharpness of the interfaces, an extra hydrogen plasma etching step was introduced between the deposition of consecutive layers, without interruption of the rf plasma. This procedure was shown to be effective in enhancing the interface sharpness.<sup>16</sup> Also, buffer layers of  $a\text{-Si}_{1-x}\text{C}_x\text{:H}$  with different C concentration were deposited over the substrate, in order to attain better periodicity, as well as to minimize the effect of the substrate roughness on the multilayers. Ultraviolet electron spectroscopy (AES) profiling, combined with the SAXRD results, provided an estimation of the interface thickness. The variation of the optical band gap of the multilayer period was obtained from absorbance measurements.

## II. EXPERIMENT

Different sets of  $a\text{-Si:H}/a\text{-Si}_{1-x}\text{C}_x\text{:H}$  multilayers were deposited onto 7059 Corning glass and  $n^+\text{-Si}$  substrates at a temperature of 250 °C, by plasma decomposition of appropriate gaseous mixtures of  $\text{SiH}_4$  and  $\text{CH}_4$  inside a glow discharge chamber, operating at a radio frequency (rf) power of 25 mW/cm<sup>2</sup>. The gas flows were controlled by mass flow controllers and the deposition times by manually operated valves. The structures were obtained by alternating 20 layers of the components (10 periods), produced without plasma interruption. An extra hydrogen plasma etching step was introduced between consecutive layers to remove the undesirable residual layer growth while changing the gas mixture. The etching time was 60 s for the M80 (M80: 80% methane in the plasma during deposition) set of samples, while for all the other sets, it was 150 s. Table I shows the relevant deposition parameters for each series of samples studied in this work.

In order to vary the carbon content in the  $a\text{-Si}_{1-x}\text{C}_x\text{:H}$  multilayer component, different concentrations of  $\text{CH}_4$  were used inside the reactor chamber. For the M80 series this value was 80%, for the M70 set 70%, and 90% for the M90. For the 90% heterostructures, the  $a\text{-Si}_{1-x}\text{C}_x\text{:H}$  layers were produced under "starving" plasma conditions.<sup>15,17</sup>

Buffer layers of  $a\text{-Si}_{1-x}\text{C}_x\text{:H}$  with thicknesses between 1000 and 1200 Å and different carbon concentrations (see Table I) were deposited directly on the substrate to decrease roughness. The thickness of the individual layers ( $d_{\text{Si}}$  and  $d_{\text{SiC}}$ ) was estimated from the deposition rate of thick films, grown under identical conditions. The expected values are depicted in Table II, as well as the deposition times and rates for each material.

The SAXRD experiments were performed in two different conventional powder diffractometers, adapted for low angle measurements in a  $\theta$ -2 $\theta$  geometry. The use of more than one setup is not due to any special requirement

TABLE I. Sample series and respective deposition conditions.

Sample series	SiH <sub>4</sub> flow <sup>a</sup> (sccm)	CH <sub>4</sub> conc. (%)	Etching time (min)	Buffer layer <sup>b</sup>
M80	50	80	1.0	none
M70-a	50	70	2.5	type 1
M90-a	10 <sup>c</sup>	90	2.5	type 1
M70-b	50	70	2.5	types 1-2
M90-b	10 <sup>c</sup>	90	2.5	types 1-2

<sup>a</sup>Silane flow for the deposition of the  $a\text{-Si}_{1-x}\text{C}_x\text{:H}$  layer. For the  $a\text{-Si:H}$  layers the silane flow was 50 sccm.

<sup>b</sup>Type 1:  $a\text{-Si}_{1-x}\text{C}_x\text{:H}$  buffer layer deposited with CH<sub>4</sub> concentration of 90%. rf power density of 150 mW/cm<sup>2</sup>. Type 2:  $a\text{-Si}_{1-x}\text{C}_x\text{:H}$  buffer layer deposited with CH<sub>4</sub> concentration of 70%. rf power density of 150 mW/cm<sup>2</sup>.

<sup>c</sup>Starving plasma deposition conditions.

in measurement procedures, but rather to daily availability of the equipment. In both cases, the step scanning mode and monochromatic CuK $\alpha$  radiation were used. The measured  $2\theta$  range extended from 0.2° up to 3°, where most of the diffraction peaks are situated.

The Auger spectra were obtained in the differential mode using a cylindrical mirror analyzer (CMA) with a coaxial electron gun. The exciting electron beam had a diameter of the order of 50  $\mu\text{m}$  and energy of 3 keV. The base pressure in the analysis chamber was  $4 \times 10^{-10}$  Torr. Depth profiles were obtained by alternating Auger analysis with 500 eV argon ion sputtering. The angle between the ion beam and sample surface was 10°, with the sample placed perpendicular to the CMA's axis. The chamber was back filled to  $4 \times 10^{-5}$  Torr of argon during sputtering.

The optical gaps ( $E_g$ ) were obtained from absorbance measurements conducted in an ultraviolet-visible-infrared spectrometer (Varian Cary-2300 model).

### III. RESULTS

Table II presents the values for the thickness of each individual layer and for the period of the multilayers, estimated from predetermined deposition rates of thick films (M80 series, M70-a and M90-a series). These values are compared with those obtained from the SAXRD results shown in Table III.

The superlattice mean period was determined by the interference Bragg equation corrected for refraction:<sup>18</sup>

TABLE II. Individual layer thickness ( $d_{\text{Si}}$ ,  $d_{\text{SiC}}$ ), period ( $d$ ) and deposition rates ( $g$ ) estimated from thick film deposits. Numbers in parentheses are the deposition times. Samples M70/4, M90/3, and M90/4 are from a series.

Sample	$d_{\text{Si}}$ (Å)	$d_{\text{SiC}}$ (Å)	$d$ (Å)	$g_{\text{Si}}$ (Å/min)	$g_{\text{SiC}}$ (Å/min)	$\bar{g}$ (Å/min)
M80/2	39(3')	52(4')	91	13.0	13.0	13.0
M80/3	52(4')	52(4')	104	13.0	13.0	13.0
M80/4	104(8')	52(4')	156	13.0	13.0	13.0
M70/4	94(6')	39(3.5')	133	15.7	11.1	14.0
M90/3	70(4.5')	39(10')	109	15.6	3.9	7.5
M90/4	94(6')	39(10')	133	15.7	3.9	8.3

TABLE III. Individual layer thickness ( $d_{\text{Si}}$ ,  $d_{\text{SiC}}$ ), period ( $d$ ) and deposition rates ( $g$ ) obtained from SAXRD measurements. Samples M70/4, M90/3, and M90/4 are from a series.

Sample	$d_{\text{Si}}$ (Å)	$d_{\text{SiC}}$ (Å)	$d$ (Å)	$g_{\text{Si}}$ (Å/min)	$g_{\text{SiC}}$ (Å/min)	$\bar{g}$ (Å/min)
M80/2	74	74	$148 \pm 2$	24.7	18.5	21.2
M80/3	96	78	$174 \pm 2$	24.0	19.5	21.8
M80/4	169	84	$253 \pm 1$	21.1	21.0	21.1
M70/4	107	53	$160 \pm 3$	17.8	15.1	16.8
M90/3	81	45	$126 \pm 3$	18.0	4.5	8.7
M90/4	108	45	$153 \pm 3$	18.0	4.5	9.6

$$m\lambda = 2d \left( 1 - \frac{\delta}{\sin^2 \theta_m} \right) \sin \theta_m, \quad (1)$$

where  $\delta = \delta_1 d_1 + \delta_2 d_2 / (d_1 + d_2)$  is the real part of the refractive index of the multilayer, with period  $d$ , individual components thickness  $d_1$  and  $d_2$ , and refractive index  $\delta_1$  and  $\delta_2$ , respectively. In our case, the sub-index 1 is related to the  $a\text{-Si:H}$  layer, while sub-index 2 refers to the  $a\text{-Si}_{1-x}\text{C}_x\text{:H}$  layer.

The  $\delta$  values were calculated without previous knowledge of  $d_1$  and  $d_2$ , by replacing in Eq. (1) the two maxima angular positions ( $\theta_m$ ) of the diffractogram, after removing the background. The experimental  $\delta$  values are compared in Table IV with those obtained by theoretical calculations.<sup>19,20</sup>

The diffractograms relative to the M80, M70-a, and M90-a series are shown in Figs. 1(a)–1(c), 2, and 3(a)–3(b), respectively. The  $E_0$  values are given in Table V.

Figure 4 presents a typical AES depth profile. The compositions were obtained using tabulated sensitivity factors.<sup>21</sup> The profiling rates and interface thickness given in Table VI were calculated from the AES and SAXRD results, using only the variation in the concentrations.

The influence of the substrate on the structural quality of the heterostructures was also studied. Figures 5(a)–5(c) present the diffractograms of three samples (M70-b series) deposited directly on glass and on two different  $a\text{-Si}_{1-x}\text{C}_x\text{:H}$  buffer layers (70% and 90% CH<sub>4</sub> concentrations in the plasma during deposition). An analogous investigation was carried out for another set of samples (M90-b series). The reason for analyzing these different sets of multilayers deposited over the same kind of substrate was to find the best experimental parameters to grow

TABLE IV. Calculated and experimental values of the x-ray optical constants.

Sample	Calculated ( $\times 10^{-6}$ )			Experimental ( $\times 10^{-6}$ )
	$\delta_{\text{Si}}$	$\delta_{\text{SiC}}$	$\delta$	$\delta$
M80/2	7.59	9.49	8.54	10.8
M80/3	7.59	9.49	8.44	10.4
M80/4	7.59	9.49	8.22	8.03
M70/4-a	7.59	9.91	8.36	8.05
M90/3-a	7.59	9.06	8.12	7.44
M90/4-a	7.59	9.06	8.02	7.60

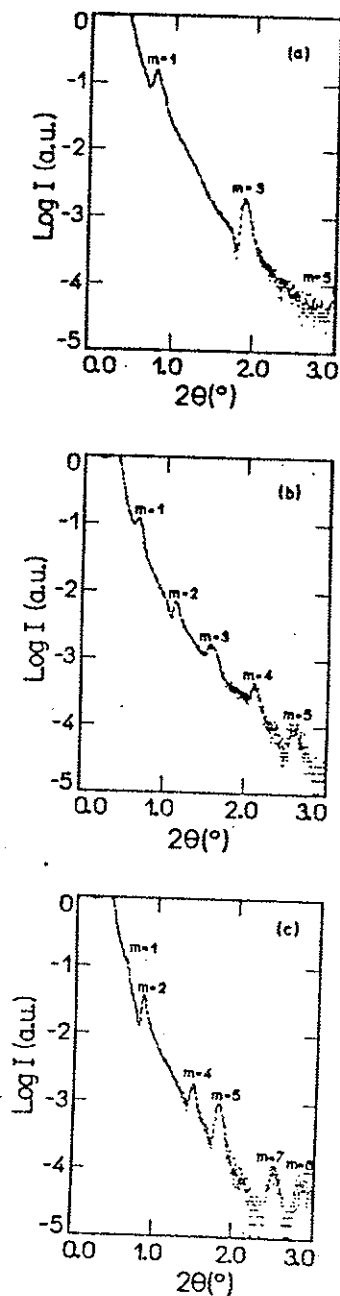


FIG. 1. SAXRD results of the M80 series: (a) M80/2, (b) M80/3, and (c) M80/4.

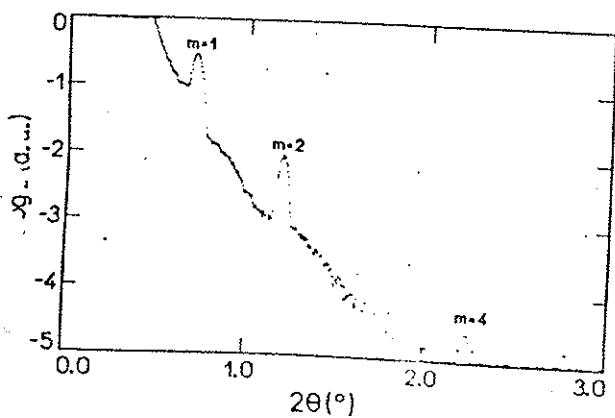


FIG. 2. SAXRD result of the M70/4-a sample.

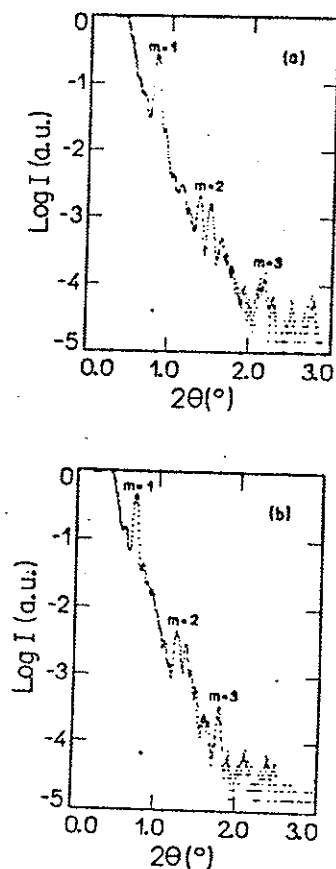


FIG. 3. SAXRD results of the M90-a series: (a) M90/3-a and (b) M90/4-a.

superlattices with sharp interfaces and reproducible periodicity. The SAXRD results, concerning the period x-ray optical constants and mean deposition rates, are presented in Table VII.

#### IV. DISCUSSION

As mentioned before, the aim of this work was the development of adequate rf glow discharge deposition conditions to produce abrupt interfaces between  $a\text{-Si:H}$  and  $a\text{-Si}_{1-x}\text{C}_x\text{:H}$  films. Our previous research demonstrated the effectiveness of an intermediary hydrogen plasma etching between the multilayer component depositions.<sup>16</sup> Comparing the SAXRD data of the M80 series (Fig. 1) with all the other series irrespective of the carbon concentration in

TABLE V. Superlattice period ( $d$ ) from SAXRD data,  $a\text{-Si:H}$  layer thickness ( $d_{\text{Si}}$ ) and optical band gap energy ( $E_0$ ).

Sample	$d$ (Å)	$d_{\text{Si}}$ (Å)	$E_0$ (eV)
M80/2	148	74	1.82
M80/3	174	96	1.76
M80/4	253	169	1.70
M70/4-a	160	107	1.97
M70/3-a	171	118	1.99
M70/2-a	179	126	1.91
M90/3-a	126	81	2.03
M90/4-a	153	108	1.90

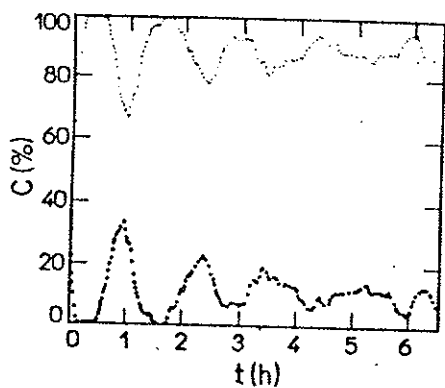


FIG. 4. AES spectrum of the M90/4-a sample: (●) Si and (○) C.

the  $\alpha$ -Si<sub>1-x</sub>C<sub>x</sub>:H layers and the substrate, the increase in H<sub>2</sub> plasma etching time always resulted in better defined interfaces.

The appearance of higher order peaks in Fig. 1 is an indication of period homogeneity, but the small peak intensities can be attributed to roughness or materials mixing at the interface. On the other hand, the results depicted in Fig. 2 show higher peak intensities that point to an improvement of the interface sharpness and mixing, which is due to the increase of the H<sub>2</sub> plasma etching time.

The SAXRD results were fundamental to fully characterize the produced amorphous multilayers, not only with regard to their periodicity, but also to the real deposition rates. The comparison between the expected and the experimental parameters, given in Tables II and III, shows that the obtained periods are always larger than their expected values. The difference is more pronounced for shorter deposition times of the individual layers. Obviously this effect is strongly reactor dependent, and it is related mainly to the speed with which the source gases can be introduced and removed from the plasma. From the SAXRD data it is also possible to determine the ratio between the individual thickness of the superlattice components, i.e.,  $d_1/d_2$ , within 10% error. For instance, the lack of second and fourth orders in the diffraction spectra is the signature of a heterostructure formed by components with identical thickness<sup>18</sup> (sample M80-2). The other features, like the lack of third and sixth order diffraction maxima (sample M80-4), carry the information that the thickness of a component layer is twice that of the other layer.<sup>18</sup>

TABLE VI. Argon ions sputtering rates ( $r$ ) and interface thickness ( $d_{int}$ ) obtained from the AES spectra and SAXRD data of samples with different period ( $d$ ).

Sample	$d$ (Å)	$r_{SiC}$ (Å/min)	$r_{Si}$ (Å/min)	$d_{int}$ (Å)
M70/4-a	160	0.98	2.71	8
M70/3-a	171	1.28	2.92	21
M70/2-a	179	1.36	4.53	27
M90/3-a	126	1.16	5.55	8
M90/4-a	153	0.73	3.63	11

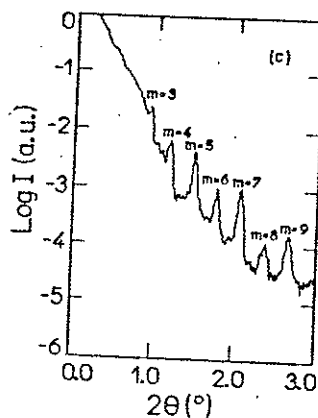
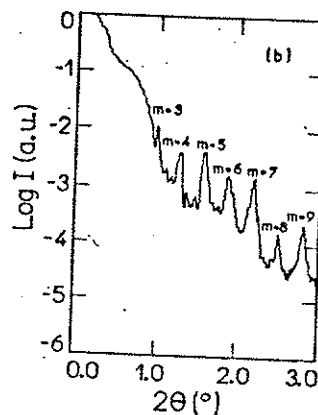
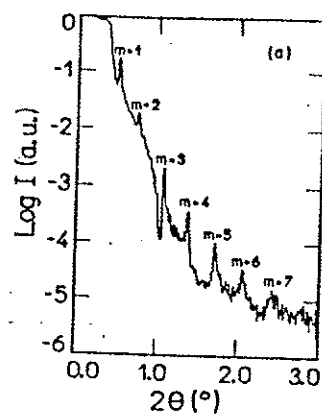


FIG. 5. SAXRD results of the M70-b series: (a) M70/4-WB, (b) M70/4-B7, and (c) M70/4-B9.

TABLE VII. Superlattice period ( $d$ ), x-ray optical constant ( $\delta$ ), and mean deposition rate ( $\bar{g}$ ) for the samples of the M70-b and M90-b series. WB=without buffer, B7=buffer of silicon carbide deposited with 70% of methane, B9=buffer of silicon carbide deposited with 90% of methane.

Sample	$d$ (Å)	$\delta$ ( $\times 10^{-6}$ )	$\bar{g}$ (Å/min)
M70/4-WB	267 ± 4	6.91	28.1
M70/4-B7	287 ± 1	5.38	30.2
M70/4-B9	303 ± 1	4.10	31.9
M90/4-WB	211 ± 1	30.5	13.2
M90/4-B7	211 ± 1	30.5	13.2
M90/4-B9	207 ± 6	28.5	12.9

The calculated and experimental values of the x-ray optical constants shown in Table IV differ, mainly due to the fact that the theoretical calculations were performed using the available published data for crystalline materials. Therefore, the calculated values do not describe correctly the x-ray optical properties of the amorphous multilayers and cannot be used in Eq. (1) to precisely determine the periodicity of the studied systems.

The optical gap ( $E_0$ ) was extrapolated from the Tauc plot,  $(\alpha h\nu)^{1/2}$  vs  $h\nu$ ,<sup>22</sup> where  $\alpha$  was obtained from optical absorption measurements (see Table V). For the M80 series, the absorption coefficient was also measured by photoconductivity, giving similar results. Within each series, the optical gap  $E_0$  increases when the thickness of the  $\alpha$ -Si:H layer decreases. This result is consistent with the existence of quantum levels within the well. The smaller the width of the well, the higher the energy of the fundamental state, thus increasing  $E_0$ .<sup>1,23</sup> The variation in the  $E_0$  values between the series arises from different interfaces and barrier materials.

Figures 2 and 3 show secondary oscillations around the peak maxima, indicating abrupt interfaces. The secondary maxima are due to interference of the diffracted beams<sup>24</sup> and can be enhanced by the presence of the buffer layer. In fact, smoother substrates, on an atomic scale, should lead to the formation of multilayers without imperfections at the interfaces caused by substrate defects. These defects usually propagate towards the top of the heterostructure, promoting roughness.<sup>25</sup>

Higher first order peak intensities were observed for the systems having the  $\alpha$ -Si<sub>1-x</sub>C<sub>x</sub>:H layers deposited with 10% CH<sub>4</sub> in the plasma (Fig. 3) as compared to those multilayers produced with 70% CH<sub>4</sub> (Fig. 2). This result shows, in spite of the differences in x-ray optical constants,<sup>26</sup> that sharper interfaces exist between  $\alpha$ -Si:H and  $\alpha$ -Si<sub>1-x</sub>C<sub>x</sub>:H, when the later is deposited with higher CH<sub>4</sub> concentration under starving plasma conditions. With this condition, more homogeneous diamond-like amorphous silicon carbide layers are expected to be formed.<sup>13-15</sup> Nevertheless, the considerable splitting of the second order maxima (Fig. 3) indicates period inhomogeneity in these high carbon concentration superlattices. This problem arises, because the starving plasma deposition conditions require a very low silane flow, which is much harder to control, thus making it difficult to deposit the superlattice with a precise period. Another point to be considered in the discussion of the interface abruptness is the influence of the intermediary H<sub>2</sub> plasma etching between the deposition steps. The improvement of the interfaces observed for the higher carbon content silicon carbide layers can be attributed to a material with less defects and/or to a different H<sub>2</sub> plasma etching smoothing process of  $\alpha$ -Si<sub>1-x</sub>C<sub>x</sub>:H with different  $x$  values.<sup>15,17</sup>

The argon ion sputtering rates for  $\alpha$ -Si:H and  $\alpha$ -Si<sub>1-x</sub>C<sub>x</sub>:H were obtained from the thickness of the individual layers, provided by the SAXRD measurements, divided by the sputtering time, given by the AES depth profile. An estimation of the interface thickness of the analyzed heterostructures (see Table VI) was done by tak-

ing the sputtering rate and the slope of the first AES depth profile peak. The reason to use only the first peak is to avoid mixing of the materials due to the sputtering process. As expected, the sputtering rate of  $\alpha$ -Si<sub>1-x</sub>C<sub>x</sub>:H is much smaller than the sputtering rate of  $\alpha$ -Si:H. This result can be related to the presence of strong C-C diamond-like bonds. The intermixing observed in the depth profile (see Fig. 4) and the differences in concentration, compared to those obtained for thick  $\alpha$ -Si<sub>1-x</sub>C<sub>x</sub>:H films deposited by the same method,<sup>15</sup> can be attributed to the sputtering process, which frequently produces a rough surface, thus exposing different layers to the probing beam simultaneously.<sup>27</sup> Also, an amorphous material is probably more prone to knock on effects than its crystalline counterpart, because of its lower density.<sup>27</sup>

The SAXRD results obtained for the samples deposited on different substrates (M70-b and M90-b series) were used to better evaluate the effectiveness of the buffer layer in enhancing the superlattice structural properties. The data again showed a higher deposition rate for deposits having smaller carbon content (see Table VII). Also, the high carbon concentration superlattices presented the same period inhomogeneities as discussed above. The appearance of higher order diffraction maxima and the increase in the diffracted intensities when the buffers are included, are indications that the heterostructures have improved periodicity and interface abruptness (see Fig. 5). Better results in terms of interface properties are achieved when the buffer is deposited with 90% methane concentration. We obtained shorter superlattice periods for rougher substrates (see Table VII). This result is consistent with a growth process in which the consecutive layers have to fill the morphological imperfections before the growth of a continuous film.

Up to now, it is impossible to establish a common rule about the interface sharpness of amorphous multilayers deposited by rf glow discharge. We still have to deal with particular improvements obtained under very well specified deposition conditions. In the literature, studies focused on direct transmission electron microscopy observations of  $\alpha$ -Si:H/ $\alpha$ -Si<sub>1-x</sub>N<sub>x</sub>:H and  $\alpha$ -Si:H/ $\alpha$ -Si<sub>1-x</sub>C<sub>x</sub>:H structures, deposited by the rf glow discharge method, came out with different conclusions.<sup>25,28</sup> Cheng *et al.*<sup>25</sup> pointed out that roughness happens close to the substrate, while Itoh *et al.*<sup>28</sup> found that imperfections are promoted by the superlattice growth process. Our results indicate a strong influence of the substrate on the structural properties of our  $\alpha$ -Si:H/ $\alpha$ -Si<sub>1-x</sub>C<sub>x</sub>:H superlattices.

## V. CONCLUSIONS

In conclusion, we demonstrated that SAXRD measurements carried on amorphous superlattices give much more information on the studied systems than the usual period determination. The use of an intermediary H<sub>2</sub> plasma etching between the layered depositions, as well as the growth of a buffer layer on top of the substrate, are responsible for an improvement in the interface sharpness. AES experiments combined with SAXRD results provided an estimation of the interface thickness, a parameter that is

an input for x-ray reflectivity simulations.<sup>18</sup> The use of diamond-like silicon carbide films is encouraged for device applications, due to their better morphological properties, in spite of the period inhomogeneities we had observed. This difficulty can be overcome by better control of the gas flow during deposition. Our deposition setup has been rebuilt to include improvements in the sample preparation procedure.

## ACKNOWLEDGMENTS

Thanks are due to J. Morais and T. A. Fazan for help with the AES measurements. We would like to thank Professor G. G. Kleiman for a critical reading of the manuscript. This work was supported by FAPESP, CNPq, and FINEP, Brazil.

- <sup>1</sup>B. Abeles and T. Tiedje, *Phys. Rev. Lett.* **51**, 2003 (1983).
- <sup>2</sup>J. Kakalios, H. Fritzsche, N. Ibaraki, and S. R. Ovshinsky, *J. Non-Cryst. Solids* **66**, 339 (1984).
- <sup>3</sup>T. Tiedje, B. Abeles, P. D. Persans, B. G. Brooks, and G. S. Cody, *J. Non-Cryst. Solids* **66**, 345 (1984).
- <sup>4</sup>B. Abeles, T. Tiedje, K. S. Liang, H. W. Deckman, H. C. Stasiewski, J. C. Scalon, and P. M. Eisenberger, *J. Non-Cryst. Solids* **66**, 351 (1984).
- <sup>5</sup>P. Santos, M. Hundhausen, and L. Ley, *Phys. Rev. B* **33**, 1516 (1986).
- <sup>6</sup>P. V. Santos and L. Ley, *Phys. Rev. B* **36**, 3325 (1987).
- <sup>7</sup>P. V. Santos, M. Hundhausen, L. Ley, and C. Viczian, *J. Appl. Phys.* **69**, 778 (1991).
- <sup>8</sup>H. Munekata and H. Kukimoto, *Jpn. J. Appl. Phys.* **22**, L544 (1983).
- <sup>9</sup>S. Nishikawa, H. Kakinuma, H. Fukuda, T. Watanabe, and K. Nihei, *J. Non-Cryst. Solids* **77&78**, 1077 (1985).
- <sup>10</sup>S. Nishikawa, H. Kakinuma, T. Watanabe, and K. Nihei, *Jpn. J. Appl. Phys.* **25**, 1141 (1986).
- <sup>11</sup>M. Yoshimoto, T. Fuyuki, and H. Matsunami, *Jpn. J. Appl. Phys.* **25**, L922 (1986).
- <sup>12</sup>S. Tsuda, H. Tarui, T. Matsuyama, T. Takahama, S. Nakayama, Y. Hishikawa, N. Nakamura, T. Fukatsu, M. Ohnishi, S. Nakana, and Y. Kawano, *Jpn. J. Appl. Phys.* **26**, 28 (1987).
- <sup>13</sup>R. Onmori, I. Pereyra, C. Sasaki, and M. N. Carreño, in *Proceedings of the 9th European Photovoltaic Solar Energy Conference*, edited by W. Palz, G. T. Wrixon, and P. Helm (Kluwer Academic, Dordrecht, 1989), p. 33.
- <sup>14</sup>C. Sasaki, A. Arasaki, M. Carreño, A. Komazawa, and I. Pereyra, *J. Non-Cryst. Solids* **115**, 90 (1989).
- <sup>15</sup>M. N. P. Carreño, I. Pereyra, M. C. A. Fantini, H. Takahashi, and R. Landers, *J. Appl. Phys.* **74**, 538 (1993).
- <sup>16</sup>M. C. A. Fantini, I. Pereyra, M. N. P. Carreño, and A. M. Andrade, *Proceedings of the 10th European Photovoltaic Solar Energy Conference*, edited by A. Luque, G. Sala, W. Palz, G. dos Santos, and P. Helm (Kluwer Academic, Dordrecht, 1991), p. 329.
- <sup>17</sup>I. Solomon, M. P. Schmidt, and H. Trán-Quoc, *Phys. Rev. B* **38**, 9895 (1988).
- <sup>18</sup>J. H. Underwood and T. W. Barbee Jr., *AIP Conf. Proc.* **75**, 170 (1981).
- <sup>19</sup>M. G. Le Boité, A. Traverse, L. Nénot, B. Pardo, and J. Corno, *J. Mater. Res.* **3**, 1089 (1988).
- <sup>20</sup>*Powder Diffraction File*, edited by W. F. McClure [Joint Committee on Powder Diffraction Standards (J.C.P.D.S.), International Center for Diffraction Data, PA, 1978].
- <sup>21</sup>L. E. Davis, N. C. Mac Donald, P. W. Palmberg, G. E. Riach, and R. E. Weber, *Handbook of Auger Electron Spectroscopy*, 2nd ed. (Perkin-Elmer, Physical Electronics Division, MN, 1976).
- <sup>22</sup>*Amorphous and Liquid Semiconductors*, edited by J. Tauc (Plenum, New York, 1974), p. 173.
- <sup>23</sup>N. Ibaraki and H. Fritzsche, *Phys. Rev. B* **30**, 5791 (1984).
- <sup>24</sup>L. Nénot, B. Pardo, and J. Corno, *Rev. Phys. Appl.* **23**, 1675 (1988).
- <sup>25</sup>R. Cheng, S. Wen, J. Feng, and H. Fritzsche, *Appl. Phys. Lett.* **46**, 592 (1985).
- <sup>26</sup>E. L. Z. Velasquez, M. C. A. Fantini, M. N. P. Carreño, and I. Pereyra (unpublished theoretical calculations).
- <sup>27</sup>R. Smith and J. M. Walls, in *Methods of Surface Analysis*, edited by J. M. Walls (Cambridge University Press, MA, 1989), Chap. 2.
- <sup>28</sup>H. Itoh, S. Matsubara, S. Muramatsu, N. Nakamura, T. Shimada, and T. Shimotsu, *Jpn. J. Appl. Phys.* **27**, L24 (1988).

# On the structural properties of $a\text{-Si}_{1-x}\text{C}_x\text{:H}$ thin films

V. Mastelaro

DEMA - UFSCar, CP 676, 13560-970, São Carlos, SP, Brazil

A. M. Flank

LURE, Bâtiment 209 D, 91405 Orsay Cedex, France

M. C. A. Fantini, D. R. S. Bittencourt

Instituto de Física - USP, CP 20516, 01452-990, São Paulo, SP, Brazil

M.N.P. Carreño and I. Pereyra

LME, DEE, POLI - USP, CP 8174, 05508-970, São Paulo, SP, Brazil

## Abstract

The structural and chemical properties of hydrogenated amorphous silicon carbide ( $a\text{-Si}_{1-x}\text{C}_x\text{:H}$ ) thin films, deposited by Plasma Enhanced Chemical Vapor Deposition (PECVD), were determined by Extended X-ray Absorption Fine Structure (EXAFS), X-ray Absorption Near Edge Spectroscopy (XANES), Small Angle X-ray Scattering (SAXS), Fourier Transform Infra-Red Spectroscopy (FTIR), Auger Electron Spectroscopy (AES) and Visible Spectrometry.

The EXAFS and XANES results show the crucial influence of the "starving" plasma deposition conditions on the structural properties of wide gap  $a\text{-Si}_{1-x}\text{C}_x\text{:H}$  films and are consistent with the FTIR and optical absorption data. The first neighbors distance of alloys with smaller carbon content or deposited at higher silane flow are very close to the mean Si-Si distance obtained for  $a\text{-Si:H}$ . On the other hand, the EXAFS spectra of films with higher carbon content ( $x > 50$  at.%) and deposited under "starving" plasma regime show Si-C distances similar to crystalline SiC (c-SiC). The presence of a typical c-SiC resonance in the XANES spectra of the same samples is an evidence that the material has a chemical order close to c-SiC.



## Introduction

Hydrogenated amorphous silicon alloys obtained by the Plasma Enhanced Chemical Vapor Deposition (PECVD) technique are used in many different optoelectronic devices <sup>1-5</sup>, mostly due to the possibility of tailoring the optical gap with variations in the gas mixture composition. In particular, hydrogenated amorphous silicon carbide thin films,  $a\text{-Si}_{1-x}\text{C}_x\text{H}$ , are used in solar cells <sup>6,7</sup> and thin film transistors <sup>2,3,8,9</sup>, always tailoring the optical gap by variations of the methane partial pressure in the gas mixture. However, for high  $\text{CH}_4$  partial pressures, these materials generally show a decrease in the optical gap, which is related to the formation of graphite-like  $\text{sp}^2$  C-C bonding instead of diamond-like  $\text{sp}^3$  C-C bonding <sup>10</sup>.

In a previous work <sup>11</sup> we demonstrated that it is possible to obtain hydrogenated amorphous silicon carbide thin films with optical gap as high as 3.7 eV, resistivity higher than  $10^{15} \Omega\cdot\text{cm}$ , very low refractive index and high carbon content ( $x \approx 70 \text{ at.}\%$ ), suggesting the presence of a diamond like C-C structure. The growth of  $a\text{-Si}_{1-x}\text{C}_x\text{H}$  films with these unusual properties is achieved under special deposition conditions, known as "starving" plasma regime. The influence of the "starving" plasma deposition conditions in the growth of wide gap amorphous silicon carbide films is presented elsewhere <sup>12</sup>. At this regime, the deposition rate is strongly dependent on the silane flow and, it is characterized as a combination of a low rf power density with a very low silane flow and high methane concentration.

In this work we extend the previous investigation on  $a\text{-Si}_{1-x}\text{C}_x\text{H}$  films, studying the dependence of their structural properties with the two deposition parameters in question: the silane flow and the methane partial pressure. These parameters determine the forms of carbon incorporation in the films and the future structural, electronic and optical properties of the material. Various techniques were used to analyze the different films: Extended X-ray Absorption Fine Structure (EXAFS) and X-ray Absorption Near Edge Spectroscopy (XANES) to explore the structural characteristics, Small Angle X-ray Scattering (SAXS) to detect the formation of microvoids, Auger Electron Spectroscopy (AES) to determine the alloy chemical composition and Visible and Infra-Red (IR) spectrometry to find the optical gap and atomic bonds inside the material.

The structural features of amorphous Si-based alloys have been addressed by means of EXAFS and XANES experiments. A previous study of  $a\text{-Si}_{1-x}\text{Ge}_x\text{:H}$  alloys<sup>13</sup> found that Ge-Ge and Ge-Si distances are independent of concentration ( $x$ ) and equal to 2.45 and 2.38 Å, respectively. The results point out that the first coordination shell around Ge is consistent with a random mixing of the two species in the alloys. The total disorder factors have been determined for both Ge-Ge and Ge-Si, being constant and equal to each other in the whole analyzed concentration range.

A. Filiponi et al.<sup>14</sup> studied by EXAFS at the Si K-edge, the structure of three series of hydrogenated amorphous Si-based alloys. Average bond-lengths and first shell compositions were determined. Concerning particularly the  $a\text{-Si}_{1-x}\text{C}_x\text{:H}$  system, it was found that the Si-Si average distance ( $R_{\text{Si-Si}}$ ) is independent of  $x$  and equal to 2.35 Å, whereas the Si-C average distance ( $R_{\text{Si-C}}$ ) undergoes a more complicate behavior, with a minimum at  $x=0.5$  and an overall variation of more than 0.1 Å. According to the authors, the results on  $R_{\text{Si-C}}$  should be carefully analyzed due to the poorer quality of the experimental data.

More recently, C. Laffon et al.<sup>15</sup> presented XANES studies of some silicon compounds. They compared the X ray absorption near edge structure of c-SiC, c-SiO<sub>2</sub> and c-Si (all crystalline compounds) and provided a qualitative analysis concerning the energy shifts and the presence of some particular features. In these compounds, each silicon atom is four coordinated, but the spectra are very different. The energy of the white line maximum depends on the electronegativities of the bonded elements. A large resonance was observed at about 15 eV from the absorption edge in all these samples. The values of  $\Delta E$ , which is the energy between the absorption edge and the resonance, are somewhat imprecise due to the width of the resonance (except in the case of c-SiC), but for all these structures the relation  $\Delta E \cdot R^2 = \text{constant}$  is verified. The resonance at about 15 eV does not exist in the  $\text{Si}(\text{CH}_3)_4$  molecule and is spread out for amorphous silicon carbide, a-SiC. They infer that this resonance is characteristic of a structural order which extends up to the Si-Si second shell and its carbon neighbors. The presence of this feature is not related to a particular shell, but to the whole set of atoms in the structure taking into account the carbon neighbors.

These previous EXAFS and XANES results will serve as guidelines for the data analysis presented in this work.

## Experiment

The amorphous silicon carbide films were deposited by the Plasma Enhanced Chemical Vapor Deposition (PECVD) method, currently referred as radio frequency glow discharge technique, from gaseous mixtures of silane and methane, in a capacitively coupled reactor. The substrate temperature was fixed at 250 °C, the deposition pressure was 1 Torr and the power density was 150 mW.cm<sup>-2</sup>. In order to analyze separately the influence of the silane flow and the gas mixture concentration on the a-Si<sub>1-x</sub>C<sub>x</sub>: H properties, two set of samples were deposited: a first set, changing the CH<sub>4</sub> partial pressure, maintaining the silane flow constant and, a second one, changing the SiH<sub>4</sub> flow for a constant (72%) CH<sub>4</sub> partial pressure. Table I depicts the deposition parameters for the produced films, the optical gap ( $E_o$ ) and the carbon content in the solid phase (x). The gyration radius and relative microvoid volume fraction of the samples were determined by SAXS, using part of the white x-ray spectrum or Mo K $\alpha$  radiation. The carbon, silicon and hydrogen forms of incorporation in the different films were determined by Fourier Transform Infra-Red (FTIR) spectrometry<sup>16</sup>.

The EXAFS and XANES data were collected at the Si K-absorption edge ( $E=1839$  eV) at the SUPERACO ring ( SA32 station) at the LURE synchrotron radiation facility in Orsay, France. The beam was monochromatized using a double crystal monochromator, equipped with two InSb monocrystals. The detection was performed in the total electron yield mode, so that the requirement of a clean surface is not a very critical issue. K edge EXAFS and XANES spectra were analyzed by subtracting a linear background, computed by least square fitting from the pre-edge region. All the XANES spectra were arbitrarily normalized on the maximum K edge peak. The EXAFS oscillation curves,  $\chi(k)$ , with  $k=[m/h^2(E-E_o)]^{1/2}$ , were obtained by a standard procedure<sup>17</sup>, normalized, background removed and Fourier transformed using the available programs for

Macintosh computers<sup>18</sup>. After a  $k^3(k)$  weighting, a Kaiser apodization function was applied over 3.6 and 10.6  $\text{\AA}^{-1}$ , with  $\tau = 2.5$ .

Crystalline and amorphous samples were taken as structural references : a-Si:H ( for Si-Si bonds), c-SiC ( for Si-C and Si-Si bonds) and c-SiO<sub>2</sub> (for Si-O bonds). In a-Si:H, due to the low H concentration, more than 90% of the silicon atoms are coordinated by other four silicon atoms situated at about 2.35  $\text{\AA}$ . In c-SiC, each silicon atom is surrounded by four carbon atoms forming the first shell ( at 1.89  $\text{\AA}$ ) and other twelve silicon atoms forming the second shell (at 3.08  $\text{\AA}$ ). In c-SiO<sub>2</sub> compound, each silicon atom is surrounded by four oxygen atoms situated at an average distance of 1.61  $\text{\AA}$ <sup>14</sup>.

## Results

The results presented in Table I show that, for films of the first set of samples, deposited under the same silane flow and different methane partial pressure, the optical gap increases monotonically with the increase of carbon content in the material up to a maximum of approximately 4 eV, attained at a carbon incorporation of about 70 at.%. On the other hand, the films of the second set of samples, deposited with increasing silane flow, but under the same methane concentration in the gas mixture, show a decrease in the optical gap for higher silane flows.

Figure 1, related to the first set of samples, depicts the infra-red absorption spectra for three samples grown at different methane partial pressure (50%, 72% and 92%) and constant (10 sccm) silane flow. For increasing methane concentration in the gas mixture, there are lower levels of carbon incorporation in the Si-C form and a non surprising decrease in the SiH<sub>n</sub> band, while the CH<sub>n</sub> (n=1,2,3) and Si-CH<sub>n</sub> bands remain almost invariant. For higher CH<sub>4</sub> concentrations, the lower availability of silicon justifies the decrease of the Si-C band but, as the other detectable carbon incorporation forms remain essentially constant, the extra carbon atoms must be incorporated in the C-C form, which are not detectable with FTIR spectrometry.

Figure 2, related to the second set of a-Si<sub>1-x</sub>C<sub>x</sub>: H films, depicts the infra-red absorption spectra of samples deposited at constant methane partial pressure (72% ) and

variable silane flow. The Si-C band is higher and the SiH<sub>n</sub> band is smaller, for samples grown at a lower silane flow. This difference is much more pronounced for samples deposited at the lowest flow (10 sccm), which corresponds to the "starving" plasma regime.

The microvoid sizes do not depend on the deposition regime. Microvoids, whose size stayed between c.a. 2.0 Å and 4.0 Å, were detected for all analyzed films, from the Guinier plot of the registered data <sup>16,19</sup>. On the other hand, the relative microvoid volume fraction ( $\eta$ ) is larger for films grown at "non-starving" plasma conditions, as shown in Table II. In the case of samples deposited at high silane flow, i.e., at "non-starving" plasma regime, the analysis of the Porod's region <sup>19</sup> did not show the -3 slope, expected for line focus geometry, indicating that the interface between the microvoids and the matrix is not abrupt.

Figures 3 and 4 present the Fourier transform of the EXAFS data. The Fourier transforms are not corrected for the phase shift parameters, so that the maximum peak positions (that corresponding to the Si-C, Si-Si or Si-O bonds) are shifted to lower values compared to the real ones. Figure 3 corresponds to the first set of samples, grown at "starving" plasma conditions and different methane partial pressure. A qualitative interpretation of these results shows that, for almost stoichiometric film ( $x=0.46$ ,  $P(\text{CH}_4)=50\%$ ), the first neighbors distance is very similar to the Si-Si mean distance in a-Si:H. In this case a coordination number equals to four is also expected, but it is difficult to assign this distance only to Si-Si bonds, since the material has a carbon content of 46 at.%. The peak profile in the Fourier transform is asymmetric and, therefore, the peak might be a superposition of similar bonding distances related to Si-Si and Si-C. On the other hand, for films having higher carbon content ( $x=0.55$  and  $x=0.70$ ), the results demonstrate clearly the existence of Si-C distances similar to the c-SiC, indicating the presence of an amorphous SiC phase with chemical order similar to c-SiC. Conversely, the Si-Si distance contributions are difficult to separate. The Si-Si bonds in the a-Si:H are situated at a distance of 2 Å, exactly between the Si-C and Si-Si second neighbors of the c-SiC (Fig. 3), making difficult to distinguish between the different Si-Si distances (related to a-Si:H and to c-SiC). Furthermore, C. Laffon <sup>20</sup> showed that the imaginary part of the Si-C and Si-Si (from c-SiC) and Si-Si (from a-Si:H) peaks are in phase opposition, so that the Si-Si

contribution situated at about 2 Å cannot be observed, even for a mixture of 20% of crystallized silicon and 80% of c-SiC.

Figure 4 presents the data related to the second set of samples, which were deposited at the same methane partial pressure (72%), but at different silane flow ( $f=10$ , 50 and 100 sccm). In this case, the number of Si-C and Si-Si bonds similar to that of c-SiC is smaller in the films deposited under "non-starving" regime, i.e., at higher flow values. However, as it has been pointed earlier, the existence of Si-Si bonds (from a-Si:H) or a decrease in the Fourier transform peak intensity, can be masked by the phase opposition effect. For samples deposited under "non-starving" regime (MVC6 and MVC7) a first peak situated at about 1.2 Å is observed. From Fig. 4, this peak can be attributed to an oxygen contribution, since it is located at a similar Si-O mean bond length than in the c-SiO<sub>2</sub>. This oxygen is probably incorporated through the sample microvoids. The intensity of this peak depends on the sample history, like for example, how long it has been exposed to air. Nevertheless, based on the relative peak intensities, the number of Si-O bonds is small in the studied samples as compared to the c-SiO<sub>2</sub> reference compound.

An attempt of fitting was performed for the two extreme cases, related to samples deposited at the highest and lowest methane partial pressure, MVC1 and MVC5, respectively. In these cases the contribution of only one kind of atom is assumed for the first peak of the Fourier Transform (Fig. 3). Figure 5 presents the filtered  $\chi(k)$  EXAFS spectra and the calculated curves obtained with the parameters shown in Table III. The a-Si:H and c-SiC were used, respectively, as reference compounds for the MVC5 and MVC1 fitting procedures. The fitting quality obtained for the MVC1 sample (Fig. 5a) is very good and the results presented in Table III confirm the existence of a high local order in the films. On the other hand, for the MVC5 sample (Fig. 5b), the fitting quality is poor. In Fig. 5b, the EXAFS experimental spectra present an intensity decrease at about 5.3 Å<sup>-1</sup> that can be due to the contribution of another kind of atom, as carbon or even silicon atoms, situated at different distances. Actually, this is an expected result, since the sample contains 46% of carbon atoms and should not be described based only on Si-Si bonding. In this case a two-shell model could improve the agreement with the experimental data. It has pointed earlier that low carbon content amorphous silicon

carbide films are formed by a random distribution of Si and C atoms, preserving the first neighbors distances of a-Si:H<sup>21,22</sup>.

Nevertheless, before attempting to obtain quantitative results from a two shell fitting, it is necessary to define the maximum number of independent parameters to be adjusted during the fitting procedure. It is a common rule for reliable simulations to take this number equal to (Npts -1), defined as  $Npts = (2\Delta k \Delta R)/\pi$ , where  $\Delta k$  is the k space range of the measured data and  $\Delta R$  is the width of the window used when Fourier transforming in R space. In this case,  $\Delta k = 7.4 \text{ \AA}^{-1}$  and  $\Delta R = 1.2 \text{ \AA}$  (medium value), that gives  $Npts = 5.7$ . Having at least six fitting parameters: neighbor number (N), mean bond length (R) and Debye-Waller factor ( $\Delta\sigma$ ), this value (5.7) is too small to lead to an accurate determination of the structural parameters based on calculations of a two or three-subshell model.

Figures 6 and 7 show the XANES region obtained for the two series of samples. The position of the absorption edge depends on the film composition. The higher is the carbon content in the film, the closer is its absorption edge to the value obtained for c-SiC, as well as the XANES line shape (see Fig. 6). Calculations based on c-SiC XANES spectrum<sup>23</sup> showed that the A resonance appears when the fifth shell of atoms is included. Another feature (B), observed at about 6 eV from the absorption edge, seems to be related to a more extended SiC cluster due to the increase of the mean free path of low kinetic energy electrons. The XANES calculations determined that the B resonance should be present for a c-SiC cluster extension of about 12 Å. The XANES results for the films deposited under the "starving" plasma regime (Fig. 6) do not show the B resonance, but only the A resonance, which is more pronounced for the samples having  $x=0.7$  and  $x=0.55$ . The fact that this resonance is spread compared to the peak width in the c-SiC reference is attributed to the amorphous characteristics of the deposited films<sup>23</sup>. For the second set of samples (deposited at the same methane partial pressure, but at different silane flow), the A resonance in the XANES spectra of Fig. 7 is clearly observed for the film deposited at the lower silane flow and damped for the other samples.

## Discussion

The results show that the structural, morphological and bonding features of the hydrogenated amorphous silicon carbide films studied in this work, deposited at different methane partial pressure or silane flow, are very distinct.

By changing the  $\text{CH}_4$  partial pressure inside the deposition chamber, the carbon concentration inside the film changes, as well as the forms of atomic bonding. As expected, the higher is the methane partial pressure, the higher is the amount of carbon incorporated in the films. On the other hand, samples grown at identical methane concentration in the gas mixture, but at different silane flows, present the same carbon content in the film matrix, but very different optical gaps, structural and morphological features. Increasingly optical gaps are achieved only with the combination of high methane partial pressure and low silane flow, characteristics of the "starving" plasma regime. Nevertheless, with the increase of carbon content in the films deposited at the "starving" plasma conditions, the FTIR results show that all bands related to silicon or carbon bonding ( $\text{Si-CH}_n$ ,  $\text{CH}_n$ ) decrease or remain constant, ruling out the possibility of a polymeric lattice formation. Therefore, the FTIR data, associated to the high optical gap and mechanical hardness of these  $\text{a-Si}_{1-x}\text{C}_x\text{H}$  films, strongly indicate that the excess of carbon is incorporated with a diamond-like C-C type of bonding.

The EXAFS, XANES and FTIR results demonstrate that the films with higher carbon content, deposited at "starving" plasma regime, preserve the distances and chemical order of c-SiC. It is interesting to point out that the EXAFS and XANES data obtained for the MVC5 sample ( $x=0.46$ , almost stoichiometric) shows a structure similar to a-Si:H. Therefore, in low carbon content films, it is possible that the material is composed by a random mixing of silicon and carbon atoms<sup>21,22</sup> and that the Si-C double layer structure of the c-SiC lattice is not maintained. Conversely, our results for high carbon content films, show that it is possible, under proper deposition conditions, to obtain an amorphous network with the short range order similar to c-SiC. The EXAFS and XANES data indicates that the deposition kinetics related to the silane flow governs the structural characteristics of the films, more than the  $\text{CH}_4$  partial pressure.



The SAXS results demonstrate that high carbon incorporation does not necessarily mean higher microvoid volume fraction. The decrease in the relative microvoid volume fraction presented for sample MVC1 when compared to MVC3 and MVC4 samples indicates that it is possible to obtain more homogeneous (in a relative scale)  $a\text{-Si}_{1-x}\text{C}_x\text{:H}$  films with high values of  $x$  and a structure similar to  $c\text{-SiC}$ , provided the "starving" plasma deposition conditions are used.

On the other hand, changing the deposition conditions from "starving" to "non-starving" regime (*i.e.*, varying the silane flow, maintaining the same methane partial pressure), gradually lead to the formation of films having more relative microvoid volume fraction, less Si-C bonds characteristics of  $c\text{-SiC}$  and shorter Si-Si bonds, going towards the values of  $a\text{-Si:H}$ . The EXAFS and XANES data show that films with the same carbon concentration, but deposited with increasing silane flow, gradually change their structural features towards  $a\text{-Si:H}$  (see Fig.4 and Fig.7). Again, the results point out that the deposition kinetics rather than the carbon concentration determines the chemical and structural properties of the  $a\text{-Si}_{1-x}\text{C}_x\text{:H}$  films. The FTIR results reveal that the higher is the silane flow the larger are the  $\text{Si-CH}_n$  vibration bands, that are commonly related to the formation of microvoids <sup>24,25</sup>.

## Conclusions

The deposition of  $a\text{-Si}_{1-x}\text{C}_x\text{:H}$  films by the PECVD technique under "starving" plasma conditions originates films with high carbon content, that are chemically and structurally similar to  $c\text{-SiC}$ , having silicon preferably bonded to carbon. A structure similar to  $a\text{-Si:H}$  is observed for almost stoichiometric films ( $x \leq 0.5$ ), or for films deposited with higher methane concentrations but at "non-starving" regime. The change from "starving" to "non-starving" plasma deposition conditions is deleterious, since the materials obtained at the later conditions present a higher relative microvoid volume fraction, more  $\text{Si-CH}_n$  bonds and a structure less alike to  $c\text{-SiC}$ . Diamond-like C-C chemical bonds are suggested in films with high optical gap.

## Acknowledgments

Thanks are due to Ms. H. Takahashi and Dr. R. Landers for the AES data.

## References

- <sup>1</sup> D.A. Anderson and W.E. Spear, *Phil. Mag.* **35**, 1 (1977).
- <sup>2</sup> A. Madan, M.P. Shaw, "Physics and Applications of Amorphous Semiconductors", Ed. Academic Press Inc., p.149 (1988).
- <sup>3</sup> *IEEE Transaction on Electron Devices* **36**(12) (1989) - special issue on amorphous semiconductor devices.
- <sup>4</sup> *Philosophical Magazine* **B60** (1989) - special issue of the Workshop on Structure and Electronic properties of Amorphous Semiconductor Superlattices.
- <sup>5</sup> P.G. Lecomber, *J. Non-Cryst. Sol.* **115**, 1 (1989).
- <sup>6</sup> Y. Tawada, M. Kondo, H. Okamoto, Y. Hamakawa, XV IEEE Photov. Spec. Conf., NY, p.245 (1981).
- <sup>7</sup> D.E. Carlson, *IEEE Transaction on Electron Devices* **36**(12), 2775 (1989).
- <sup>8</sup> C.A. Sasaki, A.T. Arasaki, M.P. Carreño, A. Komazawa and I. Pereyra, *J. Non-Cryst. Sol.* **115**, 90 (1989).
- <sup>9</sup> M.P. Carreño, I. Pereyra and A.M. Andrade, *Surf. Sci. - Lectures on Basic Concepts and Applications*, ed. F.A. Ponce and M. Cardona, Springer-Verlag Publ., p. 387 (1992).
- <sup>10</sup> R.S. Sussmann and R. Odgen, *Phil. Mag. B* **44**, 137 (1981).
- <sup>11</sup> R.K. Onmori, I. Pereyra, C. Sasaki and M.P. Carreño, *Proc. 9th European Photovoltaic Solar Energy Conf.*, ed. W. Palz, G.T. Wrixon and P. Helm, Kluwer Acad. Publ., p. 33 (1989).
- <sup>12</sup> M.N.P. Carreño and I. Pereyra, submitted to *J. Non-Cryst. Solids* (1994).
- <sup>13</sup> L. Incoccia, S. Mobilio, M.G. Proietti, P. Fiorini, C. Giovannella and F. Evangelisti, *Physical Review B* **31**, 1028 (1985).
- <sup>14</sup> A. Filipponi, P. Fiorini, F. Evangelisti and S. Mobilio, *Mat. Res. Soc. Symp.*, vol. 95, p. 305 (1987).
- <sup>15</sup> C. Laffon, A.M. Flank and P. Lagarde, *Proc. of the VI International Conf. on X Ray Absorption Fine Structures*, ed. S. Samar Hasnain, p. 604 (1990).
- <sup>16</sup> M.N.P. Carreño, I. Pereyra, M.C.A. Fantini, H. Takahashi and R. Landers, *J. Appl. Phys.* **75**, 538 (1994).

- <sup>17</sup> B.K. Teo, EXAFS: Basic Principles and Data Analysis, Inorganic Chemistry Concepts 9, (Springer Verlag, 1986).
- <sup>18</sup> A. Michalowicz, Thesis, Université du Val de Marne, France (1990).
- <sup>19</sup> A. Guinier and S.G. Fournet, "Small Angle Scattering of X-Rays", Wiley, New York (1955).
- <sup>20</sup> C. Laffon, PhD Thesis - Université Paris XI - Orsay France (1990).
- <sup>21</sup> H. Wieder, M. Cardona and C. Guarnieri, Phys. Stat. Sol. B 92, 99 (1979).
- <sup>22</sup> G. Krötz, G. Müller, G. Derst, C. Wilbertz and S. Kalbitzer, Diamond and Related Materials 3, 917 (1994).
- <sup>23</sup> Ph. Saintavit, J. Petiau, C. Laffon, A.M. Flank and P. Lagarde, Proc. of the VI International Conf. on X Ray Absorption Fine Structures, ed. S. Samar Hasnain, p.38 (1990).
- <sup>24</sup> D.L. Williamson, A.H. Mahan, B.P. Nelson and R.S. Crandall, Appl. Phys. Lett. 55, 783 (1989).
- <sup>25</sup> A.H. Mahan, D.L. Williamson, B.P. Nelson and R.S. Crandall, Solar Cells 27, 465 (1989).

## Figure Captions

**Figure 1.** Absorption vs. wavenumber of  $a\text{-Si}_{1-x}\text{C}_x\text{H}$  deposited under "starving" regime at different methane partial pressure (P).

**Figure 2.** Absorption vs. wavenumber of  $a\text{-Si}_{1-x}\text{C}_x\text{H}$  deposited with a methane partial pressure of 72% and different silane flow (F).

**Figure 3.** Fourier Transform of the EXAFS data of  $a\text{-Si}_{1-x}\text{C}_x\text{H}$  deposited under "starving" regime at different methane partial pressure (P).

**Figure 4.** Fourier Transform of the EXAFS data of  $a\text{-Si}_{1-x}\text{C}_x\text{H}$  deposited with a methane partial pressure of 72% and different silane flow (F).

**Figure 5.** First-shell filtered EXAFS spectra (—) and calculated curves (oooo) obtained with parameters from Table III. (a) MVC1 and (b) MVC5.

**Figure 6.** XANES spectrum of  $a\text{-Si}_{1-x}\text{C}_x\text{H}$  deposited under "starving" regime at different methane partial pressure (P).

**Figure 7.** XANES spectrum of  $a\text{-Si}_{1-x}\text{C}_x\text{H}$  deposited with a methane partial pressure of 72% and different silane flow (F).

TABLE I

a-Si<sub>1-x</sub>C<sub>x</sub>H samples produced with SiH<sub>4</sub> flow (F) and partial pressure of CH<sub>4</sub> (P), with optical gap E<sub>0</sub> and carbon concentration x.

SAMPLE	F(SiH <sub>4</sub> ) sccm	P(CH <sub>4</sub> ) %	E <sub>0</sub> (eV)	x
MVC2	10	98	3.7	0.66
MVC1	10	92	3.4	0.70
MVC4	10	80	3.0	0.55
MVC3	10	72	3.0	0.56
MVC5	10	50	2.0	0.46
MVC6	50	72	2.8	0.54 <sup>a</sup>
MVC7	100	72	2.6	0.51 <sup>a</sup>
MVC8	150	72	2.5	0.50 <sup>a</sup>

<sup>a</sup> Estimated from E<sub>0</sub> values.

TABLE II

a-Si<sub>1-x</sub>C<sub>x</sub>H samples and relative microvoid volume fraction ( $\eta$ ).

Sample	MVC1	MVC3	MVC4	MVC5	MVC6	MVC7
$\eta \pm 0.02$ (a.u.)	0.40	0.68	0.62	0.36	1.00	0.99

TABLE III

One Shell fit results for MVC1 and MVC5 samples.

Sample	$N_{\text{Si-C}}$ ( $\pm 0.5$ )	$R_{\text{Si-C}}$ ( $\pm 0.02$ )	$\Delta\sigma_{\text{Si-C}}$ ( $\pm 0.02$ )	$N_{\text{Si-Si}}$ ( $\pm 0.5$ )	$R_{\text{Si-Si}}$ ( $\pm 0.02$ )	$\Delta\sigma_{\text{Si-Si}}$ ( $\pm 0.002$ )
MVC1 $x=0.70$	4.5	1.91	0.04	-----	-----	-----
MVC55 $x=0.46$	-----	-----	-----	3.7	2.36	0.0002

----- : not fitted



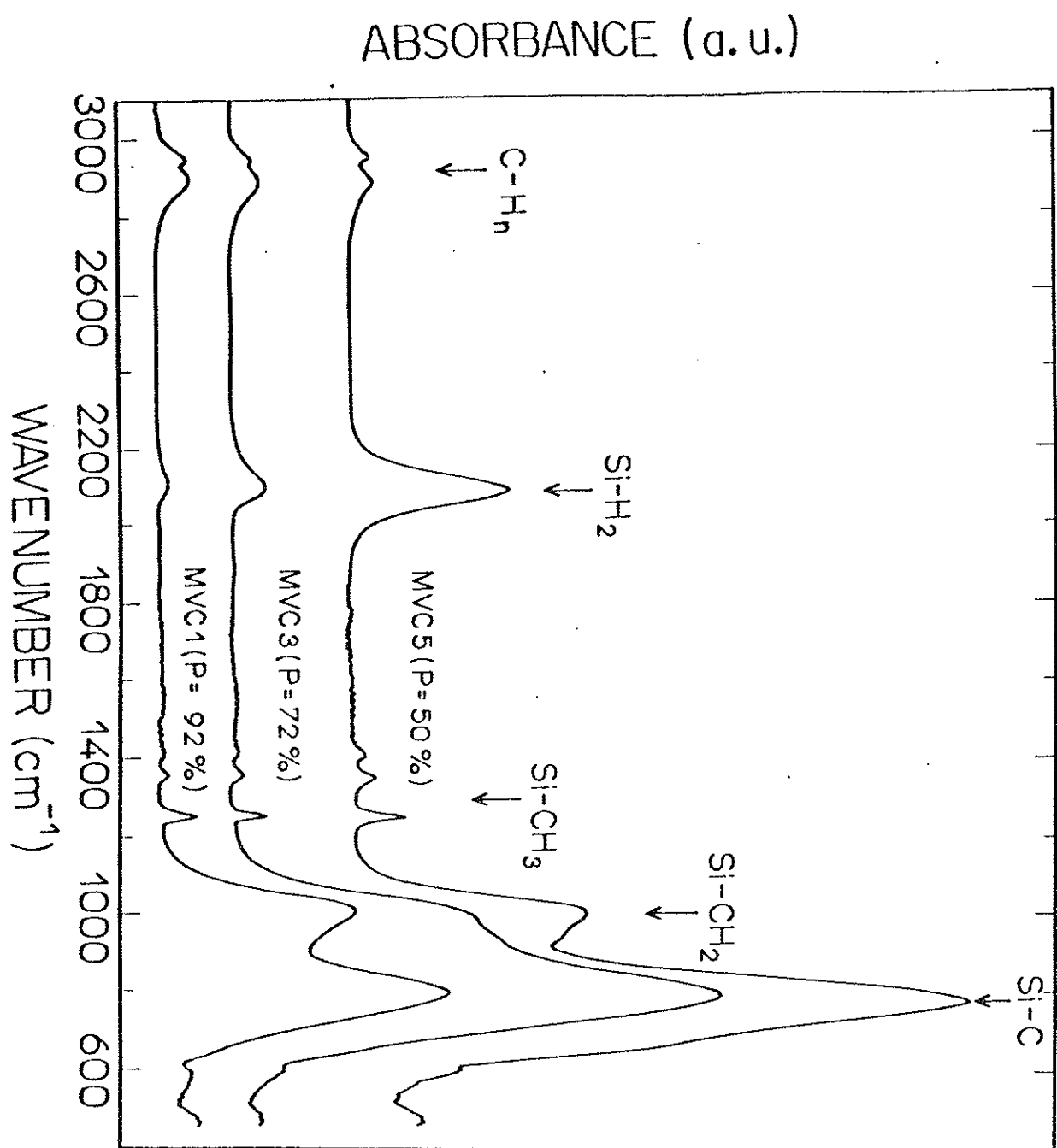


Figure 1

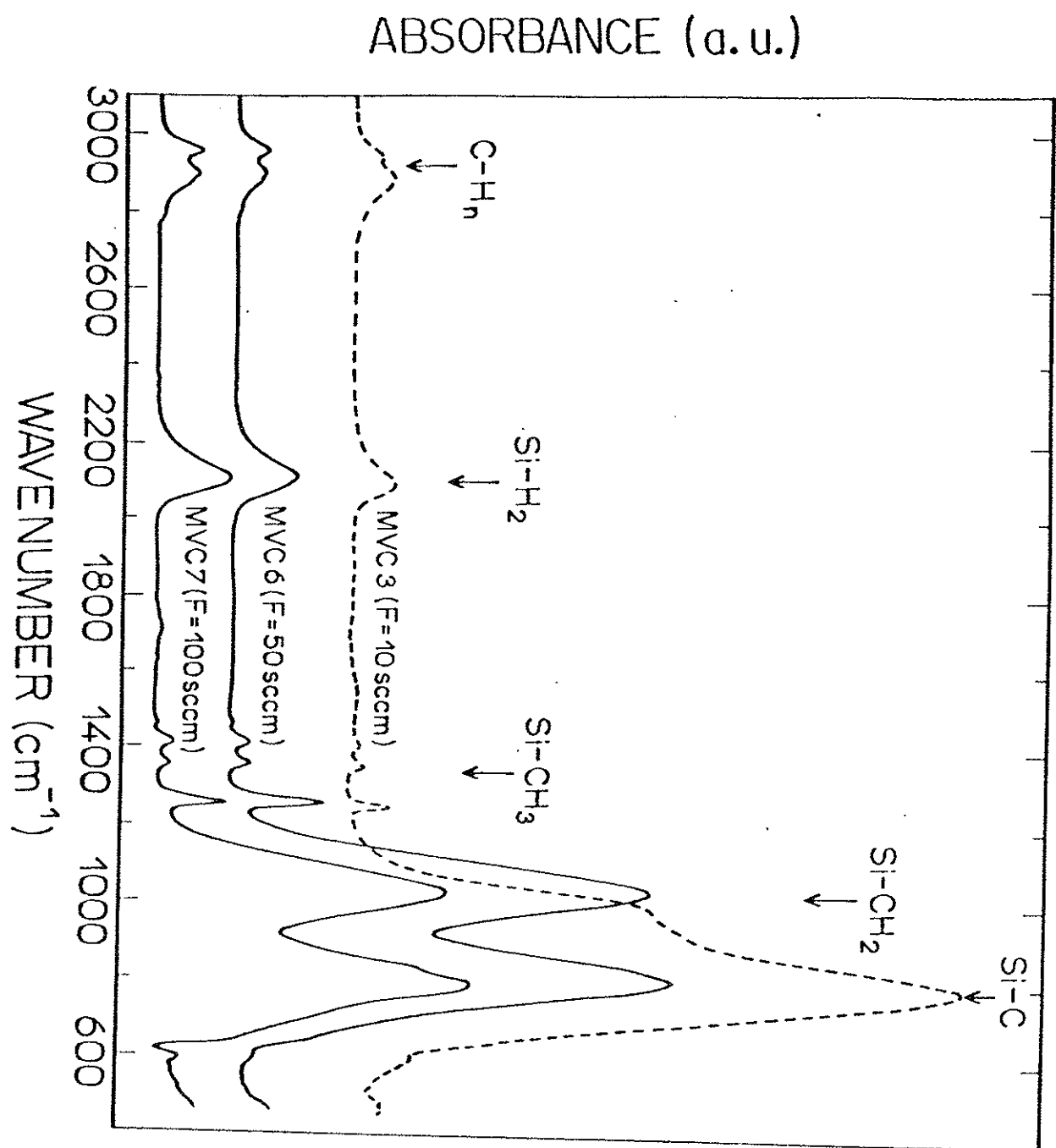


Figure 2

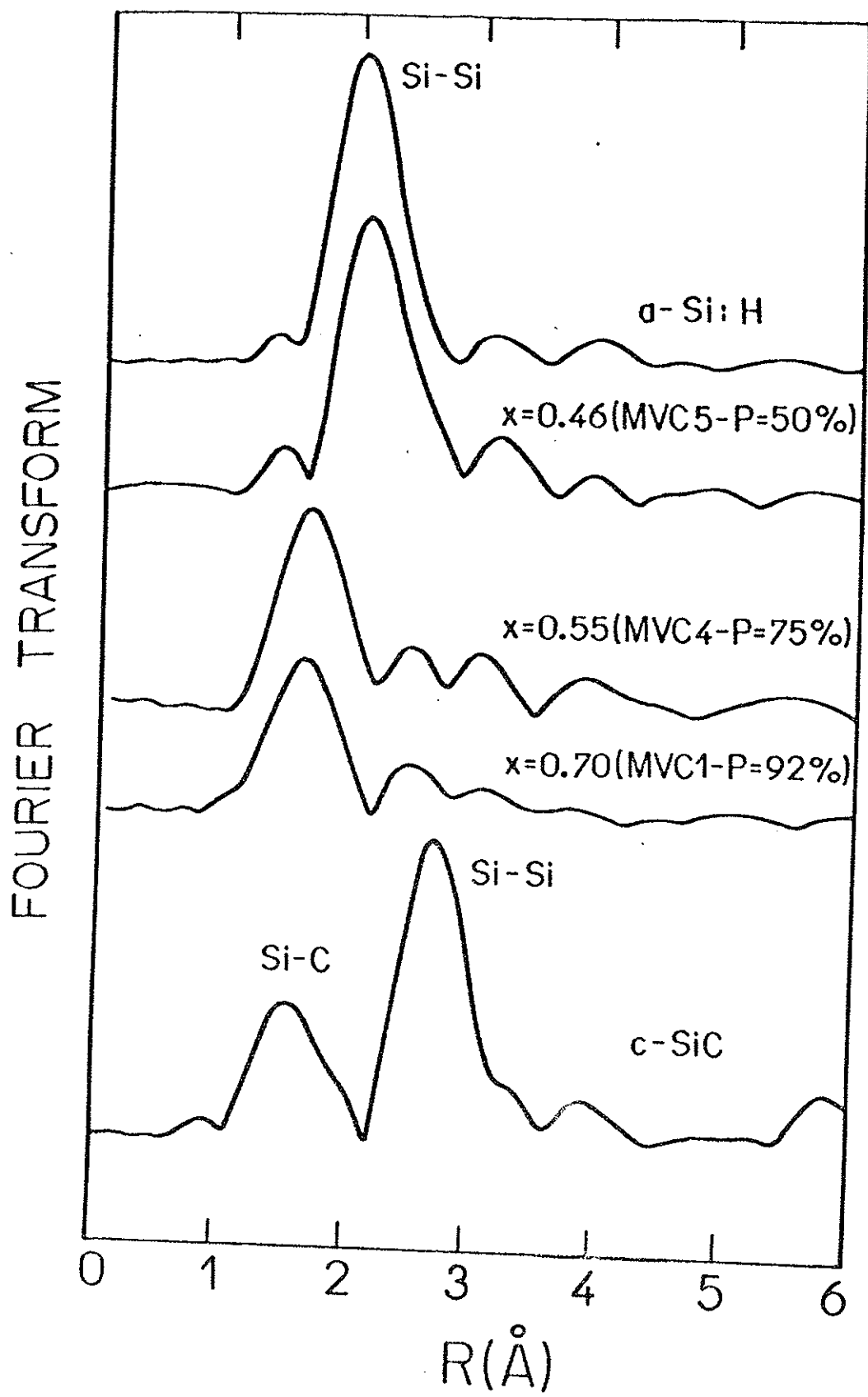


Figure 3

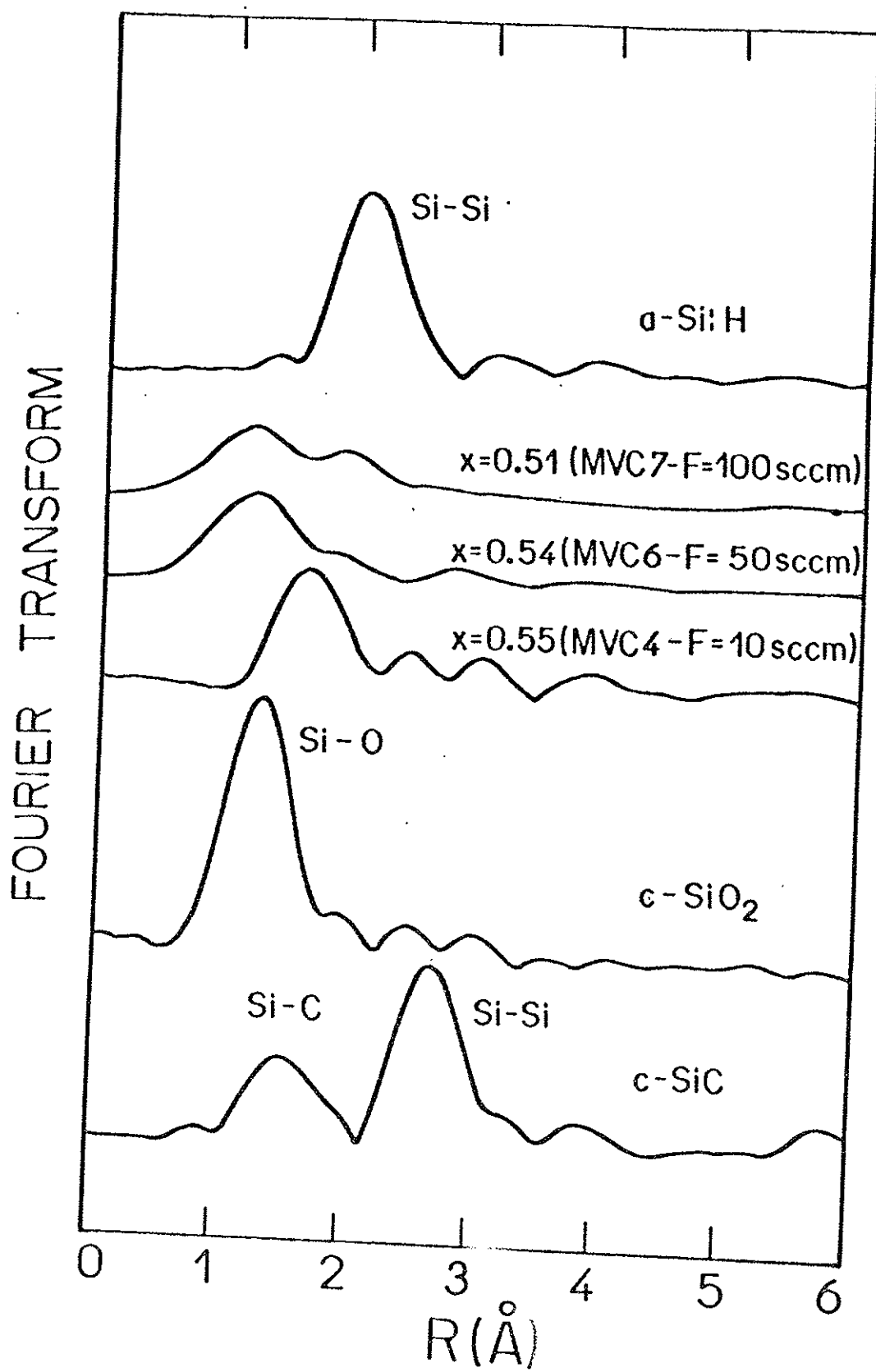


Figure 4

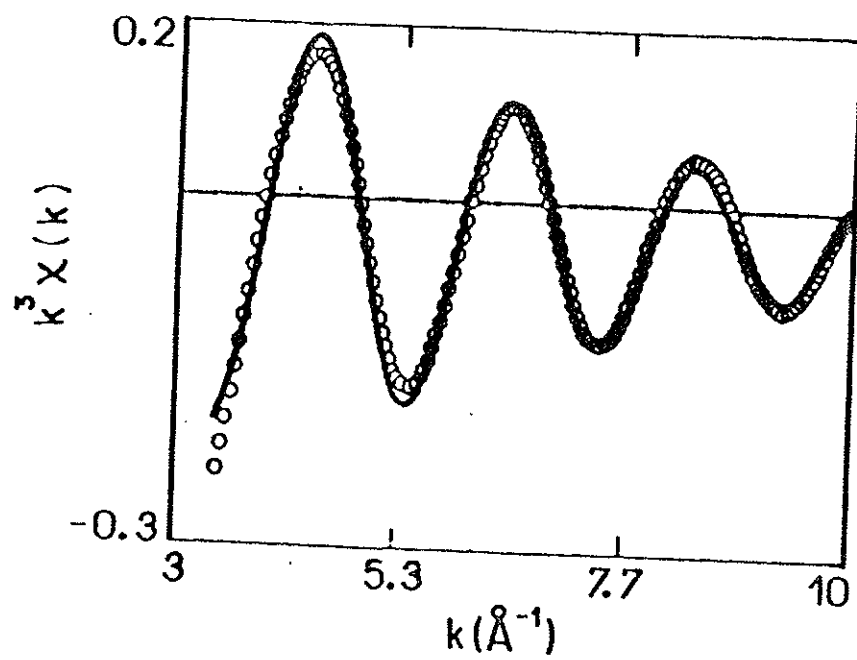


Figure 5(a)

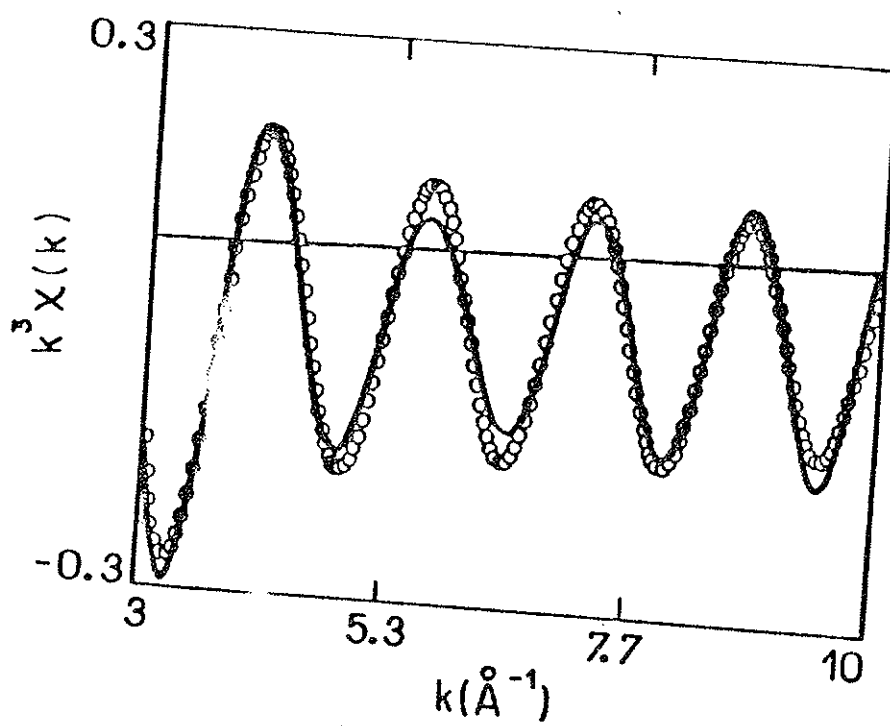


Figure 5(b)

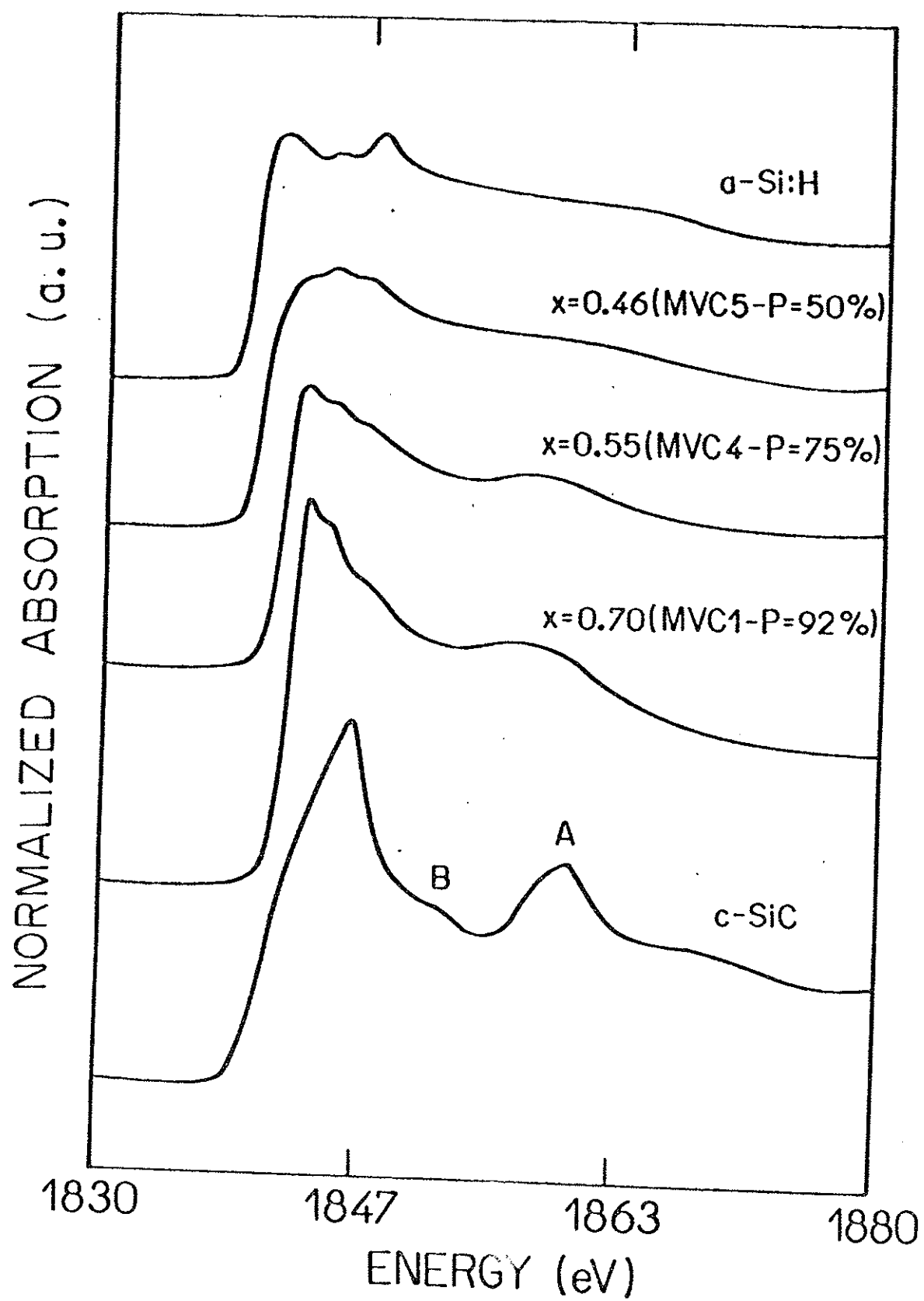


Figure 6

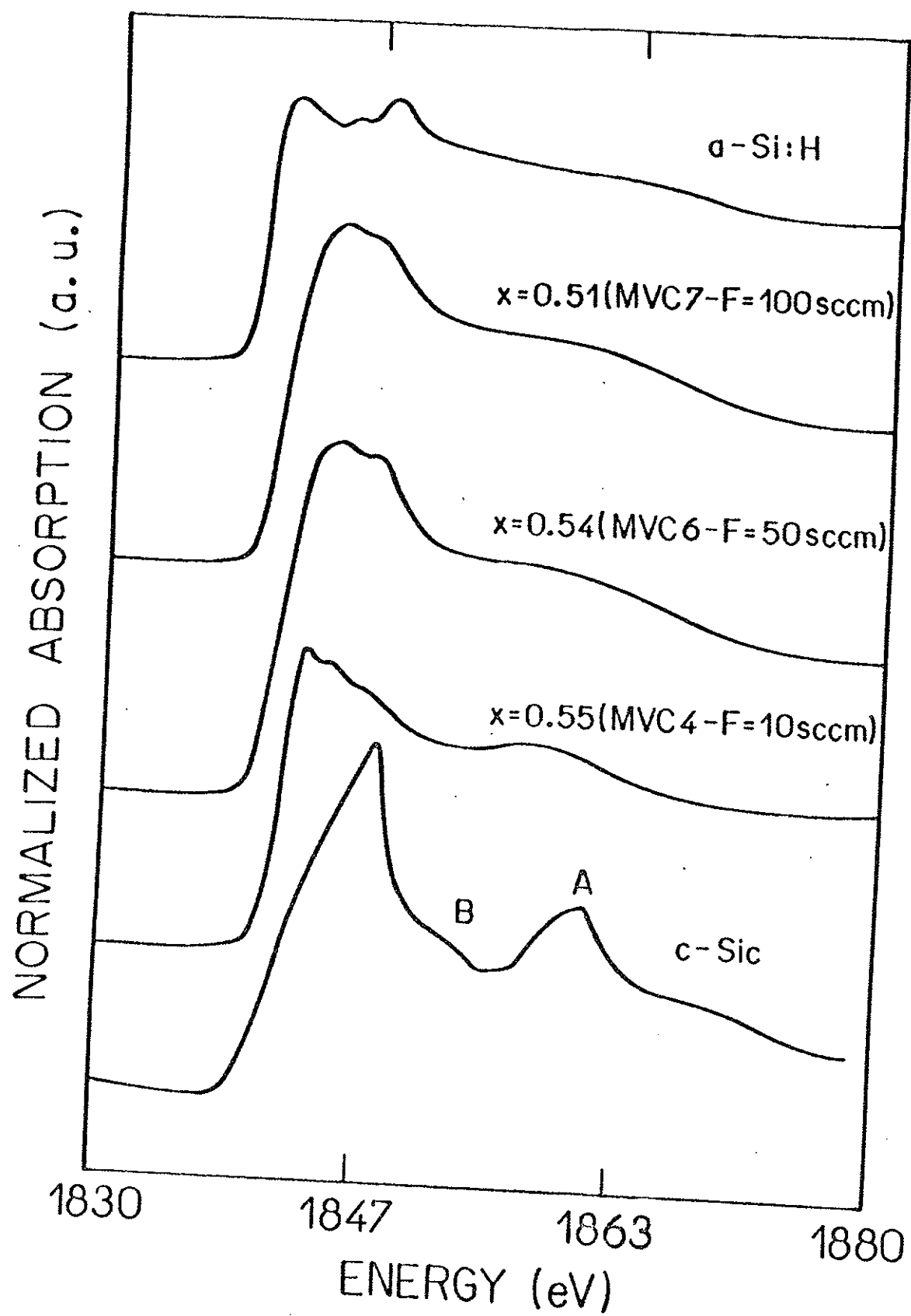


Figure 7

---

## A2. - Trabalhos sobre Materiais Eletrocrômicos

---



W. Estrada

Facultad de Ciencias, UNI, Apartado 1301, Lima, Peru

M. C. A. Fantini

IF/USP, CP 20516, CEP 01498-970 São Paulo, Brazil

S. C. de Castro, C. N. Polo da Fonseca, and A. Gorenstein<sup>a)</sup>

DFA/IFGW/UNICAMP, CP 6165, CEP 13081 Campinas, SP, Brazil

(Received 10 December 1992; accepted for publication 6 July 1993)

Cobalt oxide thin films (thickness 2000 Å) with different stoichiometries were deposited by reactive rf sputtering. The variation of the oxygen partial pressure lead to films with compositions varying from metallic cobalt to  $\text{Co}_3\text{O}_4$ , as determined by x-ray diffraction and x-ray photoelectron spectroscopy. The electrochromic properties of the films were investigated in aqueous electrolytes (0.1 M KOH). The initial electrochemical behavior of the films is strongly dependent on the film deposition conditions, but after cycling the electrochemical/electrochromic characteristics of the different deposits were quite similar. Transmittance changes and electrochromic efficiency are discussed.

## I. INTRODUCTION

Electrochromic devices for light modulation, as rear-view automobile mirrors<sup>1</sup> or "smart windows,"<sup>2,3</sup> have undergone great development in the last years. These multilayered electrochemical devices normally have a thin film of  $\text{WO}_3$  as the optical active element. Since  $\text{WO}_3$  is a cathodically coloring material,<sup>4</sup> two different routes have been followed in order to develop suitable counter electrodes. The first one proposes counter electrodes which are electrochemically compatible with the system, having high charge capacity, but are optically passive.<sup>5,6</sup> The other route proposes a "rocking chair" type device. In this last case, the counter electrode, besides being electrochemically compatible, is also optically compatible (an anodically coloring material). The great majority of "rocking chair" devices uses nickel oxide counter electrodes.<sup>7-9</sup> Other 3d transition metal oxides, as  $\text{MnO}_x$  and  $\text{TiO}_x$ , were proposed as suitable counter electrodes, but are studied less frequently.<sup>10,11</sup>

The electrochromic effect in cobalt oxide films has been little explored.<sup>11,12</sup> Recently, we pointed out this effect in electrochemically deposited  $\text{CoO}_x$  hydrate films,<sup>13</sup> showing that this compound is an anodically coloring material with suitable electrochromic behavior. In the present work, we studied cobalt oxide thin films deposited by rf reactive sputtering. The electrochemical/electrochromic behavior of films with different compositions was followed in basic aqueous electrolytes. The structure and composition of the as-grown and the aged material were analyzed by x-ray diffraction (XRD) and x-ray photoelectron spectroscopy (XPS). The electrochromic efficiency of the films was also calculated.

## II. EXPERIMENT

Thin films of cobalt oxide were prepared by rf magnetron sputtering from a high purity (99.9%) Co target onto 7059 Corning glass substrates, with or without a  $\text{SnO}_2$  coating (sheet resistivity  $\sim 16 \Omega/\square$ ). After evacuation to a pressure  $p < 8 \times 10^{-6}$  Torr, pure oxygen and argon gases were introduced inside the reaction chamber, maintained at a total pressure  $p(\text{O}_2 + \text{Ar}) = 8.5 \times 10^{-3}$  Torr. The discharge power was set at values of 100 or 150 W. Presputtering was performed for 5 min prior to deposition onto unheated substrates placed 15 cm above the target. The thickness of the films was determined by a mechanical stylus instrument ( $\alpha$ -Step 200, Tencor Instruments). The coatings were deposited under different oxygen partial pressures  $p(\text{O}_2)$ , in order to analyze the influence of the oxygen flux and the deposition rate on the structural characteristics of the films.

The XRD experiments were performed in a conventional diffractometer, operating at 0.8 kW power, using Fe-filtered Co  $K\alpha$  radiation. The  $2\theta$  angular range was between  $10^\circ$  and  $80^\circ$ , with a step scanning of  $0.05^\circ$  and counting time of 10 s. The XPS experiments were performed with an equipment ESCA-36 (McPherson Co.) using Al  $K\alpha$ . The binding energies were referenced to the C 1s line of surface carbon taken as 284.6 eV. The pressure in the chamber was kept around  $8 \times 10^{-7}$  Torr.

The electrochemical experiments were carried out in a three electrode cell. A platinum counter electrode and a saturated calomel reference electrode (SCE) were used. The working electrode was the  $\text{CoO}_x/\text{SnO}_2/\text{glass}$ . The measurements were performed with a PAR 173 potentiostat connected with a PAR 175 universal programmer. The data were registered in a X-Y<sub>1</sub>-Y<sub>2</sub> recorder.

The electrochromic effects were studied during potentiodynamic cycling in a 0.1 M KOH aqueous electrolyte, using triply distilled water and P.A. reagents. The optical transmittance measurements were carried out *in situ* using

<sup>a)</sup> Author to whom correspondence should be addressed.

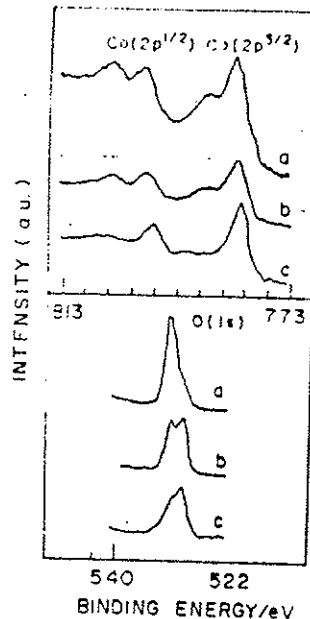


FIG. 3. XPS spectrum of as-grown samples: (a) sample grown with  $f=0\%$ ; (b) sample grown with  $f=2.8\%$ ; (c) sample grown with  $f=10.5\%$ .

longing to the three distinct regions, were also analyzed giving similar diffractograms.

Figure 3 shows the XPS spectra of  $\text{Co}(2p)$  and  $\text{O}(1s)$  lines. Figure 3(a) (upper and lower part) corresponds to a sample grown at region I ( $f=0$ , Fig. 1) and presented the  $\text{Co}(2p^{3/2})$  line at 781.3 eV, with a shake-up satellite at 6 eV, situated at higher energies [Fig. 3(a), upper part]. The spin-orbit splitting was 15.7 eV. The  $\text{O}(1s)$  line is duplicated, with the most intense peak at 529.3 eV and the less intense at a higher energy (531.6 eV) [Fig. 3(a), lower part]. Figure 3(b) (upper and lower part) corresponds to a sample grown at region II (Fig. 1). The  $\text{Co}(2p^{3/2})$  line [Fig. 3(b), upper part] is at 780.5 eV, and also shows a shake-up satellite at 6 eV. The spin-orbit splitting was 15.9 eV. The  $\text{O}(1s)$  peak [Fig. 3(b), lower part] is also double, with equal peak intensities. Figure 3(c) corresponds to a sample grown at region III (Fig. 1), and presented the  $\text{Co}(2p^{3/2})$  line at 779.7 eV, without satellites, with spin-orbit splitting of 15 eV [Fig. 3(c), upper part]. The most intense line of  $\text{O}(1s)$  is at 531.2 eV and the less intense is at 529.2 eV [Fig. 3(c), lower part]. The presence of the shake up satellite at energies of the order of 6 eV higher than the  $\text{Co}(2p^{3/2})$  and  $\text{Co}(2p^{1/2})$  lines and spin-orbit splitting of 16 eV are characteristic of  $\text{Co(II)}$ . A spin-orbit splitting of 15 eV is characteristic of  $\text{Co(III)}$  compounds.<sup>14,15</sup> Then, the spectra shown in Figs. 3(a) and 3(b) are identified as  $\text{Co(II)}$  compounds and the one shown in Fig. 3(c) as a  $\text{Co(III)}$  compound. The double line in the  $\text{O}(1s)$  spectra is also attributed to  $\text{Co-O}$  bonds (lower energy peak) and  $\text{O-H}$  bonds (higher energy peak).<sup>14,15</sup> The energy of the  $\text{Co}(2p^{3/2})$  line in Fig. 3(a) is characteristic of  $\text{Co(OH)}_2$ , showing up the formation of a compound at the surface of metallic cobalt in contact

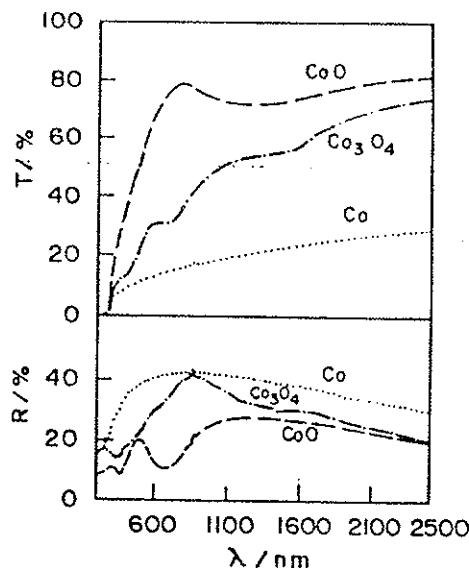


FIG. 4. Visible/near IR spectra of as-grown samples. Substrate: glass.  $\text{CoO}$  sample grown with  $f=2.9\%$ ;  $\text{Co}_3\text{O}_4$  sample grown with  $f=10.9\%$ ;  $\text{Co}$  sample grown with  $f=0\%$ .

with the atmosphere. The spectrum shown in Fig. 3(b) corresponds to a  $\text{CoO}$  compound.

The as-grown  $\text{CoO}_x$  samples were subjected to optical measurements. Spectral normal transmittance  $T$  and near normal reflectance  $R$  were measured in the  $0.35 < \lambda < 2.5$   $\mu\text{m}$  wavelength interval using a double beam spectrophotometer, as described in Sec. II. Figure 4 show these results for  $\text{CoO}_x$  deposited on single glass, at the three characteristic  $f$  regions (Fig. 1). Taking into account the results described above, the spectra are assigned in the figure as  $\text{Co}$  (sample from region I),  $\text{CoO}$  (sample from region II), and  $\text{Co}_3\text{O}_4$  (sample from region III). Coating thicknesses were 0.05, 0.09, and 0.1  $\mu\text{m}$ , respectively. The  $\text{CoO}$  film is transparent; the  $\text{Co}_3\text{O}_4$  film is rather absorbing, with a dark brown appearance and the  $\text{Co}$  film is highly absorbing with a dark grey metallic appearance (Fig. 4, upper part). Reflectance spectra at the near infrared region shows that the metallic coating is 10% more reflective than the  $\text{CoO}$  and  $\text{Co}_3\text{O}_4$  films (Fig. 4, lower part). Optical properties for coatings of the same thickness grown at the three distinct  $f$  regions (Fig. 1) are found to be similar to those shown in Fig. 4.

## B. Electrochemical characterization

Typical samples, deposited under conditions specified in the above selected  $f$  regions, were subjected to an electrochemical treatment in 0.1 M  $\text{KOH}$ . The monochromatic transmittance was followed *in situ*, as pointed out in the experimental section. Before cycling, the open circuit potential was measured. This results is shown in Fig. 5. The metallic sample has the most cathodic potential. As  $f$  increases (oxygen content in the samples increases) the potential goes to more anodic values, in qualitative agreement with the literature.<sup>17</sup> For all samples, the triangular potential sweep initiated at the respective open circuit potential.

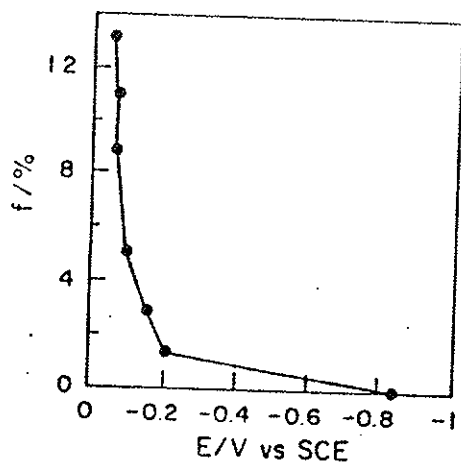


FIG. 5. Open circuit potential as a function of the oxygen molar fraction,  $f(\%) = p(\text{O}_2)/p(\text{Ar} + \text{O}_2) \times 100$ . Electrolyte: 0.1 M KOH.

Figure 6 (lower part) shows the first voltammetric cycles, for three samples (metallic Co, CoO, and Co<sub>3</sub>O<sub>4</sub>). The corresponding monochromatic transmittance changes are shown in the upper part of the figure.

The open circuit potential for the Co sample is  $E = -0.84$  V; a well defined anodic peak is first seen in the anodic scan, corresponding to the oxidation of metallic Co to a Co(II) oxide (or hydroxide). This oxidation process

causes an increase in the transmittance (Fig. 6, upper part), showing that this oxidation is a bulk and not a superficial process. Two other anodic processes are subsequently seen before oxygen evolution, corresponding to the oxidation of the film to higher valence states of Co, Co(III). The transition Co(II)  $\rightarrow$  Co(III) is followed by a decrease in transmittance (Fig. 6, upper part). This behavior is in accordance with the fact that Co<sub>3</sub>O<sub>4</sub> films are less transparent than CoO (Fig. 4, upper part). At the anodic limit of the voltammetry (onset of the oxygen evolution reaction) the transmittance attains its minimum value, and stabilizes. In the cathodic scan, at least three reduction peaks are seen; the transmittance increases in the whole cathodic scan range.

Considering now the CoO sample (open circuit potential  $E = -0.15$  V), a broad anodic peak, corresponding to the oxidation of Co(II) to Co(III) is seen before oxygen evolution (Fig. 6, lower part). Accordingly, the associated transmittance decreases. In the cathodic scan three cathodic peaks are observed, as well as an increase in the transmittance. The initial transmittance is  $\sim 75\%$ , and at the end of the cathodic cycle the maximum transmittance value decreases a little ( $T = 68\%$ ).

The Co<sub>3</sub>O<sub>4</sub> sample (open circuit potential  $E = -0.08$  V) does not show any anodic peak in the first anodic scan, but presents a very small associated transmittance change (Fig. 6, upper part). Again, the cathodic cycle there are three cathodic peaks associated with an increase in the transmittance values.

On continuously cycling, the  $J/E$  and  $T/E$  profiles suffered significant changes. The stabilized profiles, attained after 40 cycles, are shown in Fig. 7. For all samples, two anodic and two cathodic processes show up. The transmittance also begins to decrease at the potential region of the first anodic process ( $\sim -0.2$  V) and stabilizes in the potential region of the oxygen evolution reaction. The transmittance values in the bleached (reduced) state are always less than the values of the first cycle (see Fig. 6). The transmittance span for the stabilized samples is around 20%.

### C. Characterization of stabilized films

The same samples characterized by XRD and XPS (Sec. III A) were analyzed after potentiodynamic cycling (40 cycles). In these experiments, the potential excursion was interrupted at  $E = 0$  V (Fig. 7) in the anodic cycle. Samples were carefully washed with triple distilled water, and dried in air.

The XRD data for all samples showed just one diffraction peak, at  $2\theta = 23^\circ$ . A typical result is depicted in Fig. 8. This peak can be assigned to CoOOH, indicating that electrochemical cycling has the effect of changing the as-grown, polycrystalline nonhydrated films in a hydrated compound, with a less ordered structure when compared with the virgin films.

The XPS spectra for all the stabilized samples were very similar. Figure 9 shows a typical result. The Co 2p line showed no shake-up satellites and the spin-orbit separation was characteristic of Co(III). The Co 2p<sup>3/2</sup> binding

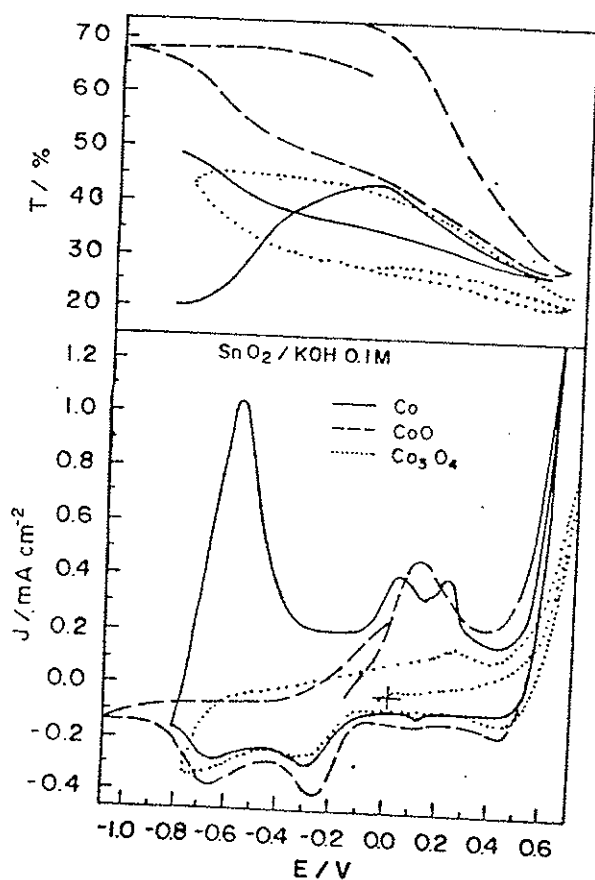


FIG. 6. Potentiodynamic  $J/E$  profiles (lower part) and associated transmittance changes ( $\lambda = 632.8$  nm) (upper part), first cycle. Electrolyte: 0.1 M KOH, scan rate: 20 mV/s.

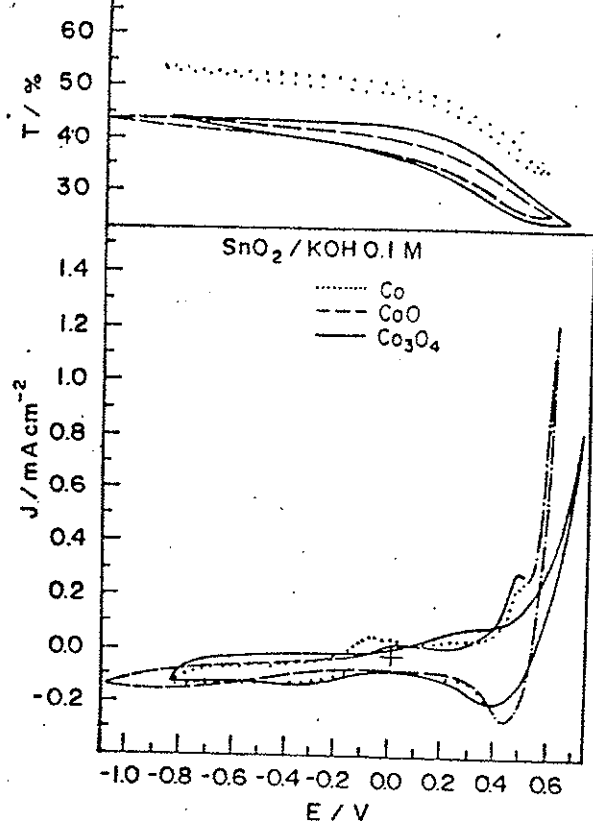


FIG. 7. Potentiodynamic  $J/E$  profiles (lower part) and associated transmittance changes ( $\lambda = 632.8 \text{ nm}$ ) (upper part), stabilized cycle. Electrolyte: 0.1 M KOH, scan rate: 20 mV/s.

Energies were around  $780.1 \pm 0.3 \text{ eV}$ , a value compatible with the one presented in Ref. 14, associated with  $\text{CoOOH}$ . The O 1s line continued to be double but the high energy component was now the dominant one, in accordance with the results obtained from the XRD experiments described above.

In order to make evident the optically active potential range for the stabilized films, the optical contrast and elec-

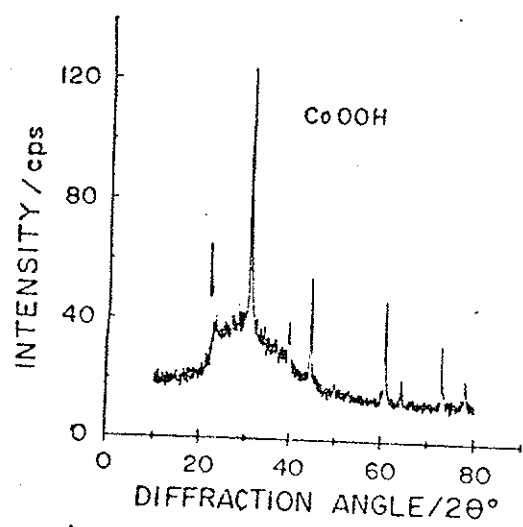


FIG. 8. XRD diagram of a stabilized sample.

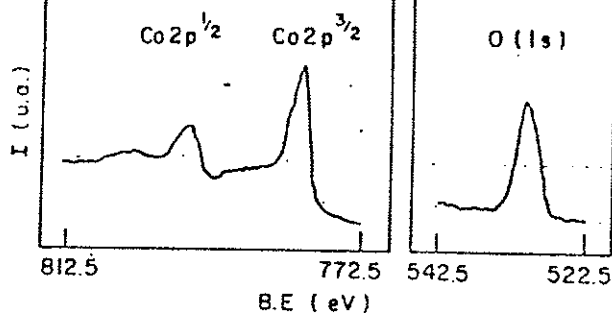


FIG. 9. XPS spectrum of a stabilized sample.

trochromic efficiencies in near-equilibrium conditions were analyzed by means of *in situ* spectrophotometric measurements. The electrochemical cell was placed in the optical path of one of the spectrophotometer beams and consecutive potential steps of 0.05 V were applied to a stabilized  $\text{Co}_3\text{O}_4$  sample. After each potential step, the electrical charge involved was recorded as well as the transmittance spectra. The optical contrast was calculated by subtracting the transmittance value at each wavelength for a given potential from the spectra obtained at the consecutive applied potential. Figure 10 shows the optical contrast, for each wavelength and potential, in a three dimensional plot. The largest optical contrast was obtained for the potential steps  $E = +0.05 \text{ V} \rightarrow E = +0.1 \text{ V}$  ( $\Delta T = 10\%$  at  $\lambda = 800 \text{ nm}$ ) and  $E = +0.25 \text{ V} \rightarrow E = +0.3 \text{ V}$  ( $\Delta T = 12\%$  at  $\lambda = 800 \text{ nm}$ ). The optical contrast is less than 6% in the cathodic potential range. In the visible range, the maximum contrast was observed around  $\lambda = 500 \text{ nm}$ . The total optical contrast at this wavelength was 30%.

The electrochromic efficiency  $\eta$  is defined as the ratio between the optical density (OD) variation and the associated charge density ( $Q$ ).<sup>13</sup>

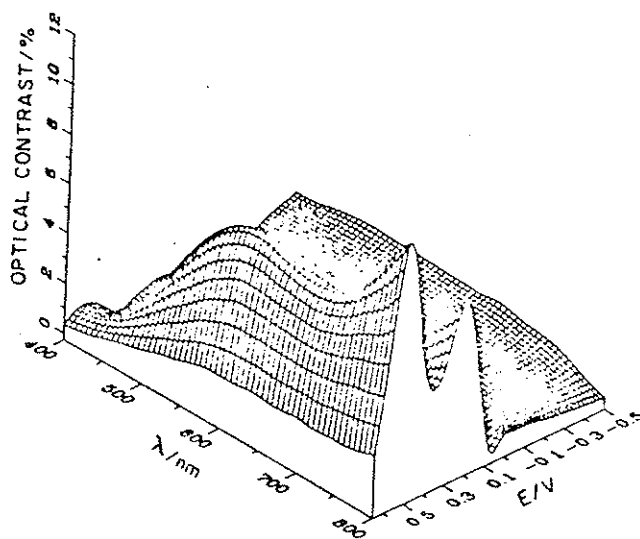


FIG. 10. Partial optical contrast, as a function of applied potential and wavelength. The sample is a stabilized electrode with as grown stoichiometry of  $\text{Co}_3\text{O}_4$ . Electrolyte: 0.1 M KOH.

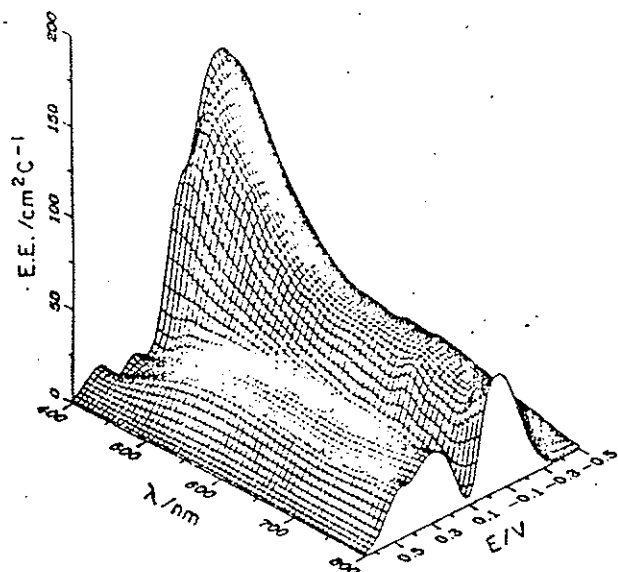


FIG. 11. Electrochromic efficiency as a function of applied potential and wavelength. Same sample as in Fig. 10. Electrolyte: 0.1 M KOH.

$$\eta = \frac{\Delta(\text{OD})}{Q} \quad (1)$$

The potential and wavelength dependence of this parameter is shown in Fig. 11 ( $\text{Co}_3\text{O}_4$  sample). The highest electrochromic efficiency ( $200 \text{ cm}^2/\text{C}$ ) is observed at cathodic potential values ( $E = -0.3 \text{ V}/-0.5 \text{ V}$ ) for small wavelengths. Two distinct potential regions with large  $\eta$  appear: the first one for the potential steps  $E = -0.2 \text{ V} \rightarrow E = -0.1 \text{ V}$  and the second for the potential steps  $E = +0.1 \text{ V} \rightarrow E = +0.2 \text{ V}$ . After 200 cycles, no changes in the potentiodynamic and transmittance profiles were observed for the stabilized samples.

#### IV. DISCUSSION

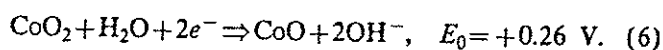
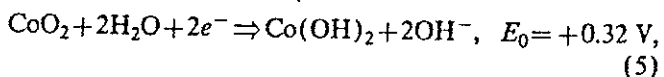
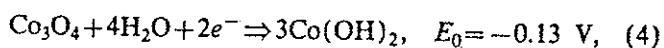
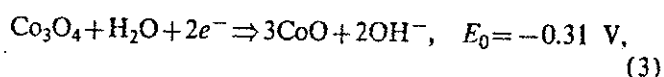
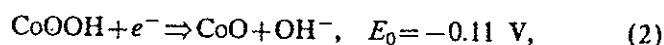
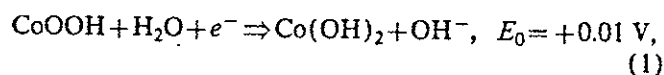
It is well known that the sputtering rate from a metal target decreases when  $p(\text{O}_2)$  increases in a gas mixture of  $\text{Ar} + \text{O}_2$ .<sup>16</sup> Figure 1 shows that  $r$  decreases if  $f$  goes from 0% to 1.3%, or if  $f$  goes from 4% to 13%. This behavior can be ascribed mainly to two effects: target oxidation and low sputter yield for  $\text{O}_2$  compared to  $\text{Ar}$ .<sup>16</sup> However, in the interval  $2\% < f < 4\%$ , there is a slight increase in  $r$ . At the present stage we do not have an explanation of this effect, but it could be due to a low resputtering process for  $\text{CoO}$ , which is formed under these conditions, as one can deduce from XRD, XPS, and optical data. In fact, XRD and XPS data indicated that for  $f \sim 3\%$  the structure of the film essentially corresponds to  $\text{CoO}$ .

The XRD, XPS, and optical measurements indicate that for high  $f$  values ( $f > 5\%$ ) a  $\text{Co}_3\text{O}_4$  structure is formed. Obviously, for  $f = 0\%$  the coating is metallic Co. As  $f$  increases,  $\text{CoO}$  probably starts to incorporate into the film. This is consistent with the optical properties shown in Fig. 4. In fact, for  $f > 0\%$  the films are less absorbing and reflecting than for  $f = 0\%$ . XRD and XPS also show the predominance of metallic character of films for  $f$  be-

tween 0 and 1.3%. In conclusion, the amount of oxygen in the gas mixture  $\text{Ar} + \text{O}_2$  will determine the structure of sputtered cobalt oxide based coatings. We can distinguish three different regions in Fig. 1:

- (i) region I,  $0 < f < 2\%$ : predominance of Co;
- (ii) region II,  $2 < f < 4\%$ , predominance of  $\text{CoO}$ ;
- (iii) region III,  $f > 5\%$ : predominance of  $\text{Co}_3\text{O}_4$ .

rf sputtered cobalt oxide films can be obtained in distinct stoichiometries by varying the sputtering parameters. However, when the samples are subjected to electrochemical cycling, they undergo successive electrochemical oxidation/reduction processes that introduce drastic changes in the compounds, as can be seen from the evolution of the potentiodynamic profiles (Figs. 6 and 7) and from the XRD and XPS results (Secs. III A and III C). A hydration process occurs in the films, changing the initial nonhydrated, well characterized oxides in compounds presenting O-H groups. It is rather difficult to assign a clear electrochemical reaction to each oxidation/reduction couple, since thermodynamic calculations indicate at least fourteen possible reactions in the potential range investigated in this work.<sup>17,18</sup> Among these electrochemical reactions, the following have a  $\text{Co(II)}$  compound as the cathodic reaction product:



In the above reactions,  $E_0$  is the standard equilibrium potential, calculated for a 0.1 M electrolyte and considering the saturated calomel electrode as the reference electrode.

The main electrochemical processes for the stabilized samples are in the 0 V/0.7 V potential range (Fig. 7). In the cathodic potential range, an almost constant current shows up, beginning at  $E = -0.05 \text{ V}$  for the original Co and  $\text{Co}_3\text{O}_4$  sample, and at around  $E = -0.3 \text{ V}$  for the original  $\text{CoO}$  sample. These processes could correspond to reactions (2) or (4), or to reaction (3), respectively. However, the total cathodic charge in the cathodic potential range is much lower than the total cathodic charge in the anodic potential range (Fig. 7). This fact shows that the electrodes at the end of the cathodic scan hardly attain a full  $\text{Co(II)}$  oxide/hydroxide stoichiometry, being probably a mixture of  $\text{Co(II)}/\text{Co(III)}$  compounds. Also it has to be noticed that the stabilized films have a transmittance in the reduced (bleached) state that is always less than the values attained in the first cycle (Figs. 6 and 7). As the as-grown  $\text{Co(II)}$  films presented the higher transmittance values (Fig. 4) the decrease in the bleached state transmittance

for stabilized samples also indicate that the film is never completely reduced to a Co(II) compound.

On the other hand, the optical contrast results (Fig. 10) indicate that the optically active electrochemical processes are mainly in the anodic potential range and should correspond, accordingly, to thermodynamic data, to transitions between different compounds of Co(III) and Co(IV), or mixtures (e.g., transitions like  $\text{Co}_3\text{O}_4 \rightarrow \text{CoOOH}$  or  $\text{Co}_3\text{O}_4 \rightarrow \text{CoO}_2$ ). However, the highest values of the electrochromic efficiency parameter (Fig. 11) are in the cathodic range for all wavelengths. The reason for this apparent discrepancy is on the definition of this parameter [Eq. (1)]. Since the optical density variation is low, as well as the electrical charge in the cathodic potential region, the corresponding  $\eta$  value is high. Then, for practical purposes, we have to consider not only the highest values of electrochromic efficiency but also the optical contrast. In this case, the optically active region is the anodic region, since the electrochromic reactions in this potential range have the highest optical contrast and the electrochromic efficiencies are comparable to the values obtained for other transition metal oxide electrochromic materials.

## V. CONCLUSIONS

In this work, cobalt oxide films were grown by rf sputtering. The oxygen content of the films was shown to depend strongly on the deposition parameters. Electrochemical cycling in aqueous media changed the originally different films into hydrated compounds, with similar stoichiometries. After around forty cycles, the films were stable and presented electrochromic behavior with efficiencies comparable with other electrochromic materials. Work is in progress to investigate the electrochromic properties of these films in nonaqueous media.

## ACKNOWLEDGMENTS

One of us (W.E.) acknowledges the International Seminar (Uppsala, Sweden) for financial support. Fapesp, CNPq, and Finep (Brazil) are also acknowledged.

- <sup>1</sup>T. E. Haas and R. B. Goldner, in *Large Area Chromogenics: Materials and Devices for Transmittance Control*, edited by C. M. Lampert and C. G. Granqvist (SPIE Optical Engineering, Bellingham, WA, 1990), 170.
- <sup>2</sup>C. M. Lampert, *Sol. Energy Mater.* **11**, 1 (1984).
- <sup>3</sup>J. S. E. M. Svensson and C. G. Granqvist, *Appl. Phys. Lett.* **45**, 828 (1984).
- <sup>4</sup>S. I. Cordoba de Torresi, A. Gorenstein, R. M. Torresi, and M. V. Vazquez, *J. Electroanal. Chem.* **318**, 131 (1991).
- <sup>5</sup>B. Valla, J. C. Tonazzi, M. A. Macedo, L. H. Dall'Antonia, M. A. Aegerter, M. A. Gomes, and L. O. Bulhões, *Proceedings of the Optical Materials Technology for Energy Efficiency and Solar Energy Conversion X*, edited by C. M. Lampert and C. G. Granqvist (SPIE, Bellingham, WA, 1991), Vol. 1536, p. 48.
- <sup>6</sup>P. Baudry, M. A. Aegerter, D. Deroo, and B. Valla, *J. Electrochem. Soc.* **138**, 460 (1991).
- <sup>7</sup>W. Estrada, A. Andersson, and C. G. Granqvist, *J. Appl. Phys.* **64**, 3678 (1988).
- <sup>8</sup>S. Passerini, B. Scrosati, A. Gorenstein, A. M. Andersson, and C. G. Granqvist, *J. Electrochem. Soc.* **136**, 3394 (1989).
- <sup>9</sup>J. Scarmínio, A. Urbano, B. J. Gardes, and A. Gorenstein, *J. Mater. Sci. Res. Lett.* **11**, 562 (1992).
- <sup>10</sup>S. I. Cordoba de Torresi and A. Gorenstein, *Electrochimica Acta* **37**, 2015 (1992).
- <sup>11</sup>T. Seike and J. Nagai, *Sol. Energy Mater.* **22**, 107 (1991).
- <sup>12</sup>L. D. Burke and O. J. Murphy, *J. Electroanal. Chem.* **109**, 373 (1980).
- <sup>13</sup>C. N. Polo da Fonseca, Marco-A. De Paoli, and A. Gorenstein, *Adv. Mater.* **3**, 553 (1991).
- <sup>14</sup>N. S. McIntyre and M. G. Cook, *Anal. Chem.* **47**, 2208 (1975).
- <sup>15</sup>C. R. Brundle, T. J. Chuang, and D. W. Rice, *Surf. Sci.* **60**, 287 (1976).
- <sup>16</sup>J. Heller, *Thin Solid Films* **17**, 163 (1973).
- <sup>17</sup>W. K. Behl and J. E. Toni, *J. Electroanal. Chem.* **31**, 63 (1975).
- <sup>18</sup>N. Sato and T. Ohtsuka, *J. Electrochem. Soc.* **125**, 1735 (1978).

# ELECTROREFLECTANCE AND PHOTORESPONSE OF $\text{NiO}_x$ THIN FILMS

M.C.A. Fantini

Instituto de Física, USP

CP 20516, 01498 - São Paulo, S.P., Brazil

A. Gorenstein

Instituto de Física, UNICAMP

CP 6165, 13081 - Campinas, S.P., Brazil

W.M. Shen and M. Tomkiewicz

Department of Physics, Brooklyn College, C.U.N.Y.

11210 - Brooklyn, N.Y., U.S.A.

## ABSTRACT

Thin films of nickel oxide obtained by reactive sputtering and deposited either at room temperature or at  $250^\circ\text{C}$  presented electrochromic properties in basic aqueous electrolytes. The structure of the films is characteristic of a polycrystalline material with preferential orientation, by which it was possible to follow the changes in lattice parameters with electrochemical intercalation, growth temperature and annealing processes. Photocurrent and electroreflectance measurements were performed in order to detect the variations in the band gap energy and in the electronic transitions as a function of the electrochromic state. The results are consistent with the presence of impurity levels due to nickel vacancies. The extracted values of the band gap energies increased for the clearer states, followed by a decrease in the carriers recombination rates.

## 1. INTRODUCTION

Thin films based on nickel oxide and hydroxide, deposited by various techniques, show electrochromic properties in the presence of an electric field in appropriate electrolytes [1].

The transmittance of those materials can be gradually and reversibly modified as a function of the electric field, for values

of clear and dark states with differences up to 70% [1]. Among those types of deposits, those obtained by vacuum techniques, show remarkable properties concerning to reversibility, response time and cyclicability [1].

Even though the knowledge of the growing conditions that lead to deposits with the desirable properties had expanded during the last years, the physical mechanisms responsible for the electrochromic phenomena are still unknown. Examples of some of the previous attempts to correlate the absorption processes with the electrochromic properties can be found in [2,3].

The aim of this paper is to report the results of our investigation of the optical properties of  $\text{NiO}_x$  films, prepared by rf-sputtering, using modulation spectroscopy techniques such as the electroreflectance and correlate it with the photoresponse, to obtain information on the electronic levels inside the material at different coloration states.

## 2. EXPERIMENTAL

The films were deposited by rf-sputtering, with a power of 100 W. For the reactive deposition a Ni target was used and an oxygen flux of 2 scc/m. During the film growth, the pressure inside the chamber was  $7 \cdot 10^{-3}$  mbar and the distance target-substrate was 180 mm. The analyzed samples were deposited over  $\text{SnO}_2$ /glass substrates ( $R_{\square} = 10 \Omega$ ), at room temperature and  $250^\circ\text{C}$ . The film thickness was evaluated by an Alpha-step profilemeter.

The cyclic voltametry was performed in a 0.1M KOH solution between -1V vs.SCE and +1V vs. SCE, with a sweep rate of 20 mV/s, followed simultaneously by the record of the transmittance at 632,8 nm (He-Ne laser).

The spectral transmittance and total reflectance of the films were measured in a Perkin-Elmer Lambda 9 UV/VIS/NIR spectrophotometer in the range between 0.3  $\mu\text{m}$  and 1.5  $\mu\text{m}$ .

The X-Ray Diffraction (XRD) measurements were performed in a conventional diffractometer, operating at 0.8 kW power, using Ni-filtered  $\text{Cu K}\alpha$  radiation. The  $2\theta$  angular variation was between



10° and 70°, with a step scanning of 0.05° and counting time of 10s.

The photoresponse and electroreflectance measurements were performed in a multi-task setup, described in ref. [4]. The photoresponse data were obtained in the spectral range of 250-600 nm, while the electroreflectance measurements, in a 0.1M KOH solution, comprised energies between 1.7 eV and 4 eV ( $330 \text{ nm} < \lambda < 730 \text{ nm}$ ).

One of the analyzed samples was submitted to a post-annealing at 300 °C by 24 hs. in air.

### 3.RESULTS

Two samples were deposited onto substrates at different temperatures. The A1 sample, grown at room temperature, was 1760 Å thick, while the other sample, A2, was deposited at 250 °C, and was 700 Å thick.

Figure 1 shows the cyclic voltamograms of the A1 and A2 together with the corresponding variation in transmittance for a 632.8 nm light.

In Figure 2 we show the spectral transmittance and total reflectance of the A1 sample. One can observe a systematic decrease in transmittance and total reflectance for more anodic bias regime. The optical constants, as well as the film thickness, can be extracted from those results [5].

In Figure 3 we show the photoresponse of the A1 sample, that was submitted to bleaching(-)/coloring(+) processes, using a current density of 1 mA/cm<sup>2</sup>.

In Figure 4 we show the electroreflectance spectra of the A1 sample, at different potentials.

In Figure 5 we present the electroreflectance spectra at a potential of 0.0 V vs. SCE, for the as-grown sample (A1) and for the same sample after annealing at 300°C in air for 24 hs.

In Figure 6 we compare the experimental result with the theoretical calculation of the line shape [4] for the as-grown A1 sample at a potential of 0.0 V vs. SCE.

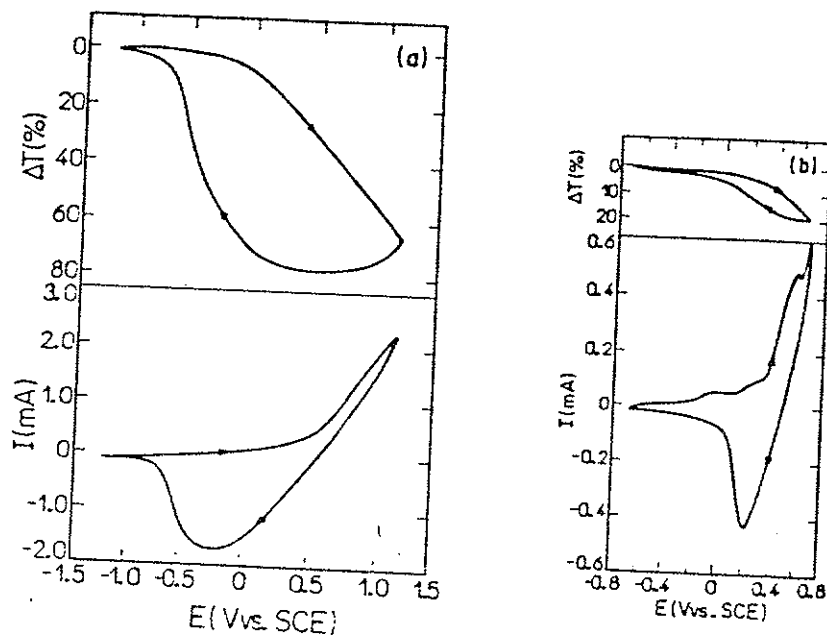


FIGURE 1. Current and Transmittance vs. Potential plots of the (a) A1 and (b) A2 samples.

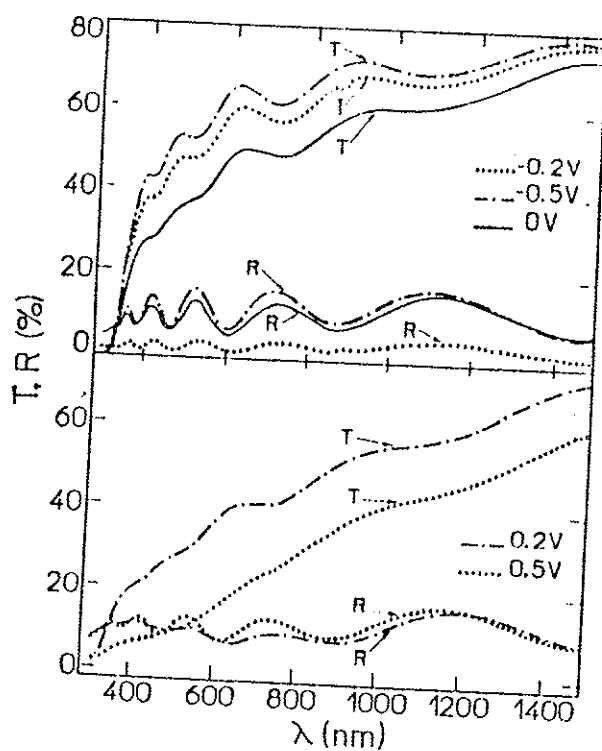


FIGURE 2. Transmittance and Reflectance spectra of the A1 sample at different applied potentials (vs. SCE).

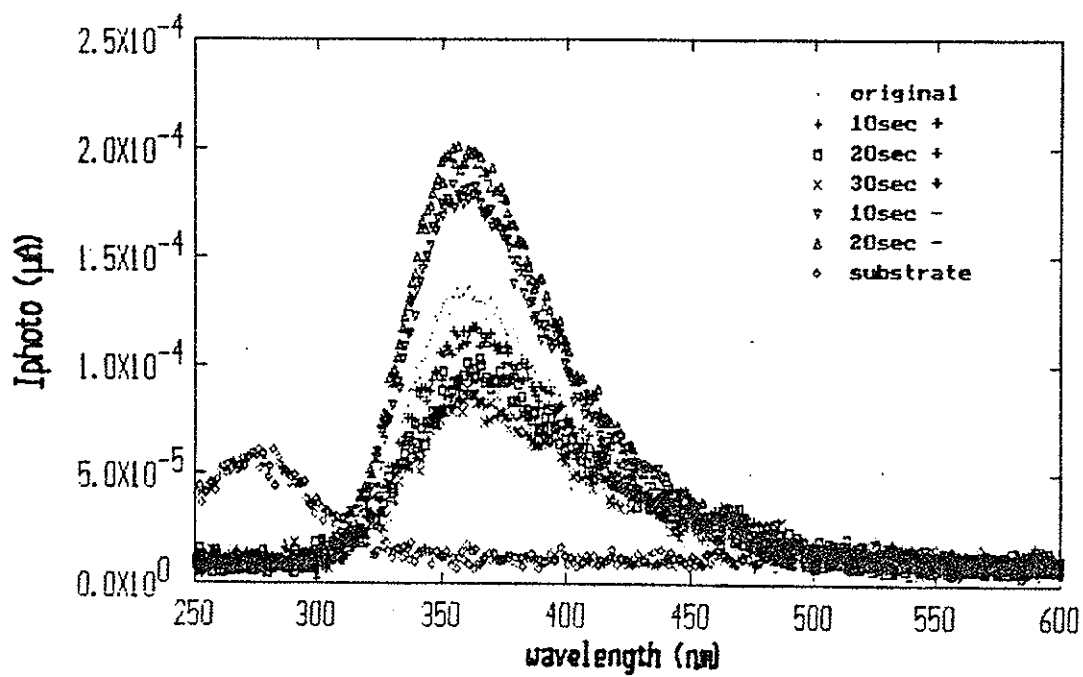


FIGURE 3. Photoresponse of the Al sample.

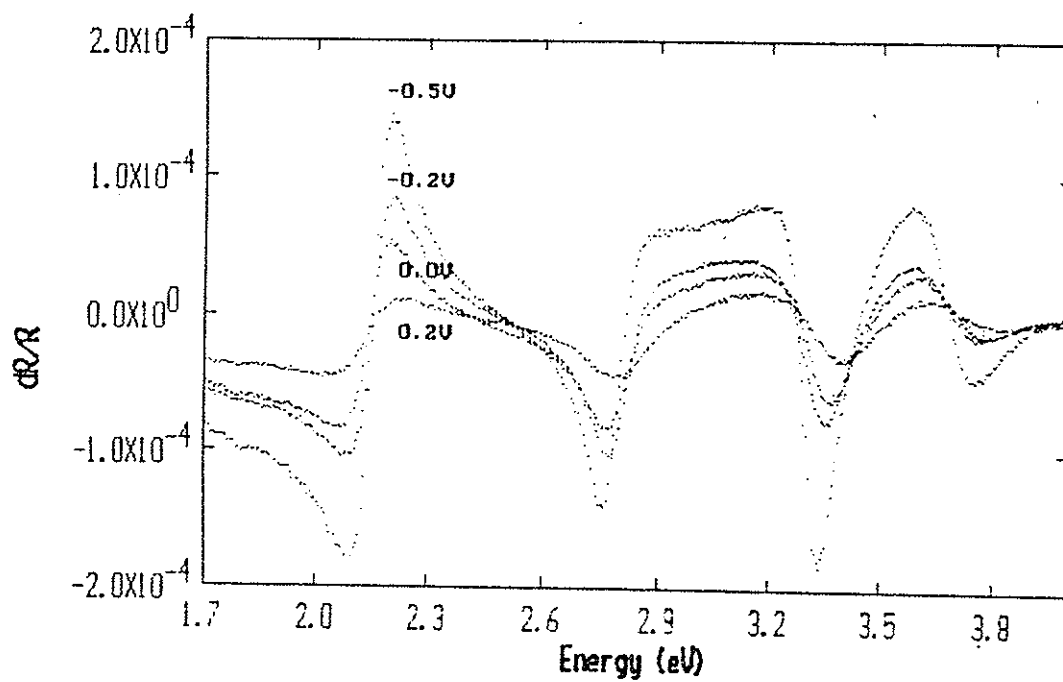


FIGURE 4. Electroreflectance spectra of the Al sample at different potentials.

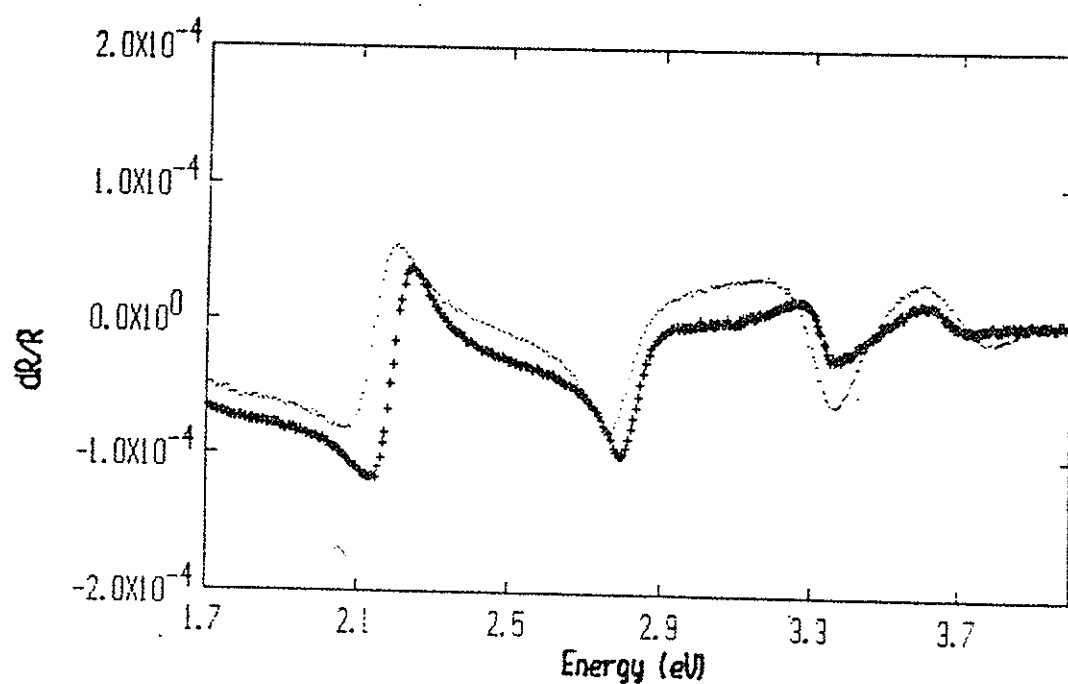


FIGURE 5. Electroreflectance spectra of the Al sample: (.) as-grown and (+) annealed.

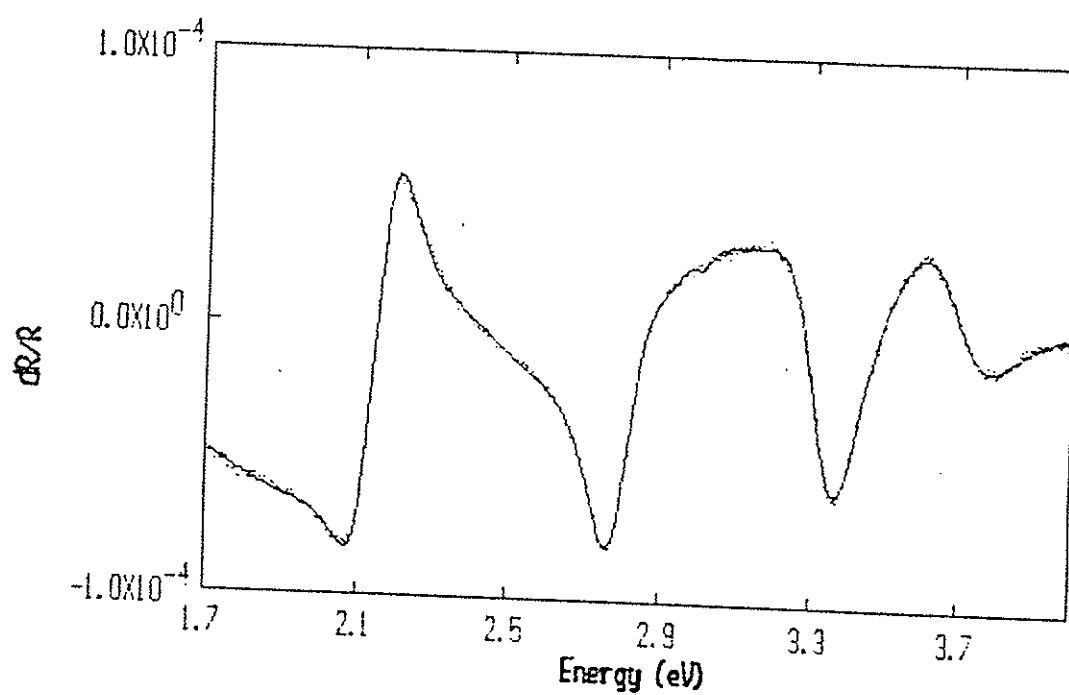


FIGURE 6. Electroreflectance of the as-grown Al sample at a potential of 0.0 V vs. SCE (.) experimental, (—) theory.

In Table I we present the data from the XRD measurements for the two samples at different conditions.  $I_{(101)}/I_{(012)}$  and  $I_{(110+104)}/I_{(012)}$  are parameters that indicate the preferential orientation of the films. Those values, as well as the lattice constants (a, b and c), must be compared to those of stoichiometric nickel oxide standards [6]. The results show that the substrate temperature is one of the parameters that governed the orientation of the deposited material.

TABLE I  
XRD Results

Sample	$\frac{I_{(101)}}{I_{(012)}}$	$\frac{I_{(110)+(104)}}{I_{(012)}}$	a = b* (Å)	c** (Å)
A1	1,1	1,1	2,979	7,243
A1-dark	1,1	1,1	2,990	7,177
A1-300°C	1,3	1,0	2,962	7,207
A2	0,4	0,3	2,999	7,362
A2-300°C	0,4	0,3	2,989	7,222
Standard	0,6	0,7	2,955	7,224

\* deviation of 0,006 Å. \*\* deviation of 0,038Å.

Table II shows the values for the indirect and direct band gap energies that were extracted from the photoresponse experiment as a function of the input charge for the A1 sample.

TABLE II  
Charge (Q) and indirect ( $E_i$ ) and direct ( $E_d$ ) band gaps. The numbers in parenthesis are for A2 sample.

Q (mC)	$E_i$ (eV)	$E_d$ (eV)
+30	2.45	3.10
+20	2.47	3.08
+10	2.51	3.10
0	2.59 (2.42)	3.13 (3.10)
-10	2.62	3.14
-20	2.62	3.14

Table III lists the energy and corresponding transitions obtained from theoretical calculations in the range of 1.7 eV and 4 eV, for the NiO single crystal [7].

TABLE III  
Electronic transitions of NiO in the range between 1.7 eV and 4 eV.

$E_i$ (eV)	Transition
1.75	$^1E_g$
1.95	$^3T_{1g}$
2.15	?
2.75	$^1T_{2g}$
2.95	$^3T_{1g}$
3.25	$^1A_{1g}$
3.52	$^1T_{1g}$

Table IV shows the parameters that were obtained from the fitting of the line shape of the electroreflectance of the Al sample under different bias conditions. Only four of the transitions that are listed in table III developed enough intensity to be resolved in the spectra.

TABLE IV  
Energy and linewidth parameters as a function of the potential.

E (V vs.SCE)	$E_1$ (eV)	$\Gamma_1$ (meV)	$E_2$ (eV)	$\Gamma_2$ (meV)	$E_3$ (eV)	$\Gamma_3$ (meV)	$E_4$ (eV)	$\Gamma_4$ (meV)
-0.5	2.158	122	2.786	117	3.295	151	3.669	216
-0.2	2.163	129	2.805	131	3.317	183	3.661	222
0.0	2.149	138	2.803	138	3.335	184	3.679	212
+0.2	2.144	192	2.816	177	3.354	255	3.708	280

Finally, Table V compares the electroreflectance parameters of as-grown and annealed (300°C for 24 hs) samples at 0.0 V vs. SCE.

TABLE V  
Energy and linewidth of the A1 sample before and after annealing

$E_1$ (eV) $\Gamma_1$ (meV)	as-grown	annealed
$E_1$	2.158	2.197
$\Gamma_1$	122	120
$E_2$	2.786	2.828
$\Gamma_2$	117	116
$E_3$	3.295	3.332
$\Gamma_3$	151	137
$E_4$	3.669	3.611
$\Gamma_4$	216	142

#### 4. DISCUSSION

The optical properties of NiO have been studied by conventional spectrophotometric techniques in a wide range of energies [7-10]. Modulated spectroscopy results are also found in the pertinent literature [11,12]. Theoretical models for the band structure of the generally called NiO compound were conducted and efforts were made in order to conciliate the calculations with the available experimental results on the optical properties [13-16].

The calculated NiO band structure models [11, 13-16] show a consensus about the conduction band levels (4s of Ni) and the valence (3d of Ni and 2p of O) band structures. Non-stoichiometric nickel oxide and cationic impurities are also discussed [15,16]. Calculations based on the  $\text{Ni}_3\text{O}_4$  stoichiometry and a spinel type of crystal lattice show that this mixed valence compound has an absorption level at about 2.15 eV [2], the same one we have observed in the electroreflectance spectra. The p-type semiconducting properties of non-stoichiometric NiO are attributed to the existence

of holes , that are located on oxygen [13,16].

From the potential evolution of the photoresponse signal one can extract the band gap energies. For the electrochromic material studied in this work we have observed a direct band gap energy of around 3 eV and an indirect transition around 2.5 eV. Towards the bleached state there is a systematic increase of those energies followed by an increase in the amplitude of the photocurrent, indicating a decrease in the carriers recombination rates. The enhancement in the indirect gap energy is more remarkable than the direct one. The deposition temperature has a considerable effect in decreasing the indirect gap energy, but hardly changes the direct gap energy (see, Table II). These observations indicate that the levels responsible for the indirect band gap are those that mostly contribute to the free carrier density and most likely to the optical transitions.

The electroreflectance measurements were sensitive enough to show the energy changes in four of the electronic transitions. The one observed at around 2.15 eV is the first experimental evidence of the presence of nickel ions with intermediary valence, i.e., the electrochromic film is nickel deficient [2].

The electroreflectance signal, as well as the photocurrent results, show an increase in amplitude and smaller recombination rates, while the bleaching process was carried on. The energy of the electronic levels have systematically decreased for the clearer states, except for the transition at 2.15 eV. For this level, the variation in the observed values was much smaller (and in a opposite direction) than that observed for the NiO transitions. Such behavior suggests "pinning" of a localized level. The combination of these results indicates a band structure of the electrochromic NiO<sub>x</sub> that varies with the coloration state, such that the levels responsible for the edges of the conduction and valence bands are more widely separate in the clear state. The comparison between the electroreflectance signal of as-grown and annealed samples strongly indicates a conduction mechanism through a localized impurity level, that can be neutralized by heat treatment [3,11].

The XRD measurements allowed, for the first time, to monitor



the three crystallographic axes of the electrochromic  $\text{NiO}_x$  thin films as a function of the sputtering deposition parameters (such as the temperature), coloration state and pos-annealing processes. The deposited material has lattice parameters larger than the stoichiometric  $\text{NiO}$ , that decrease with the heat treatment. It was observed that the coloration process implies in a decrease of the parameter in the z-direction, followed by an increase in the values corresponding to the other crystallographic axes.

#### 5.CONCLUSIONS

In this paper we have demonstrated the applicability of modulation spectroscopy techniques as a probe for the band structure of electrochromic materials. Structural changes promoted by the electrochromic effect can also be followed through XRD techniques, that precisely ascribe the crystal sites where ion insertion occurs.

#### 6.ACKNOWLEDGEMENTS

Thanks are due to Mr. Airton Lourenço for the deposition of the studied samples and Prof. I. Cisneros for the spectrophotometric measurements. Prof. H. Petrilli is also thanked for the helpfull discussions.

#### REFERENCES

1. "Large Area Chromogenics: Materials and Devices for Transmittance Control", ed. C.M.Lampert and C.G.Granqvist, SPIE Publ., 1991.
2. K.M.E. Miedzinska, B.R. Hollebone and J.C.Cook, J. Phys. Chem. Solids 49, 1355, 1988.
3. T.M.J. Nilsson and G. A. Niklasson, SPIE, 12, 129, 1990.
4. W.M. Shen, M.C.A. Fantini, M. Tomkiewicz and J.P. Gambino, J. Appl. Phys. 66, 1759, 1989.
5. M.Born and E. Wolf, in "Principles of Optics", Pergamon Press, 1975.
6. Joint Committee for Powder Diffraction Standards (JCPDS), 1973.

7. R. Newman and R.M. Chrenko, Phys. Rev. 114, 1507, 1959.
8. P.J. Gielisse, J.N. Plendl, L.C. Mansur, R. Marshall, S.S. Mitra, R. Mykolajewycz and A. Smakula, J. Appl. Phys. 36, 2446, 1965.
9. I.G. Austin, B.D. Clay and C.E. Turner, J. Phys. C, ser. 2, 1, 1418, 1968.
10. R.J. Powell and W.E. Spicer, Phys. Rev. B, 2, 2182, 1970.
11. J.L. McNatt, Phys. Rev. Lett. 23, 915, 1969.
12. G. Larramona and C. Gutiérrez, J. Electrochem. Soc. 137, 428, 1990.
13. D. Adler and J. Feinleib, Phys. Rev. B, 2, 3112, 1970.
14. K. Wandelt, Surface Science Reports 2, 1, 1982.
15. J.B. Goodenough, in Prog. Sol. St. Chem. 5, pg. 145, 1971.
16. P. Kuiper, PhD Thesis, Rijks-Universiteit, Groningen, 1990.

# Valence Band Studies of Electrochromic $\text{NiO}_x$ Thin Films

M. C. A. Fantini

*Instituto de Física, Universidade de São Paulo*

*C.P. 20516, 01452-990, SP, Brazil*

A. Gorenstein

*Instituto de Física, Universidade Estadual de Campinas*

*Caixa Postal 6165, 13081-970 Campinas, S.P., Brazil*

K. Subramanian, N. Mainkar, R. L. Stockbauer and R.L. Kurtz

*Department of Physics and Astronomy, Louisiana State University*

*Baton Rouge, LA, 70803-4001, U.S.A.*

Received May 13, 1994

Electrochromic nickel oxide thin films were deposited by RF reactive sputtering, onto glass substrates covered with tin dioxide, using different oxygen flux. Variations in the oxygen flux influence the film crystalline structure and stoichiometry, and are related to the electrochromic performance. The films were characterized by cyclic voltammetry, visible spectrophotometry, x-ray diffraction (XRD) and ultraviolet photoemission spectroscopy (UPS). The cyclic voltammetry and visible spectrophotometry results determine the electrochromic performance of the films, in a 0.1 M KOH aqueous electrolyte at different potentials. The XRD data identify the lattice parameter variations due to the (de)- intercalation process and preferred orientation of the films. The UPS results, obtained in a synchrotron radiation facility (CAMD, Baton Rouge, LA, U.S.A.), were used to monitor the valence bands of the films at different coloration states. The film deposited at the smallest oxygen flux (0.5 sccm) is nickel, with a small amount of oxygen, and has a metallic dark appearance. For the next higher oxygen flux (1.0 sccm) the film is nickel oxide, having a preferred orientation in the (012) direction of the hexagonal cell and a clear as-grown color. For all the other higher fluxes, the material is nickel oxide with (101) preferred orientation and dark. The transmittance span is correlated to the crystalline structure and diffusion coefficient of ions inside the films. The results pointed to modifications in the film composition due to the electrochromic intercalation process. The emergence of bands related to the  $\text{OH}^-$  concentration in the UPS spectra indicate that the bleached material has a higher number of valence states connected to this radical. On the other hand, the decrease in the occupation of these bands observed for the colored state is followed by an increase in conduction band states over the Fermi energy, and account for changes in the optical and electronic properties of the material. Measurements of the UPS spectra at different exciting energies provide the observation of a resonance in the valence band region.

## I. Introduction

Non-stoichiometric nickel oxide ( $\text{NiO}_x$ ) thin films, deposited by sputtering, are well known due to their dynamic optical properties<sup>[1-3]</sup>. The growth of high-performance  $\text{NiO}_x$  coatings for applications in electrochromic devices depends critically on understanding how the deposition parameters affect the compo-

sition, structure and electrochemical behavior. The growth parameters that have to be optimized for the sputtering method are the rf power, the substrate temperature and the oxygen flux. In a previous work we briefly discussed the effect of substrate temperature on the resulting material properties [3]. In this paper, we present a systematic study of the influence of the

TABLE I. Oxygen flux (f), sample thickness (t) and deposition rate (r).

Sample	f(sccm)	t( Å)	r( Å/ sec)
237	0.5	3000	3.3
236	1.0	3150	3.5
233	2.0	2200	1.2
234	4.0	1620	0.68
235	6.0	1900	0.70

oxygen flux on the resulting  $\text{NiO}_x$  deposit. The optical properties of the films were determined by spectrophotometry and monochromatic transmittance measurements. The films were also characterized by X-Ray Diffraction (XRD) to determine their structural features, by cyclic voltammetry to evaluate their electrochemical/electrochromic behavior and by Ultraviolet Photoemission Spectroscopy (UPS) to elucidate the valence band characteristics at the different coloration states.

## II. Experimental

The samples were reactively deposited from a nickel target (99.99%) in an oxygen plus argon atmosphere, under a  $7 \times 10^{-3}$  mbar total pressure, an rf power of 100 W, at room temperature and with target-substrate distance of 150 mm. The films were deposited onto  $\text{SnO}_2/7059$  Corning glass substrates ( $R = 20 \Omega/\square$ ) using different oxygen fluxes:  $f = 0.5, 1.0, 2.0, 4.0$  and  $6.0$  sccm. The thickness of the films were determined by a profilometer. Table I depicts the differences on sample deposition conditions, as well as the film thickness.

The electrochemical experiments were conducted in 0.1M KOH aqueous electrolyte, prepared with PA reagents and tri-distilled water. Various galvanostatic steps of  $50 \mu\text{A}$  by 10 min (sample typical area of  $1.5 \text{ cm}^2$ ) were used to evaluate the chemical stabilization of the films. Simultaneously, cyclic voltammetry ( $-1.0 \text{ V}$  vs. SCE and  $1.0 \text{ V}$  vs. SCE, scanning rate of  $20 \text{ mV/sec}$ ) and transmittance changes were recorded, using a He-Ne laser ( $\lambda = 632.8 \text{ nm}$ ) and a silicon photodetector. The spectral transmittance and total reflectance of the films were measured by a Perkin-Elmer Lambda 9 UV/VIS/NIR spectrophotometer in the range between 350 nm and 850 nm.

The XRD measurements were performed ex-situ on samples submitted to galvanostatic steps of  $50 \mu\text{A}$  for 20 min., using Ni filtered  $\text{Cu-K}\alpha$  radiation and step scanning mode, with steps of  $0.020^\circ$  and counting time of 40 sec.

The UPS measurements were performed using the Center for Advanced Microstructures and Devices (CAMD) synchrotron light source. The measurements employed photons in the energy range of 30 - 650 eV delivered by a plane grating monochromator.<sup>[4]</sup> Angle-integrated spectra were obtained with a display-type analyzer<sup>[5]</sup> and have been normalized to incident photon flux. The overall resolution was about 1 eV at the highest uv photon energies used here and about 0.25 eV in the photon energy range used to study the Ni 3p resonance. The measurements were performed for one  $\text{NiO}_x$  sample, grown with the highest oxygen flux,  $f = 6.0$  sccm (235 in Table I). This sample was measured in the as-grown, cycled, bleached and colored states, using the same ex-situ conditions employed in the XRD characterization to change the optical properties of the films.

## III. Results

The film deposited at the smallest oxygen flux (0.5 sccm) is mostly nickel, probably with a small amount of oxygen, as determined by the XRD measurements, and has a metallic dark appearance. For the next higher oxygen flux (1.0 sccm) the film is nickel oxide, having a preferred orientation in the (012) direction of the hexagonal cell and a clear as-grown color. For all the other higher fluxes, the material is nickel oxide with (101) preferred orientation and dark. Figs. 1 and 2 show diffractograms, corresponding to (101) and (012) reflections. It is remarkable the difference in the crystalline orientation of the film deposited at  $f = 1.0$  sccm when compared to the other obtained samples. Also, Fig. 1 depicts differences in crystalline plane distances among samples at the same optical status, as well as modifications in these distances due to the intercalation/de-intercalation process. Table II presents the calculated unit cell values. The  $\text{NiO}_x$  film deposited with small oxygen flux has a more compressed cell and a smaller variation in unit cell dimensions occurring at the bleaching/coloring procedure. Moreover,

TABLE II Unit cell volume in the as-grown ( $V_a$ ), bleached ( $V_b$ ) and colored ( $V_c$ ) states and percentage difference ( $V_{bc}$ ).

Sample	$V_a(\text{\AA}^3)$	$V_b(\text{\AA}^3)$	$V_c(\text{\AA}^3)$	$V_{bc}(\text{\AA}^3)$
236	55.08	55.21	55.11	0.2
233	57.29	57.54	56.92	1.1
234	56.63	57.43	56.82	1.1
235	57.20	57.35	57.02	0.6
NiO	54.68	—	—	—

$\delta V = 0.37 \text{ \AA}^3$  (error in Volume)

for all films the cell dimensions are larger than that of stoichiometric NiO. The calculation of unit cell volumes was based on the determination of diffraction maxima, using a Lorentzian function for the line profile and a straight line background, as it is exemplified in Fig. 3. The changes observed in the lattice parameters ( $a$  and  $c$  of the hexagonal unit cell) upon de-intercalation, i.e., from bleached to colored state, showed that  $a$  always decreased. On the other hand,  $c$  increased for the sample deposited with  $f = 1.0$  sccm and decreased for all the other samples, deposited at larger oxygen flux.

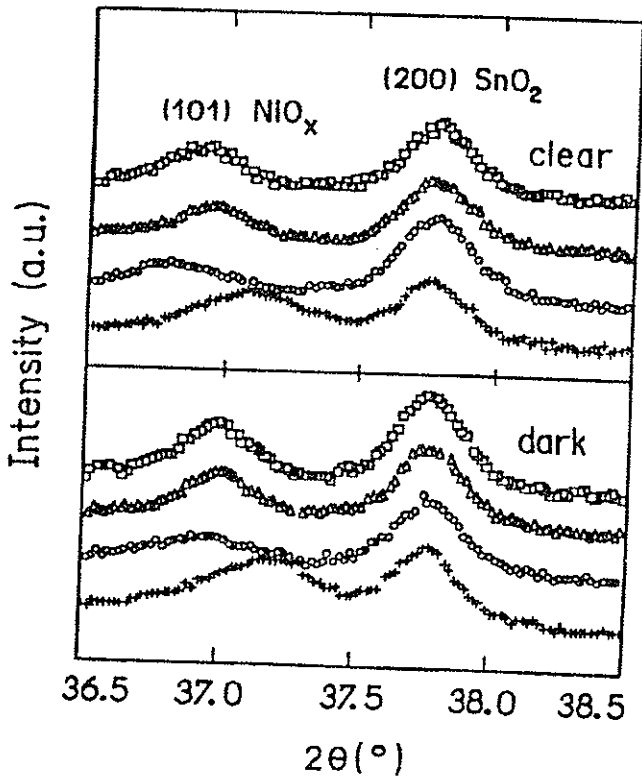


Figure 1: XRD patterns of the samples deposited at  $f = 1.0$  sccm (+), 2.0 sccm (o), 4.0 sccm ( $\Delta$ ) and 6.0 sccm ( $\square$ ): (101) reflection.

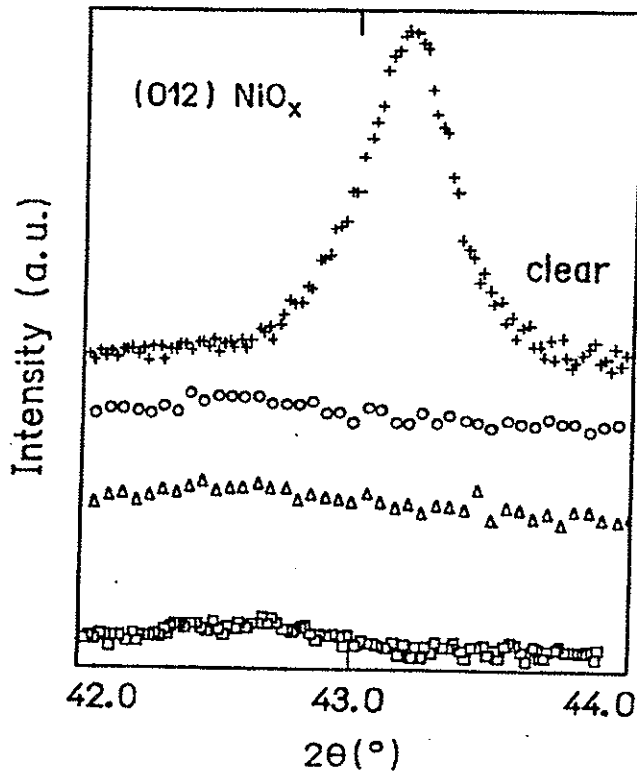


Figure 2: XRD patterns of the samples deposited at  $f = 1.0$  sccm (+), 2.0 sccm (o), 4.0 sccm ( $\Delta$ ) and 6.0 sccm ( $\square$ ): (012) reflection.

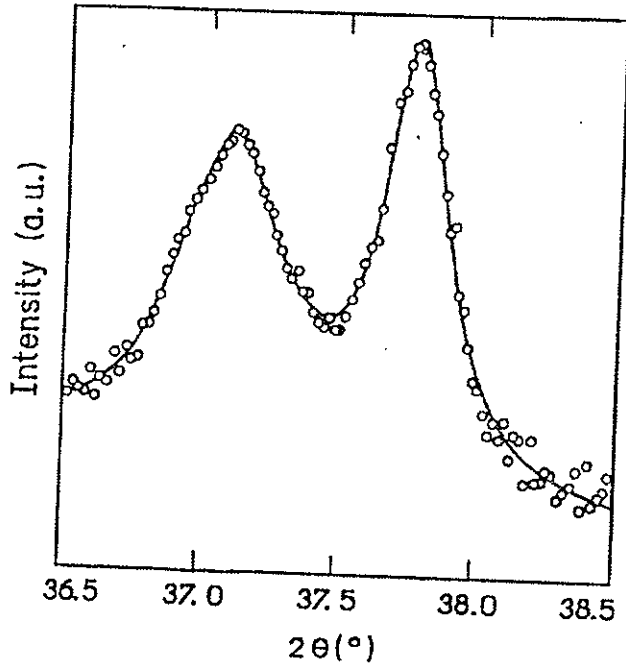


Figure 3: Lorentzian fitting (straight line) of the experimental diffracted intensity (open circles) vs.  $2\theta$  for the sample deposited with  $f = 1.0$  sccm in the bleached state. The peak at  $\sim 37.2^\circ$  is the (101) NiO reflection and the other at  $\sim 37.8^\circ$  corresponds to the (200)  $\text{SnO}_2$  reflection of the substrate.

The analysis of the diffracted integrated intensity provided the preferred orientation of the films, defined as  $P$ :

$$P = \frac{I(hkl)}{\sum I(hkl)}$$

The crystallite size,  $D_{(hkl)}$ , is obtained from the line-width<sup>[6]</sup> with a deviation of  $\pm 15$  Å. The degree of crystallinity,  $n$ , normalized to the larger integrated intensity presented by the 236 sample, is calculated using the total diffractive power of each film.

Table III shows the above mentioned parameters.

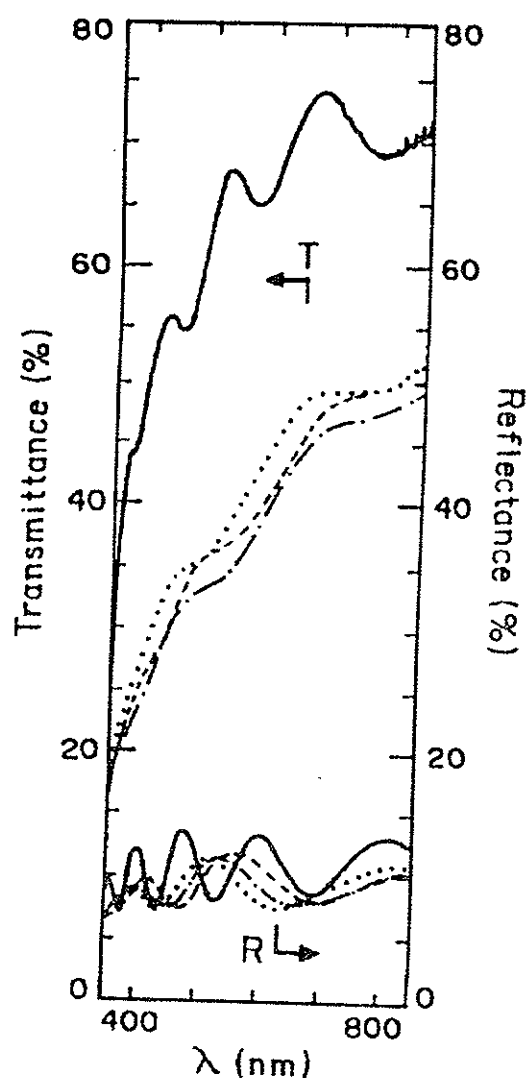


Figure 4. Spectral transmittance ( $T$ ) and reflectance ( $R$ ) of the samples deposited with  $f = 1.0$  sccm (—),  $2.0$  sccm (---),  $4.0$  sccm (•••) and  $6.0$  sccm (—•—).

The results demonstrate quantitatively that the preferred orientation along the (012) direction of the NiO

hexagonal cell, achieved with the smaller oxygen flux, gradually changes to a preferred orientation along the (101) crystalline direction as the oxygen flux increases. Nevertheless, the number of crystallites in this latter direction is always larger than the corresponding number for stoichiometric NiO. Also, the crystallite size follows the same trends observed for the preferred orientation, i.e., there is an increase in the crystalline size with the increase of the oxygen flux. The degree of crystallinity, which can be defined as the amount of crystalline phase per unit volume, ( $n$ ), is larger for the smaller oxygen flux; for larger  $f$ -values, the fluctuation of  $n$  may be related to deposition rate.

Fig. 4 shows the spectral transmittance and total reflectance of the as-grown nickel oxide films in the visible region. It is remarkable the higher transmittance recorded for the sample deposited with  $f = 1.0$  sccm. The monochromatic transmittance was simultaneously recorded with the cyclic voltammetry. All the samples presented the same variation between minimum and maximum transmittance during the first cycle, around 60%. For the samples deposited with  $f = 2.0, 4.0$  and  $6.0$  sccm, the results revealed that the minimum transmittance decreases with cycling, reaching stabilization at around the 20<sup>th</sup> cycle. This decrease can reach 60% of the initial value. In the mean time, the maximum transmittance also decreases with cycling, but at a smaller rate. The consequence is an increase in the transmittance span after cycling, around 70%, typically, minimum of 10% and maximum of 80% at the 40<sup>th</sup> cycle. On the other hand, for the sample deposited at  $f = 1.0$  sccm, the minimum transmittance does not stabilize. The transmittance span attains for the 40<sup>th</sup> cycle a reasonable value of around 80% (minimum of 16% and maximum of 95%), but both minimum and maximum transmittance values continue decreasing, leading to a variation of only 52% (minimum of 4% and maximum of 56%) after the 150<sup>th</sup> cycle.

Galvanostatic experiments (constant current density) were also performed. In this case, the resulting transmittance change for the different films is very similar. However, the time variation of the transmittance shows that the electrochemical process presented by the sample deposited at  $f = 1.0$  sccm is much more slower.

TABLE III. Preferred orientation (P), crystallite size (D in Å) and degree of crystallinity (n).

Sample	P <sub>(101)</sub>	P <sub>(012)</sub>	P <sub>(110)+(104)</sub>	D <sub>(101)</sub>	D <sub>(012)</sub>	D <sub>(110)+(104)</sub>	n
236	0.315	0.583	0.102	177	238	106	1.00
233	0.437	0.328	0.235	208	90	164	0.48
234	0.443	0.350	0.233	299	83	165	0.67
235	0.557	0.210	0.233	304	118	168	0.54
NiO	0.261	0.435	0.304	—	—	—	—

The same transmittance span is attained for this sample after a time delay two times greater than those obtained in the experiments performed with the other samples. Fig. 5 shows the cyclic voltammetry and monochromatic transmittance results obtained for the films after various galvanostatic steps.

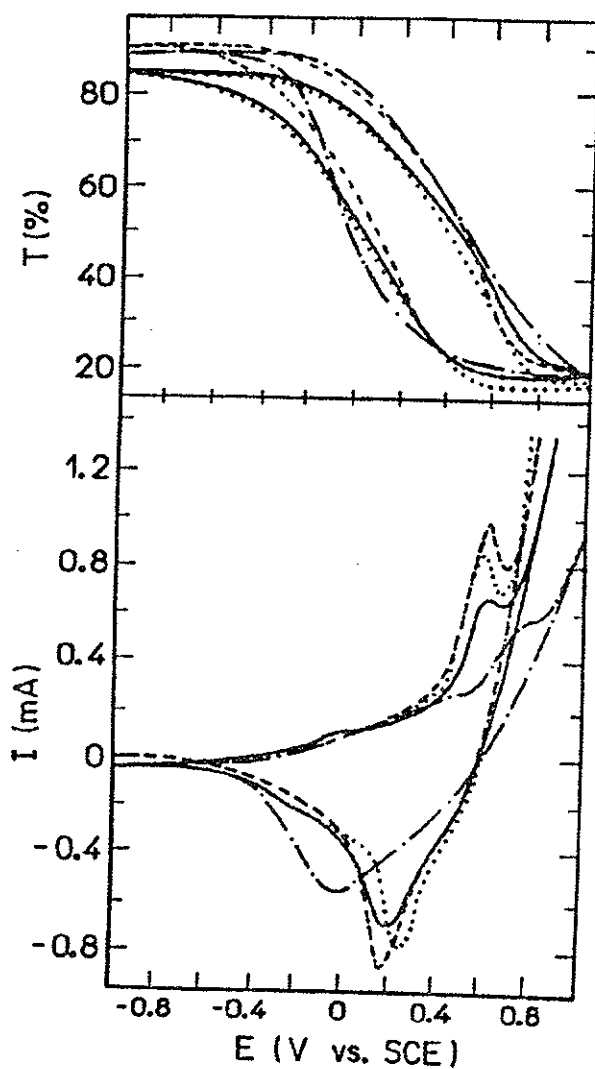


Figure 5. Current (I) and transmittance (T) vs. Potential (E) plots of the samples deposited with  $f = 1.0$  sccm (—●—), 2.0 sccm (---), 4.0 sccm (····) and 6.0 sccm (●●●).

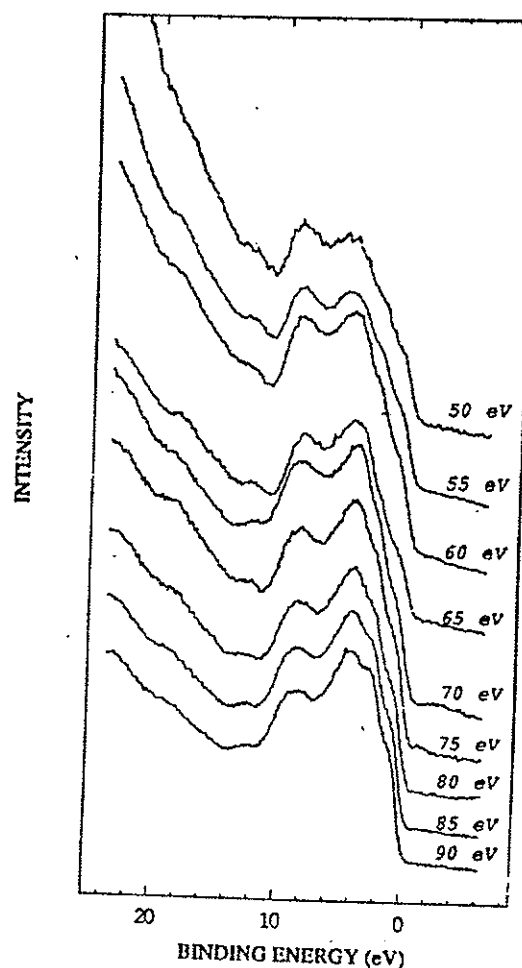


Figure 6. Valence band resonance spectra for different incident photon energies ( $h\nu$  in eV).

Fig. 6 shows a typical UPS resonance spectra of the film at the cycled state for different incident photon energies. The differences in peak intensities are due to the Ni-3p threshold resonance at about 66 eV [7]. The whole valence spectrum was described by three Gaussian functions, whose fitting quality is depicted in Fig. 7. The obtained binding energies have been assigned to transitions related to valence band electronic states of pure NiO and NiO with adsorbates [7-10]. Fig. 8 presents the binding energies obtained for the analyzed sample at different coloration states for  $h\nu = 70$  eV. Fig.

TABLE IV. Binding energy (B.E.) and integral intensity (I) obtained from the UPS measurements of 235 sample ( $f = 6.0$  sccm)

Peak $\sim 8$ eV				
Sample status	as-grown	cycled	bleached	colored
B.E.(eV)	7.98	7.69	7.69	7.92
I ( $10^{-7}$ a.u.)	8.01	3.23	10.2	1.38
I (%)	35	38	41	35
Peak $\sim 4$ eV				
Sample status	as-grown	cycled	bleached	colored
B.E.(eV)	3.31	3.31	3.79	3.97
I ( $10^{-7}$ a.u.)	13.2	4.87	12.2	1.98
I (%)	57	57	49	50
Peak $\sim 1$ eV				
Sample status	as-grown	cycled	bleached	colored
B.E. (eV)	0.39	0.56	1.38	1.19
I ( $10^{-7}$ a.u.)	1.78	0.46	2.36	0.59
I (%)	8	5	10	15

9 and Table IV compile the relevant results concerning, respectively, the integral intensity as a function of photon energy and, for a fixed incident energy, variations in peak position and intensity due to different optical and chemical sample status. The work function of the film at different coloration state did not show any remarkable change, which may be possibly connected to surface coverage of species during electrochemical processing or air exposure. Also, we did not observe any unusual difference in the measured total yield of the films at the whole available photon energy range (30 - 650 eV).

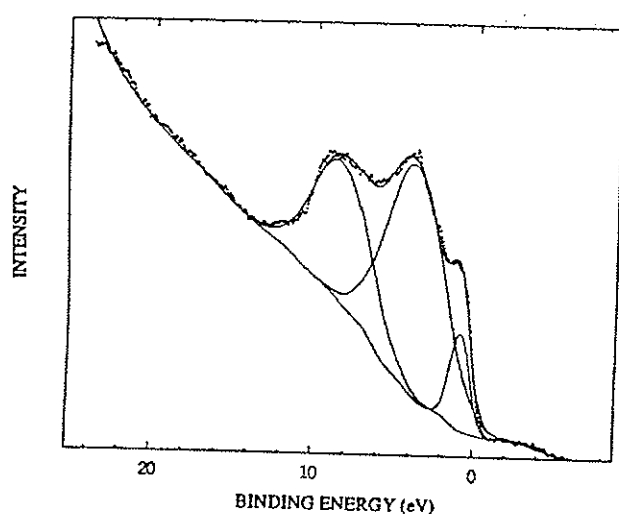


Figure 7. Fitting of valence band spectra by three Gaussian functions.

#### IV. Discussion

Modifications on the chemical and structural properties of  $\text{NiO}_x$  thin films, deposited by reactive rf sputtering, are achieved by changing the oxygen flux inside the deposition chamber<sup>[11]</sup>. These differences can be responsible for variations in the electrochemical/electrochromic performance. First, it is relevant to understand how the oxygen flux affects the material properties and, second, it is important to determine the oxygen flux range that produces  $\text{NiO}_x$  films with highest electrochromic performance. The parameters to be correlated are stoichiometry, preferred crystalline orientation, crystallite size, degree of crystallinity, transmittance span and electrochemical stability. In this work we concentrated on the electrochromic, crystalline and optical properties of the different deposited  $\text{NiO}_x$  thin films.

Due to the fact that the film obtained with  $f = 0.5$  sccm is nickel, instead of nickel oxide, it will not be considered in the further discussion.

The unit cell volume of the sample deposited with  $f = 1.0$  sccm, as well as its variation upon bleaching and coloring is much smaller than the values attained for samples deposited at higher oxygen flux, but the transmittance span after galvanostatic steps is the same for all the different films. On the other hand, other structural parameters like the degree of crystallinity, preferred orientation and crystallite size also depend on the oxygen flux. The film deposited with  $f = 1.0$  sccm presented the highest degree of crystallinity, a larger number of crystallites with the (012) face parallel to the substrate surface and also a larger crystallite size in this same direction, comparatively to the other crystal faces. For higher  $f$  values (2.0, 4.0 and 6.0 sccm), the preferred orientation becomes the (101) crystallographic direction and the crystallite size in this direction increases with the oxygen. The observed differences on the crystalline properties can be attributed to the deposition rate, since it is dependent on the oxygen flux, being higher for the smaller values of  $f$ .

For  $f = 1.0$  sccm the  $\text{NiO}_x$  thin film is more transparent in the visible region, even though it is thicker (see Table I and Fig. 4). This result is probably related to stoichiometry<sup>[12]</sup>. In fact, deviations from



stoichiometry play an important role in the optical, ionic and electronic properties of the materials. In the case of nickel oxide, the non-stoichiometry has been attributed to excess of oxygen (nickel vacancies) leading to the formation of  $\text{Ni}^{+3}$  ions in the nickel oxide matrix and to a decrease of transmittance in the visible range<sup>[12]</sup>. Previous results on the stoichiometry of one similar  $\text{NiO}_x$  sample grown with  $f = 2.0$  sccm, using Rutherford Back-Scattering measurements, provided  $x = 1.07 \pm 0.02$ <sup>[13]</sup>. It is reasonable to argue that the stoichiometry of the sample deposited at the lowest oxygen flux is much near the stoichiometric compound, which is transparent in the visible range, than the samples grown with higher flux. However, for this film ( $f = 1.0$  sccm), the monochromatic transmittance do not stabilize, gradually changing to smaller values under electrochemical cycling. This sample has the slowest time response, indicating a diffusion coefficient lower than for the other samples. Thin film diffusion coefficients are known to greatly depend on the stoichiometry and crystal structure, since the later determines the ionic channels inside the material. In the present case, an ionic transport mechanism linked to the number of oxygen vacancies (hopping ionic transport) should be assumed, since the sample deposited at the lowest oxygen flux is a compound with composition near  $x = 1$ , in spite of the greater crystallinity that should induce a higher diffusion coefficient. As the experimental parameters used in the electrochemical experiments were the same for all samples, the time scale of the experiment was probably not enough to let the full intercalation/de-intercalation process happen. The optical behavior, then, should be attributed to the slower kinetics of the electrochemical reaction. Also irreversible incorporation of ionic or neutral species in the oxide matrix should not be discarded. In fact, in earlier works<sup>[14,15]</sup> we pointed out that alkaline ions also participate in the electrochromic reaction. It is also known that doping of nickel oxide with these ions ( $A = \text{Li}$ , etc.) originates a dark, p-type semiconductor,  $\text{NiO}_x\text{A}_{(1-x)}$  compound<sup>[16]</sup>. In order to clarify all these points, work is underway to determine the stoichiometry of the films analyzed in this paper.

The fact that the crystal lattice volume is practi-

cally the same for the sample deposited with  $f = 1.0$  sccm (Table II) in the as-grown and colored states, even though there is a huge difference in the monochromatic transmittance (70% for as-grown and 16% for colored films), also indicates that either an incomplete intercalation/de-intercalation process or an irreversible incorporation of species occurs for this film. It is important to observe that, independent of the oxygen flux, the obtained films always have crystal lattice parameters larger than the values of stoichiometric  $\text{NiO}$  and, therefore, the lattice should be able to accept intercalating ions. It has to be pointed out that  $\text{NiO}_x$  films after electrochemical cycling in aqueous electrolyte do not suffer an hydration process with a consequent amorphization of the crystal structure as has been observed in  $\text{CoO}_x$  films<sup>[17]</sup>, in spite of similar physical and electrochemical characteristics of  $\text{NiO}_x$  and  $\text{CoO}_x$ . All these findings point to the fact that reversibility and large transmittance span, desirable in any electrochromic material, can be achieved in films that combine a proper stoichiometry and structure.

There is not very much information concerning changes in the electronic structure of these non-stoichiometric  $\text{NiO}_x$  thin films that can be related to electrochromism, in spite of an extensive literature related to the optical and electronic properties of  $\text{NiO}$ <sup>[12,16,18,19]</sup>. Another complication in analyzing, this type of films resides on the fact that the valence band features depend not only on stoichiometry, but also on sample crystalline characteristics<sup>[20]</sup>. The conduction band of these films is frequently explored through the study of the optical properties in the ultra-violet, visible and near-infrared regions, necessary to evaluate the electrochromic performance<sup>[1-3]</sup>. There are also studies using X-ray Photoemission Spectroscopy (XPS) that focus in modifications in the core levels related to the electrochromic process<sup>[2]</sup>. Investigations about the valence band of these compounds are scarce, even though important changes upon intercalation/de-intercalation of species are to be expected, since the valence band levels are related to bonding.

The electronic structure of transition metal oxides like  $\text{NiO}$  has been a controversial subject for a long period of time. The experimental observation that  $\text{NiO}$

is a good insulator, instead of a metal as predicted by band theory due to the Ni 3d unfilled band, is the starting point. In the Mott-Hubbard picture the controversy was explained by a strong intra-atomic Coulomb interaction between the Ni 3d electrons. In this case the band gap energy is determined by the energy difference ( $U_{dd}$ ) between Ni  $d^7$  and Ni  $d^9$  configurations. More recently, it was shown that the first ionization states are not Ni  $3d^7$  but  $3d^8\bar{L}$ , where  $\bar{L}$  is a hole in the O 2p ligand band. In this last case the band gap is a charge transfer gap between ligand holes states and Ni  $3d^9$  states. If the charge transfer energy  $\Delta < U_{dd}$  the gap is determined by the charge transfer energy and the width of the ligand band; this is the case predicted for  $\text{NiO}$ [8,21,22]. The presence of holes induced by doping with acceptors or non-stoichiometry have also been addressed[19,22].

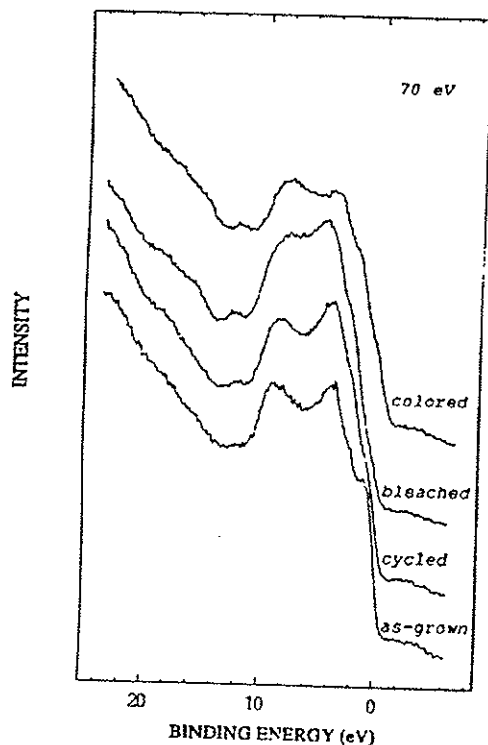


Figure 8. UPS data for the 235 sample at different coloration state, measured with an incident photon energy  $h\nu = 70$  eV.

The electronic properties of electrochromic nickel oxide thin films were also analyzed in previous works[2,3,11], whose common conclusion is the existence of nickel vacancies in the material giving rise to a p-type semiconductor. The observed extra energy levels are compatible with the compound  $\text{Ni}_3\text{O}_4$  [11]. Another in-

teresting finding, not well understood, is the insensitivity of the Ni 2p core levels to the coloration/bleaching process, while the O 2s levels are modified[2]. Another observation is the appearance of an indirect band gap transition, that is affected by the intercalation process, but not in an extent to justify the huge optical changes observed during the electrochemical/electrochromic process. On the other hand, the direct band gap is almost insensitive to the same process[3]. This type of correlation between optical and electronic behavior is reasonable if a charge transfer mechanism through impurity levels separated by small energy gaps is assumed. Dielectric characterization of similar films also points towards this qualitative analysis of electrochromic  $\text{NiO}_x$  band structure[23].

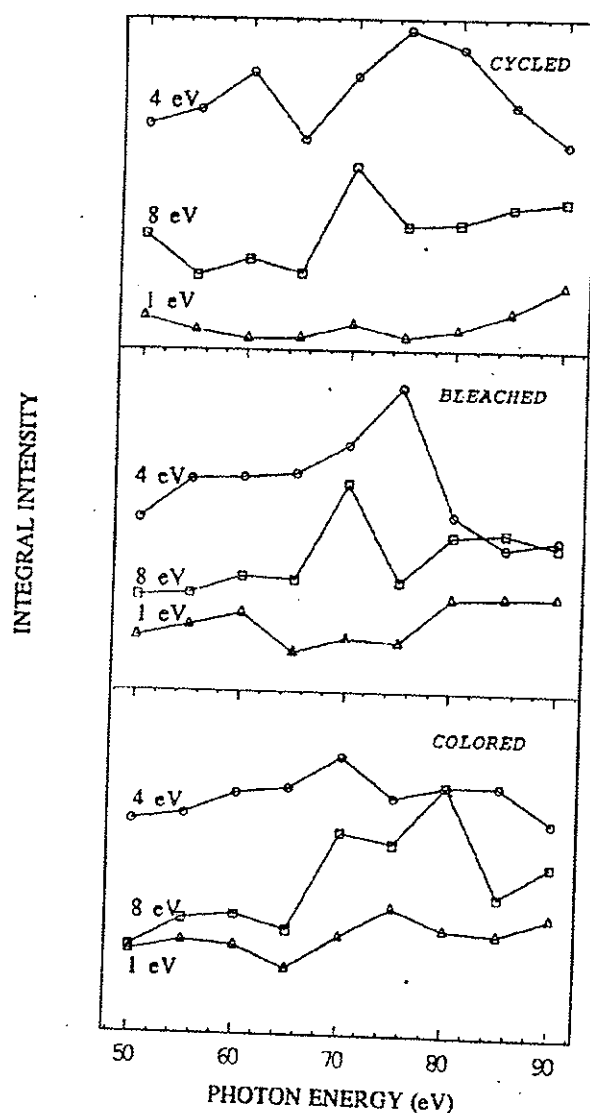


Figure 9. Integral intensity of the three valence band structures as a function of the incident photon energy.

The valence band spectra obtained at the various incident photon energies (Fig. 6) clearly demonstrate the resonance effect promoted by the Ni 3p electrons. The quantitative analysis of this effect is shown in Fig. 9, where it is observed an increase in the integral intensity for  $h\nu > 65$  eV, not only in the peaks assigned to Ni 3d levels, but also in those related to O 2p and adsorbed  $\text{OH}^-$ . The band feature at around 1 eV, associated to Ni 3d levels, showed a larger resonance effect in the colored film. We expect a stronger influence of the nickel in the spectra of dark  $\text{NiO}_x$ , due to de-intercalation of species that are responsible for charge compensation at the nickel vacancies and changes in the electron and hole conductivity. The most interesting findings of the UPS measurements appear comparing the results obtained for the sample at different coloration states (Fig. 8 and Table IV). Since the as-grown film is opaque and the cycled sample is much more transparent (cycled, stopping at the bleached state), we would expect similarities in the valence band of cycled and bleached samples, as well as in the as-grown and colored ones. Nevertheless, the valence band features of as-grown and cycled films are in some extent similar, since there is a well defined valley between the peaks centered around 4 eV and 8 eV. On the other hand, the samples after electrochemical processing (bleached and colored) present a more smeared band structure, that can be related to freshly adsorbed species on the surface. In fact, the small band observed at around 12 eV in the electrochemical treated films can be associated to  $\text{OH}^-$  [10]. The energy of the peak centered around 8 eV is equal for the cycled and bleached films and very similar for the other two samples. Moreover, the larger relative intensity of the structure at 8 eV, observed by in the bleached film, is consistent with the fact that it is associated to the  $\text{OH}^-$  radicals, which are expected to be present in a larger concentration in the bleached film, than in the colored one [15]. The decrease in the intensity contribution of the structure around 4 eV, related to Ni 3d and O 2p levels, can also be explained by the adsorption of species during electrochemical processing. The relative intensity of the peak associated to Ni 3d levels ( $\sim 1$  eV) is higher for the film in the as-grown state when compared to the cycled one. This result

can be explained by a decrease in the number of holes originated by nickel vacancies, caused by electrochemical charge compensation in the bleached state. The comparison between bleached and colored films spectra reveals the existence of levels crossing the Fermi energy, forming a type of conduction band in the colored film. In this case the formation of many levels inside the gap, separated by small charge transfer energies, can explain the modification in optical and electronic properties of  $\text{NiO}_x$  electrochromic material in the bleached and colored states. This band model is consistent with a charge transfer mechanism of hopping carriers across impurity levels and is also compatible with previous experimental data [3,23].

## V. Conclusion

Differences in electrochemical/electrochromic performance and structural properties of  $\text{NiO}_x$  films originated from the variation of oxygen flux during the reactive rf sputtering growth process were analyzed. There is a limitation to deposit  $\text{NiO}_x$  electrochromic thin films: for  $f < 0.5$  sccm the deposited material is nickel.  $\text{NiO}_x$  films were obtained for higher oxygen flux ( $f > 1.0$  sccm). The deposition rate is dependent on the oxygen flux, being higher for the smaller values of  $f$ . The transmittance span of the films after a number of galvanostatic steps is the same, regardless differences in the structural and optical properties of the as-grown films, but electrochemical stable films only can be achieved for higher flux of oxygen ( $f > 2$  sccm). The valence band structure modifications observed for the films at different coloration states points to a model of charge transfer mechanism created and destroyed by narrow impurity levels.

## Acknowledgments

We thank Mr. A. Lourenço for sample preparation and to Ms. P. S. P. Cardona and Mr. F. F. Ferreira for help in the XRD measurements.

## References

1. *Large Area Chromogenics: Materials and Devices for Transmittance Control*, edited by C. M. Lampert and C.G. Granqvist, (SPIE Proceedings Series, Bellingham, 1991).

2. A. M. Anderson, W. Estrada, C. G. Granqvist, A. Gorenstein and F. Decker, in *Optical Material Technology for Energy Efficiency and Solar Energy Conversion IX*, edited by C. M. Lampert and C. G. Granqvist, (SPIE Proceedings Series, Bellingham, 1990) vol. 1272, p. 96.
3. M. C. A. Fantini, A. Gorenstein, W. M. Shen and M. Tomkiewicz, in *Optical Materials Technology for Energy Efficiency and Solar Energy Conversion XI*, edited by A. Hugot-Le Goff, C. M. Lampert and C.G. Granqvist, (SPIE Proceedings Series, Bellingham, 1992), vol.1728, p. 41.
4. "Preliminary Performance and Experiments from the High-Resolution Plane-Grating Monochromator at CAMD" Z. Qu, K. Subramanian, N. Mainkar, R. Kurtz, R. Stockbauer, A. Mihill and V. Saile, Nucl. Instrum. and Methods in Phys. Res. A (in press).
5. R. L. Kurtz, S. W. Robey, L. T. Hudson, R. V. Smigly, and R. L. Stockbauer, Nucl. Instrum. Methods A319, 257 (1992).
6. H. P. Klug and L. E. Alexander, in *X-Ray Diffraction Procedures for Polycrystalline and Amorphous Materials* (Wiley, New York, 1974), 2nd. edition.
7. M. R. Thuler, R. L. Benbow and Z. Hurych, Phys. Rev. B 27, 2082 (1983).
8. G. A. Sawatzky and J. W. Allen, Phys. Rev. Lett. 53, 2339 (1984).
9. J. M. McKay and V. E. Henrich, Phys. Rev. Lett. 53, 2343 (1984).
10. J. M. McKay and V. E. Henrich, Phys. Rev. B 32, 6764 (1985).
11. K. M. E. Miedzinska, B. R. Hollebone and J. G. Cook, J. Phys. Chem. Sol., 49, 1355 (1988).
12. R. Newman and R.M. Chrenko, Phys. Rev., 114, 1507 (1959).
13. J. V. Martins, M. H. Tabacniks, M. C. A. Fantini and A. Gorenstein, Proc. Intern. Workshop on Surf. Eng., Rio de Janeiro (1993), p.42.
14. I. C. Faria, R. M. Torresi and A. Gorenstein, Electrochimica Acta, 38, 2765 (1993).
15. M. C. A. Fantini, I. C. Faria, R. M. Torresi and A. Gorenstein, Proc. 184th Meeting of the Electrochem. Soc., New Orleans, (1993), p. 131.
16. D. Adler and J. Feinleib, Phys. Rev. B 2, 3112 (1970).
17. W. Estrada, M. C. A. Fantini, S. C. Castro, C. M. P. Fonseca and A. Gorenstein, J. Appl. Phys. 74, 5835 (1993).
18. J. L. McNatt, Phys. Rev. Lett. 23, 915 (1969).
19. J. van Elp, H. Eskes, P. Kuiper and G. A. Sawatzky, Phys. Rev. B 45, 1612 (1992).
20. M. D. Reichtin and B. L. Averbach, J. Phys. Chem. Solids 36, 893 (1975).
21. J. Zaanen, G. A. Sawatzky and J. W. Allen, Phys. Rev. Lett. 55, 418 (1985).
22. P. Kuiper, Phd Thesis, Rijks-Universiteit, Groningen, (1990).
23. T. M. J. Nilsson and G. A. Niklasson, in *Optical Materials Technology for Energy Efficiency and Solar Energy Conversion IX*, edited by C. M. Lampert and C. G. Granqvist, (SPIE Proceedings Series, Bellingham, 1990), vol. 1272, p. 129.

ON THE STRUCTURAL PROPERTIES OF ELECTROCHROMIC  $\text{NiO}_x$   
SPUTTERED THIN FILMS

M.C.A. Fantini

Instituto de Física, USP, CP 66318, 05389-970 São Paulo (SP) Brazil

I.C. Faria, R.M. Torresi and A. Gorenstein

Instituto de Física, UNICAMP, CP 6165, 13084-100 Campinas (SP) Brazil

ABSTRACT

The structural properties of rf-sputtered electrochromic  $\text{NiO}_x$  thin films were investigated by X-Ray Diffraction (XRD). The degree of crystallinity, the preferred crystalline orientation and the lattice parameters were analyzed for samples deposited at different conditions and at the bleached and colored states. Aqueous electrolytes containing LiOH, NaOH, KOH, RbOH or CsOH were used. The XRD results were correlated to changes in stress and mass induced by the electrochemical process. The degree of crystallinity determine the stress in the film, being larger for a less crystalline network. The experimental results indicate the participation of the alkaline ion in the electrochromic reaction and a mechanism of ionic intercalation/de-intercalation process that involves the bulk of the crystallites as well as the grain boundaries.

## INTRODUCTION

Anhydrous and hydrous nickel oxide (or oxy-hydroxide) thin films, deposited by different techniques, are well known electrochromic materials [1-3]. Nickel oxide ( $\text{NiO}_x$ ) is considered a good candidate in technologies employing electrochromics, since it is an anodic coloring material, optically and electrochemically compatible with the well known tungsten trioxide. The desirable film characteristics for a large range of devices include a short response time ( $< 100$  ms), large optical density variation ( $> 50\%$ ), memory effect and long durability ( $10^5 - 10^7$  cycles) [3]. The operation of devices based on the switchable optical properties of electrochromics depends on ion transport, which limits the response time to the milliseconds range. Nevertheless, for many practical purposes, like the so-called "smart windows", a very fast response time is not essential. Electrochromic efficiencies between 20 and  $30 \text{ cm}^2\text{C}^{-1}$  are easily attained for  $\text{NiO}_x$ , independent on the technique employed to produce the films. On the other hand, the achievement of large area, uniform and stable films, with long lifetime, is not a straightforward task, becoming the crucial technological issue to be addressed. Among the various deposition methods, those employing chemical [4,5] and electrochemical [5-13] techniques give rise to hydrous and porous films with fast response times (20 ms [1]) and with noticeable electrochromic efficiencies ( $50 \text{ cm}^2\text{C}^{-1}$  [7]). However, films grown by these methods are not very uniform nor stable [6], showing degradation effects in the best cases at around  $10^3$  coloring/bleaching cycles [11,12]. Many experimental procedures have been proposed to improve the durability

of these less expensive and easily deposited thin films, including heat treatments [9], alloying [10], non-aqueous electrolytes [12] and other deposition strategies [5,11,13]; however, it seems a common sense among specialists that these films are not suitable for practical applications, being necessary the development of other commercially compatible deposition methods to produce durable electrochromic nickel oxide films. Among these methods, those employing vacuum technology, as e-beam evaporation [14-18] and dc or rf sputtering [19-28] provide films with high stability ( $\sim 10^5$  cycles) good electrochromic efficiency ( $\sim 35 \text{ cm}^2\text{C}^{-1}$ ) and response time as fast as 500 ms. Prototypes of devices using nickel oxide as optically active material are reported in the literature [29,30].

During the past ten years the research on electrochromic  $\text{NiO}_x$  has provided an useful amount of knowledge, but there are still scientific and technological issues to be solved, or that are hardly understood. For instance, the understanding of the mechanisms responsible for the electrochromic behavior in this material depends on the information about the intercalation reaction and the nature of the intercalating ions, as well as the dependence of the electrochromic performance on the morphology, structure and stoichiometry of the deposited films. The aim of this paper was to determine, by means of X-Ray Diffraction (XRD), lattice parameters variations of rf-sputtered  $\text{NiO}_x$  thin films, caused by bleaching and coloring in different alkaline aqueous electrolyte, in order to determine the dependence of the lattice parameters on the electrolyte constituents.

material is in the colored state, as it would be expected if the oxidation reaction is a deintercalation process. Figure 2 shows the stress changes  $\Delta\sigma$  as a function of charge density in different electrolytes, in the anodic (coloring) cycle. For all electrolytes, there is a tensile stress, corresponding to a global volume decrease of the film. In the cathodic cycle (not shown) the reverse behavior is observed. The stress changes depend on the electrolyte.  $\Delta\sigma$  changes linearly with inserted/extracted charge, and attain maximum values. The slope  $\Delta\sigma/\Delta Q$  is similar for the LiOH, RbOH and CsOH and greater than those observed for the NaOH and KOH electrolytes. Figure 3 shows the mass changes as a function of charge density (anodic cycle) for this series of samples in LiOH, NaOH, KOH, RbOH, and CsOH electrolytes. The data were obtained with the quartz microbalance (EQCM). There is a mass increase in the anodic cycle, in the potential region of the main electrochemical processes. Again, the mass changes are different in different electrolytes. The mass variation is minimum for the LiOH electrolyte and maximum for the CsOH electrolyte, with intermediate values for the other electrolytes.

The polycrystalline series of samples, named N, were produced to determine more precisely the variation in the lattice parameters, when the films are cycled in different electrolytes. Figure 4 shows the XRD data obtained for the (111) reflection of the N series of samples, in the bleached and colored states. Table II presents the lattice parameters, as well as the volume variation between bleached and colored states. Figure 5 depicts the stress results. Again,  $\Delta\sigma$  as a function of charge density shows a tensile stress in the anodic cycle. The stress changes also depend on the electrolyte, as



material is in the colored state, as it would be expected if the oxidation reaction is a deintercalation process. Figure 2 shows the stress changes  $\Delta\sigma$  as a function of charge density in different electrolytes, in the anodic (coloring) cycle. For all electrolytes, there is a tensile stress, corresponding to a global volume decrease of the film. In the cathodic cycle (not shown) the reverse behavior is observed. The stress changes depend on the electrolyte.  $\Delta\sigma$  changes linearly with inserted/extracted charge, and attain maximum values. The slope  $\Delta\sigma/\Delta Q$  is similar for the LiOH, RbOH and CsOH and greater than those observed for the NaOH and KOH electrolytes. Figure 3 shows the mass changes as a function of charge density (anodic cycle) for this series of samples in LiOH, NaOH, KOH, RbOH, and CsOH electrolytes. The data were obtained with the quartz microbalance (EQCM). There is a mass increase in the anodic cycle, in the potential region of the main electrochemical processes. Again, the mass changes are different in different electrolytes. The mass variation is minimum for the LiOH electrolyte and maximum for the CsOH electrolyte, with intermediate values for the other electrolytes.

The polycrystalline series of samples, named N, were produced to determine more precisely the variation in the lattice parameters, when the films are cycled in different electrolytes. Figure 4 shows the XRD data obtained for the (111) reflection of the N series of samples, in the bleached and colored states. Table II presents the lattice parameters, as well as the volume variation between bleached and colored states. Figure 5 depicts the stress results. Again,  $\Delta\sigma$  as a function of charge density shows a tensile stress in the anodic cycle. The stress changes also depend on the electrolyte, as

transport along the film, but the ion exchange reaction takes place from the boundaries to the bulk of the crystallites, being governed by the availability of defects, or stoichiometry, as well as by the preferred crystalline orientation, or the proper pathway of open ionic channels.

Among the characterization procedures, XRD is a very simple, useful and non destructive tool, either to explore the thin films structural features or to follow modifications in composition and structure caused by the reversible intercalation process [38]. The idea to use XRD to look for lattice parameter modifications caused by cycling identical samples in different electrolytes was based on the hypothesis that also the alkaline cations, besides  $H^+$ , may reversibly enter and leave the crystal network. This hypothesis was supported by previous findings that point to the participation of other ions, like the alkaline and  $OH^-$  ions, in the electrochromic/electrochemical reaction [5,17,18,39,40].

In order to discuss the structural properties of non-stoichiometric  $NiO_x$ , it is necessary to present the crystal structures assigned to  $NiO$ .

Nickel oxide crystallizes in a rhombohedral, or hexagonal, structure (space group  $R\bar{3}m$ ) for temperatures below the Néel temperature of  $(253 \pm 3)^\circ C$  [41-43]. The lattice parameters are  $a=2.954 \text{ \AA}$  and  $c=7.236 \text{ \AA}$ . The nickel atoms are located at the (0,0,0) position and oxygen at (0,0,0.5). The  $+(2/3 \ 1/3 \ 1/3, 1/3 \ 2/3 \ 2/3)$  positions for both atoms are also allowed [44,45]. The atoms in the hexagonal packing are more concentrated close to the a-b plane and to the crystal faces, leaving open channels in the

transport along the film, but the ion exchange reaction takes place from the boundaries to the bulk of the crystallites, being governed by the availability of defects, or stoichiometry, as well as by the preferred crystalline orientation, or the proper pathway of open ionic channels.

Among the characterization procedures, XRD is a very simple, useful and non destructive tool, either to explore the thin films structural features or to follow modifications in composition and structure caused by the reversible intercalation process [38]. The idea to use XRD to look for lattice parameter modifications caused by cycling identical samples in different electrolytes was based on the hypothesis that also the alkaline cations, besides  $H^+$ , may reversibly enter and leave the crystal network. This hypothesis was supported by previous findings that point to the participation of other ions, like the alkaline and  $OH^-$  ions, in the electrochromic/electrochemical reaction [5,17,18,39,40].

In order to discuss the structural properties of non-stoichiometric  $NiO_x$ , it is necessary to present the crystal structures assigned to  $NiO$ .

Nickel oxide crystallizes in a rhombohedral, or hexagonal, structure (space group  $R\bar{3}m$ ) for temperatures below the Néel temperature of  $(253 \pm 3)^\circ C$  [41-43]. The lattice parameters are  $a=2.954 \text{ \AA}$  and  $c=7.236 \text{ \AA}$ . The nickel atoms are located at the (0,0,0) position and oxygen at (0,0,0.5). The  $+(2/3 \ 1/3 \ 1/3, 1/3 \ 2/3 \ 2/3)$  positions for both atoms are also allowed [44,45]. The atoms in the hexagonal packing are more concentrated close to the a-b plane and to the crystal faces, leaving open channels in the

the crystallite sizes of our non-stoichiometric  $\text{NiO}_x$  samples are too small, with a consequent broadening of the diffraction peaks, preventing the observation of some peak splitting, characteristic of the hexagonal structure.

It is important to mention that the structure of Ni-deficient  $\text{NiO}$ ,  $\text{NiO}_x$  with  $x > 1$ , is of spinel type and attributed to the compound  $\text{Ni}_{15}\text{O}_{16}$ , *i.e.*,  $x = 1.067$  [48]. The Rutherford Back-Scattering (RBS) analysis of our films, deposited at room temperature,  $P_t = 7 \times 10^{-3}$  mbar,  $f = 2$  sccm and  $P_{rf} = 100$  W provide  $x = 1.07 \pm 0.02$ ; nevertheless, the use of the spinel structure to describe our films structural properties is an unnecessary complication.

The results described in the previous section clearly pointed out an intercalation reaction, since both volume (stress and XRD data), and mass changes (EQCM) were observed. In particular, the XRD results demonstrate that the intercalation of ions in the electrochromic film is a bulk type phenomenon. The mechanical stress and mass changes were extensively discussed in a previous paper [40], being discarded the  $\text{OH}^-$  incorporation as the main process to explain the results obtained in different alkaline electrolytes. The results indicate that the proton deintercalation process occurs simultaneously with cation intercalation in the coloring cycle. Considering the ionic radius of the different alkaline cations and the possibility of hydration, the stress and mass data are concordant. However, the observed volume changes are a consequence of lattice parameter variations, that can be different in the various electrolytes, and

the crystallite sizes of our non-stoichiometric  $\text{NiO}_x$  samples are too small, with a consequent broadening of the diffraction peaks, preventing the observation of some peak splitting, characteristic of the hexagonal structure.

It is important to mention that the structure of Ni-deficient  $\text{NiO}$ ,  $\text{NiO}_x$  with  $x > 1$ , is of spinel type and attributed to the compound  $\text{Ni}_{15}\text{O}_{16}$ , *i.e.*,  $x = 1.067$  [48]. The Rutherford Back-Scattering (RBS) analysis of our films, deposited at room temperature,  $P_t = 7 \times 10^{-3}$  mbar,  $f = 2$  sccm and  $P_{rf} = 100$  W provide  $x = 1.07 \pm 0.02$ ; nevertheless, the use of the spinel structure to describe our films structural properties is an unnecessary complication.

The results described in the previous section clearly pointed out an intercalation reaction, since both volume (stress and XRD data), and mass changes (EQCM) were observed. In particular, the XRD results demonstrate that the intercalation of ions in the electrochromic film is a bulk type phenomenon. The mechanical stress and mass changes were extensively discussed in a previous paper [40], being discarded the  $\text{OH}^-$  incorporation as the main process to explain the results obtained in different alkaline electrolytes. The results indicate that the proton deintercalation process occurs simultaneously with cation intercalation in the coloring cycle. Considering the ionic radius of the different alkaline cations and the possibility of hydration, the stress and mass data are concordant. However, the observed volume changes are a consequence of lattice parameter variations, that can be different in the various electrolytes, and

should depend on the degree of crystallinity and surface crystallographic orientation of the films.

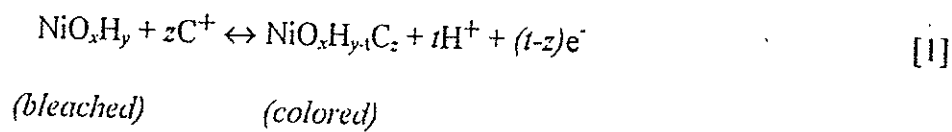
Due to the poor crystallinity of the samples named M, the XRD results (Fig. 1 and Table I) are difficult to be analyzed. The unit cell volume decreases upon coloring in both analyzed electrolytes, being consistent with the stress data. However, the volume change between bleached and colored states in the different electrolytes are similar and within the experimental error. The EQCM data (Fig. 3) show a global mass increase in the anodic cycle and different mass/charge ratios for the various electrolytes.

The same consistency between unit cell volume variation ( $\Delta V$ ) and stress data ( $\Delta\sigma$ ) is also observed for sample named N (Figs. 4, 5 and Table II), in different electrolytes. Moreover, the quantitative analysis of the obtained  $\Delta V$  values clearly show a smaller variation the Li-based electrolyte when compared to larger values obtained for the other electrolytes, which agrees with the  $\Delta\sigma$  data.

The stress data of these two series of samples (M and N) display larger  $\Delta\sigma$  values for the less crystalline film (M-series). Therefore, the degree of crystallinity affect the stress in the films, being desirable to grow more crystalline films to attain smaller changes in volume during cycling, since large stress variations could be deleterious to devices durability. More  $\text{Li}^+$  ions are exchanged than  $\text{K}^+$  [40], but as  $\text{Li}^+$  is lighter than  $\text{K}^+$ , smaller mass variation is observed in the former case (Fig. 3). In principle, the intercalation process supports the idea of atoms in substitutional or interstitial atomic positions. The size of  $\text{Li}^+$  ion, 0.68 Å, is the order of  $\text{Ni}^{2+}$  ionic radius

(0.70 Å), and consequently  $\text{Li}^+$  can replace Ni vacancies in substitutional positions with slight changes in the unit cell volume. This reasoning can be the explanation for the small variation in the stress of the M-sample cycled in the LiOH electrolyte, when compared to the others. On the other hand, important changes in lattice parameters are expected for the heavier and bigger ions, either in substitutional or interstitial positions, but since less ions are exchanged, the stress does not increase proportionally with the atomic number of the alkaline ion. However, it is impossible with the present data to distinguish among the two possibilities of ion intercalation sites inside the crystallites, or even to rule out the presence of ions at the grain boundaries.

In conclusion, the XRD experimental results indicate, together with the stress and EQCM data, that the alkaline ion participates in the electrochromic reaction. Due to the mass increase upon coloring, the alkaline ion (C) enters the crystal lattice, while hydrogen leaves it, according to the proposed exchange process:



## CONCLUSIONS

The XRD results showed that the intercalation process takes place in the bulk of the crystallites and is responsible for lattice parameter variations between bleached and colored states of the electrochromic material. The degree of crystallinity can explain the differences observed in the stress data, showing the influence of the grain boundaries at

## REFERENCES

1. C.M. Lampert, *Solar Energy Mater.*, 11, (1984), 1.
2. A. Donnadiou, *Mater. Sci. Eng.*, B, (1989), 185.
3. S.K. Deb, *Solar Energy Mater. and Solar Cells*, 25, (1992), 327.
4. A. Gorenstein, F. Decker, M. Fantini and W. Estrada in 'Large Area Chromogenics: Materials and Devices for Transmittance Control', C.M. Lampert and C.G. Granqvist, Editors, SPIE Publ., Bellingham, WA, U.S.A., (1991), 71.
5. Z.C. Orel, M.G. Hutchins and G. Mc Meeking, *Solar Energy Mater. and Solar Cells*, 30, (1993), 327.
6. C.M. Lampert, T.R. Omstead and P.C. Yu, *Solar Energy Mater.*, 14, (1986), 161.
7. M.K. Carpenter, R.S. Connell and D.A. Corrigan, *Solar Energy Mater.*, 16, (1987), 333.
8. M. Fantini and A. Gorenstein, *Solar Energy Mater.*, 16, (1987), 487.
9. S. Morisaki, K. Kawakami and N. Baba, *Jpn. J. Appl. Phys.*, 27, (1988), 314.
10. D.A. Corrigan and M. K. Carpenter in 'Large Area Chromogenics: Materials and Devices for Transmittance Control', C.M. Lampert and C.G. Granqvist, Editors, SPIE Publ., Bellingham, WA, U.S.A., (1991), 299.
11. J. Joseph, H. Gomathi and G.P. Rao, *Solar Energy Mater.*, 23, (1991), 1.
12. D.A. Corrigan, *Solar Energy Mater. and Solar Cells*, 25, (1992), 293.
13. M. Chigane and M. Ishikawa, *J. Chem. Soc. Faraday Trans.*, 88, (1992), 2203.



14. P. Delichère, S. Joiret, A. Hugot-Le-Goff, K. Bange and B. Hetz, *J. Electrochem. Soc.*, 135, (1988), 1856.
15. C.R. Otterman, A. Temmink and K. Bange, *Thin Solid Films*, 193/194, (1990), 409.
16. T. Seike and J. Nagai, *Solar Energy Mater.*, 22, (1991), 107.
17. S.I. Cordoba -Torresi, C. Gabrielli, A. Hugot-Le Goff and R. Torresi, *J. Eletrochem. Soc.*, 138, (1991), 1548.
18. A. Nemetz, A. Temmink, K. Bange, S.I. Cordoba -Torresi, C. Gabrielli, R. Torresi and A. Hugot-Le-Goff, *Solar Energy Mater.*, 25, (1992), 93.
19. J. S. E. M. Svensson and C.G. Granqvist, *Appl. Phys. Lett.*, 49, (1986), 1566.
20. S. Yamada, T. Yoshioka, M. Miyashita, K. Urabe and M. Kitao, *J. Appl. Phys.*, 63, (1988), 2116.
21. W. Estrada, A.M. Andersson and C.G. Granqvist, *J. Appl. Phys.*, 64, (1988), 3678.
22. A. Gorenstein, F. Decker, W. Estrada, C. Esteves, A. Andersson, S. Passerini, S. Pantaloni and B. Scrosati, *J. Electroanal. Chem.*, 277, (1990), 277.
23. D.A. Wruck, A.M. Dixon, M. Rubin and S.N. Bogy, *J. Vac. Sci. Technol.*, 19, (1991), 2170.
24. G. Campet, B. Morel, M. Bourrel, J.M. Chabagno, D. Ferry, R. Garie, C. Quest, C. Geoffroy, J.J. Videau, J. Portier, C. Delmas and J. Salardenne, *Mater. Sci. Eng.*, B, (1991), 303.
25. F. Decker, R. Pileggi, S. Passerini and B. Scrosati, *J. Electrochem. Soc.*, 138, (1991), 3182.

26. R.S. Conell, D.A. Corrigan and B.R. Powell, *Solar Energy Mater. and Solar Cells*, 25, (1992), 301.
27. J. Scarminio, W. Estrada, A. Andersson, A. Gorenstein and F. Decker, *J. Electrochem. Soc.*, 139, (1992), 1236.
28. D.A. Wruck and M. Rubin, *J. Electrochem. Soc.*, 140, (1993), 1097.
29. C.G. Granqvist, *Thin Solid Films*, 193/194, (1990), 730.
30. C.G. Granqvist, *Solid State Ionics*, 53-56, (1992), 479.
31. J. Scarminio, A. Gorenstein, F. Decker, S. Passerini, R. Pillegi and B. Scrosati, *SPIE Proc. Series*, 1536, (1991), 70.
32. C. Gabrielli, M. Keddad and R.M. Torresi, *J. Electrochem. Soc.*, 138, (1991), 2657.
33. G. Sauerbrey, *Z. Phys.*, 144, (1955), 206.
34. C.A. Melendres, W. Paden, B. Tani and W. Walczak, *J. Electrochem. Soc.*, 134, (1986), 762.
35. D.A. Corrigan and S.L. Knight, *J. Electrochem. Soc.*, 136, (1989), 613.
36. J.S.E.M. Svensson and C.G. Granqvist in 'Large Area Chromogenics: Materials and Devices for Transmittance Control', C.M. Lampert and C.G. Granqvist, Editors, SPIE Publ., Bellingham, WA, U.S.A., (1991), 285.
37. A. Agrawal, H.R. Habibi, R.K. Agrawal, J.P. Cronin, D.M. Roberts, R.S. Caron-Popowich and C.M. Lampert, *Thin Solid Films*, 221, (1992), 239.
38. W. Estrada, M.C.A. Fantini, S.C. Castro, C.M.P. Fonseca and A. Gorenstein, *J. Appl. Phys.*, 74, (1993), 5835.

39. R. Barnard, C.F. Randell and F.L. Tye, *J. Appl. Electrochem.*, 11, (1991), 517.
40. I.C. Faria, R.M. Torresi and A. Gorenstein, *Electrochimica Acta*, 38, (1993), 2765.
41. H.P. Rooksby, *Nature*, 152, (1943), 304.
42. H.P. Rooksby, *Acta Cryst.*, 1, (1948), 226.
43. N.C. Tombs and H.P. Rooksby, *Nature*, 165, (1950), 442.
44. Powder Diffraction Files, Joint Committee of Powder Diffraction Standards (J.C.P.D.S.) of the International Center for Diffraction Data, Swarthmore, PA, U.S.A. (1992).
45. International Tables for X-Ray Crystallography, Vol. I, N.F. Henry and K. Lonsdale, Editors, Kynoch Press, Birmingham, U.K. (1969).
46. D. Adler and J. Feinleib, *Phys. Rev. B*(2), (1970), 3112.
47. J.B. Goodenough, *Prog. Sol. St. Chem*, 5, (1971), 145.
48. K. Katada, K. Nakahigashi and Y. Shimomura, *Jpn. J. Appl. Phys.*, 9, (1970), 1019.

TABLE I

Lattice Parameter (a) and unit cell volume (V) of the M series of samples

Sample	a (Å)	V (Å <sup>3</sup> )
M-a	4.2181±0.0034	75.05±0.18
M-b (KOH)	4.2235±0.0010	75.34±0.005
M-c (KOH)	4.2037±0.0028	74.28±0.15 (1.06)
M-b (LiOH)	4.2194±0.0036	75.12±0.19
M-c (LiOH)	4.2031±0.0073	74.25±0.39 (0.87)

Numbers in parenthesis are the volume difference between bleached and colored states.

a: as-grown/ b: bleached/ c: colored

TABLE II

Lattice Parameter (a) and unit cell volume (V) of the N series of samples

Sample	a (Å)	V (Å <sup>3</sup> )
N-a	4.2223±0.0037	75.27±0.20
N-b (LiOH)	4.2221±0.0028	75.26±0.15
N-c (LiOH)	4.2133±0.0076	74.79±0.40 (0.47)
N-b (NaOH)	4.2331±0.0049	75.85±0.26
N-c (NaOH)	4.2177±0.0050	75.03±0.27 (0.82)
N-b (KOH)	4.2353±0.0057	75.97±0.31
N-c (KOH)	4.2208±0.0065	75.19±0.35 (0.79)
N-b (CsOH)	4.2316±0.0053	75.77±0.29
N-c (CsOH)	4.2174±0.0099	75.01±0.53 (0.76)

Numbers in parenthesis are the volume difference between bleached and colored states.

a: as-grown/ b: bleached/ c: colored

## FIGURE CAPTIONS

Figure 1 - X-ray diffractograms obtained for two as-grown samples, named M and N, deposited on ITO/thick glass, using Cu K $\alpha$  radiation ( $\lambda = 1.5418 \text{ \AA}$ ).

Figure 2 - Stress changes in the anodic cycle for different electrolytes of the M-series of samples, deposited on ITO/thin flexible glass.

Figure 3 - Mass variation in the anodic cycle for different electrolytes of the M-series of samples deposited on Au/Cr/quartz crystal.

Figure 4 - X-ray diffractograms obtained for the N samples, deposited on ITO/thin flexible glass and galvanostatically bleached/colored in different electrolytes ( $\lambda = 1.5418 \text{ \AA}$ ).

Figure 5 - Stress changes in the anodic cycle for different electrolytes of the N-series of samples, deposited on ITO/thin flexible glass.

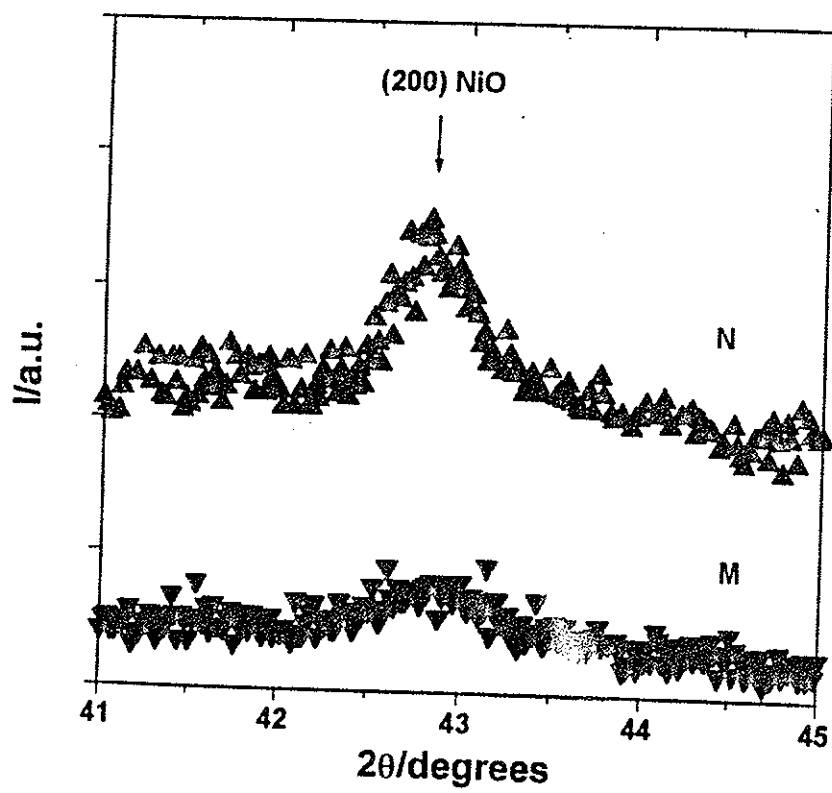
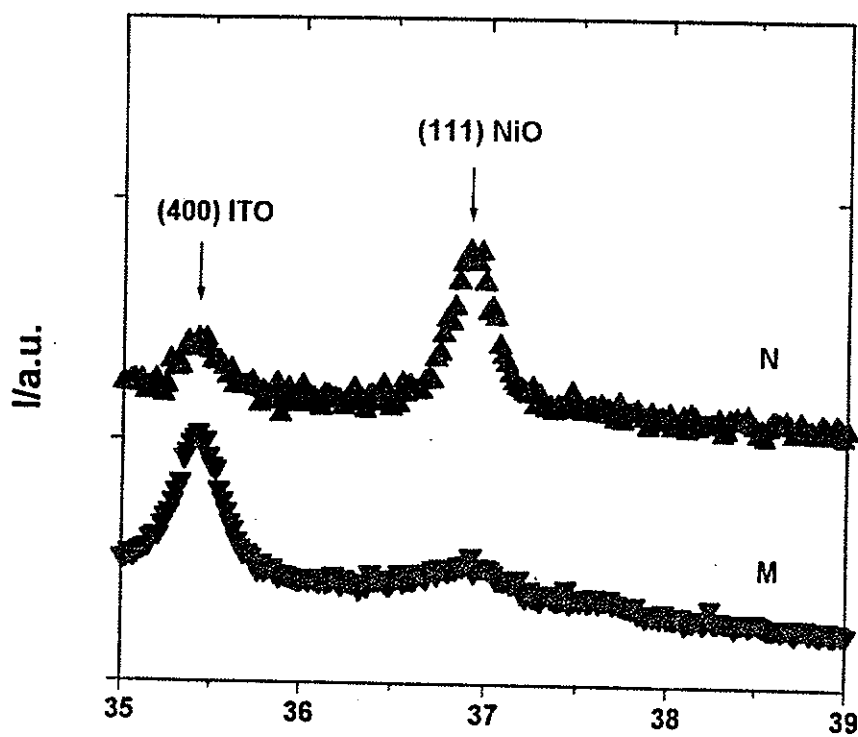


Fig. 2

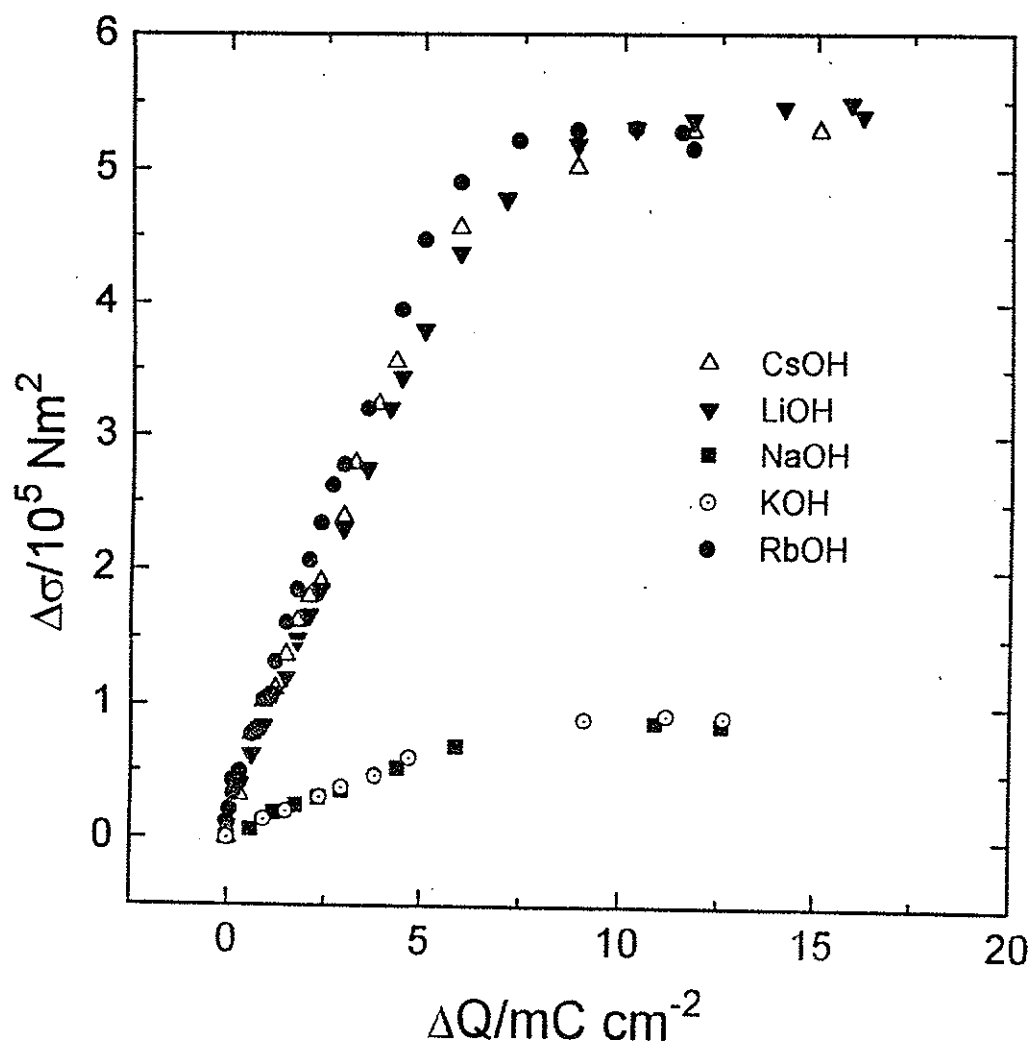
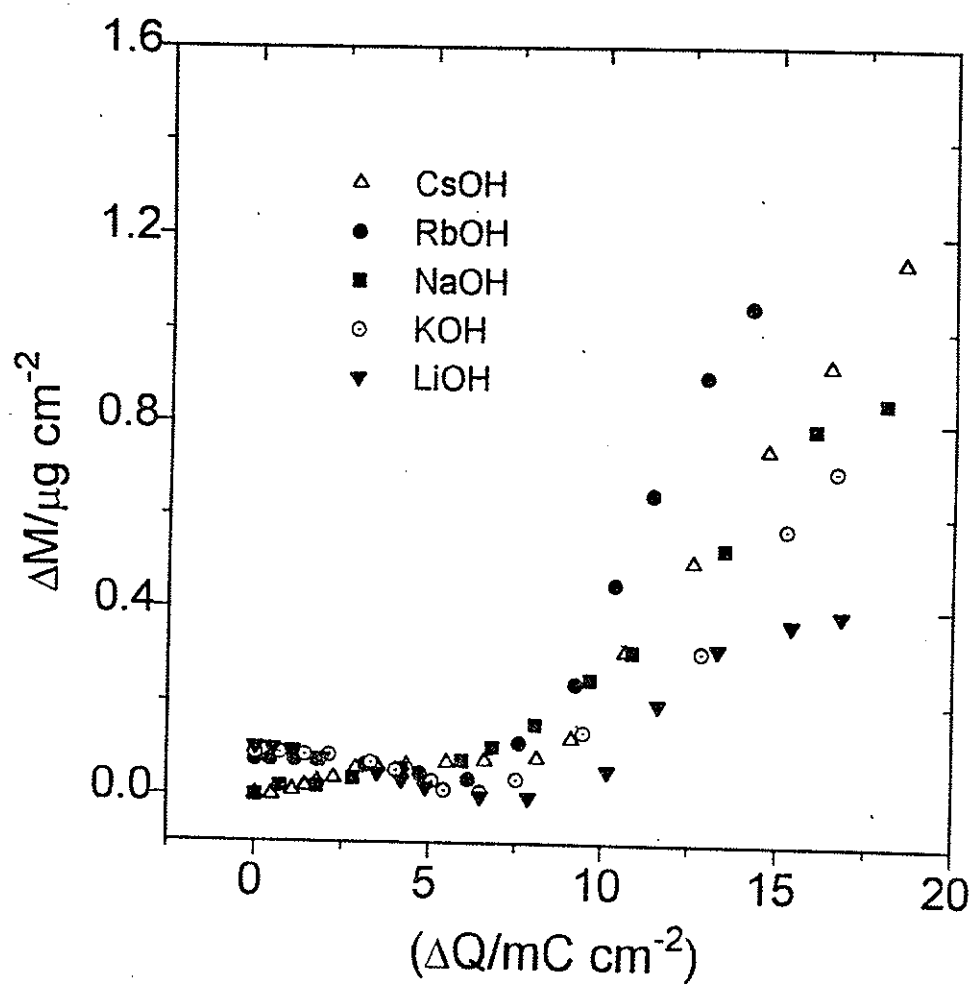
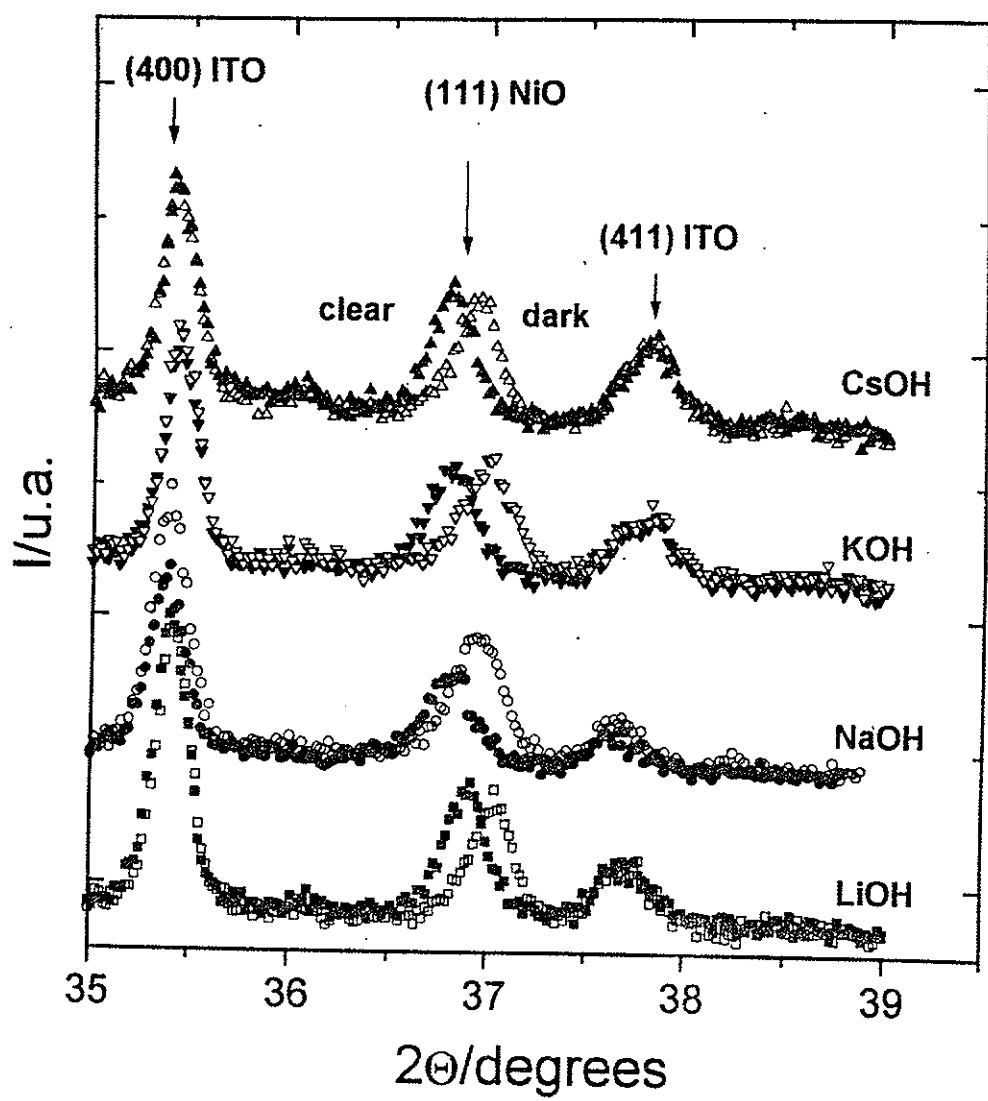


Fig. 1







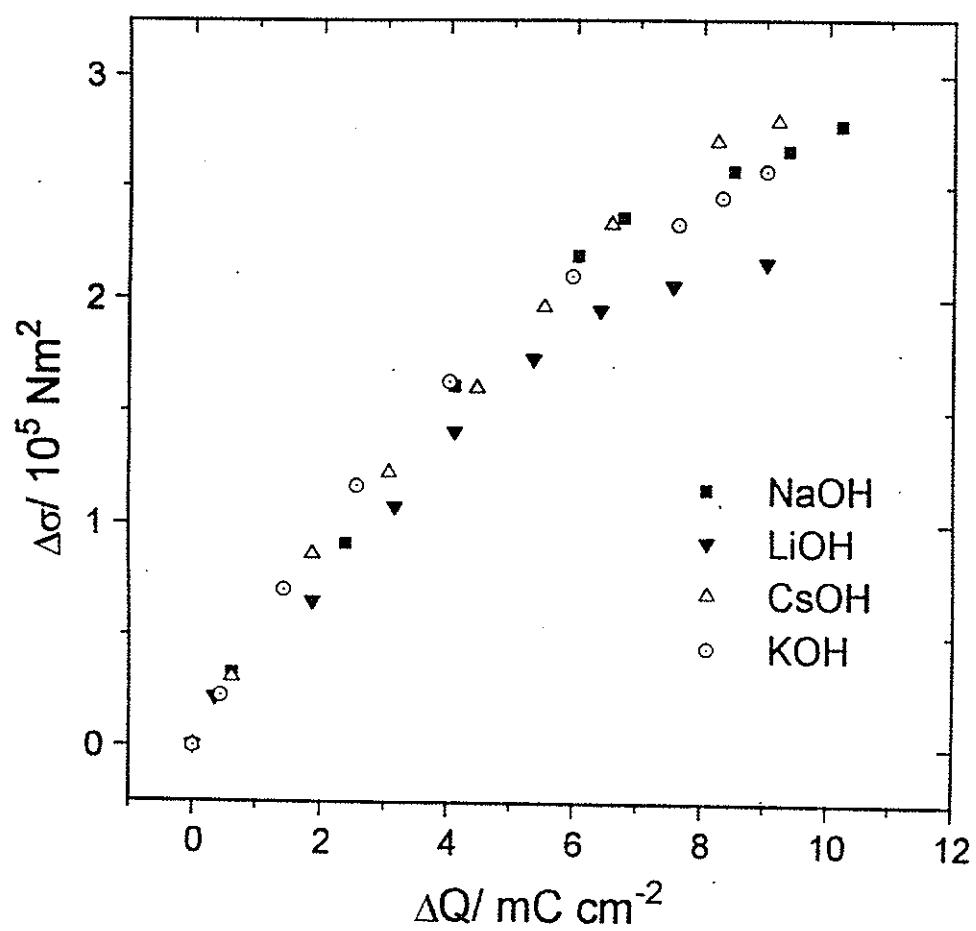


Fig 5

---

### A3. - Trabalhos sobre Supercondutores e Precursores

---

## On the formation kinetics of Bi-Sr-Co-O phases

P.A. Suzuki, R.F. Jardim<sup>1</sup> and M.C.A. Fantini

*Instituto de Física, Universidade de São Paulo, CP 20516, 01498 São Paulo, Brazil*

Received 18 August 1991

The cationic substitution of Cu by Co in the Bi-based superconductor was studied in order to determine the optimal sintering conditions to produce single-phase materials. X-ray diffraction experiments combined with differential thermal analysis (DTA) and electrical resistivity were utilized as the diagnostic techniques. The phase dependence on the starting stoichiometries as well as the atmosphere and temperature employed during the sintering process were established. Samples in the Bi-Sr-Co-O system were heat treated under both air and nitrogen atmospheres in the temperature range  $800 < T < 900^\circ\text{C}$ . The formation of  $\text{Bi}_2\text{Sr}_2\text{CoO}_y$  is favored at higher temperatures and in reducing atmosphere, while the  $\text{Bi}_2\text{Sr}_3\text{Co}_2\text{O}_y$  compound occurs for lower temperatures and in a partially oxidized ambient. The Co valence state in these compounds and the facility to grow single crystals are discussed.

### 1. Introduction

The critical temperature ( $T_c$ ) dependence on the number  $n$  of Cu-O layers in Bi-based superconductors has been studied in order to better understand the origin of superconductivity in high- $T_c$  materials [1,2]. It was found that the  $\text{Bi}_2\text{Sr}_2\text{Ca}_{n-1}\text{Cu}_n\text{O}_y$ ,  $n=1, 2$ , and 3, compounds present incommensurate modulated structures [3,4]. The correlation between the modulation and the possible appearance of superconducting properties in the Bi-Sr-M-O,  $M=\text{Fe, Co, and Mn}$ , systems was extensively investigated [5-9]. The cationic substitution of Cu by Fe resulted in phases with  $n=2, 3$ ; for Co in phases with  $n=1, 2$ , and for Mn it was observed with  $n=1, 2, 3$ . These layered stoichiometric compounds are not superconducting and present commensurate modulations, except for the Co  $n=2$  phase, which shows commensurate and incommensurate modulations in its structure [6].

An important result was obtained in a partial Bi substitution by Pb for the compounds with Mn [10]. That substitution produces a non-superconducting phase, with no evidence for structural modulations,

which is induced by an additional annealing under oxygen. These results showed that the modulations originate in the Bi-O layers by insertion of extra and periodic rows of oxygen atoms. The presence of structural modulations is not a sufficient condition for the appearance of the superconducting properties.

The fact that those materials are isostructural to the Cu-based Bi compounds, but showing commensurate modulations, allows the complete determination of their crystalline structures. This can be a useful guideline for the complete understanding of the structural properties of the Cu-based superconducting phases. However, it has been observed that the phases obtained by those cationic substitutions are strongly dependent on both sintering temperature and atmosphere [5-9]. Another point is that the related literature on the formation processes of those compounds is incomplete and presents some contradictions.

Our aim in this work is to study the formation kinetics of Bi-Sr-Co-O compounds, hoping to clarify the necessary sintering parameters to prepare single-phase materials. We chose to investigate this special system because we found it easier to prepare the  $n=1$  polycrystalline single-phase materials and to grow single crystals.

<sup>1</sup> Present address: Institute for Pure and Applied Physical Sciences, University of California at San Diego, La Jolla, CA 92093-0075, USA.

## 2. Experimental procedure

Samples with 2-2-0-1 ( $n=1$  phase) and 2-3-0-2 ( $n=2$  phase) stoichiometries (samples with  $n=1, 2$  respectively when the superconductor notation Bi:Sr:Ca:Co is utilized) were prepared by the solid state reaction method. The appropriate amounts of  $\text{Bi}_2\text{O}_3$ ,  $\text{SrCO}_3$ , and  $\text{Co}_3\text{O}_4$ , all of them with purity higher than 99.9%, were mixed and ground. The powders were calcined in air at  $780^\circ\text{C}$  for 50 h and then sintered at fixed temperatures between 800 and  $900^\circ\text{C}$  for 24 h. Samples with the 2-2-0-1 stoichiometry were treated both in air and nitrogen while those ones with the 2-3-0-2 proportion were treated only in air. In order to identify possible additional phases a  $\text{BiSrO}_x$  (1:1 at.%) sample was prepared at  $800^\circ\text{C}$ .

The phase identification was obtained by X-ray diffractometry (XRD) utilizing Ni filtered Cu K $\alpha$  radiation and a  $2\theta$  angular scanning range between 5 and 40 degrees. The lattice parameters were obtained through the refinement of observed peaks utilizing a least-squares program.

Differential thermal analysis (DTA) experiments up to  $1200^\circ\text{C}$  were performed on two samples in order to study the  $n=1$  kinetics formation more accurately.

Electrical resistivity measurement was made on the  $n=1$  single-phase sample by the dc four-lead method. The temperature was measured with a calibrated platinum resistance thermometer between 100 and 300 K.

## 3. Results and discussion

The XRD diffractograms taken of samples with  $n=1$  heat treated in nitrogen at several temperatures is shown in fig. 1. The  $n=1$  and  $n=2$  phase identification by XRD is almost immediate due to the presence of well-defined and characteristic reflections at low angles for both phases. The  $n=1$  and  $n=2$  phases can be distinguished by the (002) reflections at  $2\theta=7.54^\circ$  and  $5.95^\circ$ , respectively, when the Cu K $\alpha$  radiation is used. The results indicate that the  $n=2$  phase, coexisting with other phases, is present in samples heat treated at lower temperatures (see fig. 1a). Those peaks of the non-identified addi-

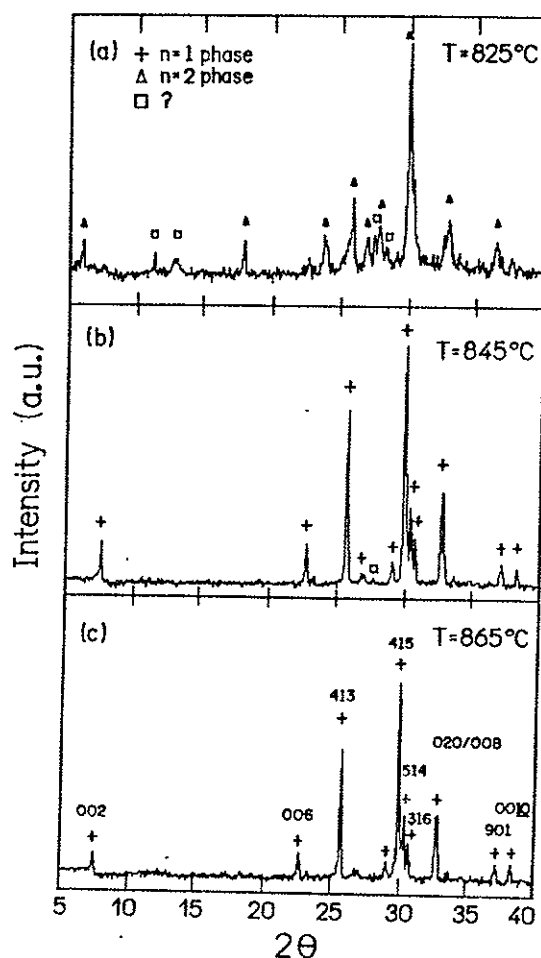


Fig. 1. The X-ray diffraction patterns of the 2-2-0-1 stoichiometric samples heat treated in nitrogen atmosphere at several temperatures: (a)  $825^\circ\text{C}$ , (b)  $845^\circ\text{C}$ , and (c)  $865^\circ\text{C}$ .

tional phases and the  $n=2$  compound decrease in intensity with increasing heat-treatment temperature (see fig. 1b). For temperatures above  $845^\circ\text{C}$  the reflections associated with the  $n=2$  phase are not detected and the compound is single phase with the  $n=1$  structure. The calculation of the lattice parameters for the orthorhombic structure resulted in  $a=21.82 \pm 0.04 \text{ \AA}$ ,  $b=5.46 \pm 0.02 \text{ \AA}$ , and  $c=23.52 \pm 0.04 \text{ \AA}$ , in good agreement with those reported in the literature [9].

The  $n=2$  phase, whose superstructure has not been determined yet, has  $c=29.8 \text{ \AA}$  [6]. The complete structure determination of this phase has been dif-

difficult since only (00 $\ell$ )-type reflections are easily identified. No vestiges of the  $n=3$  phase were observed.

The results shown in fig. 1 suggest that the  $n=2$  phase formation is favored at low temperatures, while the  $n=1$  phase is at higher ones. Another important feature is that there is no evidence for competition between those phases in our results. At 825°C there is no vestige for the  $n=1$  phase, while the  $n=2$  coexists with some additional phases. Then, at 845°C, it was possible to index almost all reflections associated with the  $n=1$  phase plus just one additional reflection possibly associated with a spurious phase. This suggests that the  $n=2$  decomposition associated with additional phases is a fundamental condition for the appearance of the  $n=1$  compound. As we have no evidence of a liquid phase, it is possible that the  $n=1$  phase is formed by an eutectoid reaction. Experiments are in progress in order to clarify this point.

The XRD results for air-treated samples with the 2-2-0-1 stoichiometry are shown in fig. 2. At 825°C, it is possible to index at least three phases in the sample studied. The  $n=2$  compound and a binary oxide phase Bi-SrO $_x$  (1:1 at.%) were determined and small reflections possibly associated with an additional phase were also observed. Once more the presence of the  $n=1$  phase at low temperatures was not observed. However, at 845°C the  $n=1$  and  $n=2$  compounds coexist with the additional phase, showing a difference when compared with the former results. For the nitrogen heat-treated samples, at 845°C (fig. 1b), no evidence was observed for the  $n=2$  phase, and the sample was almost single phase. Here, the picture is quite different. This result is more pronounced in the sample air-treated at 865°C (see fig. 2c) where the  $n=1$  and  $n=2$  phases coexist with small amounts of an additional phase. These results suggest that the  $n=1$  phase is favored at higher temperatures and that its formation is strongly environment dependent, as observed in the literature [8,9]. It was observed that the  $n=1$  phase could be obtained only in reducing atmospheres. Another point is that the observed  $n=2$  phase presence at higher temperatures in air is a strong indication that the reducing atmosphere should inhibit the  $n=2$  phase formation and accelerate its decomposition.

The results described above are also useful in or-

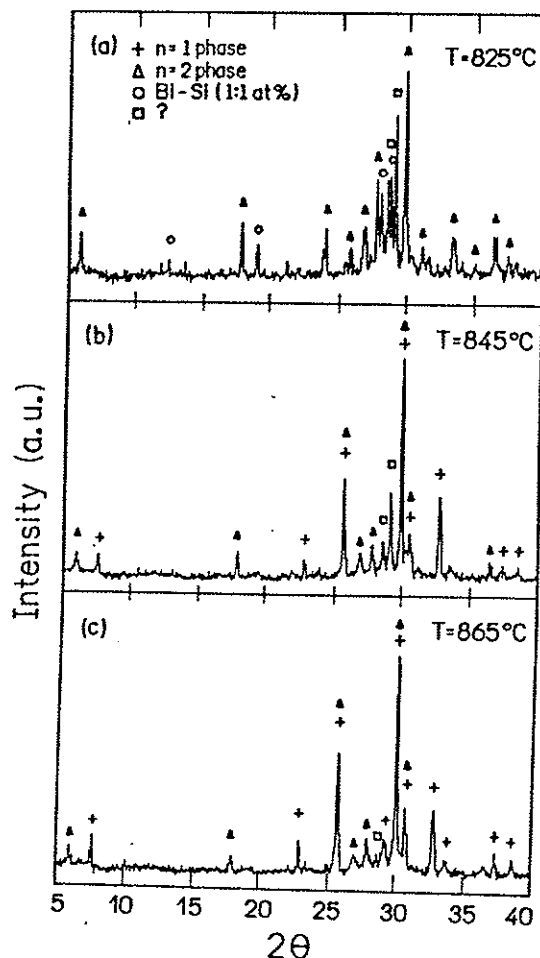


Fig. 2. The X-ray diffraction patterns of the 2-2-0-1 stoichiometric samples heat treated in air at (a) 825°C, (b) 845°C, and (c) 865°C.

der to discuss the Co valence state for these phases. For the  $n=1$  phase the Co valence state should be lower than that present for  $n=2$ , since the  $n=1$  single-phase material is obtained only in reducing atmospheres. This supposition has support from recent XPS measurements made on the same materials [6]. There it was reported that the  $n=2$  compound presents a +3 valence state and that a value between +2 and +3 was observed for the  $n=1$  phase. Another interesting point is associated with the oxygen content in the  $n=1$  phase. Further attempts to vary the oxygen concentration in that phase by heating it at low temperatures (400°C) in air for 24 h resulted

in a diffractogram with small differences in peak positions within the experimental accuracy. High-temperature annealing (600°C) even for a brief time interval of 3 h resulted in the  $n=1$  phase decomposition towards the  $n=2$  phase, as well as the appearance of additional compounds.

The XRD results for the air-treated 2-3-0-2 compound are shown in fig. 3. Again, it is possible to observe the  $n=2$  phase at low temperatures (fig. 3a) with a small amount of additional phases. While the diffractogram shown in fig. 3a can be associated with an almost single-phase material, it is possible to calculate the  $c$  parameter for that sample. We obtained  $c=29.85 \pm 0.05$  Å, which is in good agreement with

previous data reported in the literature for an  $n=2$  single-phase material obtained in a strong oxygenated atmosphere [6]. For higher temperatures, the  $n=2$  phase coexists with the  $n=1$ , as observed in fig. 2. There it is shown that the air-treated 2-2-0-1 sample and the  $n=2$  phase do not disappear at higher temperatures. A calculation of the ratio between the (002) X-ray peak intensities corresponding to the  $n=1$  and  $n=2$  phases, at both 845 and 865°C for both 2-2-0-1 and 2-3-0-2 air-treated samples, revealed that the  $n=1$  phase reflections are most intense for the 2-2-0-1 composition, indicating that the 2-2-0-1 stoichiometry favors the  $n=1$  phase formation.

In view of the above XRD results on the 2-2-0-1 and 2-3-0-2 starting stoichiometries, it is possible to suggest that the proportion of the starting materials is not sufficient to guarantee the formation of a desired single phase. Additional parameters such as heat-treatment temperature and atmosphere during the annealing, are also important.

In order to better characterize the samples, DTA measurements (not shown) were performed on two samples with starting 2-2-0-2 stoichiometry. The results can be summarized as follows. The  $n=1$  single-phase material showed a large peak between 775 and 875°C during ramping, probably associated with two near transitions. Another result was obtained in a multiphase sample, sintered at 820°C in air. Peaks were observed at 795 and 860°C during the ramping. Both samples had liquid-phase vestiges at about 900°C. The two transitions observed in the multiphase sample can be attributed to the  $n=2$  and  $n=1$  phase formation, respectively, by means of the XRD results reported above. The large transition observed for the single-phase sample is indicative of the decomposition of small amounts of spurious phases that could not be detected by XRD.

After the DTA measurements little platelet-like crystals were observed on the solidified flux surface on both samples. The XRD patterns of the total solidified fluxes are shown in fig. 4. The  $n=1$  phase was predominant and none of the (00 $l$ ) reflections belonging to the  $n=2$  phase were detected. The absence of the  $n=2$  phase, inhibited by the He atmosphere utilized in the DTA measurements and high temperatures, is in accord with our previous XRD results. Another point is that these results reinforce

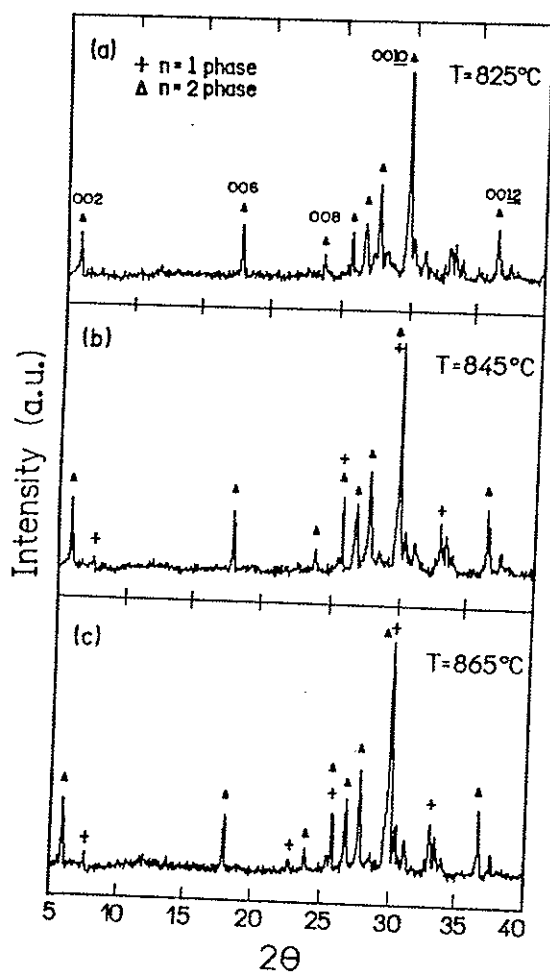


Fig. 3. Diffractograms of the 2-3-0-2 stoichiometric samples heat treated in air at (a) 825°C, (b) 845°C, and (c) 865°C.



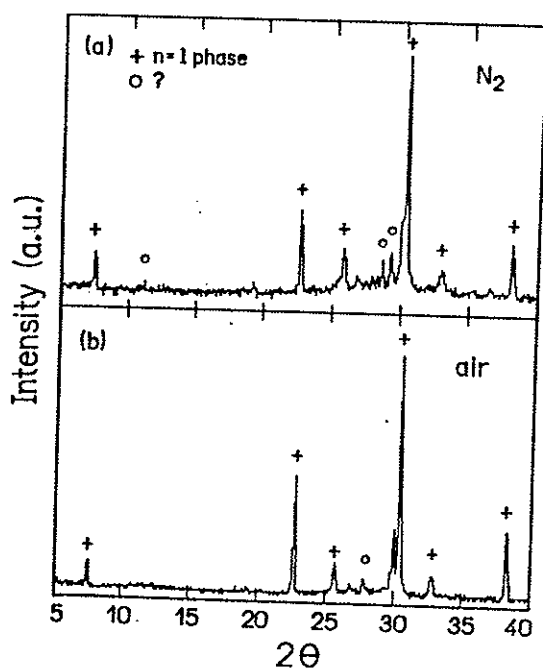


Fig. 4. The X-ray diffraction patterns of the solidified flux obtained after DTA measurements of the following samples: (a) the  $n=1$  single phase treated in nitrogen and (b) the 2-2-0-1 stoichiometric multiphase sample air-treated at 820°C.

the Co valence state described above. The X-ray peaks assigned to the  $n=1$  phase clearly demonstrate a strong preferential orientation along the  $c$  direction.

A Laue geometry diffraction experiment showed evidence of single-crystal formation. The growth of those single crystals in a simple measuring process revealed two important features: the ability to grow those crystals with no flux and at a fast cooling rate (around 10°C/min).

The electrical resistivity versus temperature for the  $\text{Bi}_2\text{Sr}_2\text{CoO}_x$  compound is displayed in fig. 5. The resistivity increases monotonically with decreasing temperature for temperatures down to 80 K. While the data were not fit by either correlated or non-correlated variable-range hopping processes, an activation process was obtained. By plotting the logarithm of the measured conductivity versus the inverse of the temperature (insert fig. 5), a straight line was obtained. This conductivity range typically corresponds to one of a semiconductor material presenting an ionic conduction with an activation energy of 0.235 eV. Similar activation energies were obtained

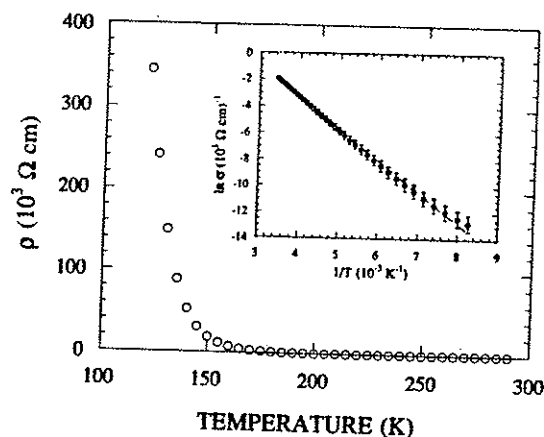


Fig. 5. Electrical resistivity dependence on the temperature for the polycrystalline  $\text{Bi}_2\text{Sr}_2\text{CoO}_x$  compound between 100 and 300 K. The insert shows the log of the conductivity versus the inverse of the temperature that results in a straight line which can be fitted by the Arrhenius law.

in the  $\text{BiPbSr}_2\text{MO}_x$  phases,  $M=\text{Co, Mn}$ . The values are 0.32 and 0.42 eV for Co and Mn, respectively [10].

#### 4. Conclusions

This work reports a systematic study on the kinetics of formation of the  $n=1$  and  $n=2$  phases of  $\text{Bi}_2\text{Sr}_{n+1}\text{Co}_n\text{O}_x$  compounds. The results show that the proper starting stoichiometry is not sufficient to obtain single-phase materials. Thus, other parameters such as atmosphere and temperature should be carefully considered.

The  $n=1$  single-phase compound was obtained in heat treatments performed in nitrogen, but not in air. On the other hand, the  $n=2$  phase is formed in a partially oxidizing atmosphere, indicating that this phase is unstable in a reducing environment. This is important experimental evidence for the discussion of the Co valence state in the  $n=1$  and  $n=2$  compounds. This work also reports an ability to grow single crystals of the  $n=1$  Co-based Bi compound without flux and at a high cooling rate.

The experimental results also contribute to the investigation of the probable conditions to produce an  $n=2$  single-phase material. Efforts are underway to grow this material, so that its unknown structure, or

at least its lattice parameters, can be determined by means of X-ray experiments.

#### Acknowledgement

Professor S. Moehlecke is greatly acknowledged for his helpful suggestions as well as critical reading of this manuscript. Professor C.C. Becerra is also thanked for reading the manuscript. Thanks are also due to A.C. Neiva for the DTA measurements. Two of us (PAS and RFJ) would like to thank the CNPq (Brazil) for financial support.

#### References

- [1] J.M. Tarascon, W.R. McKinnon, P. Barboux, D.M. Hwang, B.G. Bagley, L.H. Greene, G.W. Hull, Y. le Page, N. Stoffel and M. Giroud, *Phys. Rev. B* 38 (1988) 8885.
- [2] A. Maeda, M. Hase, I. Tsukada, K. Noda, S. Takebayashi and K. Uchinokura, *Phys. Rev. B* 41 (1990) 6418.
- [3] M.A. Subramanian, C.C. Torardi, J.C. Calabrese, J. Gopalakrishnan, K.J. Morrissey, T.R. Askew, R.B. Flippen, U. Chowdhry and A.W. Sleight, *Science* 239 (1988) 1015.
- [4] Y. Gao, P. Lee, P. Cooper, M.A. Subramanian and A.W. Sleight, *Science* 241 (1988) 954.
- [5] W.R. McKinnon, E. Tselepis, Y. le Page, S.P. McAlister, G. Pleizier, J.M. Tarascon, P.F. Micelli, R. Ramesh, G.W. Hull, J.V. Waszczak, J.J. Rhyne and D.A. Neumann, *Phys. Rev. B* 41 (1990) 4489.
- [6] J.M. Tarascon, R. Ramesh, P. Barboux, M.S. Hedge, G.W. Hull, Y. le Page, W.R. McKinnon, J.V. Waszczak and L.F. Schneemeyer, *Solid State Commun.* 71 (1989) 663.
- [7] Y. le Page, W.R. McKinnon, J.M. Tarascon and P. Barboux, *Phys. Rev. B* 40 (1989) 6910.
- [8] J.M. Tarascon, P.F. Micelli, P. Barboux, D.M. Hwang, G.W. Hull, M. Giroud, L.H. Greene, Y. le Page, W.R. McKinnon, E. Tselepis, G. Pleizier, M. Eibschutz, D.A. Neumann and J.J. Rhyne, *Phys. Rev. B* 39 (1989) 11587.
- [9] J.M. Tarascon, Y. le Page, W.R. McKinnon, E. Tselepis, P. Barboux, B.G. Bagley and R. Ramesh, in: *Proceedings of the MRS Meeting, San Diego, CA, USA, April 1989*.
- [10] J.M. Tarascon, Y. le Page, W.R. McKinnon, R. Ramesh, M. Eibschutz, E. Tselepis, E. Wang and G.W. Hull, *Physica C* 167 (1990) 20.

# Investigations on the texture of Bi-based superconductor tapes

P. A. Suzuki and M. C. A. Fantini\*

*Instituto de Física, Universidade de São Paulo, CP 20516, 01498-970 São Paulo (SP) (Brazil)*

(Received January 6, 1993; in revised form May 29, 1993)

## Abstract

The effects of successive thermomechanical treatments on the texture and morphology of Bi-based (2223) superconductor Ag-sheathed tapes were analyzed and related to the critical current density. Pressing and rolling mechanical processes were compared. X-ray diffraction results showed a large increase in the crystalline density and preferred orientation in the initial steps, and saturation after the third cycle of mechanical effort-heating. Scanning electron microscopy photographs showed differences in the morphological aspects of pressed and rolled tapes; the grains of the pressed tapes presented piled-up platelets parallel to the tape surface, a factor that was associated with the current density.

## 1. Introduction

Since the discovery of the new high  $T_c$  superconductor compounds, efforts have been made to develop flexible Ag-sheathed superconductor tapes. Many studies have been carried out to determine optimum sintering conditions for attaining higher critical current densities ( $J_c$ ). Up to now,  $J_c$  values between  $10^4$  and  $10^5$  A cm<sup>-2</sup> were obtained for Bi-based tapes ((Bi,Pb)<sub>2</sub>Sr<sub>2</sub>Ca<sub>n-1</sub>Cu<sub>n</sub>O<sub>y</sub> with  $n=2$  and  $n=3$ ) [1-6] and for YBa<sub>2</sub>Cu<sub>3</sub>O<sub>7-x</sub> based melt textured polycrystalline samples [7, 8] at  $T=77$  K and  $B=0$ .

Sintering of the Bi-based tapes requires optimization of the temperature, composition and texture of the superconductor powder. Some authors have shown that the powder packing density, connectivity between grains, and preferred crystal orientation in the tape are directly related to improvements in the conduction quality of the material. The packing density is increased by cold rolling or cold pressing [2, 3, 6, 9-11]. The intergrain connectivity is obtained by heat treatment [2-5, 10, 12-14]. A specific preferred orientation of the grains in the tapes is required [1-3, 9, 10] because the current conduction is confined to the plane parallel to the Cu-O layers [15, 16] (*i.e.* the crystallographic *a-b* plane).

Highly oriented Bi-based superconductor tapes are easily produced. One of the advantages over YBaCuO-based tapes [3] is the attainment of oriented grains with

a more homogeneous depth profile [2, 17]. Moreover, texturing of YBaCuO-based tapes occurs by a partial melting reaction that takes place in a small and high temperature range, making difficult the production of long Ag-sheathed samples. Formation of the 2223 Bi compound ( $n=3$ ) occurs through a liquid phase reaction of the low  $T_c$  phase (2212 or  $n=2$ ). The presence of the 2212 phase is fundamental for achieving good contact at the grain boundaries, a major parameter for increasing  $J_c$  [2, 3, 13, 18].

In this paper, we report our results on the texture of (Bi,Pb)<sub>2.2</sub>Sr<sub>2</sub>Ca<sub>2</sub>Cu<sub>3</sub>O<sub>y</sub> tapes obtained by the powder-in-tube method. A comparative study was carried out between pressing and rolling mechanical processes. The variations in density, crystallite size and preferred orientation of the powder in the tapes were systematically investigated by means of X-ray diffraction (XRD) and scanning electron microscopy (SEM) data analysis.

## 2. Experimental details

The oxides Bi<sub>2</sub>O<sub>3</sub>, PbO, SrCO<sub>3</sub>, CaCO<sub>3</sub> and CuO were mixed in a crucible to form the Bi<sub>1.8</sub>Pb<sub>0.4</sub>Sr<sub>2</sub>Ca<sub>2</sub>Cu<sub>3</sub>O<sub>y</sub> powder (2223 stoichiometry) by the solid reaction method. The material was calcined for 24 h at 840 °C in air, ground and submitted to a new heat treatment for 100 h in the same conditions. The composition of the resulting powder, as determined by XRD, was predominantly the 2212 phase. The 2223 compound was not detected.

The powder was inserted in an 8 mm inner diameter Ag tube and beaten. The section of the tube was

\* Author to whom correspondence should be addressed.

reduced by rotative swage to about 1 mm diameter. One tube was pressed and another tube was rolled, in order to conduct a comparative study of the two mechanical processes. The pressed tape was cut in pieces of 50 mm length and submitted to four cycles of heat treatment ( $T=850^{\circ}\text{C}$  for 110 h) and pressing. The same procedure was followed for the rolled pieces. After each process, one sample was extracted and opened. Both sides were examined by XRD and SEM. The samples were named by the first letter of each step: P for pressing, R for rolling and H for heat treatment. For example, the tape prepared in the following sequence: (pressing, heating, pressing) was designated PHP.

XRD measurements were performed in the opened tape surface using Ni filtered Cu-K $\alpha$  radiation (0.8 kW) with step-scanning mode ( $0.05^{\circ}$  for 30 s) in the angular range between  $20^{\circ}$  and  $63^{\circ}$ . About 75% of the total diffracted intensity of the powder samples is confined in the considered angular region.

SEM inspections were performed using an energy of 5 kV and  $3500\times$  magnification.

The critical current density  $J_c$  was measured after each heat treatment by the four point probe method in liquid nitrogen ( $T=77\text{ K}$  and  $B=0$ ). The criterion of  $1\text{ }\mu\text{V cm}^{-1}$  was used.

### 3. Results

The XRD reflections of the 2223 phase were identified through comparison with a diffractogram obtained by microcomputer simulation [19], using the following information from ref. 20: lattice parameters ( $a=5.407(6)\text{ \AA}$ ,  $b=5.407(6)\text{ \AA}$ ,  $c=37.051(7)\text{ \AA}$ ), space group Bbmb and atomic positions. For purposes of comparison, the diffractogram depicted in Fig. 1(a) belongs to a typically non-oriented 2223 powder sample. Figures 1(b) and 1(c) depict a sequence of diffractograms obtained at the end of each heating step, for both pressed and rolled tapes. After the first heat treatment, the powder constituents are the 2223 and 2212 superconductor phases plus some unknown species. These unreacted species and the 2212 compound are expected to decompose during the next heating steps, promoting a better connectivity between the 2223 grains [2, 13]. In fact, after the second heat treatment, a significant amount of the 2212 and spurious phases decomposed. The third heat treatment results (not shown) produced patterns similar to the former. The diffractograms after the fourth heat treatment show the 2223 phase and small amounts of unidentified materials, one of these probably being the 2201 compound [21]. A strong (00 $l$ ) crystalline orientation is observed.

The total thickness of the tapes, listed in Table 1, decreased with the number of pressing and rolling steps. Rolling was more effective than pressing for thickness reduction.

Table 2 shows the critical current density, measured after each heat treatment H at  $T=77\text{ K}$  and without magnetic field. The  $J_c$  measured after the mechanical step alone were null. The  $J_c$  value after the first H step was very low. The second H step raised  $J_c$  by about two orders of magnitude, for both pressed and rolled tapes. The third and fourth H processes held the  $J_c$  quite constant for the pressed sample, at about  $1200\text{ A cm}^{-2}$ . For the rolled tapes, however,  $J_c$  decreased. Larger critical current densities were achieved for the pressed tapes. The results will be discussed in detail later.

The XRD data were corrected for an exposed area factor, since the samples were narrower than the incident beam. The diffracted intensity was multiplied by the ratio between the areas of the sample and the X-ray incident beam. Absorption correction was not required, because the powder thickness was larger than the X-ray penetration depth. Each reflection was fitted to a Gaussian shape. The background level, maximum intensity, full width at half maximum (FWHM), and peak angular position were determined. The integrated intensity was calculated using Gaussian parameters. The statistical fluctuation in the intensity data was estimated to be around 2%. No measurable deviation in peak positions was found. The preferred orientation was determined using all reflections in the studied angular range, with a factor  $P$  defined as  $P=\Sigma I(00l)/\Sigma I(hkl)$  [1].

Both sides of each sample were measured in the diffractometer, and the average value, with its respective dispersion bar, was considered for further analysis. The differences obtained in the XRD data of the same tape are attributed to a non-homogeneous crystalline orientation of the powder. In many cases the opening of the tapes, necessary to perform the XRD measurements, did not occur precisely at the middle of the tape cross-section. A higher (00 $l$ ) preferred orientation at the Ag interface than in the bulk is expected [2], and this may be responsible for the deviations mentioned.

Information about variations in the average crystallite size can be obtained from the FWHM of the pure diffractive peaks [22]. The experimental (0024) reflection was used for this purpose. The Rachinger correction was performed to eliminate the  $K\alpha_2$  contribution [22]. The experimental peak can be expressed as a convolution relation between instrumental profile and pure profile [22]. The instrumental broadening  $b$  was determined from the FWHM of the (311) reflection of a standard silicon sample ( $2\theta=56.2^{\circ}$ ). Using the

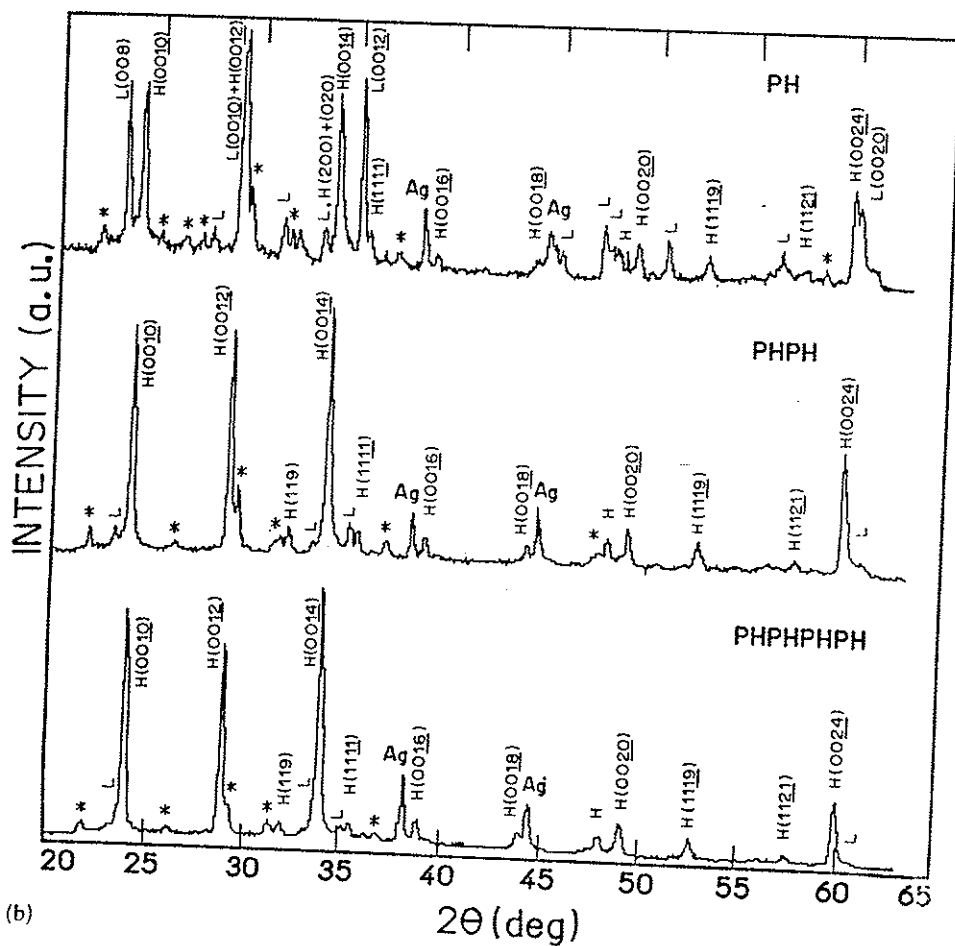
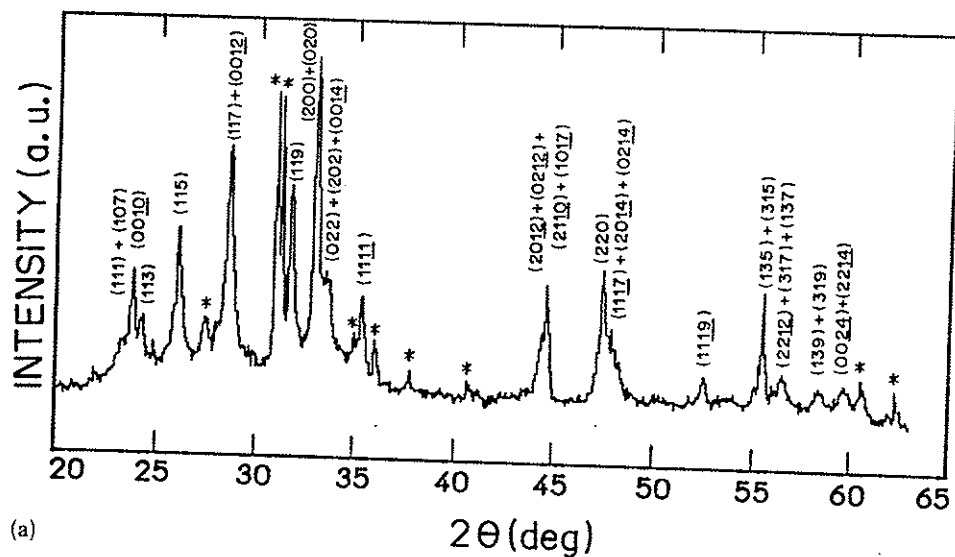


Fig. 1. (continued)



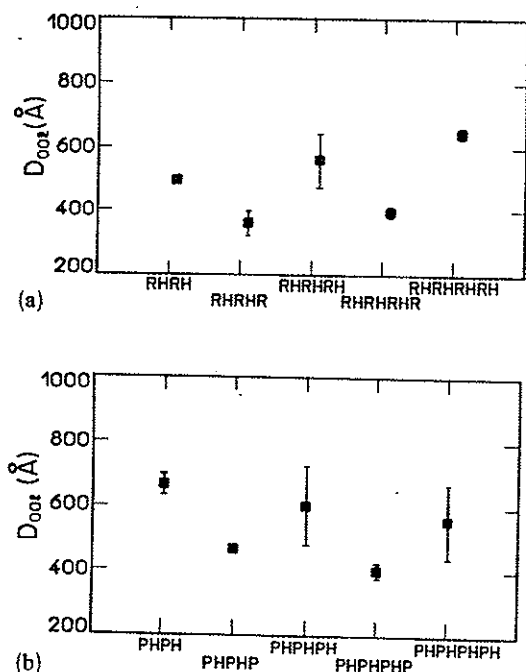


Fig. 2. Average crystallite size of (a) rolled and (b) pressed tapes.

the (0010) integrated intensity, from 0.45 to 2.2 for pressing and from 0.30 to 2.1 for rolling, was reached. The integrated intensity of the (119) reflection stayed constant within the error bars. These results are evidence of gradually increased preferred orientation in the (001) direction as the sequence of thermomechanical processes take place.

The preferred orientation of the grains for the rolled and pressed tapes are shown in Fig. 4. The  $P$  factor growth is more intense during the beginning of the sintering process and stabilizes after the third heating step. The  $P$  factor determined for the simulated powder diffractogram was 0.11, which is very small in comparison with the values attained for the tapes. It was not possible to determine the  $P$  value for the powder experimental pattern of the 2223 phase depicted in Fig. 1, due to superposition of (001) and (hk1) reflections.

Figure 5 shows SEM images of the pressed tapes cross-section. The increase of the grain size after heat treatment (Figs. 5(a) and 5(b)) and the break-up of the grains after the mechanical process are clearly observed (Figs. 5(b) and 5(c), Figs. 5(d) and 5(e)). A new heat treatment promotes regrowth of the grains (Figs. 5(c) and 5(d), Figs. 5(e) and 5(f)), and decreases the number of grain boundaries that obstruct the current passage. The micrographs also show that the mechanical effort/heat treatment combination produced grains in an oriented platelet form.

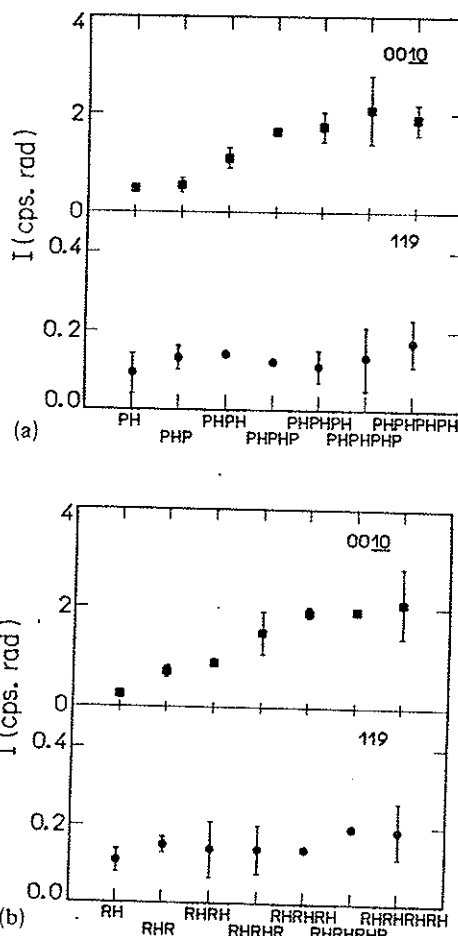


Fig. 3. Integrated intensity of (0010) and (119) diffraction peaks of (a) pressed and (b) rolled tapes.

Figure 6 shows SEM pictures of rolled tapes. The heating step promotes connectivity between grains (Figs. 6(a) and 6(b), Figs. 6(c) and 6(d)) and the mechanical effort step causes break-up of the grains (Figs. 6(b) and 6(c)), as in the pressed tapes. A comparison between pressed and rolled tapes shows morphological differences between the different tapes. The pressed sample presented a tendency to form piled-up platelets, while the rolled tape showed isolated thin platelets almost entirely. The origin and consequences of these differences will be discussed later.

#### 4. Discussion

Technological applications of the new high  $T_c$  superconductors require optimization of many processing parameters, beginning with the ability to produce long and flexible wires (tapes) or homogeneous large area thin films, and continuing with the improvement of

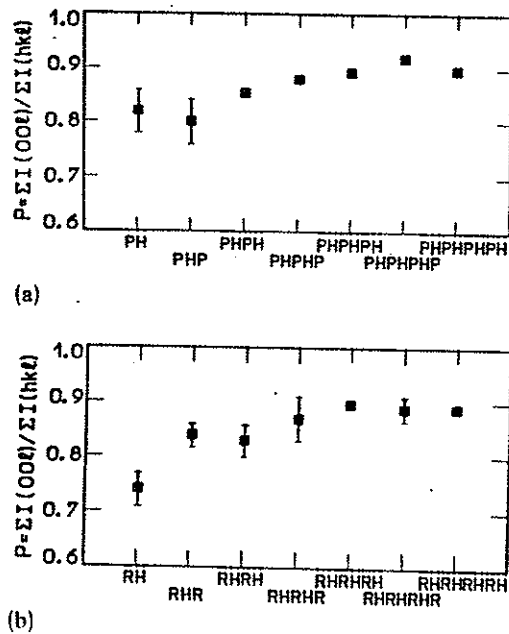


Fig. 4. Preferred orientation of (a) pressed and (b) rolled tapes.

relevant physical properties, e.g. high critical current densities at proper temperature ranges and magnetic fields [3, 5, 17, 18, 23]. In particular, the production of superconductor tapes involves enhancement of different factors such as (i) homogenization of the high  $T_c$  phase; (ii) fine dispersion of non-superconducting phases; (iii) good alignment of grains in a preferred crystallographic orientation; and (iv) strong bonding of grains at grain boundaries. All of these parameters are optimized by thermomechanical processing.

The aim of our work was to follow variations in the critical current density caused by one of the above mentioned parameters, that is the tape microstructure. The rise of  $J_c$  was accompanied by a systematic and detailed XRD and SEM analysis carried out on pressed and rolled tapes.

The critical current density values attained in this work are smaller than the best values in the literature [1–6], due to the large thickness of our tapes. It is known that the decrease in tape thickness is usually followed by an increase in  $J_c$ . The reason for this behavior is the surface orientation of the grains during the mechanical processing that is also responsible for the thickness reduction [2, 3, 10, 17]. Our results are similar when compared to  $J_c$  values reported in the literature for tapes having similar thickness [3]. The fact that our  $J_c$  values are not optimized does not invalidate our study of the influence of microstructural parameters on the rise of  $J_c$ , since the experimental evidence furnishes guidelines for the improvement of the critical current density.

Large variations in the density and preferred orientation, accompanied by the rise of  $J_c$ , were observed up to the third cycle. These parameters attained saturation for further steps, confirming that three cycles are sufficient to rise  $J_c$  close to the maximum [2, 3, 24]. Our XRD results showed that, after the second cycle, only a small amount of the 2212 phase remains in the powder. There are indications that the decomposition of the 2212 phase and other species, via a liquid phase reaction, leads to formation of the 2223 phase and promotes the connections at the grain boundaries that improve  $J_c$  [2, 3, 13, 25]. The importance of the grain boundary improvements to the  $J_c$  enhancements are reported in the literature [4, 5]. In our samples, an abrupt rise of two orders of magnitude in  $J_c$  after the second heat treatment is related to the decomposition of those phases to form the 2223 compound (see Figs. 1(b) and 1(c)). However, in the next heating steps, we believe that the amount of the 2212 phase was not enough to join the grains together; therefore, the grain connections were not completely restored. Besides the thickness restriction already mentioned, the low  $J_c$  values obtained are also attributed to poor intergrain connectivity, probably caused by the missing 2212 phase that should be present until the last heating step. Preparation of new samples in order to optimize the heating conditions are in progress.

As far as we know, values of the crystallite size are not reported in the literature, despite the fact that XRD is one of the techniques most used to characterize superconductor tapes [1–3, 10, 17, 25]. The crystallite sizes, determined from our XRD data, in the direction perpendicular to the surface ( $c$ -direction) are around 500 Å. They break-up under tension and recrystallize during the heat treatment (see Fig. 2). The thickness of the platelets, seen in the SEM images, can be associated with this parameter. The same pictures show that the grains in the plane parallel to the surface ( $a$ - $b$  plane) have different sizes, in the micrometre range. They are associated with the crystallite size in the  $a$ - $b$  direction, which is not accessible to XRD measurements. They also break-up during the mechanical effort and recrystallize by annealing (see Figs. 5 and 6). The morphological aspects of our tapes are similar to those reported by other authors [4, 5].

Comparing the  $J_c$  values obtained for the two different tapes, we can see that the rolled samples had smaller current densities when compared to the pressed samples for the same number of cycles, although they have smaller thickness (see Table 1). This discrepancy could be explained by assuming that only a perpendicular force acts during pressing, while there is also a force component parallel to the surface during rolling. Since this parallel component exists, the platelets of the rolled tapes are not able to pile-up (see Fig. 6),



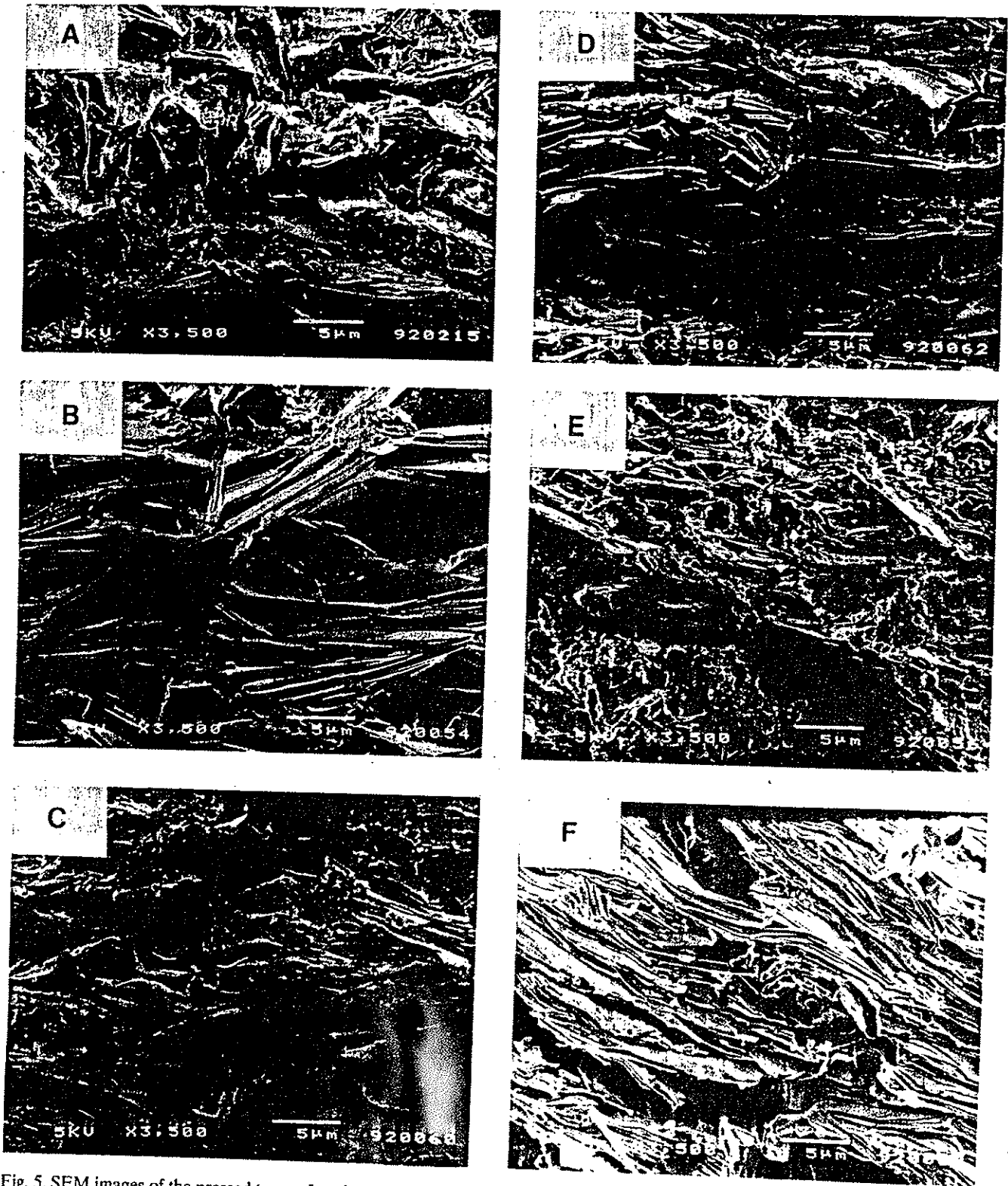


Fig. 5. SEM images of the pressed tapes after the following thermomechanical steps: (A) PHP; (B) PU PH; (C) PHPHP; (D) PHPHPH; (E) PHPHPHP; (F) PHPHPHPH.

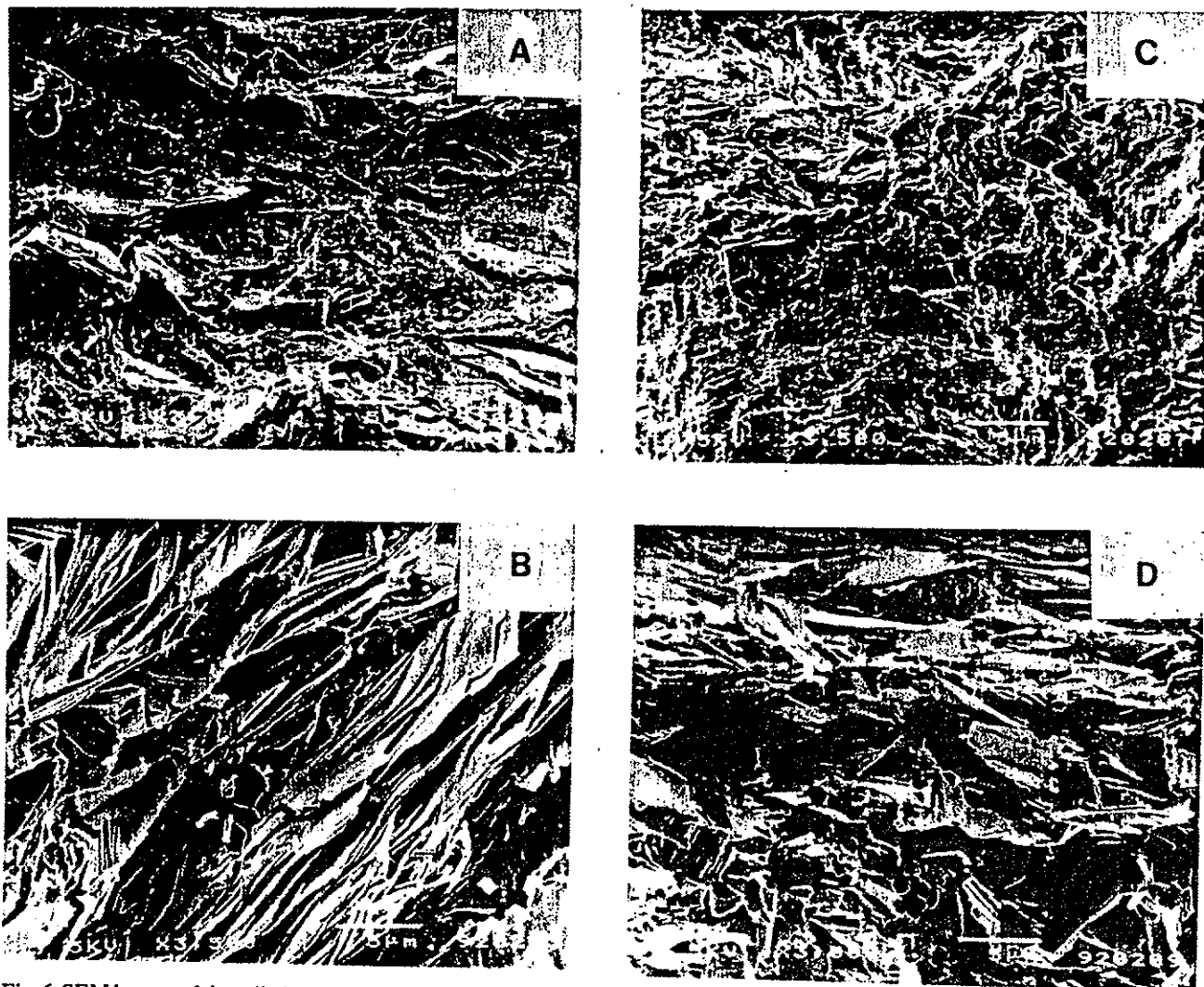


Fig. 6. SEM images of the rolled tapes after the following thermomechanical steps: (A) RHR; (B) RHRH; (C) RHRHR; (D) RHRHRH.

although the crystallite size in the  $c$ -direction presents some growth (see Fig. 2). On the other side, the pressing method causes a slight decrease in the values of  $D_{(001)}$ , but the platelets are easily stacked (see Fig. 5). These results show that the thinner piled-up platelets allow a higher critical current flow, because the neighbor grains are properly connected through a large boundary area. Those findings are in agreement with earlier results comparing the effectiveness of pressing over rolling [10, 11, 24] and are also consistent with the brickwall model of current flow [25, 26].

Texturing is claimed as a major factor for high  $J_c$  values [1, 3]. The parameters used in the pertinent literature to define the texture are not unified. Therefore, a quantitative comparison between our results (*i.e.* the  $P$  values) and other published data is meaningless. Nevertheless, a qualitative inspection leads to the conclusion

that the degree of preferred orientation obtained in this work is similar to that attained by the tapes showing the highest critical current densities.

## 5. Conclusions

Variations in density, crystallite size and preferred orientation were determined during the sintering process of superconducting tapes, by a systematic analysis of XRD data. SEM images were used to clarify some morphological aspects, such as the break-up of large grains after either pressing or rolling, the increase of powder density and the orientation of the grains in the form of platelets.

The pressing (rolling) added to the heat treatment procedure caused the preferred orientation and the